# DNA Origami
## A substrate for the study of Molecular Motors

**SHELLEY WICKHAM**

A thesis submitted in partial fulfillment of
the requirements for the degree of
Doctor of Philosophy at the University of Oxford


New College
University of Oxford
Hilary Term 2011

# DNA Origami - a substrate for the study of molecular motors

Shelley Wickham, New College.
(Department of Physics)

Thesis submitted for the degree of Doctor of Philosophy
at the University of Oxford, Hilary Term 2011.

## Abstract

DNA origami is a method for constructing 2-dimensional nanostructures with arbitrary shapes, by folding a long piece of viral genomic DNA into an extended pattern (Rothemund, 2006). In this thesis DNA origami nanostructures that incorporate active transport are developed, by combining rectangular DNA origami tiles with either synthetic DNA motors, or the protein motor $F_1$-ATPase.

The transport of an autonomous, unidirectional, and processive 'burnt-bridges' DNA motor across an extended linear track anchored to a DNA origami tile is demonstrated. Ensemble fluorescence measurements are used to characterise motor transport, and are compared to a simple deterministic model of stepping. The motor moves 100 nm along a track at 0.1 $nms^{-1}$. Atomic force microscopy (AFM) is used to study the transport of individual motor molecules along the track with single-step resolution. A DNA origami track for a 'two-foot' DNA motor is also developed, and is characterised by AFM and ensemble fluorescence measurements.

The burnt-bridges DNA motor is then directed through a track network with either 1 or 3 bifurcations. Ensemble fluorescence measurements demonstrate that the path taken can be controlled by the addition of external control strands, or pre-programmed into the motor.

A method for attaching the rotary motor protein $F_1$-ATPase to DNA origami tiles is developed. Different bulk and single-molecule methods for demonstrating protein binding are explored. Single-molecule observations of rotation of the protein motor on a DNA origami substrate are made, and are of equivalent data quality to existing techniques.

# Acknowledgements

Many people have contributed to the work presented in this thesis through guidance, experimental assistance and equipment or funding.

Firstly, I would like to thank my supervisors **Prof. Andrew J Turberfield** and **Dr. Richard Berry**, for a wealth of ideas and advice throughout my time at Oxford. They provided the initial ideas for the work in this thesis, and saw the project right through to editing this document. Richard's patience with my greater focus on the DNA motor side of the project was particularly appreciated, as was the advice given by both supervisors in applying for postdoctoral positions.

A number of researchers in Oxford made indispensable contributions to my education in biochemical techniques, and to the work in this thesis. **Dr Jonathan Bath**, in the DNA group, taught me all the basics from how to pipette DNA to cell culture, and spent much time puzzling over DNA origami and motor designs with me. Most importantly he persuaded Varian to fix our fluorimeter in the last 6 months of this work, without which Chapter 5 would not exist. **Christophe Erben** helped me to modify and purify the tris-NTA DNA, and **Mireya Mckee** gave me much advice on HPLC techniques and DNA labelling.

In the Berry group, **Dr Tom Bilyard** and **Dr Wei-Meng Ho** provided the $F_1$-ATPase used in this work, and also a huge amount of practical advice that was critical in getting the protein to bind to DNA tiles. The $F_1$ spinning experiments and analysis were done in close collaboration with **Dr Bradley Steel**, and benefited a great deal from **Ashley Nord's** work on perfecting the laser dark-field microscope set-up.

In August and September 2009, I was very lucky to be able to visit the Sugiyama Laboratory at Kyoto University, Japan. **Prof. Hiroshi Sugiyama** was very enthusiastic about the collaboration, and incredibly supportive both during and after my visit. During this time the preliminary high-speed AFM observations were made. After I returned to Oxford, the experimental measurements were continued by **Yousuke Katsuda** and **Kumi Hidaka**. The huge amount of AFM data required to produce the static and movie analysis of the DNA motors in this thesis are a testament to Hidaka-san's expertise and patience with the AFM. All the Sugiyama Lab members were very kind and generous in helping me to enjoy my time in Japan, and to experience the beauty and culture of Kyoto.

During my time as a D.Phil student at Oxford I received financial support from the Clarendon Bursary, Overseas Research Student scheme, and the Oxford-Australia Scholarship Fund. My visit to Kyoto University was generously funded by a CREST Fellowship, from the Japan Science Technology Agency.

More generally, I was very lucky to have been a member of the DNA and Berry groups at Oxford University. Both groups provided an excellent atmosphere of shared knowledge and ideas

in which to work. In addition to Jon, Christophe and Mireya, **Helen Carstairs**, **Anthony Genot** and **Daniele Selmi** provided me with much practical advice and help when I first joined the DNA group. The other D.Phil students I started with, **Richard Muscat**, **Parminder Lally** and **Anthony Walsh** made lab work much more interesting, and Parminder and I spent many late nights and weekends in the office commiserating with each other on the dullness of writing up and the brokenness of the fluorimeter. Later members **Adam Wollam**, **Carlos Sanchez** and **Robert Machinek** brought important new skills, such as coffee and mulled wine production, to the group. Members of the Berry group, including **Matt Baker**, **Richard Branch** and **Teuta Pilotza**, provided some very interesting group meetings, and excellent dinners.

On a more personal note, my time at Oxford would not have been the same without the great friends I made through being a member of the **New College** MCR. During my first year in England I was very lucky to live with **Paul**, **Sophie** and **Gargi**. **Sylvie Mardigian**, **Georgina Lindsay** and **Penelope Sullivan** made my last few years in Oxford an amazingly fun and memorable time.

Finally, I dont think I would have gotten through this D. Phil without my family and **James Harvey**. James and I have helped each other through the draining experience of finishing and writing up our theses, and he has always managed to cheer me up when things weren't going well and it all seemed impossible. My mother **Nicki Wickham** has always supported me and patiently listened when I try to explain what I do. Her shipments of tim-tams, milo and soy-sauce, and her visits to Oxford and plane tickets home have kept me going through my time in England.

Shelley Wickham
Oxford, January 2011

*To John Wickham*

# Contents

Chapter 1

# Introduction

DNA is a excellent nanoscale building material. It has a well known and regular nanoscale geometry, predictable intra- and intermolecular interactions, a combination of stiffness on the nanoscale and flexibility at higher scales or in single strands (Travers and Thompson, 2004; Travers, 2004), and it is easy to chemically synthesise, manipulate and characterise (Liu et al., 2005). By the mechanism of Watson-Crick base pairing, DNA nanostructures are able to self-assemble in large numbers, of order $10^{13}$, in 'single pot' reactions.

The field of DNA nanotechnology has been driven by the high yields of complex structures obtained and simple manufacturing processes. A wide range of different DNA structures (Nangreave et al., 2010) and machines (Bath and Turberfield, 2007; Simmel, 2009) have been developed, as well as DNA structures which incorporate other functional materials, such as proteins or metallic nanoparticles. A number of potential applications have been proposed, from use in patterning nanoelectronics, to immobilising proteins for structure and interaction studies, and even as logical devices.

However, these synthetic structures fall far behind those found in living organisms in both complexity and functionality. In biological systems, the active transport of smaller components is used to assemble and operate more complex structures than can be achieved in a single step. By similarly incorporating active transport into synthetic DNA nanostructures, a much wider range of structures and functions will be possible. For example, artificial assembly lines that mimic the ribosome in cells. This thesis aims to develop and characterise active DNA systems, which combine molecular motors with DNA nanostructures.

The DNA systems developed in this thesis are based on DNA Origami. This is a method for making nanostructures by folding one long piece of DNA into an extended pattern, which is held in place by many short synthetic 'staple' strands. It can be used to construct arbitrary 2-dimensional shapes (Rothemund, 2006), as well as complex 3-dimensional objects (Shih et al., 2004; Douglas, Dietz, Liedl, Högberg, Graf and Shih, 2009; Dietz et al., 2009). Each staple strand is unique, and the origami tile consists of an array of addressable sites, or pixels, suitable for the addition of functional elements such as proteins or nanoparticles.

This thesis demonstrates the use of DNA origami as a substrate for different types of molecular motors. A rectangular DNA origami tile is assembled and characterised, and then adapted for use with either synthetic DNA motors (Figure 1.1 A) or the naturally occuring rotary protein motor $F_1$-ATPase (Figure 1.1 B). This allows for the most detailed characterisation of DNA motor transport across a linear track of many motor cycles to date. Furthermore, the 2-dimensional nature of the origami substrate provides a unique method for investigating DNA motor transport on complex track geometries with junctions and corners. This represents a significant advance in molecular robotics: the synthetic motors are able to negotiate complex environments in response to external or pre-programmed instructions. Finally, for the $F_1$-ATPase system, the molecular motor protein is integrated into

a hybrid protein-DNA nanostructure, and single-molecule measurements of the active protein component of the structure are made. This provides a method for harnessing natural protein motors for use in synthetic systems; it also provides a new tool for the immobilisation and biophysical study of the protein motor itself.

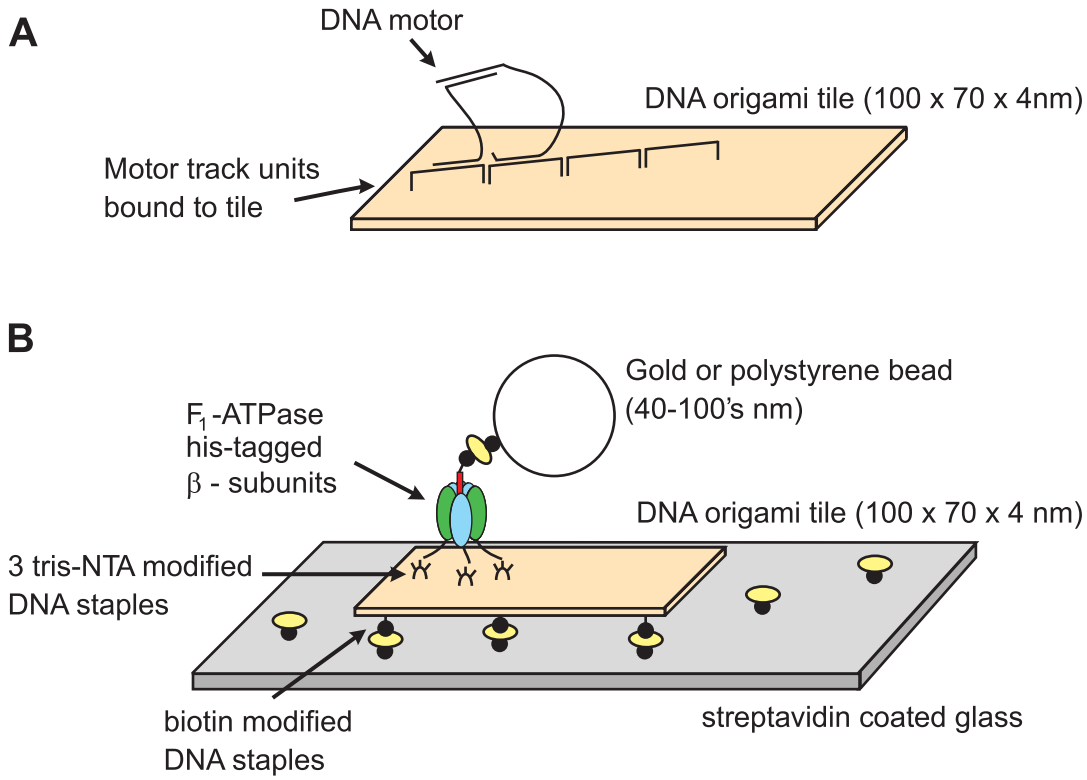


Figure 1.1: The overall scheme of this thesis. A rectangular DNA origami tile acts as a substrate for: **A** a track bound DNA nanomotor, and **B** rotation studies of the motor protein $F_1$-ATPase.

**Thesis structure:**

The remaining sections of Chapter 1 provide an overview of relevant background work. A review of self-assembling DNA nanostructures is given, focusing on recent applications of DNA origami. Natural and synthetic molecular motors are introduced, followed by a detailed review of DNA motor mechanisms and applications. The final section of the chapter contains a description of the structure and mechanism of the motor protein $F_1$-ATPase.

Chapter 2 contains general results for the DNA origami structures used in the course of this work. Chapters 3 and 4 describe the development of linear DNA origami tracks for two DNA motor designs. In Chapter 3, transport of an autonomous, unidirectional, and processive 'burnt-bridges' style motor across a DNA origami tile is demonstrated. In Chapter 4 a track for a more sophisticated 'two-foot' DNA motor is investigated. Chapter 5 extends the work on motor transport to bifurcating tracks with junctions. Chapter 6 presents a method for anchoring the rotary motor protein $F_1$-ATPase to origami tiles, which is then used in single-molecule rotation measurements. Chapter 7 gives a final summary of the work presented in the thesis, as well as general conclusions and avenues for future research.

## 1.1 Self-assembling nanostructures

Traditional methods for making nano-scale objects and devices take the 'top-down' approach, where larger devices are used to machine bulk materials down into smaller structures. A classic example is the photolithography and resist techniques used to manufacture solid-state logic devices, such as microprocessors. An alternative approach, described as 'bottom up', is to build structures up from smaller precursors, either by deposition or, more interestingly, by designing systems that are able to self-assemble. Material science examples include using scanning tunneling microscopes (STM) to arrange individual atoms on a surface (Eigler and Schweizer, 1990), and carbon nanotubes (Iijima and Ichihashi, 1993) or block-copolymers (Stoykovich et al., 2005) that self-assemble into well-ordered structures.

However, it is in biological systems that the most sophisticated self-assembling structures are observed. The cytoskeletal scaffold of cells and the protein capsules of viruses are examples of complex and in some cases dynamically re-modelled nanostructures. The protein motors that form an intricate part of cell metabolism, motion and signal transfer are complex linear and rotary nano-machines. This has lead to the development of biomimetic self-assembling nanostructures, that are both inspired by natural systems and actually made from biomolecules like DNA and polypeptide chains. This section describes the development of such nanostructures, with a focus on those made from DNA.

### 1.1.1 Self-assembly with DNA

The first synthetic DNA nanostructures were proposed as a modification of the 4-arm Holliday-Junction (HJ) motif found in DNA recombination events (Seeman, 1982). Such junctions consist of four arms joined at a central node and may

be constructed from four oligonucleotides (oligos) incorporating complementary sequences that hybridise to form the arms (Figure 1.2 A). As long as the sequences on either side of the node are non-complementary, the junction will be immobilised. Each arm finishes with a short piece of single-stranded DNA (ssDNA) called a 'sticky end'. Hybridisation of complementary sticky ends between different tiles can assemble the junctions into a larger array. The array is assembled by adding the component oligos together in solution, and annealing the sample by heating and cooling slowly to allow the strands to form the minimum energy structure.

These principles have been used to construct a huge range of synthetic DNA structures. Modifications of the HJ design lead to the more rigid double crossover (DX) motif, which has been tiled to form 2-dimensional arrays up to $\mu$m in size (Winfree et al., 1998). Typically structures are made from short synthetic DNA oligos, but may also incorporate longer DNA strands built up by polymerase amplification (PCR) of shorter oligos (Shih et al., 2004; Lubrich et al., 2005). Different junction geometries are possible (He and Mao, 2006), and arrays may be formed with only a single repeated oligo sequence (Liu et al., 2006). The nucleated assembly of DX tiles into an array can be designed to follow computational rules to form fractal patterns (Rothemund et al., 2004) or to implement counting algorithms (Barish et al., 2005).

### Functionalised DNA nanostructures

DNA arrays have been functionalised with a number of different molecules. Proteins have been attached through the noncovalent biotin-streptavidin interaction (Yan, Park, Finkelstein, Reif and LaBean, 2003; Park et al., 2006), DNA or RNA aptamers (Liu et al., 2005; Cheglakov et al., 2008), DNA binding properties of the proteins (Malo et al., 2005), or modification of the DNA with Ni-NTA (Nitrilotriacetic acid) to bind His-tags on recombinant proteins (Goodman et al., 2009).

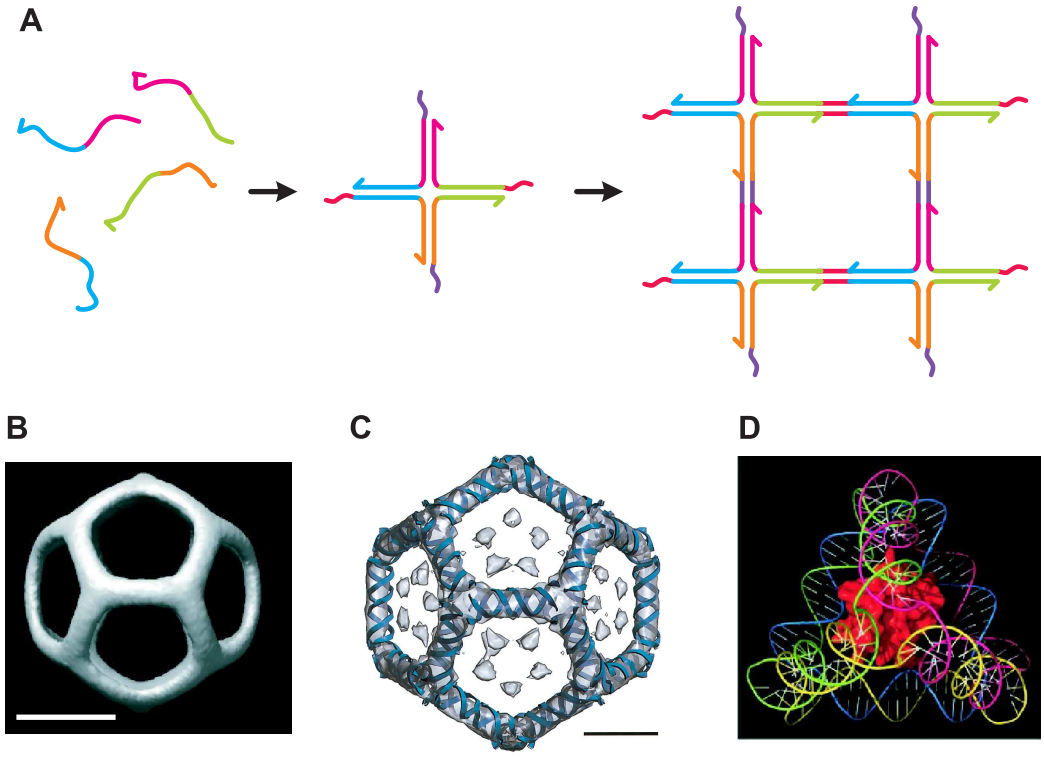


Figure 1.2: Self-assembling DNA nanostructures. **A** Watson-Crick base pairing leads complementary nucleotide sequences to form a duplex in solution, and can be used to design ssDNA strands that will self-assemble into a 4-arm Holliday Junction (HJ). Sticky-ends (red and purple) can be used to tile junctions into larger arrays. **B** These principles can be used to assemble a range of complex structures, such as a synthetic dodecahedron (He et al., 2008). Scale bar 20 nm. **C** A naturally occuring dodecahedral RNA cage found in the virus capsid of the Pariacoto virus (Tang et al., 2001) has a similar structure, but is ∼40× smaller. Scale bar 50 Å. **D** A synthetic DNA tetrahedron encapsulating a molecule of the protein cytochrome C (Erben et al., 2006).

Various metallic nano-particles have also been attached, for example producing 2-D arrays of 10 nm gold nanoparticles (Sharma et al., 2006), with the aim of using the metal-DNA elements as components of a nanoelectronic circuit. Organic molecules may be similarly arranged by a DNA backbone, and polymerised together (Zhu et al., 2003).

An interesting recent application of a 2-D DNA lattice is as an artificial extracellular matrix for tissue culture (Aldaye et al., 2010). The lattice is functionalised with the protein human fibronectin, and good attachment of human cervical cancer cells is seen only when both the DNA scaffold and protein are present. The persistence length of the lattice can be altered by adding ssDNA segments to the HJ arms. More flexible lattices produce more rounded cells, with an increased number of substrate-bound integrin receptors. The integrin pathway activates other cellular responses, and changing the properties of the DNA lattice leads to detectable changes in the levels and localisation of several proteins in the cells.

### DNA polyhedra

DNA structures are not limited to 2-dimensions. A 3-D DNA lattice has been assembled (Zheng et al., 2009), as well as a range of different DNA polyhedra (Figure 1.2 B, D). The final shape of DNA polyhedra can be controlled either by sequence design (Goodman et al., 2005; Zhang and Seeman, 1994; Shih et al., 2004) or by altering the flexibility of vertices (He et al., 2008). An alternative approach is to use organic molecules with fixed bond angles at vertices, and dsDNA as edges (Aldaye and Sleiman, 2007). Such designs have a striking resemblance to structures found in nature, such as the dodecahedral cage of genomal RNA found in the Pariacoto virus (Tang et al., 2001) (Figure 1.2 C).

Polyhedra can be modified with proteins or nanoparticles in the same way as arrays. A DNA tetrahedron has been used to encapsulate the protein cytochrome

C (Figure 1.2 D) (Erben et al., 2006), and triangular prisms can encapsulate gold nanoparticles (Lo et al., 2010). Such designs have potential for use in drug-delivery, as they can be triggered to open only on reaching a specific drug target.

#### Templated DNA structures

The first DNA structures were built up by the rational design of short synthetic oligonucleotides, of order 100's of nucleotides. An alternative approach is to take a much longer ssDNA strand and use short synthetic 'helper' strands to fold it up into a well-defined structure (Shih et al., 2004). The long scaffold or template strand can be ligated together from shorter synthetic strands (Yan, LaBean, Feng and Reif, 2003), and amplified by polymerase chain reactions (PCR) (Shih et al., 2004). Longer template strands can be taken directly from a single-stranded viral genome, allowing for much larger and more complex structures (Rothemund, 2006). This method is known as 'scaffolded DNA origami', and can be used to assemble arbitrary 2-dimensional shapes. As this technique is used extensively in this thesis, DNA origami is discussed in more detail in Section 1.2.

### 1.1.2 Switchable DNA machines

Alongside the development of DNA nanostructures, a number of DNA machines have been developed. The first was a simple DNA device in which two duplexes can be held together either at both ends, or only one, forming a DNA 'tweezer' that can be opened or closed. The device switches between states in response to the addition of signalling ssDNA strands (Yurke et al., 2000) (Figure 1.3 A). Switching occurs through toe-hold mediated strand displacement, where a sticky-end can be used to initiate replacement of one strand in a duplex with another longer one (Yurke and Mills Jnr, 2003). A similar device results in the rotation of one helix of a cross-over tile (Yan et al., 2002), again in response to a ssDNA control strand.

Many copies of this second device have been incorporated into a larger DX tile array (Ding and Seeman, 2006). Other examples include a switchable HJ array, in which one arm of the HJ changes length (Feng et al., 2003), and DNA tetrahedra (Goodman et al., 2005) or prisms (Aldaye and Sleiman, 2007) that are opened by elongating one edge duplex.

The DNA tweezers have been the subject of a theoretical study, using a coarse-grained nucleotide model to calculate the free energy landscape for the full reaction cycle (Ouldridge et al., 2010). This provides additional information about the rates of strand displacement. In particular, the opening control strand displaces the first tweezer arm more slowly than the second. The theoretical model can be used to test possible causes for this. It was found that the displacement rate is reduced by hairpin formation in the long ssDNA section of the control strand, and also by steric restriction as more nucleotides of the control strand are drawn closer into the tweezer complex. There are many variables that can be altered in the design of DNA devices like the tweezer, and the DNA motors described in Section 1.3.2. By providing a much better understanding of the way small design variations can affect the rate of strand displacement, such models should provide a useful tool in improving device design.

The trigger strands for these DNA devices do not have to be added externally, but can also be produced in solution by some other process. For example, the tweezers can be triggered by an output mRNA strand from an *in vitro* transcription reaction regulated by the lac operon (Dittmer et al., 2005). The external signal is instead the addition of lactose. Another device design contains photo-activated azobenzene-modified DNA that can be switched between trans and cis states by visible and UV light. This controls the secondary structures of a DNAzyme, either preventing it from cleaving an RNA substrate or allowing cleavage depending on the signal provided by external illumination (Zhou et al., 2010).

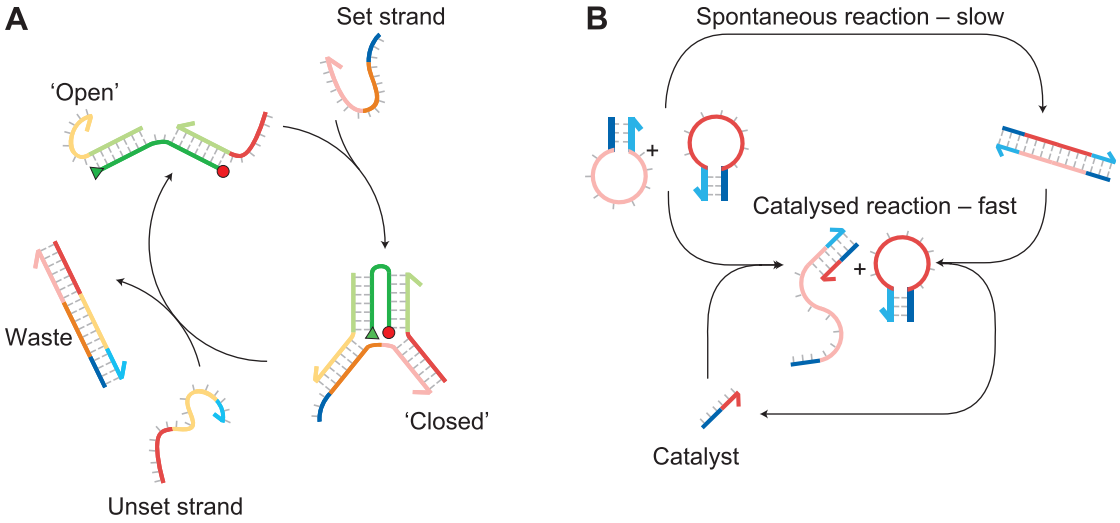


Figure 1.3: DNA machines. **A** DNA tweezers can switch between open and closed states, in response to the addition of a 'set' or 'unset' control strand (Yurke et al., 2000). The control strand binds to a ssDNA toe-hold (yellow or blue). **B** Complementary DNA hairpins interact slowly due to their secondary structure. The reaction can be catalysed by a ssDNA strand that binds to a toehold on one loop and opens the hairpin (Turberfield et al., 2003). Hairpin loops can be used as a fuel source for DNA machines and motors. Images from (Bath and Turberfield, 2007).

A modified DNA tweezer can be used to detect pH; the two arms are held together by an I-tetraplex motif, which is closed at low pH (5) and open at high pH (7.3) (Modi et al., 2009). Interestingly, this pH switch has been shown to be equally effective *in vivo*, and has been used to track pH changes from the early (pH 6.2) to late endosome (pH 5.5), and then to the lysosome (pH 5) in *Drosophila* hematocytes (Modi et al., 2009). The pH switch is taken up into the cell by a receptor mediated pathway, either targeting the negatively charged DNA, or a protein tag attached to the device, and remains intact for 2 hours.

### DNA logic

Designs in which the state of a DNA system is altered by toe-hold interaction can be extended to produce a series of DNA logic gates, where the output depends on a combination of inputs. A number of increasingly complex *in vitro* systems have been demonstrated. For example, a DNA logic system has been designed to detect a combination of 4 mRNAs, which are known to be either up or down-regulated in the presence of prostate cancer, and output a therapeutic ssDNA molecule in response (Benenson et al., 2004). In another example, a set of gates acts to play a game of noughts and crosses; the user adds trigger strands and the system computes a move accordingly (Stojanovic and Stefanovic, 2003). More recent work has involved producing a basis set of DNA gates that may be re-used for a range of different functions, and devising a convenient notation for such systems to aid the design of ever more complex functions (Yin et al., 2008).

DNA devices have also been bound to a linear DNA track, and through the use of sequentially added DNA strands, induced to move along it (Shin and Pierce, 2004). This type of DNA 'walker' or motor is the focus of Chapters 3, 4 and 5 of this thesis, and different designs and walking mechanisms are discussed in more detail in Section 1.3.2.

### 1.1.3 Bio-inspired nanostructures from other materials

The simple rules of DNA hybridisation make the assembly of DNA structures relatively easy to control, and a number of computing tools are available to aid in sequence design and to predict strand interactions (Zadeh et al., 2010; Markham and Zuker, 2005; Goodman, 2005; Douglas, Marblestone, Teerapittayanon, Vazquez, Church and Shih, 2009). However, DNA is relatively unreactive. In contrast, the increased structural and chemical diversity of proteins means protein-based devices could have a wider range of functions and also be faster and more efficient. Unfortunately, the relationship between the polypeptide chain of a protein and its final folded state is still far from well understood, and this has hampered the development of protein nanostructures. Nevertheless, a number of protein nanostructures have been developed. Proteins have been assembled in periodic arrays (Moll et al., 2002). A more generalised system based on an $\alpha$-helical coiled coil motif, which can self-assemble in a controlled way into multicomponent structures, has also been demonstrated (Bromley et al., 2008; Bromley, Sessions, Thomson and Woolfson, 2009). These building blocks are currently being used as the basis for a new, protein based, synthetic molecular motor (Bromley, Kuwada, Zuckermann, Samii, Blab, Gemmen, Lopez, Curmi, Forde, Woolfson and Linke, 2009).

The properties of RNA lie somewhere in between DNA and proteins. A number of DNA machines incorporate RNA components, such as in DNAzymes that catalytically cleave the phosphate backbone of an RNA substrate (Tian et al., 2005; Pei et al., 2006; He and Liu, 2010; Stojanovic and Stefanovic, 2003). The assembly of nanostructures made entirely from RNA is a small but emerging field (Chworos et al., 2004; Guo, 2010). Alternatively, structures can be made entirely from much smaller organic molecules. For example, two segments of a chiral, helical alkene can be induced to rotate through multiple cycles of 360° about a central carbon bond in response to UV illumination and temperature changes, forming

a unidirectional rotary molecular motor (Koumura et al., 1999). A simple linear motor, similar in concept to the DNA motors described later in this Chapter has also been made entirely from organic molecules (von Delius et al., 2010). In this device switching is externally driven by cycling between acidic and basic reaction conditions, and the step size of $\sim 7$ Å is approximately $10\times$ smaller than for DNA motors discussed in Section 1.3.2.

There are potential benefits to using all of the different building materials discussed above. In the future, hybrid structures made from a combination of materials may prove the most well controlled and functional. Nevertheless, many of the concepts and techniques developed in DNA nanotechnology can provide more general insights, which will be applicable to systems built from a range of different materials.

## 1.2 DNA Origami

DNA origami is a recently developed method for making complex DNA structures in a single step (Rothemund, 2006). A single-stranded piece of circular DNA (ssDNA) from the M13mp18 bacteriophage, 7249 nucleotides (nt) long, forms the template strand of the design. This ssDNA is essentially treated as a random sequence of bases, and shapes are designed by rastering the template strand across the outline (Figure 1.4 A i-iii). To hold the template in place, 200-250 synthetic 'staple' strands are designed to link adjoining DNA strands in the design, such that the final tile consists of double-stranded DNA (dsDNA). For example, for a rectangular design the final tile consists of a raft of 24 parallel 288-basepair (bp) double helices tethered to each other at 16 bp intervals by the crossover of staples.

Once the staple strands are chosen, they are added in excess to the template DNA in solution. The mixture is annealed by heating to 95°C to remove existing

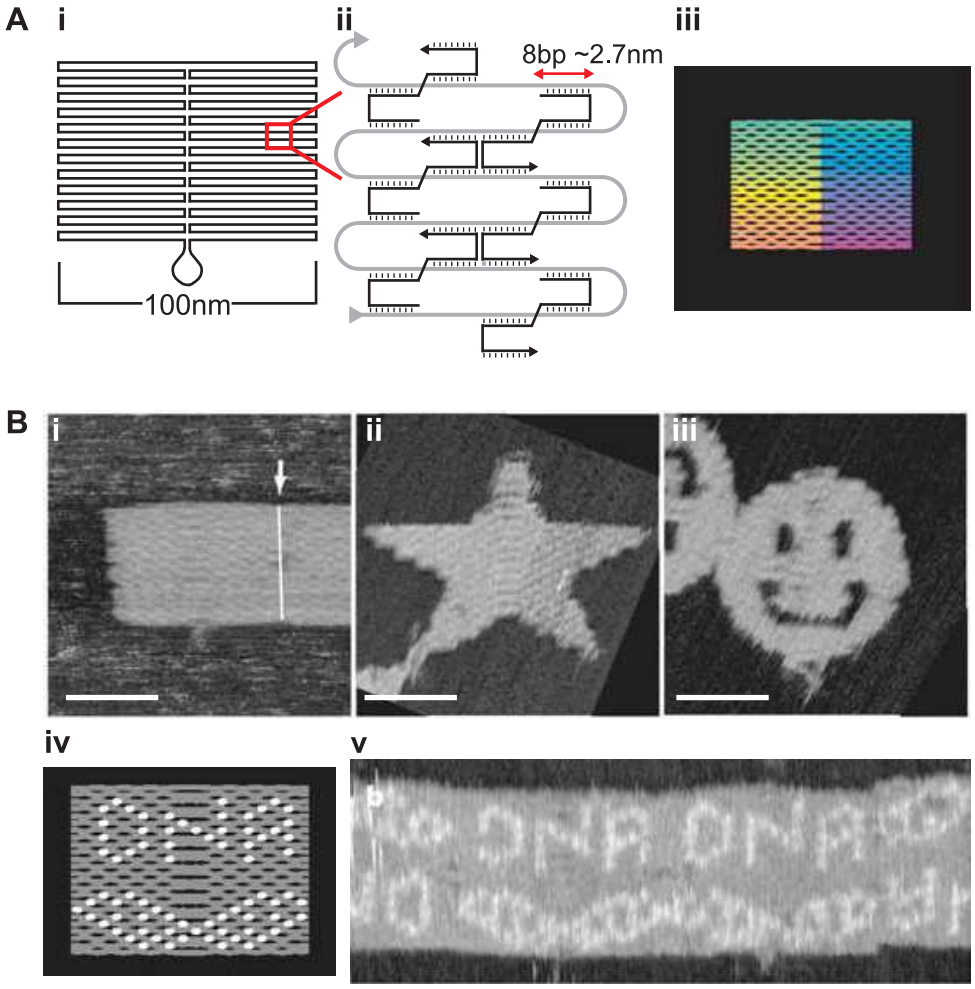


Figure 1.4: 2-dimensional DNA origami. **A** The long template strand, a piece of viral genomic DNA, is rastered across the outline of the shape (i) and cross-linked by short synthetic DNA staples (ii). The final origami tile consists of dsDNA (iii). **B** Many different shapes have been successfully assembled (i-iii). The origami tiles form an array of addressable pixels that can be decorated with hairpins (iv-v) (Rothemund, 2006). Scale bars 50 nm.

secondary structure, and then cooling slowly, typically over 1.5 hrs, to allow the tiles to form. The two-dimensional structure is stabilised by links between adjoining helices and can be imaged by atomic force microscopy (AFM) (Figure 1.4B i-v). Rectangular tiles have dimensions of approximately 100 x 70 nm. In contrast to the extended arrays described in the previous section, DNA origami have a well-defined and controllable size and shape, and each staple binding domain is a uniquely addressable site in the design. Staples can be modified, most simply with DNA hairpins, to produce complex designs with features as small as 6 nm (Figure 1.4 B v). For any origami design the staple sequences are entirely determined by the raster pattern, and thus the design process does not require complex analysis of all possible interactions between the many staples. This makes origami design a manageable task, and computational design tools exist (Douglas, Marblestone, Teerapittayanon, Vazquez, Church and Shih, 2009).

Various extensions or modifications of the DNA origami method have been published. Assembly is possible at constant temperature by slow removal of the denaturing agent formamide by dialysis, producing tiles of the same quality as thermal annealing (Jungmann et al., 2008). Larger tiles can be made in a hierarchal assembly by using the template strand to link small domains of origami together (Zhao et al., 2010). Annealing from lower maximum temperatures does not effect yield or quality, and can be used if thermally unstable modified staple strands are used in tile assembly (Sharma et al., 2007). Generally the designs are extremely robust and reproducible, with yields of $\sim 90\%$. The DNA tiles can also be labelled with gold nanoparticles (Sharma et al., 2007) or proteins (Chhabra et al., 2007; Sacc et al., 2010; Numajiri et al., 2010; Stephanopoulos et al., 2010; Subramani et al., 2010; Shen et al., 2009).

DNA origami tiles are typically characterised by AFM and agarose gel electrophoresis. Characterisation of fluorophore labelled DNA structures is also pos-

sible with fluorescence microscopy. Super-resolution single-molecule fluouesence techniques, such as FIONA (Fluorescence Imaging with Nanometer Accuracy) (Yildiz and Selvin, 2005) have recently been used to characterise several DNA origami systems (Steinhauer et al., 2009; Lund et al., 2010; Jungmann et al., 2010). The length scale of the tile is appropriate for the resolution of these methods, for example in FIONA resolution of $\pm 1.5$ nm can be achieved. The spacing of two fluorophores at either end of a tile, designed to be 89.5 nm, was measured as $88.2 \pm 9.5$ nm (Steinhauer et al., 2009). Transient hybridisation of short (10-nt) fluorophore-labelled ssDNA probes to tiles can also be used for PAINT (points accumulation for imaging in nanoscale topography), a stochastic super-resolution imaging method (Jungmann et al., 2010).

A number of recent advances have been made towards forming larger arrays by tiling DNA origami (Endo, Sugita, Katsuda, Hidaka and Sugiyama, 2010; Li et al., 2010; Zhao et al., 2010) and also towards being able to controllably place DNA origami on larger scale nano-patterned surfaces (Kershner et al., 2009; Gao et al., 2010). Together, these methods should provide a way of bridging the gap between top-down fabrication methods, with feature sizes of order 100's of nm, and the smaller-scale self-assembled structures described here. This will improve our ability to measure properties of the systems, particularly as an electrical read-out, and they may become useful components in the general nanotechnology toolbox. For example, to direct the assembly of other components.

### 1.2.1 Extension to 3-dimensions

Following the success of DNA origami as a technique for making 2-dimensional shapes, the method was extended to 3-dimensions (Douglas, Dietz, Liedl, Högberg, Graf and Shih, 2009). The first 3-D designs were variations on a six-helix bundle motif, which in cross-section has a hexagonal arrangement of DNA helices (Figure

1.5 A, C). Tensegrity structures, braced by ssDNA strands can also be formed (Liedl et al., 2010). 3-dimensional DNA origami structures require much longer annealing times, up to 150 hrs, and are very sensitive to buffer $Mg^{2+}$ concentrations. Yields are also much lower, and the correct structures must be gel purified from incomplete or incorrectly folded structures. Characterisation of 3D origami is typically by transmission electron microscopy (TEM) (Douglas, Dietz, Liedl, Högberg, Graf and Shih, 2009), which can be used for single particle reconstruction (Andersen et al., 2009) (Figure 1.5 B).

By altering the number of base-pairs between each staple cross-over, the 3-D origami shapes can be bent or twisted with a bend radius of up to 180° (Dietz et al., 2009). Bending is achieved by placing strain on each DNA helix through under or overwinding. In its natural state the pitch of the DNA double helix is 10.5 bp per helix turn. By including more bp/turn at one side of a six -helix bundle and fewer at the other side, the whole bundle will bend (Figure 1.5 C). In the original origami design, placement of the cross-links forces the twist to be 10.7 bp/turn. This results in slight underwinding of the DNA, and a global right-handed twist of the tile compensates for the strain. Indeed, further work has revealed that, when joined end-to-end in long chains, the original DNA origami tiles form spirals rather than flat ribbons. It is possible to design corrugated 'zig-zag' DNA tiles, with a more optimal twist of 10.5 bp/turn, that form flat ribbons instead (Li et al., 2010). This method involves using alternating 14 and 28 bp crossover spacings, giving exactly $\frac{4}{3}$ or $\frac{8}{3}$ of a turn between links. Adjacent helices are then offset in the plane of the tile with a dihedral angle of 120°.

Alternative methods for making 3-D origami are to construct faces of a cube or rectangular prism from 2D origami and then fold them up (Figure 1.5 B) (Andersen et al., 2009; Endo et al., 2009; Ke et al., 2009). Such structures tend to be more flexible, but can be switched between 2D and 3D form. For example, a DNA box

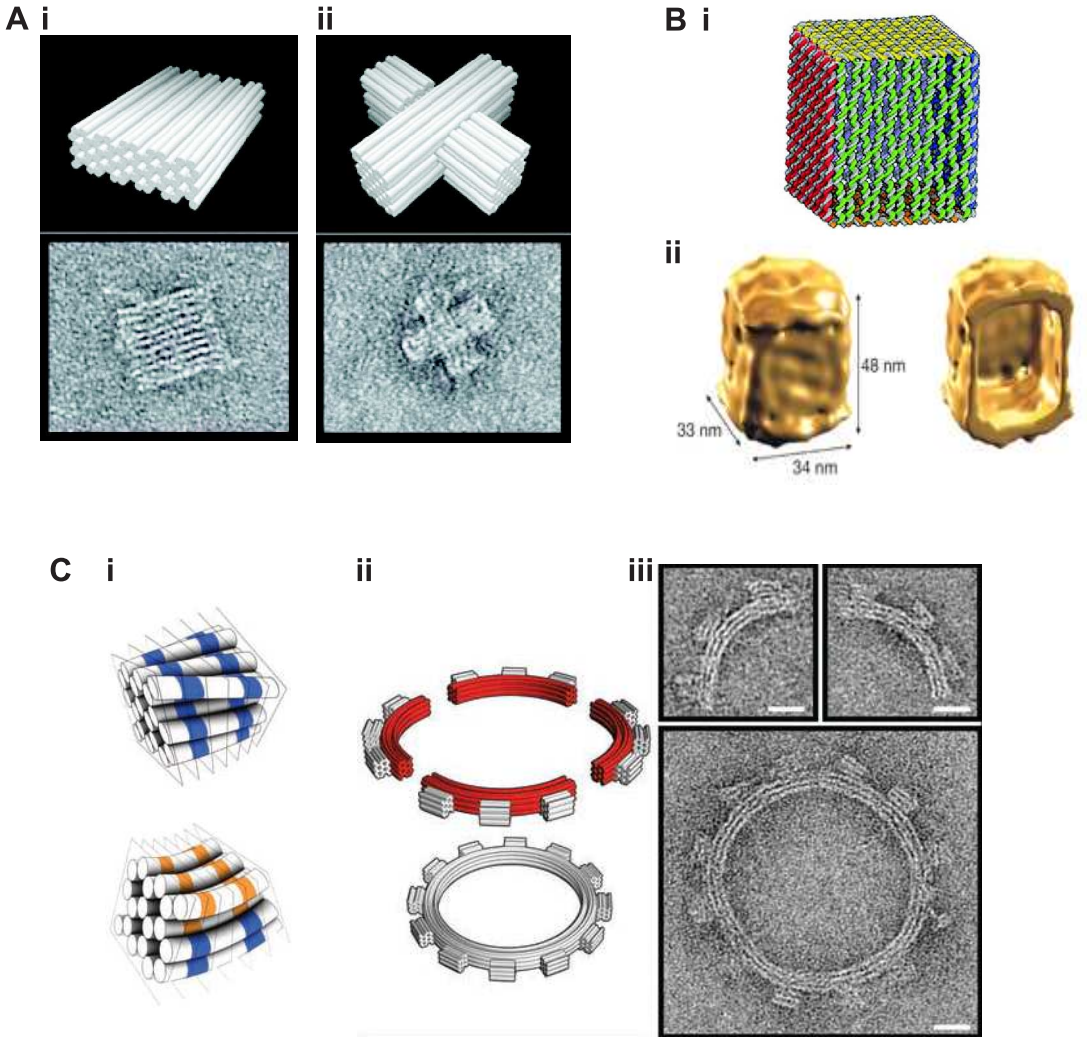


Figure 1.5: 3-dimensional DNA origami. **A** 3D origami structures can be assembled with hexagonally packed helices and observed by TEM (i-ii) (Douglas, Dietz, Liedl, Högberg, Graf and Shih, 2009). **B** 2D origami shapes can also be folded up into 3D structures such as this DNA box, which was characterised by TEM and single particle reconstruction (Andersen et al., 2009). **C** In the helix bundle structures, increasing or decreasing the number of basepairs per helix turn can result in global twist (i) or bending (ii). Blue strands are underwound, and orange overwound, compared to relaxed DNA (10.5 bp/turn). Complex objects, such as this cog (ii,iii) can be assembled (Dietz et al., 2009). Scale bars 20 nm.

lid can be opened or closed (Andersen et al., 2009). A möbius strip DNA origami has also been made, and when cut down the middle can create topological objects such as supercoiled rings and catenane structures (Han et al., 2010).

### 1.2.2 Applications

In concluding the introduction of DNA origami, Rothemund suggests that one of its 'obvious applications' is as a substrate for complex protein assemblies and diverse nanostructures (Rothemund, 2006). As described in Section 1.1.1, many methods exist for modifying DNA arrays with proteins and nanoparticles which can then be extended for use with origami tiles. Several key examples of functional structures made from DNA origami are given below.

#### Detection of biomoelcules

Rectangular DNA origami tiles have been used as a 'molecular chip' for detecting un-amplified RNA (Ke et al., 2008), proteins (Sharma et al., 2007) and DNA (Zhang et al., 2010) signals in heterogeneous solutions, such as cell extracts. When the taget molecule binds to the tile, a change in height and stiffness is observed under AFM. Tiles with different probes can be identified with a unique hair-pin marker, and multiplexed in solution. This concept has been demonstrated with high sensitivity (nM to 100's of pM) and for ssDNA a single nucleotide difference in a 4-nt toe-hold can be detected (Zhang et al., 2010). Such small variations, known as single nucleotide polymorphisms (SNPs), are the most abundant in the human genome and are commonly used as disease biomarkers. However, the reliance of these methods on AFM as a detection method is a weakness, as it is not an easy or high-throughput technique for testing many samples.

A number of different methods have been developed for binding proteins to DNA tiles, which extends their potential to act as a protein detection system. A

number of orthogonal binding systems are available, including biotin-streptavidin (Numajiri et al., 2010), Ni-NTA - Histidine linkages (Shen et al., 2009), 'snap-tag' and 'Halo-tag' linkers (Sacc et al., 2010), as well as covalently linking a modified staple strand to a cysteine residue on the protein (Stephanopoulos et al., 2010). The last method has been used to attach the most complex protein to a DNA origami so far, a virus capsid of 180 identical subunits arranged into a spherical particle 27 nm in diameter, with over 90% labelling of the tiles. Toe-hold exchange has also been used to bind and release target proteins (Numajiri et al., 2010).

### Biophysical study of proteins

More interestingly, recent work has developed methods for using DNA origami to facilitate the study of proteins. Indeed, the potential use of 3-D DNA lattices as a template for crystallising proteins for x-ray structure determination was one of the original motivations for work in this field (Seeman, 1982). Such applications are close to being realised (Malo et al., 2005; Zheng et al., 2009). Six-helix DNA bundles also have potential for use in aligning proteins for NMR structure determination (Douglas et al., 2007).

In addition to structural information, DNA structures can also be used to investigate protein activity. A recent study was able to show directly that human topoisomerases, which reduce supercoiling of DNA, have two DNA binding sites (Subramani et al., 2010). The enzyme binds independently to a dsDNA target in solution and also to a second target strand fixed to an origami tile.

Several studies have used a DNA origami 'frame' to study the interaction of proteins with a DNA duplex (Figure 1.6 A and B)(Endo, Katsuda, Hidaka and Sugiyama, 2010*a*; Endo, Katsuda, Hidaka and Sugiyama, 2010*b*; Sannohe et al., 2010). Many proteins that bind to and modify DNA must bend the double helix in order to do so. The DNA frame provides a method for stretching out a duplex

with different tensions, a shorter (64 nt) strand exactly spans the window, while a longer (74 nt) strand is anchored more flexibly. For example, the site-specific DNA methylation enzyme M.*Eco*RI bends the DNA helix by ∼55°. If the target site is successfully methylated, the DNA cannot be cut by subsequent addition of the restriction enzyme *Eco*RI. By treating DNA frames with the two enzymes, and observing the number of cut duplexes, it was shown that methylation of the longer more flexible duplex is far more efficient (Endo, Katsuda, Hidaka and Sugiyama, 2010*a*). The frames have similarly been used to test the effect of duplex tension on a DNA repair enzyme (Endo, Katsuda, Hidaka and Sugiyama, 2010*b*).

A further study considered the formation of a tertiary G-quadruplex structure between the two strands strung across the window (Sannohe et al., 2010), and was able to investigate the sequence and buffer conditions under which such structures form. The use of high-speed AFM (Ando et al., 2001) in these studies allowed the direct observation of these biologically relevant processes for the first time. DNA repair is vital in all cells, while site specific methylation is an important method for epigenetic gene regulation, and G-quadruplex motifs are found in human telomerases.

### Scaffolds for other nanostructures and materials

As mentioned above, it is also possible to pattern DNA origami with metallic nanoparticles (Sharma et al., 2006). An interesting extension of this is a study that uses DNA origami to control the geometry of two single-walled carbon nanotubes (SWNTs), to form a junction between them (Figure 1.6 C) (Maune et al., 2009). If the junction is made between a metallic and a semi-conducting nanotube, and the DNA tile between them is able to act as an insulator, this would result in a CNT field effect transistor (FET). The nanotubes were arranged on the tiles, deposited on a $SiO_2$ surface and electrodes patterned on by electron-beam to allow

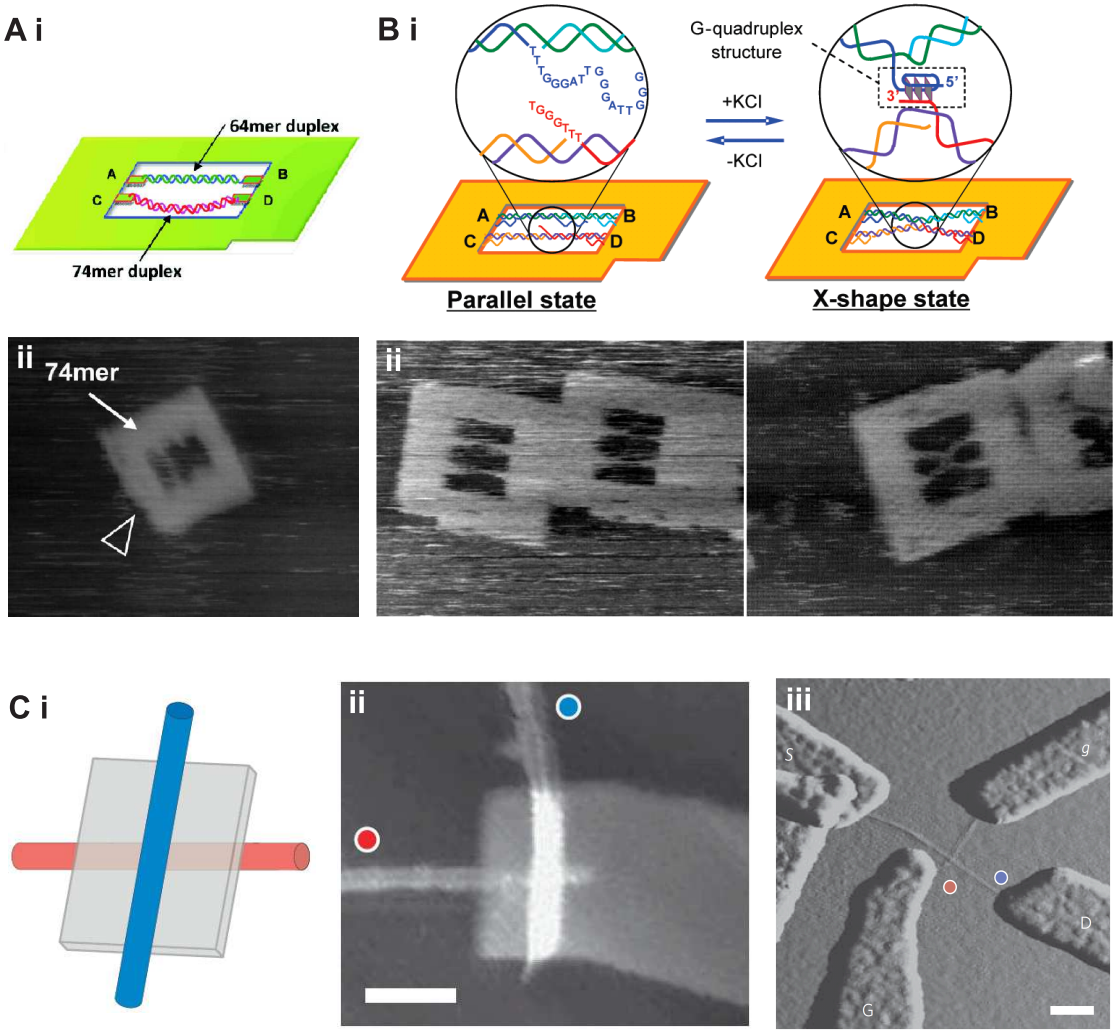


Figure 1.6: Applications of DNA origami. **A** Origami frames can be used to alter the tension of a duplex spanning the window (i), and the effect of this on the activity of DNA modifying enzymes determined (ii) (Endo, Katsuda, Hidaka and Sugiyama, 2010*a*). **B** Similarly, two strands each containing half the sequence of a G-quadruplex can span the window (i). The formation of a quadruplex leads to an observable transition from the parallel to the X-shape state, and the conditions required for quadruplex formation tested (Sannohe et al., 2010). **C** Origami tiles can be used to assemble other nanostructures, such as carbon nanotubes, with specific orientations (i-ii). This allows for the formation of a field effect transistor (FET), which can be connected to external electrodes (iii) and electrically characterised (Maune et al., 2009).

measurement of the electrical properties of the device. This method had a very low yield of devices, but could be improved if the origami tiles were deposited in a more controlled way on a surface pre-patterned with electrodes.

DNA origami has also been used as a substrate for the direct observation of simple chemical reactions (Voigt et al., 2010). Biotin attached to the DNA tiles is easily detected by AFM after the addition of streptavidin (SA). Selective cleavage of DNA-biotin linkers, by reduction with DTT (1,4,-dithiothreitol) or singlet oxygen generated from light, can be observed by the absence of SA binding. The formation of chemical bonds can also be detected: if the species added to the tile is biotin-modified, SA binding will only be observed if the bond has been formed. This was tested with 2 alkyne and azide 'click' reactions, and an NHS-ester and amine reaction. The tiles were deposited on a mica surface, and then washed with each reaction solution in turn. The yield of each step was ∼85% and for all three together ∼40%. Importantly, no misplaced biotin was observed. This provides a unique method for directly observing chemical reactions, and could reveal heterogeneity in the sample. It could also be a useful method for monitoring the chemical assembly lines discussed in Section 1.3.3.

### Active DNA Origami

An active DNA structure, inspired by bacterial movement, has been designed to be pushed along in solution by a polymerising dsDNA tail (Venkataraman et al., 2007). An origami tile is used as the 'cell body', and strands on it's edge are modified to catalyse the formation of propelling 'tails' from DNA strands in solution via a hybridisation chain reaction. While AFM images show the tails form as predicted, experiments to quantify movement of the tile in solution have not yet been performed. DNA origami can also act as a substrate for synthetic DNA motors (Lund et al., 2010; Gu et al., 2010), as discussed in Section 1.3.2.

## 1.3 Molecular Motors

### 1.3.1 Active transport in biology

In the words of Richard Feynman; "Biology is not simply writing information; it is *doing something* about it" (1959). The internal structures of the cell are assembled and controlled through a complex set of linear and rotary motors, as are many interactions of the cell with its environment (Alberts et al., 2002). Protein machines bind to DNA in the nucleus, untwist and fold it, polymerases translocate along the DNA double helix opening it and transcribing the information into RNA. Ribosomes move along RNA 'reading' the sequence and translating the information into proteins.

Linear protein motors, such as kinesin, myosin and dyenin, organise the cytoskeleton and transport cargos around the cell. Kinesins are involved in vesicle transport and microtubule spindle organisation, and contribute to chromosome separation during mitosis. Myosins transport cargo along actin, and also act to stabilise bundles of actin filaments, while dyenins interact with membrane organelles. Arrays of motor proteins and filaments drive larger scale movement: myosin-actin systems are responsible for muscle contraction, and dyenin-microtubule systems for the beating of cilia.

All three classes of linear protein motor have a double-headed structure, and kinesin and myosin have been shown to walk hand-over-hand along their track (Yildiz et al., 2003; Yildiz et al., 2004). A number of single molecule studies have been used to study the mechanisms of these motors, and they have been shown to be extremely fast and processive. In gliding assays with purified protein, myosin achieves velocities of up to 4.5 $\mu ms^{-1}$ (Suzuki et al., 1997) and kinesin run lengths of to to $\sim$1 $\mu$m (with 16 nm step size) at 0.8 $\mu ms^{-1}$ (Svoboda and Block, 1994) have been observed. The motors are also very efficient: for kinesin one molecule

of ATP is hydrolyzed per step (Coy et al., 1999).

There are also several rotary protein motors. The bacteria flagellar motor is a complex protein assembly of over 40 distinct proteins, that rotates at up to 100 Hz propelling bacteria at speeds of 25 $\mu ms^{-1}$ through viscous media (Berg et al., 2002; Berg, 2003). The motor can switch direction in response to signalling proteins on the chemotaxis pathway, allowing the bacteria to move towards favourable conditions. The F- and V-ATPases found in cells, that act to synthesise or hydrolyse ATP, are fixed direction rotary motors. One such ATPase, $F_1$-ATPase, is investigated in the course of this thesis, and considered in more detail in Section 1.4.

Significant effort has been put towards harnessing these protein machines for active transport in synthetic nanoscale devices. For example, teams of kinesin heads can be linked together by modifying the protein to include a DNA binding zinc finger motif, and then linking many heads to the same DNA duplex to act as a molecular shuttle (Taira et al., 2006; Carstairs, 2008). However, our lack of a complete understanding of these complex protein systems hampers our ability to control and direct them. While synthetic motors, made from DNA, protein or small molecules, fall far behing natural systems in their efficiency and speed, the benefit of *de novo* design is that the systems are better understood and can be controlled with a much higher degree of precision.

### 1.3.2 Synthetic DNA motors

As outlined at the start of this Chapter, one of the aims of this project is to produce a DNA origami based track for a synthetic molecular motor made from DNA. Taking inspiration from the natural systems described above, the active transport of smaller building blocks could be used to build up larger and more complex synthetic structures than can be assembled in a single step. To build such a sys-

tem requires synthetic motors that are unidirectional, processive and autonomous. That is, they can move large distances in a controlled manner without dissociating from the track, and without the need for externally added signal strands at each step.

### Externally switched motors

The first DNA motors were externally switched DNA machines, similar to those described in Section 1.1.2, bound to a linear DNA track. The track is usually formed by dsDNA, with a series ssDNA anchorages or 'stators' (Shin and Pierce, 2004; Sherman and Seeman, 2004), but it can also be formed by a circular piece of ssDNA (Tian and Mao, 2004). The sequential addition of DNA strands induces the motor to move from one motor site to the next, by unbinding and then rebinding a ssDNA segment of the motor (Shin and Pierce, 2004; Sherman and Seeman, 2004) (Figure 1.7 A). These 'clocked' DNA motors can be designed with either a hand-over-hand gait similar to myosin and kinesin (Shin and Pierce, 2004), or with an 'inchworm' gait (Sherman and Seeman, 2004). These two designs both require the addition of two control strands per step, one to lift the motor foot and the other to rebind it to the next stator, and thus are quite slow. For the motor design in Figure 1.7, the mechanism was tested with one control strand added approximately every 20 min (Shin and Pierce, 2004). Directionality is achieved by the order in which the control strands are added, and the two examples were tested on short test tracks of 4 and 2 steps respectively.

### Autonomous Motors

Further work lead to the design of autonomous DNA motors, which are able to move without the constant addition of triggering strands to the reaction mixture. Such motors can be powered by catalytic hydrolysis of the DNA backbone (Bath

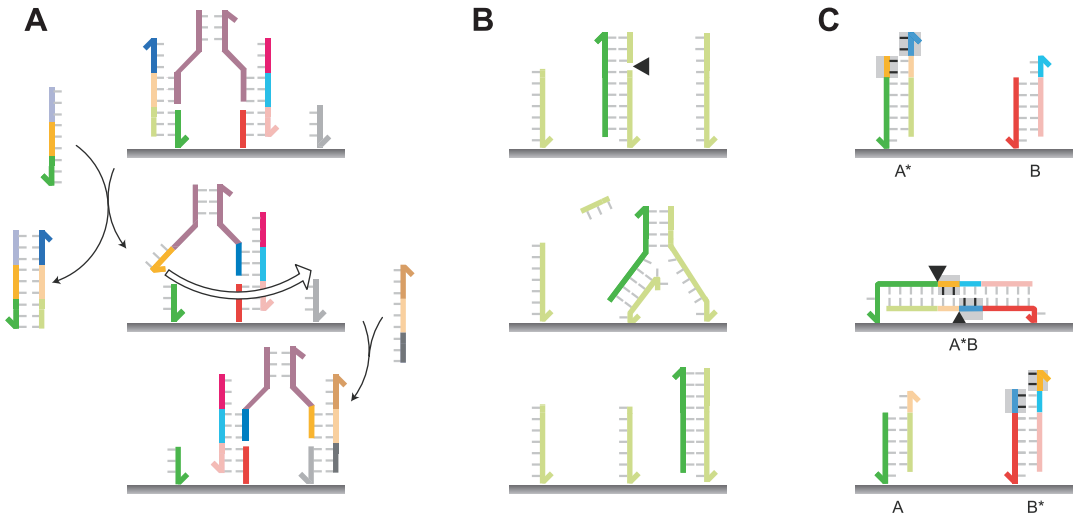


Figure 1.7: Mechanisms of three simple DNA motors. **A** An externally clocked bipedal DNA motor that walks hand-over hand across ssDNA stators (Shin and Pierce, 2004). The first control strand binds to the toe-hold on the back foot (left) and removes it from the track. A second control strand binds the same foot to the next downstream stator. **B** An enzyme driven autonomous DNA motor, known as the 'burnt-bridges' motor (Bath et al., 2005). When the ssDNA motor (dark green) binds the to track stator (light green), the duplex forms a recognition site for a nicking enzyme (arrow). Once the DNA back-bone is nicked, the small piece of the stator dissociates, and it is more energetically favourable for the motor to move onto the next stator by branch migration. **C** Another autonomous motor design, the toe-holds on adjacent stators hybridise and are ligated by an enzyme, once ligated they are cut by a restriction enzyme in solution. An offset between the ligation and nicking sites results in a 6 nt 'cargo' sequence being transferred down the track (Yin et al., 2004). Motor B is used in Chapters 3 and 5.

et al., 2005; Chen et al., 2004; Pei et al., 2006), either by an enzyme in solution or a DNAzyme incorporated into the motor itself, and may be linked to ATP hydrolysis (Yin et al., 2004). After the track site the motor occupies is cut or modified by the enzyme, it will be more energetically favourable for the motor to move onto the next intact site (Figure 1.7 B). Directionality can be imposed by destroying the track sites that have been visited (Bath et al., 2005; Chen et al., 2004; Pei et al., 2006), or by a unidirectional reaction cycle (Yin et al., 2004). An example of the latter is the motor in Figure 1.7 C, in which the motor-track duplex is ligated and then cut, the cut duplex has different sticky ends, which cannot rebind to the same substrate (Yin et al., 2004). Another mechanism for imposing directionality is by coordinating the conformational changes of two motor domains of a bipedal motor, a similar mechanism to that of processive kinesin and myosin (Bath et al., 2009). This two-foot motor is used in Chapter 4.

Autonomous DNA motors can also be driven by a DNA fuel (Turberfield et al., 2003; Green et al., 2006; Bois et al., 2005; Yurke and Mills Jnr, 2003; Seelig, Yurke and Winfree, 2006). Two complementary fuel strands interact slowly to form a duplex, because of the hairpin secondary structure of one or both of the strands (Figure 1.3 B). Reaction rates can be up to $10^4\times$ slower than for strands without hairpins (Turberfield et al., 2003). The DNA motor contains a toehold region to open up one of the hairpins, and this catalyses the fuel duplex formation. Thus, by controlling the kinetics of fuel duplex formation, the energy released (1.4 kcal $\text{mol}^{-1}$ per bp) can be used to drive the motor forwards along the track. Motor-catalysed duplex formation with two hairpin fuels strands can proceed of order $30\times$ faster than the uncatalysed reaction (Turberfield et al., 2003), and the effect of loop and toe-hold length on reaction rates has been quantified (Green et al., 2006). For a purified 'kissed' complex of two 2-stranded loops, the difference between the two rates can be up to two orders of magnitude larger (Seelig,

Yurke and Winfree, 2006). The free energy stored in a kissed complex of two 40-nt 2-stranded loops, each with two 15-nt neck regions, is estimated to be -55 kcal $mol^{-1}$ (Seelig, Yurke and Winfree, 2006). For comparison, the free energy for ATP hydrolysis is -7.3 kcal $mol^{-1}$, although ATP is a much smaller molecule and therefore a more efficient energy store.

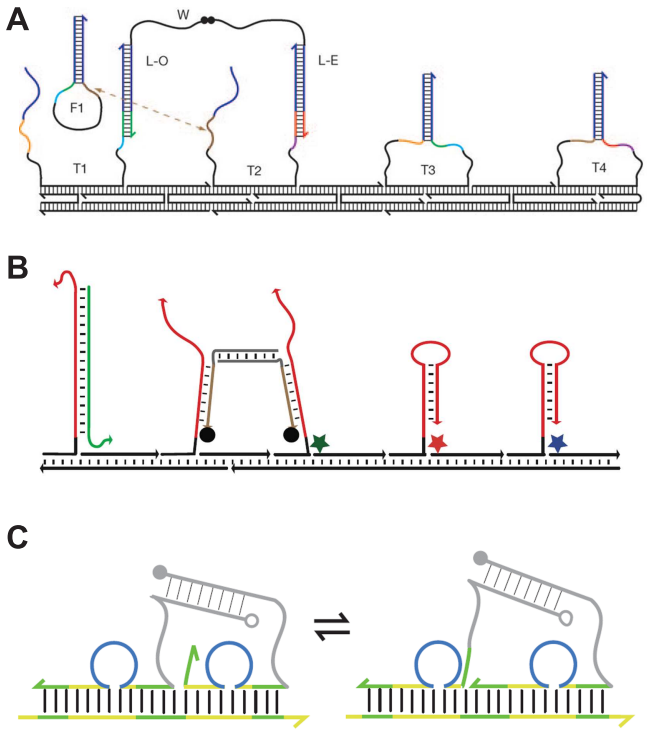


Figure 1.8: Autonomous bipedal DNA motors powered by DNA fuel loops. **A, B** Two examples of bipedal motors that catalyse duplex formation of hairpins in solution with hairpins on the track (Omabegho et al., 2009; Yin et al., 2008). The first motor (A) take 2 steps processively across a 49 nm DX tile, the arrangement of the track means the back foot is always lifted. The second motor (B) is less well designed, at each step there is an equal chance of either stepping forward or dissociating from the track. Both these motors modify the track sites they have visited. **C** A two-foot DNA motor, where directionality is achieved by coordination between the two feet, powered by DNA hairpins (Green et al., 2008). This motor track is reusable.

A number of bipedal DNA motors powered by DNA fuel loops have been designed (Figure 1.8) (Yin et al., 2008; Green et al., 2008; Omabegho et al., 2009). Again, directionality may be imposed by a unidirectional reaction cycle (Yin et al., 2008; Omabegho et al., 2009) or cooperation between the two feet (Green et al., 2008). Having two feet can improve the processivity of the motor, as long as the design permits only one foot to be lifted at a time (Green et al., 2008; Omabegho et al., 2009). For a version of the two-foot DNA motor with a DNA fuel (Figure 1.8 C), the stall force of the motor, the maximum force it can exert, has been estimated as ∼3pN, comparable to that of myosin V and kinesin (Green et al., 2008).

### Extended tracks

The DNA motors discussed above have all been tested on short test tracks, typically only allowing 1-3 steps. Longer stepping cycles are often prevented by the flexibility of the motor track, particularly in the case of the two-foot motor (Figure 1.8 C). Recently, a stochastic DNA 'spider' with many legs (Pei et al., 2006), has been shown to move longer distances, of up to 100 nm, by biased diffusion across a 2-D array of attachment sites anchored to a DNA origami tile (Lund et al., 2010) (Figure 1.9). Motor transport was demonstrated by AFM and single molecule fluorescence, but the resolution was too low to show individual steps, and at best differentiates between 3 positions along the track. The many feet of this motor essentially undergo a biased random walk across the tile. The spider cleaves each substrate it visits and is less likely to revisit those sites. The directionality is not well-controlled, and the motor may visit each site many times before it eventually reaches the finishing point. 70% of spiders were found to reach the end of the track in 90 min. Increasing the number of feet reduces the likelihood that the motor will dissociate. However, processivity is increased at the expense of motor speed,

as it requires a 2-D rather than linear track and the potential for back tracking is greater. It is estimated that on average 50 cleavage events are required to move from one side of the tile to the other.

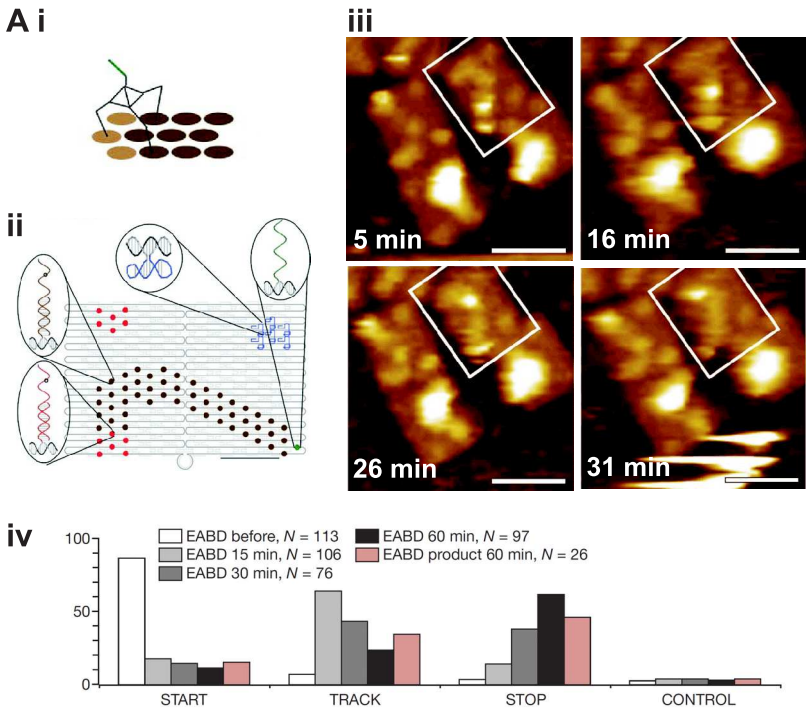


Figure 1.9: **A** DNA 'spider' (Lund et al., 2010). The spider has 3 DNAzyme legs (**i**) that bind to and cleave a 2D array of substrate strands anchored to a DNA origami tile (**ii**). Cleaved sites are revisited at a lower frequency than uncleaved sites. Reaching the other side of the tile (90 nm) takes ∼30 minutes, and approximately of 50 cleavage events. (**iii**) A single movie of 4 frames was obtained, and shows a motor moving on the highlighted tile. The motor position is not well-defined, and individual stepping events are not seen. (**iv**) AFM imaging at 5 time points provides a histogram of spider positions, at 3 locations along the track. Scale bars 100 nm.

### 1.3.3 Motors for assembly

A number of applications have been proposed for DNA motor devices. For example, as a synthetic ribosome that constructs molecules in response to instructions encoded in the track (Bath and Turberfield, 2007; Simmel, 2009), or as logic devices (Bath and Turberfield, 2007). Two recent publications have investigated the use of DNA motors on molecular assembly lines. The first example is a variation of the switched DX junction, described in Section 1.1.2 (Ding and Seeman, 2006). A clocked 3-foot DNA motor takes 3 steps across a DNA origami tile, after each step a nearby DX junction is switched by the addition of another control strand, to bring a gold nanoparticle close enough to the motor to bind to it (Figure 1.10 B) (Gu et al., 2010). The stoichiometry of the resulting particles is controlled by the different gold NPs loaded onto the track. While the designed particles were observed, the yield was low.

The second example is an autonomous DNA motor that assembles small organic molecules (He and Liu, 2010). This makes use of the fact that, in a chemical reaction at low concentration, the reaction rate is very slow. However, if both reactants are linked to complementary ssDNA strands, hybridisation of the DNA can be used to bring reactants together. In the vicinity of the duplex, the local concentration will be high enough to dramatically increase the reaction rate (Gartner and Liu, 2001; McKee et al., 2010). Several reactants can be combined in a single 'pot' and the order of reactions controlled by the order in which the DNA strands are hybridised together. A defined sequence of 4 molecules has been programmed by the addition of external control strands (McKee et al., 2010). A DNA motor system has assembled 3 molecules, linked by peptide bonds, (He and Liu, 2010) (Figure 1.10 A), and is based on an existing DNAzyme motor design (Chen et al., 2004).

Overall, these initial results are very promising. Limits to both the motor

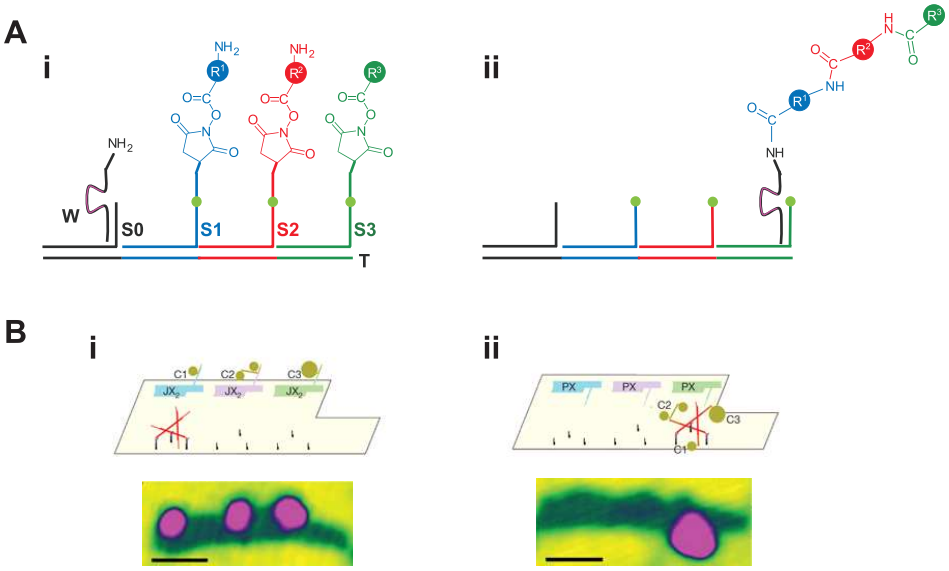


Figure 1.10: DNA based molecular assembly lines. **A** A track for an autonomous DNAzyme motor is pre-loaded with small organic molecules. As the motor walks down the track the molecules are linked together with peptide bonds in a defined sequence (He and Liu, 2010). **B** A clocked motor acts to assemble three sets of different gold nanoparticles into a unit (Gu et al., 2010). The stoichiometry of the final unit is defined by the track. AFM images of the initial and final states are shown below. Individual NPs are only resolved by TEM. Scale bars 50 nm.

systems described are the small number of steps achieved, and low product yields. The yield particularly suffers because each track is a single-use substrate, and could be improved by designing a system in which the motor track can act as a catalyst, with each track unit re-used to produce many products.

As well as the ability to program in the desired molecule, such molecular assemblers are of great interest for two reasons. The first is the ability to translate DNA structures, that are evolvable, into synthetic structures. Thus, *in vitro* selection experiments could be used to drive the evolution of molecules with desired properties. A simple example has shown selectivity for streptavidin binding affinity (Gartner and Liu, 2001), and analogous methods are used very successfully to evolve highly specific protein-binding DNA aptamers (Wilson and Szostak, 1999). The second is the ability of DNA ligands to promote asymmetric catalysis, where the chirality of the DNA is translated to the product of a catalyst that would normally produce a racemic mixture of products (Boersma et al., 2010). As the bioactivity of many molecules depends strongly on chirality, asymmetric products are highly sought after for therapeutic applications.

## 1.4 $F_1$-ATPase: A rotary protein motor

An alternative to designing a synthetic molecular motor, such as those described in Section 1.3.2, from scratch is to take an existing protein motor and adapt it for new purposes. If the motor can be controlled, this approach could lead to much faster and more efficient transport systems. One such cellular motor, $F_1$-ATPase, is considered in this thesis and is introduced in this Section.

$F_OF_1$-ATP synthase is an enzyme that synthesises ATP from ADP, using proton flow through a membrane. ATP is the chemical energy source for almost all cellular processes, and its synthesis by $F_OF_1$ is fundamental in all cells from bacte-

ria through to animals (Yasuda et al., 2001). The protein consists of a membrane bound $F_O$ portion and a water soluble $F_1$ portion. On its own, the $F_1$ unit hydrolyses ATP, and is referred to as $F_1$-ATPase (Shimabukuro et al., 2003). Previous work has revealed that this enzyme acts as a rotary motor. While the motion of single $F_1$ molecules has been observed with high enough resolution to reveal single steps, we still do not completely understand how the free energy of ATP hydrolysis is converted into the mechanical rotation of the protein.

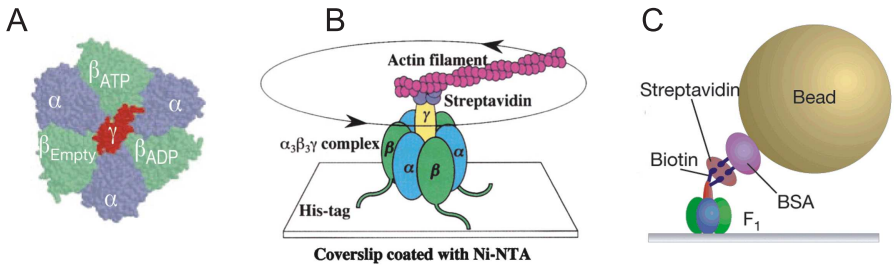


Figure 1.11: Images from rotation studies of $F_1$-ATPase. **A:** The protein structure of $F_1$, the $\gamma$-subunit is surrounded by a ring of 6 alternating $\alpha$ and $\beta$ subunits. Image courtesy of (Yasuda et al., 2001). **B:** The configuration used to first demonstrate the rotation of $F_1$ (Noji et al., 1997). **C:** A similar configuration using gold beads (40 nm) instead of actin filaments (1-4$\mu$m) to detect motion, this reduces the load on the motor, making substeps in the rotation detectable (Yasuda et al., 2001).

### 1.4.1 Structure

The crystal structure of bovine mitochondrial $F_1$ was the first to be determined, and consists of a ring of 6 alternating $\alpha$ and $\beta$ subunits, and a rod-shaped central $\gamma$ unit (Figure 1.11, A) (Abrahams et al., 1994). $F_1$ from yeast (Kabaleeswaran et al., 2009) and *E. coli* (Hausrath et al., 1999) were subsequently shown to have very similar structures. The crystal structure, along with other data, suggested

some sort of rotary motor, with reactions in the $F_O$ and $F_1$ portions coupled by rotation about a common shaft (Boyer, 1997). This idea was confirmed by direct observation of a rotating actin filament bound to the $\gamma$-subunit (Noji et al., 1997), making it the smallest known rotary motor. The central $\gamma$-subunit acts as a rotor ($\sim$1 nm) inside the stator barrel of three $\alpha$-subunits and three $\beta$-subunits ($\sim$10 nm diameter). The catalytic sites are located on $\beta$ subunits, at the interface with the next $\alpha$ subunit (Junge et al., 2009). At a given point in time, each subunit has a different ATP binding affinity, with $k_d$'s from $\sim 10^{-10}$ to $\sim 10^{-4}$ M. During a motor cycle, each $\beta$ goes through a sequential change in binding affinity, and the three $\beta$ subunits are thought to act cooperatively to drive rotation (Ariga, 2008).

### 1.4.2 Rotation studies

The original rotation studies involved fixing $F_1$ protein from a thermophilic bacterium to a surface coated with Ni-NTA by 10-Histidine tags on each $\beta$-subunit, and then attaching a long actin filament to the $\gamma$-subunit (1-4 $\mu$m) (Noji et al., 1997) (Figure 1.11 B). The rotation of the actin filament, at $\sim$4 Hz, was observed only in the presence of ATP, and was unidirectional. The motor was found to rotate in discrete 120° steps. Further work used a similar set-up to consider the load dependence of the motor's motion. Long filaments exert a viscous drag on the motor and reduce enzyme turnover by up to 1000×. The work done in each step is close to the free energy of hydrolysis of one molecule of ATP (Yasuda et al., 1998). The torque does not depend strongly on angle, and has a mean value of $\sim$56pN nm (Junge et al., 2009).

In later studies, the actin filament was replaced by 40 nm gold (Yasuda et al., 2001) or 0.2 $\mu$m carboxylate beads (Shimabukuro et al., 2003) (Figure 1.11 C), and bead rotation was imaged by laser dark-field microscopy. This allowed the rotation of the motor to be studied under much smaller loads, revealing further

stepping behaviour. Under low ATP conditions the 120° step was divided into an ATP-limited 90° step and an ATP-independent 30° step (Yasuda et al., 2001). In later work this was refined as an 80° step due to ATP binding, and a 40° step related to ADP release, separated by two ∼1 ms dwells (Shimabukuro et al., 2003). The first dwell relates to ATP cleavage, and the second to product release. ADP and Pi are thought to be released separately, and an excess of either in solution can extend the dwell time (Ariga, 2008).

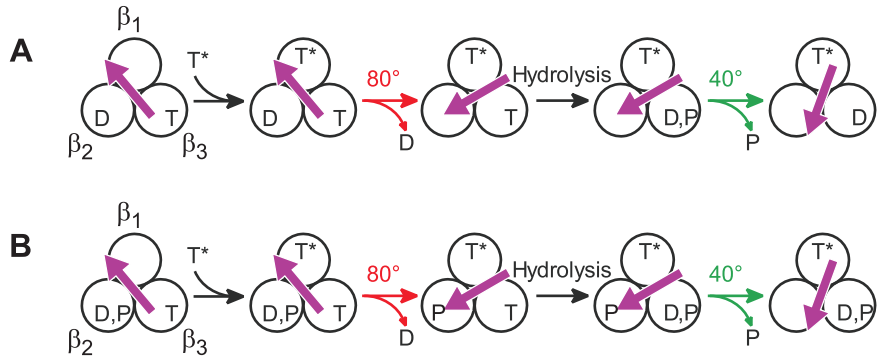


Figure 1.12: Proposed mechanism of $F_1$-ATPase rotation. The diagrams show the coupling between the chemical and mechanical cycle, and the coordination between the three $\beta$ subunits. Each $\beta$ is represented by a circle, and the orientation of the $\gamma$ is indicated by the direction of the purple arrow. The phosphate ion is released one phase later in scheme B. Image adapted from (Junge et al., 2009).

This data leads to a proposed model for $F_1$ rotation in which the $\beta$ units act cooperatively (Ariga, 2008)(Figure 1.12). Binding of an ATP to site $\beta_1$ drives the 80° rotation and simultaneous release of ADP from $\beta_2$. This allows cleavage of ATP at $\beta_3$, which in turn allows Pi release from either $\beta_2$ (Figure 1.12 B) or $\beta_3$ (Figure 1.12 A), driving the 40° rotation, and leaving $\beta_2$ ready to bind a new ATP. Thus, an ATP is only hydrolysed 200° of rotation after binding, and the ADP released after 240°. Interestingly, ATP cleavage does not directly produce rotation but rather allows for the release of the products (Grubmeyer et al., 1982).

The rotation of a strain of $F_1$ from *Escherichia coli* has also been probed

using gold beads, similar to the description above (Nakanishi-Matsui et al., 2007; Nakanishi-Matsui et al., 2006), and stochastic fluctuations in its rotation have also been observed. This strain is assumed to operate in an essentially similar manner to the thermophile $F_1$, with the key difference that *E. coli* operates at 37°C and thermophile $F_1$ at around 60°C (Nakanishi-Matsui et al., 2007). It is the *E. coli* strain of $F_1$ that will primarily be used in the context of this project. $F_1$ protein from the yeast *Saccharomyces cerevisiae* is also used in this thesis (Wang et al., 2007). This protein has been characterised in single-molecule rotation studies using a laser dark-field microscope (Sowa et al., 2010). Yeast $F_1$ is observed to take 120° steps, similarly to the *E. coli* protein (Bradley Steel, Unpublished data, 2010).

While the motion of single $F_1$ molecules has been observed with high enough resolution to reveal single steps, the conversion of the free energy of ATP hydrolysis into mechanical rotation is still not completely understood. Recent work has proposed the use of optical tweezers as a force-clamp, to measure the torque produced by the motor (Pilizota et al., 2007). Other work has used magnetic tweezers to externally drive $F_1$ rotation, either in the forwards (CCW) or backwards direction. Each $F_1$ molecule is isolated in a micro-fabricated well, which acts as a closed system. After release of the external force, the speed of the motor is proportional to the ATP concentration in the well, and can be used to measure how much ATP was either synthesised or hydrolysed by driving the motor backwards or forwards respectively (Itoh et al., 2004; Rondelez et al., 2005; Iko et al., 2009). As expected, when a backwards external rotation is applied, the $F_1$ acts to synthesise 3 ATPs per turn, as it is thought to do when coupled to $F_O$ in the cell (Itoh et al., 2004; Rondelez et al., 2005).

To drive $F_1$ externally, it must be firmly attached to a surface. In almost all previous work, the protein has been fixed to a surface coated in Ni-NTA by 6 or

10 histidine residues on each $\beta$ subunit (Figure 1.11 B). Unfortunately, the high coverage of Ni-NTA on these surfaces means that the protein may drift across it when a force is exerted on it. Another approach that has been considered is to attach the $F_1$ protein to electron-beam patterned surfaces, producing hybrid protein and inorganic nanostructures (Soong et al., 2000). The inorganic substrate consists of $SiO_2$ posts of diameter 50-120 nm capped with Ni metal, designed to bind a single protein and lift it away from the bulk substrate by 2.5 $\mu$m. Nano-fabricated 'propellers', 750 or 1400 nm long, were used as markers to observe motion. The precisely defined propeller and post geometry allow for more accurate calculations of the drag force on the marker, and leads to a revised estimate of motor efficiency of 50-80%. This method results in very long-lived complexes ($\sim$2.5 hrs), but the significant increase in design complexity does not result in a better yield of spinners ($\sim$1 %), and stepping behaviour was not observed. DNA origami should provide a more useful substrate for rotation assays of $F_1$-ATPase, as three tris-NTA attachment sites may be placed in a specific configuration to securely bind one $F_1$ motor to each tile and prevent drift. Origami substrates are also much simpler to assemble than the nano-patterned surface described above.

Furthermore, $F_1$ is such a small and efficient rotary motor, it may also be a useful active component for building hybrid DNA-protein nanostructures. A simple example of this is an $F_1$-ATPase based DNA sensor, where a gold nanorod is coupled to the $\gamma$ unit by a DNA linker strand with a biotin on each end (York et al., 2008). The two ends of the dsDNA strand are only brought together in the presence of a 40-nt target DNA strand, and the % of rotating nanorods in the presence of the target is 10$\times$ higher than the background level. Attaching the $F_1$ motor to more sophisticated DNA nanostructures, such as origami tiles, will improve our ability to harness its rotary motion for use in DNA-protein devices.

Chapter 2

# General DNA Origami Techniques

This chapter presents a general introduction to the fundamental properties of DNA origami, and the techniques and conditions suitable for their synthesis, purification and characterisation. Such methods were largely unknown at the start of this work, and were important in the application of DNA origami to the study of molecular motors as discussed in later chapters. The results here are intended to give an overview. Full protocols for the experimental methods used in this Chapter and the following Chapters are given in detail in Appendix A. Section 2.9 introduces the main experimental techniques used in later Chapters.

## 2.1 Design principles

The basic DNA origami design discussed in this thesis is the previously published rectangular tile with a central seam (Rothemund, 2006). The shape was chosen for its high yield (approx. 90%) and relative simplicity. In this design, adjacent turns of the ssDNA template (genome of bacteriophage M13mp18) strand are cross-linked every 16 bp (approximately 1.5 helix turns), by a uniform set of 216

32-nt staples. This forms a rectangular tile of 24 288-basepair (bp) parallel double helices (Figure 2.7). The spacing of crossovers is such that the nucleotide position at the centre of a staple is directly on top of the helix (facing out of the page) and the nicks are directly beneath (facing into the page) (Figure 2.1 A). This results in a hexagonal array of addressable pixels on either face of the rectangle, depending on whether the centre or end of a staple strand is modified. The placement of crossovers in this tile design results in helices with an average twist of 10.7 bp/turn. This slight underwinding of the helices is expected to lead to a global right-handed twisting of the tile (Dietz et al., 2009; Li et al., 2010). The twist of the tile is discussed in more detail in Section 2.6.

## 2.2 Synthesis and Characterisation

Origami samples were initially synthesized following the original protocol, with 1.6 nM template DNA and a 100× excess of each staple (Rothemund, 2006) (Appendix A.2). The tiles were characterised by Atomic Force Microscopy (AFM) (Appendix A.3). This technique produces high resolution (<1 nm) images of individual origami tiles deposited on a mica surface, in their native buffer conditions. The images are generated from the height of the sample, as measured by the interaction of an AFM cantilever tip with the sample as it is scanned across the surface. The tip and sample are both degraded by the process of imaging. The resolution obtained depends strongly on the quality of the tip, with much variation from one tip to the next. With good AFM conditions, it is possible to clearly resolve the central seam of the tile and the internal weave of the DNA helices (Figure 2.2 A). More typically, images similar to Figures 2.3 and 2.8 are obtained, in which the shape of the tiles is well-defined, and some details of the central seam are detectable. As noted by Rothemund, the key to achieving higher resolution AFM

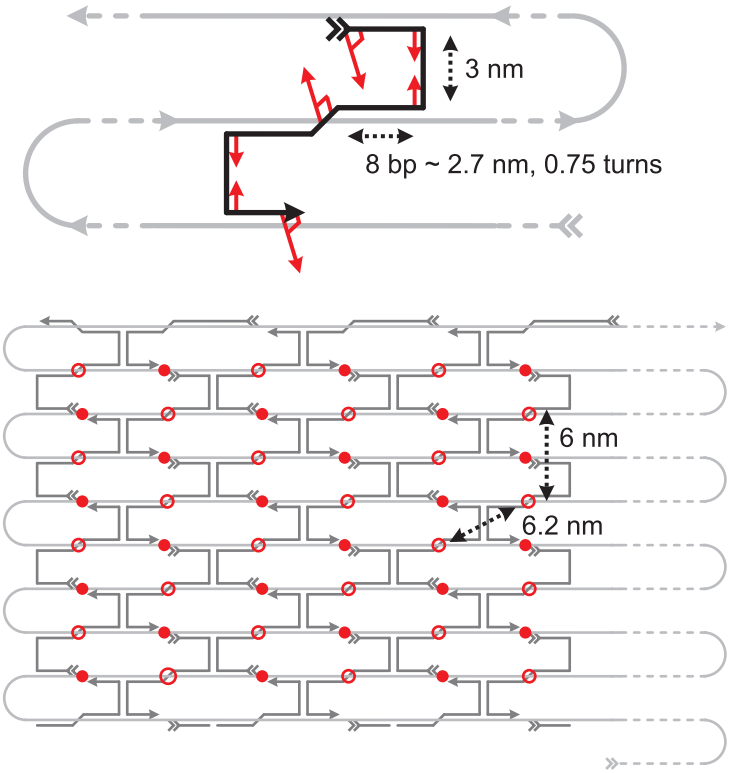


Figure 2.1: Schematic of the DNA origami staple pattern. **A** Individual staple strands form a double 'horse-shoe' shape of dimensions shown. The centre and ends of each staple are positioned on opposite surfaces of the tile. Red lines indicate the phase of the DNA helix. **B** The staples (dark grey) form a hexagonal array of pixels, all pointing up, for staple centre (red circles), or down, for nicks (red dots). The characteristic spacing is ∼6 nm in all directions. The template strand is shown in light grey.

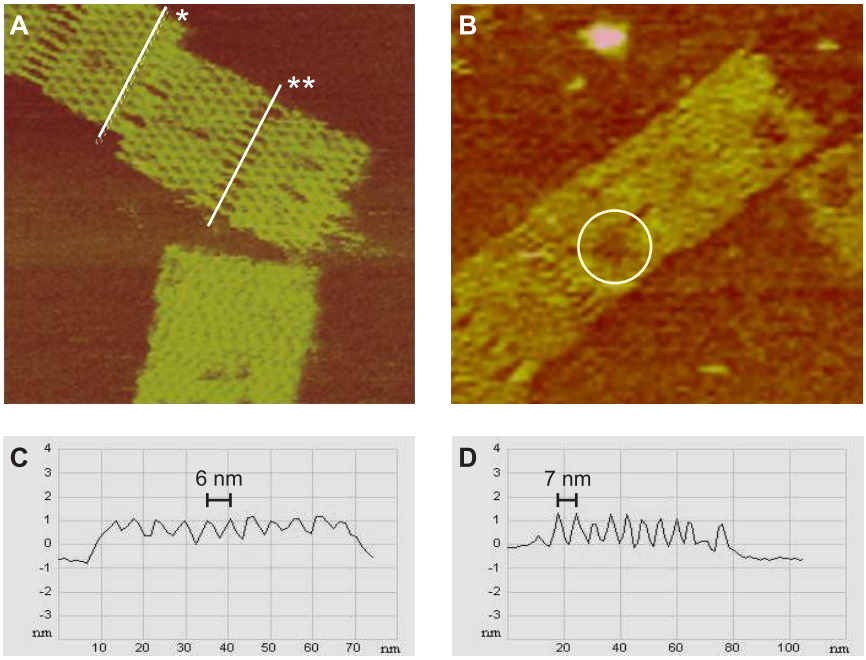


Figure 2.2: AFM images of the basic origami tile. This sample was initially synthesised with a 'hole', or defect, of five missing strands (**B**). The missing strands were added after annealing, and found to insert into the correct position and fill the holes. The repaired tiles are shown in **A**. Height profiles **C** and **D** correspond to cross-sections along the lines marked * and ** (A), individual helices are visible. The vertical spacing between crossovers is indicated.

images was to keep trying fresh cantilevers (Rothemund, 2006).

As in previous work, the rectangle was found to have dimensions ∼100 nm x 70 nm, and to form chains joined along the short edge of the rectangle (Rothemund, 2006). The chains are thought to be caused by base-stacking interactions between the blunt ends of helices on adjacent tiles. To prevent this interaction, a loop of 4 thymine nucleotides is included at the external turn of staple strands at these edges, similarly to (Rothemund, 2006). Both edge types are shown in Figure 2.3. The inclusion of T-loops reduces stacking, with over 80% of tiles occurring as singles. This is useful if tiles are to be deposited on a surface for single-molecule experiments, as it gives a more even distribution.

Different synthesis conditions were tested, with varying template and staple strand concentrations. The quality of tiles was assessed by AFM and the results are summarised in Table 2.2. The AFM assessment is somewhat subjective, especially as tiles may be damaged by repeated scanning with the AFM cantilever. 'Good' tiles are of similar appearance to those in Figure 2.8. Tiles with large holes, similar to those in Figure 2.2 B, or with no tiles observed after multiple attempts, are considered 'bad'. Based on these results, origami samples in later chapters were typically synthesised with 50 nM template DNA and a 5× staple excess. The maximum temperature of the annealing protocol was also varied, similarly to previous work (Sharma et al., 2007; Dietz et al., 2009). No difference in quality was observed, and this method can be used if modified staple strands are not stable up to 95°C.

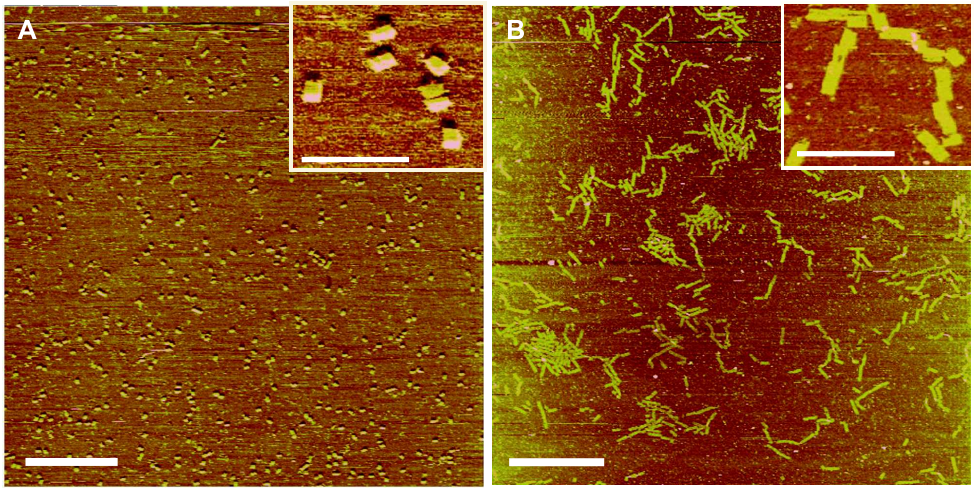


Figure 2.3: AFM images showing the effect of different edge staples. Replacing plain edge staples (**B**) with 4-T Loop staples (**A**) reduces stacking and aggregation of the tiles. Scale bars 2$\mu$m for main images, and 500 nm for zoomed insets.

| M13 DNA | Staple strands | Tiles | Temperature (Max) |
|---|---|---|---|
| 1.6nM | 160nM | Good | 95° |
| 1.6nM | 16nM | Bad | 95° |
| 10nM | 100nM | Good | 95°, 75°, 65° |
| 10nM | 50nM | Good | 95°, 75°, 65° |
| 10nM | 20nM | Good | 95°, 75°, 65° |
| 50nM | 150nM | Good | 95° |
| 50nM | 250nM | Good | 95° |

Table 2.1: Summary of origami synthesis conditions.

## 2.3 Purification

For many purposes it is useful to remove the excess staple strands from solution after origami synthesis. This is particularly true for modified staple strands. For example, in fluorescence experiments excess staples will give a high background signal. Several methods for origami purification were compared: centrifugal filtration, hand-packed ion-exchange columns, and hand-packed size-exclusion columns (Appendix A.5).

For filtration, origami samples were added to centrifugal filter units, with a known molecular weight cut-off, then topped up with buffer and spun to remove the excess staples and buffer. This process can be repeated a number of times to improve efficiency. After purification, tiles were checked for damage by AFM. Attempts to image each sample were repeated until resolution at least as good as that in Figure 2.7 was obtained. These images were of sufficient quality to detect large defects and mis-shapen tiles, but not single missing staples. Samples filtered with 50 kDa filters were found to be damaged, while 100 kDa filters resulted in no damage. Generally, centrifugation at speeds greater than 1000 g resulted in damaged and fragmented tiles.

Two types of column purification were also tested. The ion-exchange (DEAE) columns bind weakly anionic molecules, such as DNA, in low salt buffer (100 mM NaCl). Increasing the salt concentration of the buffer causes DNA to elute from the column; the exact salt concentration required for this depends on the length of the DNA. Thus, the columns provide a method for separating the short staple strands from the larger origami tiles. The size-exclusion (sephacryl s-300) columns consist of a matrix of porous beads. Small molecules enter the beads, and are delayed by the column, larger molecules cannot enter the beads and are eluted much faster. The beads used have a DNA cut-off of 118 bp: the origami are much larger than this and will pass straight through the column, while the 32-nt staples will enter

the beads and be retained. Both columns can be hand-packed with small bead volumes, to achieve good sample retention. For ion-exchange columns, buffer is added and allowed to flow through under gravity. For size-exclusion columns, the sample is added and spun in a centrifuge to collect the purified fraction, and this process is repeated to improve efficiency. Samples from either column purification method were assessed by AFM and found to be undamaged.

Purification efficiency was assessed by agarose gel electrophoresis (Appendix A.4). This technique uses an electric field applied to a gel matrix, in this case of agarose, to separate DNA molecules of the basis of their size. Larger DNA structures, such as origami tiles, move towards the cathode more slowly than shorter DNA strands, such as the staple strands. Gels stained with a DNA dye reveal distinct staple and origami bands; comparison of the intensity of the staple band for unpurified and purified samples gives a measurement of purification efficiency (Figure 2.4). Filtration was found to be effective after a number of buffer rinses, as was the ion-exchange column. The size-exclusion column is equally effective after several spins, is the fastest of the three methods, and unlike the ion-exchange column does not result in a high salt concentration in the final sample. This method was used to purify all samples used in later chapters. An additional benefit of the size-exclusion column is that the purified sample is transferred into the column buffer, and the method can be used to exchange buffers while maintaining the same tile concentration. Origami samples require a certain amount of $Mg^{2+}$ (12.5 mM) during synthesis. Once tiles had been synthesised they can be transferred to a lower $Mg^{2+}$ buffer (2 mM), and were found to be stable. Generally, unpurified tiles were found to be stable over 1 month. After purification, degradation of tiles was observed by AFM after 2-3 days, and so tiles were only purified directly before use.

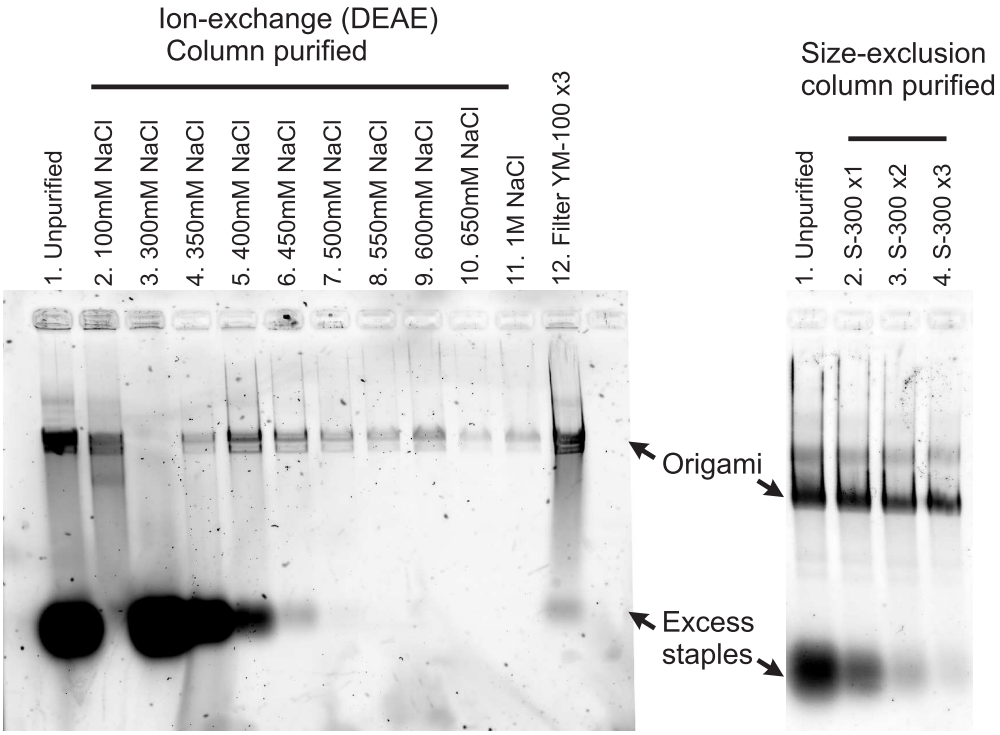


Figure 2.4: Agarose gel analysis of origami purification methods (0.75% gel). **A** Lane 1 is an unpurified sample of ∼10 nM tiles with a total of ∼10 $\mu$M excess unbound staple DNA. Lanes 2-11 are fractions eluted from a ion-exchange (DEAE) column at increasing salt concentrations: above 500mM only origami tiles are obtained. Some origami tiles do not bind to the column and are lost in the first wash (lane 2). Lane 12 is the same sample filtered 3 times in a 100 kDa filter. **B** Comparison of an unpurified sample (lane 1) with samples purified by repeated size-exclusion (S-300) columns (lanes 2-4). All 3 methods are successful, size-exclusion was found to be the most convenient.

## 2.4 HPLC

It is possible to process origami samples on a pre-packed version of the ion-exchange column with a conventional High Pressure Liquid Chromatography system (HPLC) (Appendix A.6). In this case a salt gradient is produced by a pump system, and applied to the column under high pressure. After elution from the column the sample is passed through an absorption and a fluorescence detector. DNA is detected by characteristic absorption at 260 nm, and fractions can be collected for use in further experiments.

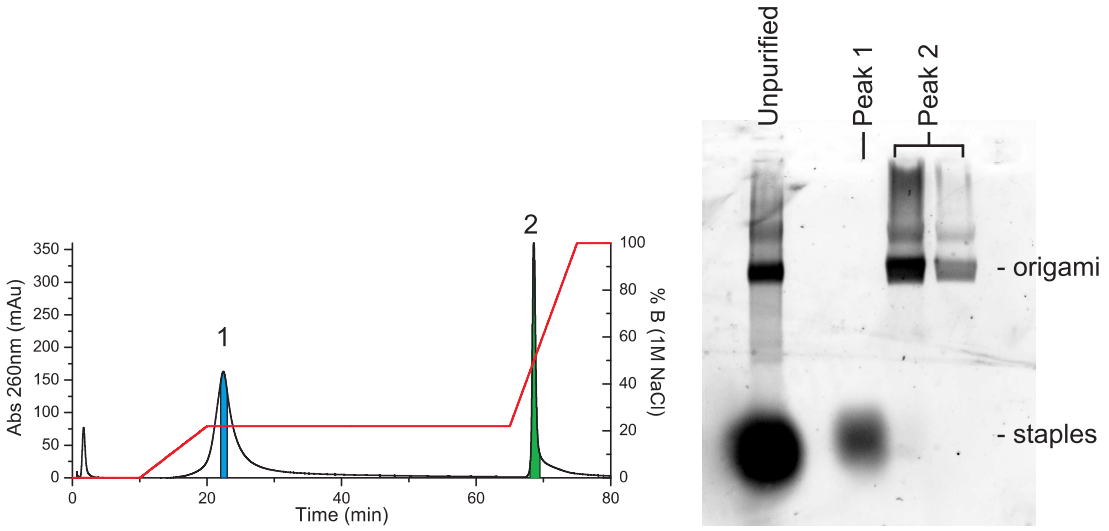


Figure 2.5: Ion-exchange HPLC of DNA origami. The DNA absorption signal (left) shows clear separation between staples (1) and DNA origami tiles (2) in an increasing NaCl gradient (red). Analysis by agarose gel electrophoresis (right) confirms that peaks 1 and 2 correspond to staples and origami tiles respectively. Two sequential fractions from peak 2 were loaded in lanes 3 and 4.

This method is less useful for purification, because it results in more diluted samples (∼500 $\mu$L) with a high salt concentration (∼550 mM) and takes around 70 minutes to process one sample. However, it provides additional quantitative information about the sample. For example, it can be used to measure the relative

amount of fluorophore-modified staple strand incorporated into the tile (Section 2.5). A representative HPLC trace and gel of the corresponding peaks is shown in Figure 2.5. Origami can be similarly analysed by HPLC with a pre-packed size-exclusion column, and this method is used in Chapter 6.

## 2.5 Defect Repair

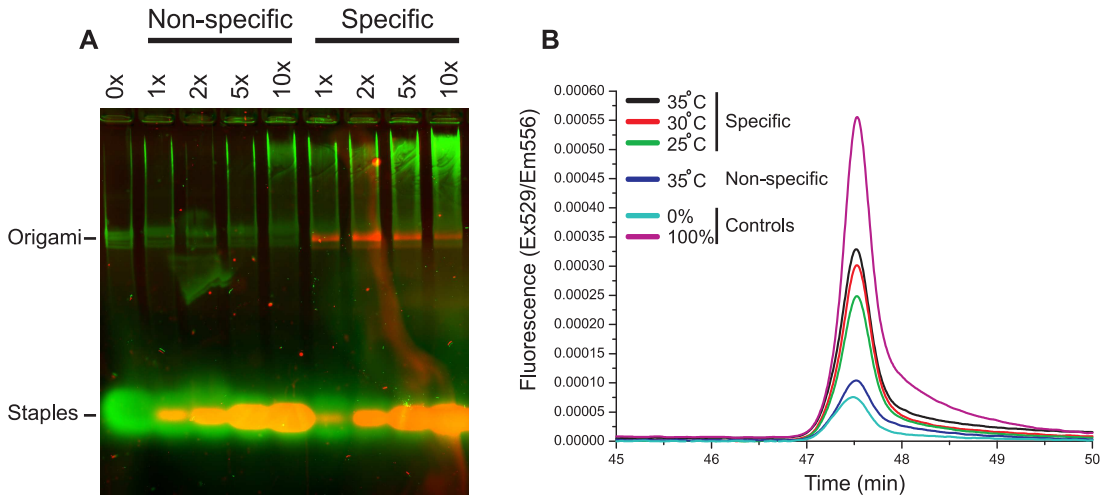


Figure 2.6: Origami tile repair. **A** Agarose gel electrophoresis of DNA origami tiles, lacking one staple, incubated with a fluorophore-labelled staple at 37°C. SyBr gold stained DNA is shown in green, and the fluorophore-labelled staple (TAMRA) is shown in red. **B** Quantification of staple incorporation by HPLC. The fluorescent staple migrates with the defective origami in either gel or HPLC trace if it matches the sequence of the missing staple, ('specific') and not otherwise ('non-specific').

In initial AFM experiments, origami tiles with large defects, or holes, were produced by omitting selected staple strands during synthesis. The defective tiles were observed to repair themselves after incubation with the missing staples at room temperature, without high-temperature annealing. AFM images of defective tiles, missing 5 adjacent staples, before and after repair are shown in Figure 2.2. This property could provide a useful method of incorporating thermally unstable

| Excess | Time (hours) | Temp(°C) | Inclusion (%) |
|---|---|---|---|
| 5x | 1 | 25 | 130 (28) |
| 1x | 1 | 25 | 29 |
| 1x | 1 | 30 | 38 |
| **1x** | **1** | **35** | **46 (6)** |
| 1x | 2 | 25 | 49 (14) |
| 1x | 17 | 25 | 62 (21) |
| 1x | 17 | 30 | 80 (19) |

Table 2.2: Efficiency of Origami Tile Repair for different incubation conditions

strands into the tiles, for example pre-hybridised duplexes. Tile repair was investigated further by assembling tiles with a single missing staple, and then incubating them with a fluorophore-labelled strand. The fluorescent strand was found to be incorporated into the origami only if it matched the sequence of the missing staple. Figure 2.6 A shows agarose gel analysis of tile repair for different incubation concentrations. In all cases the fluorescent staple with the correct sequence migrates with the origami band in the gel, indicating successful tile repair.

Tile repair was quantified by ion-exchange HPLC, and results are given in Figure 2.6 B. The fraction of defective tiles that were repaired by incorporation of the fluorophore-labelled staple is estimated by calculating the area of the fluorescence peak at the time point when DNA origami elute (∼47 min, Figure 2.6). The exact amount of DNA loaded on the column varies from one run to the next. To adjust for this, the fluorescence peak area is normalised by the area of the corresponding peak in the DNA absorption trace. The normalised fluorescence is compared to the corresponding signal for a tile prepared with the staple present during initial assembly (5× excess) (100% control). Non-specific interaction was also quantified, and is minimal. Repair efficiencies were measured for a range of incubation conditions and are given in Table 2.5. This repair property is used to load DNA motors, hybridised to a specific origami staple, at the start of a track in Chapters 3 and 5.

## 2.6 Minimised Twist Design

As mentioned in Section 2.1, the original origami rectangle design (Rothemund, 2006) is expected to have a global right-handed twist as a result of slight underwinding (10.7 bp/turn) of the DNA helices between crossover positions (Dietz et al., 2009). An alternative tile was designed to reduce global twist. In the reduced twist tile, six nucleotides of the template strand are 'skipped' along each of the 24 helices. At each of these 'skip' points , the staple strand is shortened by 1 nt, and all following sequences are shifted up by 1 nt so that no bulge in the template strand remains (Figure 2.7 A). This results in a fully dsDNA tile, with a longer loop of remainder DNA (Figure 2.7). The skipped bases are evenly distributed across the tile (Figure 2.7 C). The resulting tile consists of 72 32-nt staples and 144 31-nt staples. It has 24 282-bp helices cross-linked on average every 15.6 bp. This gives a more optimal average twist value of 10.4 bp/turn (Dietz et al., 2009).

The approach taken to reduce the twist of the tile in this thesis is to achieve an optimal average twist across the whole design, and to ignore local effects. This method is quite different to another reduced twist design recently published (Li et al., 2010). In that case the crossovers are deliberately placed to give a non-integer number of turns, alternating between 1 turn and 120°, and 2 turns and 240°. This is thought to produce corrugated tiles, and AFM images show that the short edge of the rectangle is reduced from ∼70 nm to 52 nm.

The reduced twist tile design was successfully synthesized, and characterised by AFM and agarose gel electrophoresis. Tiles of similar quality and yield to the original design were imaged by AFM (Figure 2.8 A and B). The tiles were measured to be 94±5 by 70±5 nm (N=30), no significant difference to the original design. Gel electrophoresis detected a slight shift between the two designs (Figure 2.8 C). Reduced twist tiles run closer to plain M13 template DNA in a gel than the original twisted tiles, which suggests they have a smaller cross-sectional area.

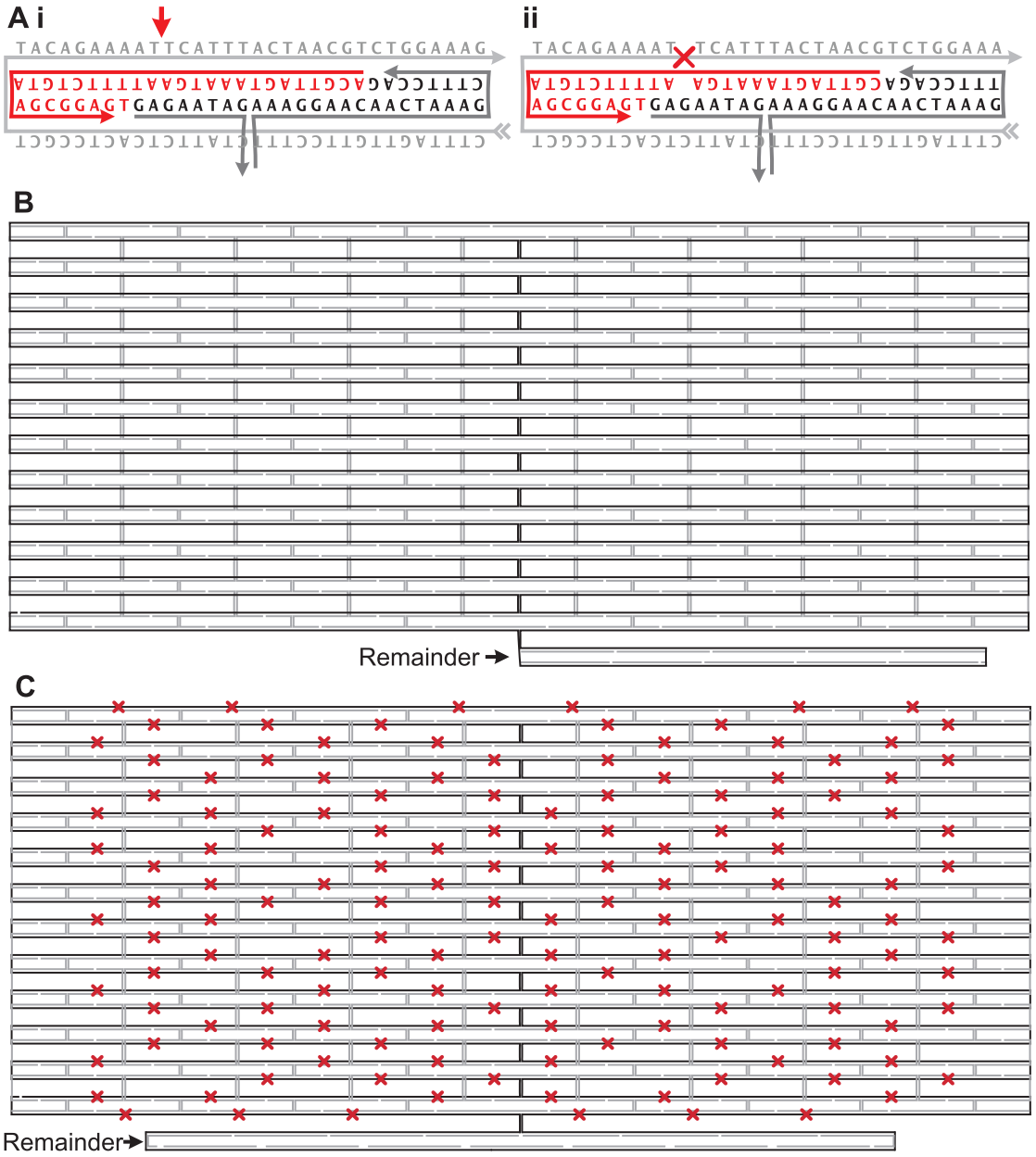


Figure 2.7: Original (**B**) and reduced twist (**C**) origami designs. In the new design six bases of the template stand are skipped along each of the 24 helices (red crosses). **A** A single skipped base in detail: at a selected point (red arrow), the staple strand is shortened by 1 nt, and all following DNA sequences are shifted up by 1 nt so that no bulge in the template strand remains. The extra nucleotides of the template strand form a longer remainder loop at the bottom of the tile, 244 nt instead of 100 nt.

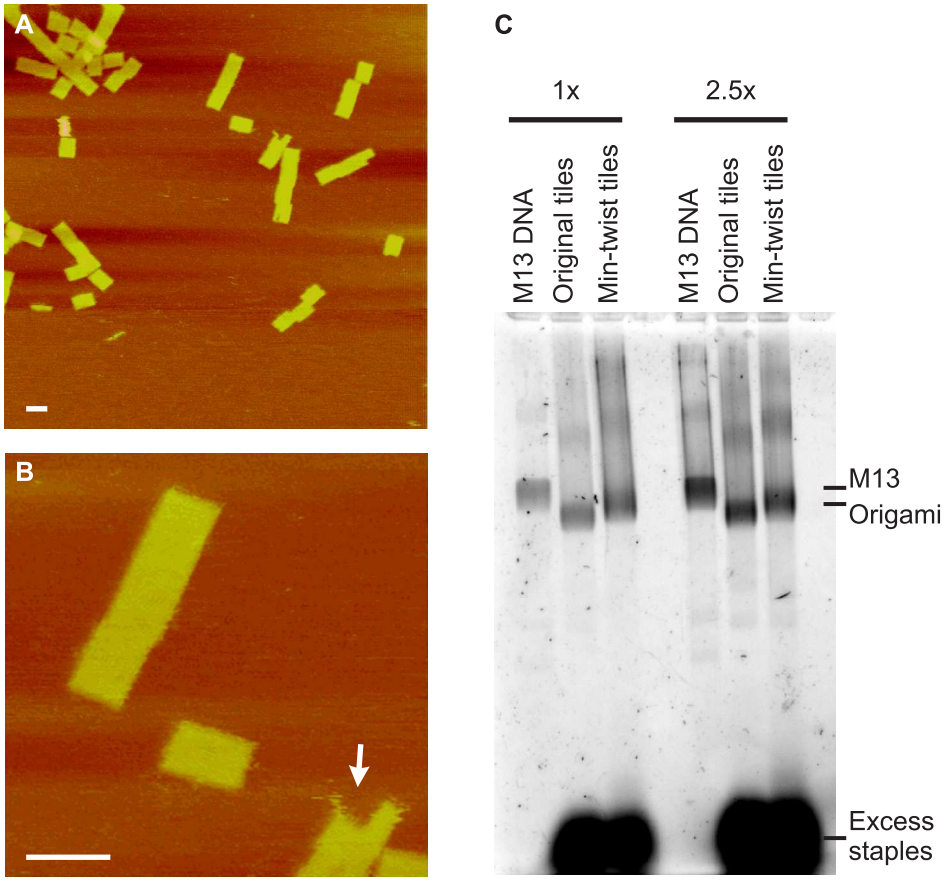


Figure 2.8: Analysis of reduced twist origami design. **A, B** AFM images show origami tiles the same size as the original design (scale bars 100 nm). The tiles are generally of good quality, a broken tile seen in these images was damaged by repeated AFM scans (arrow). **C** Agarose gel electrophoresis (1.5 %) shows a similar yield for both tile types. The reduced twist tiles run closer to the control M13 DNA band, suggesting a reduced cross-sectional area.

## 2.7 Fluorescence Microscopy

Origami tiles can be observed by fluorescence light microscopy, in a similar way to previous work on DNA arrays (Goodman et al., 2009; Erben, 2007) (Appendix A.7). The tiles were added to a flow cell, incubated for $\sim$ 10 minutes, and then stained with SyBr gold, a fluorescent DNA dye. Excess dye is washed out, and the samples observed on a standard microscope in epifluorescence mode. With high $Mg^{2+}$ buffer (30 mM), many tiles were observed to stick non-specifically to the glass coverslip (Figure 2.9 A). Control samples with no DNA were used to confirm that the fluorescence observed is due only to the DNA tiles (Figure 2.9 C). For many protein or enzyme based systems, high $Mg^{2+}$ buffers are unsuitable. The protocol was also tested with a low $Mg^{2+}$ buffer (2 mM), which is compatible with the $F_1$-ATPase experiments in Chapter 6. A smaller, but significant, number of tiles were observed on the coverslip in these conditions (Figure 2.9 B). Nonspecific sticking of the tiles to glass was found to be sufficient for immobolisation, even under low $Mg^{2+}$ buffer conditions and after multiple wash steps.

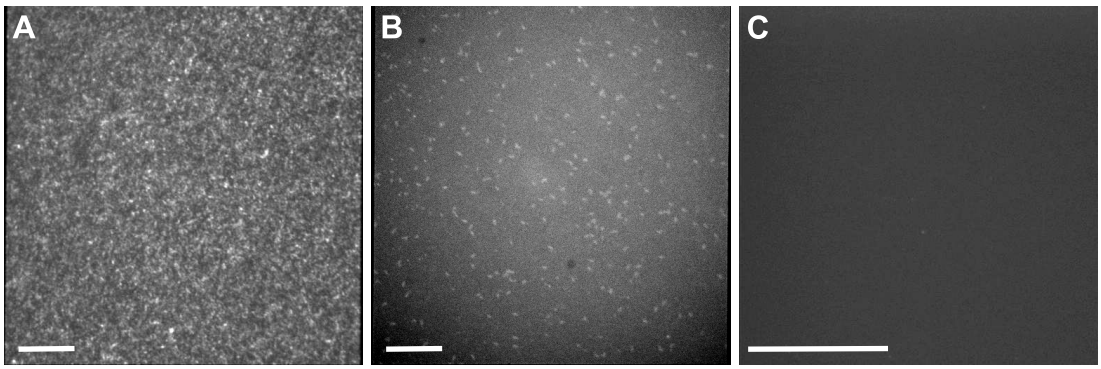


Figure 2.9: SyBr gold stained DNA origami tiles under epifluorescence. **A** In high salt buffer (1×TAE, 30 mM $Mg^{2+}$) many origami tiles stick nonspecifically to the glass. **B** Reducing the $Mg^{2+}$ concentration of the buffer to 2 mM results in a smaller, but non-zero, number of tiles stuck to the glass after the staining and wash steps. This buffer is compatible with the $F_1$ protein used in Chapter 6 (10mM MOPS, 50 mM KCl, 2 mM $Mg^{2+}$). **C** No DNA control. Scale bars 20 $\mu$m.

## 2.8 Quantum Dot and Streptavidin labelling

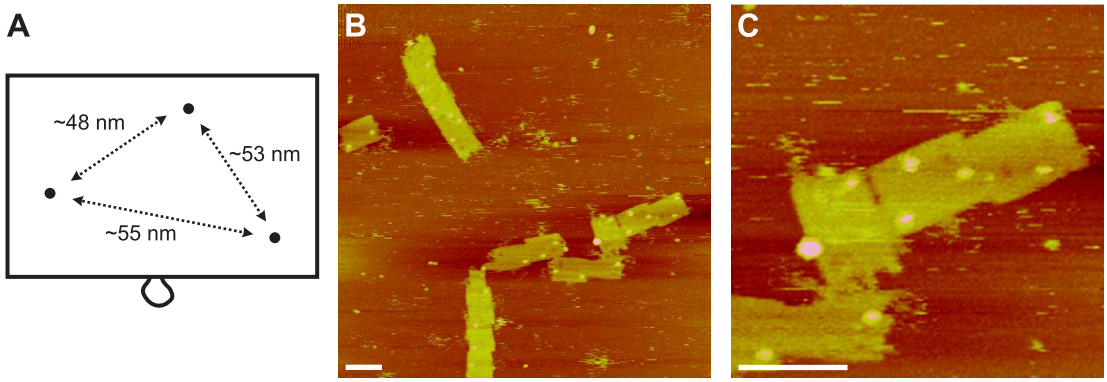


Figure 2.10: AFM images of a biotin-streptavidin origami tile. **A** Schematic of the biotin modified sites; the origami tiles are annealed with 3 5'-modified biotin staple strands. **B** Tiles were deposited on mica and incubated with a stoichiometric amount of free streptavidin; unbound protein was washed away before imaging by AFM. The protein modifications to the tiles show up clearly, and in **C** the central tile has all three attachment sites visible.

Methods for labelling origami tiles with fluorescent quantum dots (Qdots) were tested (Appendix A.8). Biotin modified staple strands can be incorporated in tiles under standard annealing conditions. When free streptavidin (SA) is mixed with the biotin-labelled origami, AFM images show specific binding to the modified staples (Figure 2.10). It was found that AFM samples must be washed with buffer repeatedly after being deposited on mica to remove excess protein and achieve good image quality. The biotin modified tiles can also be incubated with SA-coated Qdots. Binding is observed by agarose gel electrophoresis (Figure 2.11); the bound Qdots migrate with the DNA origami band. The size of the Qdots (∼20nm) is relatively small compared to that of the tile, and only a slight gel shift between labelled and unlabelled tiles was observed even after long run times (Figure 2.11 B).

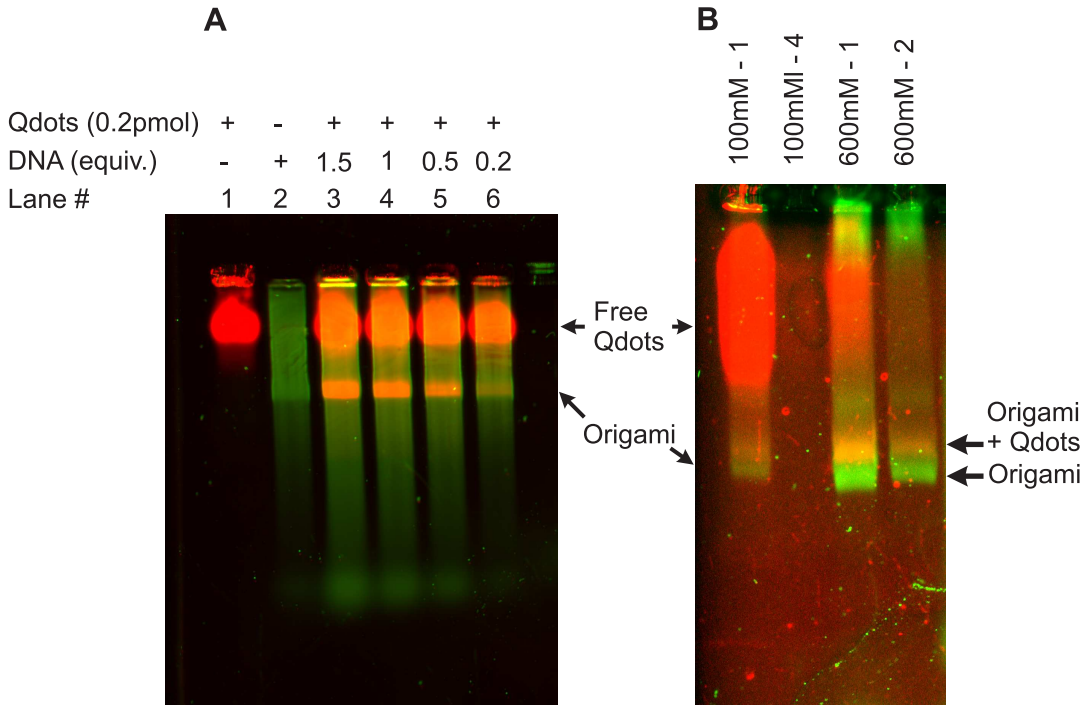


Figure 2.11: Agarose gel electrophoresis of biotin-modified origami tiles labelled with red quantum dots. **A** Red Qdots are incubated with biotin origami at a range of concentrations. In all cases, bound Qdots co-migrate with the DNA origami band, faster than free dots. **B** Purification on an ion-exchange column separates free Qdots, which do not bind to the column (lanes 1 and 2), from those on DNA tiles, which only elute in a high salt buffer (lanes 3 and 4). A slight shift between labelled and unlabelled origami tiles was detected. In all lanes, red is Qdot fluorescence (488/665 nm) and green is SyBr gold stained DNA (488/530 nm).

Qdots bound to origami tiles can be purified away from those that are unbound, following methods developed for labelling Qdots with ssDNA (Carstairs et al., 2009). The sample is added to a hand-packed version of the ion-exchange column used in Section 2.3. The hand-packed column is required because the Qdots are known to bind permanently to the plastic frit at the base of pre-packed columns (Carstairs et al., 2009). Free Qdots do not bind to the column, and are washed out with a number of rinses. A high salt buffer is then used to elute the DNA tiles and DNA-Qdot tiles together (Figure 2.11). This was found to be a suitable method for removing the excess of free Qdots, and significantly reduces the background fluorescence of the sample.

These labelling methods were developed for use in single-molecule experiments on DNA origami motors. The SA label is a good topographical marker under AFM, and is used in Section 4.4. While not used in this thesis, it is thought that the Qdot label will be useful for single-molecule fluorescence studies of DNA motors.

## 2.9 Additional Experimental Techniques used in later Chapters

### Fluorescence quenching experiments

Förster resonance energy transfer (FRET) is energy transfer between a donor fluorophore and an acceptor fluorophore in close proximity (<1 nm) through non-radiative dipole-dipole coupling (Förster, 1965). When the two fluorophores are brought close together, a characteristic reduction of donor emission is observed. This reduction, or quenching, of the donor emission can be used to monitor the movement of fluorophore-labelled DNA devices (Yurke et al., 2000; Bath et al., 2005). In Chapters 3, 4 and 5 a variation on this technique is used, in which

a fluorescence quenching molecule attached to a DNA motor is brought close to fluorophores on the motor track. The quencher reduces donor emission, similarly to FRET between two fluorophores, but does not re-emit this energy at visible wavelengths. Fluorescence, at multiple wavelengths, of a bulk sample ($\sim 100\ \mu$L) is measured over time in a fluorimeter (Appendix A.9).

### Poly-acrylamide gel electrophoresis

An agarose gel matrix has a pore size suitable for the separation of DNA origami tiles from staple strands in gel electrophoresis. To separate shorter (100's nt) DNA strands from each other a gel matrix with a smaller pore size is required. A poly-acrylamide (PA) gel matrix is used in Chapter 5 for gel electrophoresis analysis of short synthetic components of the DNA motor designs. The experimental method for PA gels is similar to that for the agarose gels discussed above (Section 2.3), and detailed protocols are given in Section A.4.

### High-speed AFM

The AFM system used to image the DNA origami samples in this Chapter has an optimal scan rate of 1 frame ($512 \times 512$ pixels) every 512 s. In Chapters 3 and 4, an AFM system with a much faster scan rate, up to 10 Hz, is used. Details of both AFM systems are given in Section A.3. The high-speed AFM is located in the Sugiyama Laboratory, Kyoto University, Japan. AFM Data collected in Kyoto is identified at the beginning of each Chapter.

## 2.10 Conclusions

This Chapter presents a number of DNA origami methods developed in the course of this thesis. Such methods were fundamental in achieving the results presented in the following Chapters. In particular, the size-exclusion purification method with hand-packed columns was used for all samples in Chapters 3, 5 and 6. The ability to repair defective DNA tiles without thermal annealing is used to load DNA motors at a particular location along a track in Chapters 3 and 5. The HPLC analysis method, adapted for use with a pre-packed size-exclusion column, provides the key result of protein-binding in Chapter 6. Other work has also benefited from the results shown here (Parminder Lally, D.Phil Thesis, 2011), and this Chapter should provide a useful resource for future work on DNA origami.

Chapter 3

# DNA origami track for a 'Burnt-bridges' DNA motor

In this chapter the movement of a 'burnt-bridges' type DNA motor across an extended DNA origami track is demonstrated. The system consists of a simple directional and processive motor fuelled by hydrolysis of the DNA phosphate backbone, catalysed by a restriction enzyme. It is shown that the motor can be loaded at one end of a track displayed on a two-dimensional DNA origami substrate. Ensemble fluorescence measurements are then used to show the motor is transported, autonomously and at constant average speed, the full length of the track, a distance of ∼100 nm, corresponding to 16 consecutive steps. High-speed AFM measurements reveal mechanistic detail by direct, single-molecule observation of individual steps. This precisely controlled, long-range transport is a fundamental step towards the development of more complex systems that can be programmed and routed by instructions encoded in the nucleotide sequences of track and motor.

**AFM Data Contributions**

The AFM data in this Chapter was collected on a high-speed AFM in collaboration with the Sugiyama Laboratory, Kyoto University, Japan. All experiments and protocols were designed by the author, and are described in detail in Appendix A.3. Initial AFM experiments were refined during a visit by the author to Kyoto University in August and September 2009. For the data presented in this Chapter, samples were prepared either by the author (Figure 3.2) or by Y. Katsuda (all others), and all images were obtained by microscope technician K. Hidaka. AFM movie data was analysed to produce the kymographs in Figures 3.16, 3.17, 3.18 and 3.19 by the author at Oxford University, UK. Analysis of static images for the histograms in Figures 3.14 and 3.15, and the height profile data in Figure 3.20, was provided by Y. Katsuda and K. Hidaka, at Kyoto University, Japan.

## 3.1 Motor and Track design

The motor discussed in this chapter is a strand of ssDNA that is complementary to a ssDNA stator. When the motor strand binds to a stator, the resulting motor-stator duplex contains the recognition site for a nicking restriction enzyme, that catalyzes hydrolysis of a specific backbone linkage of the stator (Heiter et al., 2005). The nicking enzyme, Nt.BbvCI, recognises the dsDNA sequence `CC-TCAGC`, and cuts the sense strand between and second and third nucleotides. This enzyme is an engineered heterodimeric form of a restriction enzyme, BbvCI, from *Bacillus brevis*, which in the wild-type form cuts both strands of the duplex (Heiter et al., 2005).

Once the stator is cut, the short 6-nt fragment dissociates from the duplex, driving movement of the motor from the cut stator to an adjacent intact stator (Bath et al., 2005). The length of the cut motor-stator duplex (16 bp ∼5.44 nm) is similar to the spacing between stators (∼6 nm). Figure 3.1 shows the designed

transfer mechanism: thermal dissociation of the 6-nt cut fragment is followed by strand exchange initiated by hybridization of the bases revealed at the 3' end of the motor. Directional movement is imposed because all stators in the wake of the motor have been cut (a 'burnt bridges' mechanism). The first stator forms two extra basepairs with the motor to help bias the initial motor position. The last stator has a modified sequence that creates a mismatch in the motor-stator duplex, protecting it from the enzyme and trapping the motor (Bath et al., 2005).

Previous studies of this design considered motor behaviour on a short test track of only three stators, all non-identical. This is extended here to a linear track of 15 identical stators, flanked with special start and stop stators. The track is assembled on a rectangular DNA origami tile measuring approximately 100 nm by 70 nm (Rothemund, 2006) (Figures 3.1, 3.2, 3.13). Two tile designs were used, the original DNA origami rectangle with seam (Rothemund, 2006), and a reduced twist origami rectangle as discussed in Section 2.6. In both cases, selected staples were extended to include the 22-nt stator sequence at the 5' end (Figure 3.1 B). For AFM experiments additional staples were also modified with a hairpin at the centre (Rothemund, 2006), to act as registration markers (Figure 3.13). Both the ssDNA stators and the motor-stator duplex are visible in AFM images. Figure 3.2A shows the array of stators running diagonally across the tile with a separation of 6 nm, and Figure 3.2B shows the same tile design with a motor strand loaded at the start of the track.

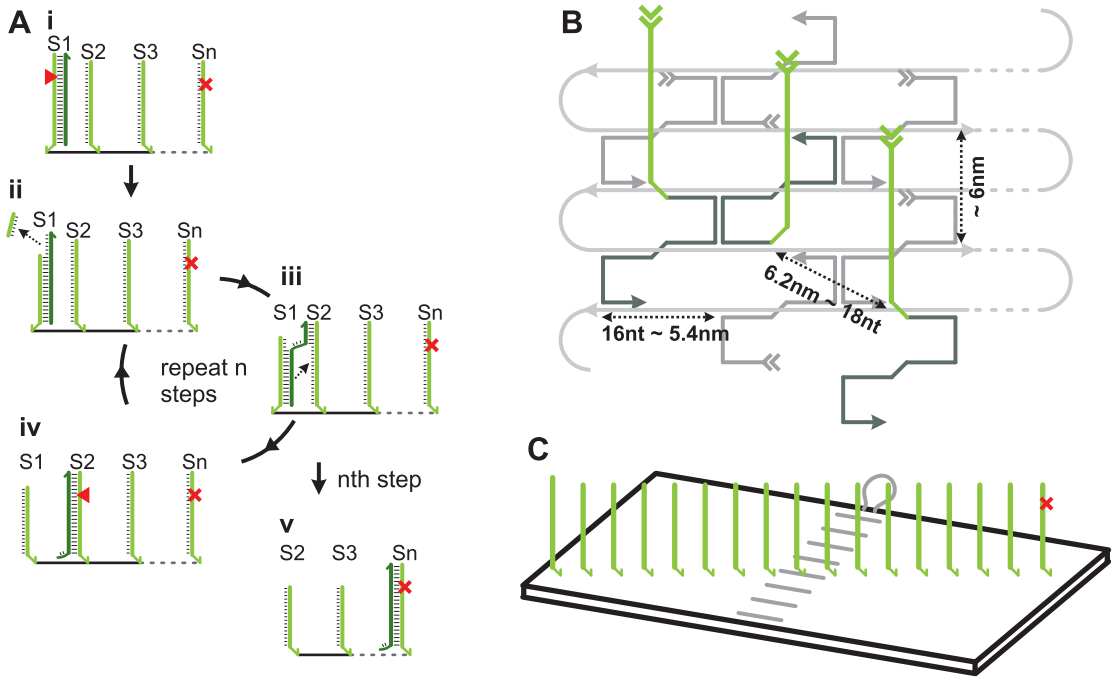


Figure 3.1: 'Burnt-bridges' DNA motor and track. **A** Motor mechanism: **i** the ssDNA motor (dark green) binds to a ssDNA stator (light green), **ii** nicking enzyme cuts the dsDNA motor-stator duplex at a defined location (red triangle), revealing a 6-nt toehold at the 3' end of the motor, **iii-iv** the toehold facilitates transfer of the motor to the adjacent intact stator by branch migration, **v** motor is trapped at the final stator by a mismatch in the nicking enzyme restriction site (red cross). **B** Stator sequences are added to the 5' end of DNA origami staples, with a spacing of ∼6 nm. **C** Layout of the motor track on a DNA origami tile, up to 17 stators can be placed diagonally across a single tile.

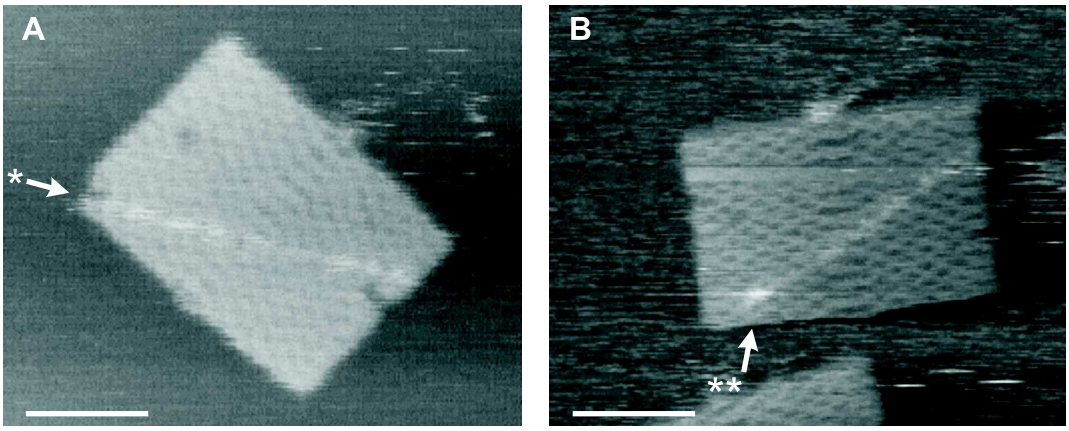


Figure 3.2: AFM images of the 'Burnt-bridges' DNA motor and track. The motor can be precisely positioned on the track by omitting the first stator during tile assembly (**A**), then repairing the tile by addition of the missing stator hybridized to the motor (**B**). Arrows highlight the defect in the tile before (*) and after (**) repair with the motor-stator duplex. Scale bars 50 nm.

## 3.2 Ensemble Fluorescence Measurements

Initial observations of motor transport across the DNA origami tracks were made by ensemble fluorescence quenching measurements, as introduced in Section 2.9. The motor is modified to carry a quenching group past a sequence of fluorophores at specific locations along an 8-stator track ($S_1$-$S_8$), as shown in Figure 3.3. Detailed experimental protocols are given in Appendix A.9.

### 3.2.1 Loading the Motor

In order to make ensemble measurements of the many motor-track systems in solution, they must first be synchronised. That is, motors must all be loaded at $S_1$. If the motor strand is simply added to the complete track, it has an equal chance of binding to any of the 6 identical 22-nt stators. For the enzyme buffer conditions (50 mM $Na^+$, 12.5 mM $Mg^{2+}$), the $\Delta G^\circ$ for motor binding to the three stator types, $S_1$, $S_{2-7}$, $S_8$, are estimated at 37°C as -28.4, -25.7, -22.1 kcal $mol^{-1}$ respectively

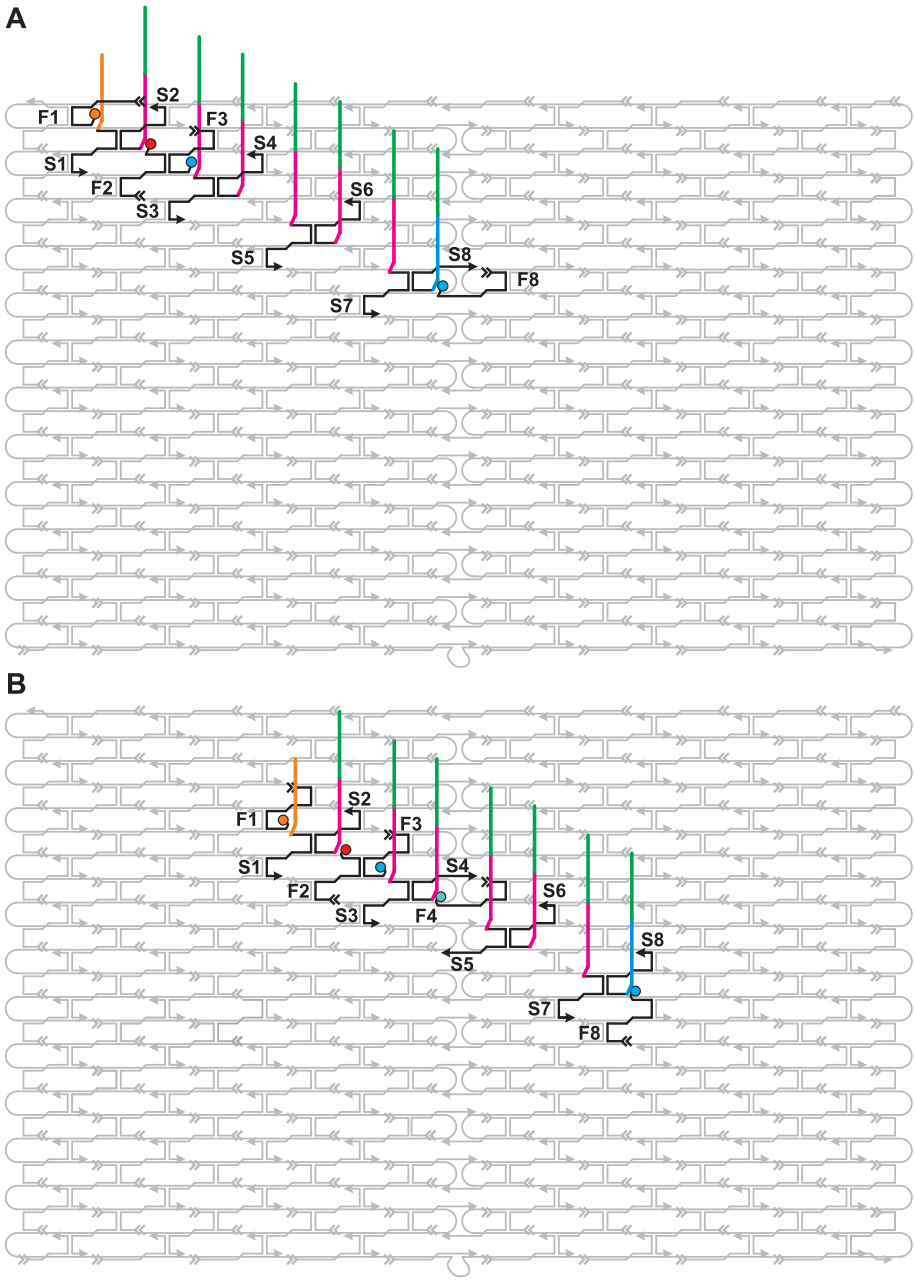


Figure 3.3: 'Burnt-bridges' DNA origami track designs for ensemble fluorescence measurements. **A** The track is placed in the top left of the original origami tile type (Rothemund, 2006). **B** The track is placed in the centre of a reduced twist DNA origami rectangle (Section 2.6).

(Markham and Zuker, 2005). This gives a predicted equilibrium distribution of the motor on stators $S_1$:$S_{2-7}$:$S_8$ of $76 : 24 :\ll 1$, which is only slightly biased towards the 24-nt first stator $S_1$. Thus, methods for achieving a better loading bias were investigated.

The first loading method takes advantage of the ability of an origami tile assembled with a defect to be repaired by incubation with the missing staple strand, without thermal annealing, as discussed in Section 2.5. The motor is loaded at a specific position by omitting the staple bearing the corresponding stator when the tile is assembled (Figure 3.4 Ai). The motor strand is separately hybridised to the missing stator strand. This stator staple, bearing the motor, is then inserted in the correct place by incubating it with the defective tile at 37 °C for 1 hour. Excess staples and motor-stator duplex are purified away from the origami tiles, and the fluorescence of the sample measured over time.

Figures 3.4 B and C show fluorescence results for a tile labelled with fluorophores $F_2$ and $F_8$ at stators $S_2$ and $S_8$ respectively. On the addition of enzyme, a transient dip is seen in the signal for $F_2$ as the motor-quencher moves past this location. A slow increase in the quenching of $F_8$ is consistent with the motor reaching and being trapped at position $S_8$. In comparison, for samples with no enzyme the fluorophore traces remain flat. However, if the motor must travel the full length of the track there should be a delay before it can begin quenching fluorophore $F_8$ at the final position. Such a delay is supported by a kinetic model presented in Section 3.2.4, but was not observed in this data. The $F_8$ signal begins decreasing immediately after the addition of enzyme. This suggests that a significant number of motors start in the middle of the track, and reach $F_8$ faster than those that start at the beginning of the track. This may be due to either incorrect loading, or diffusion of the motor along the track before initiation of active transport.

Two designs were considered to improve the loading efficiency. Firstly, to pre-

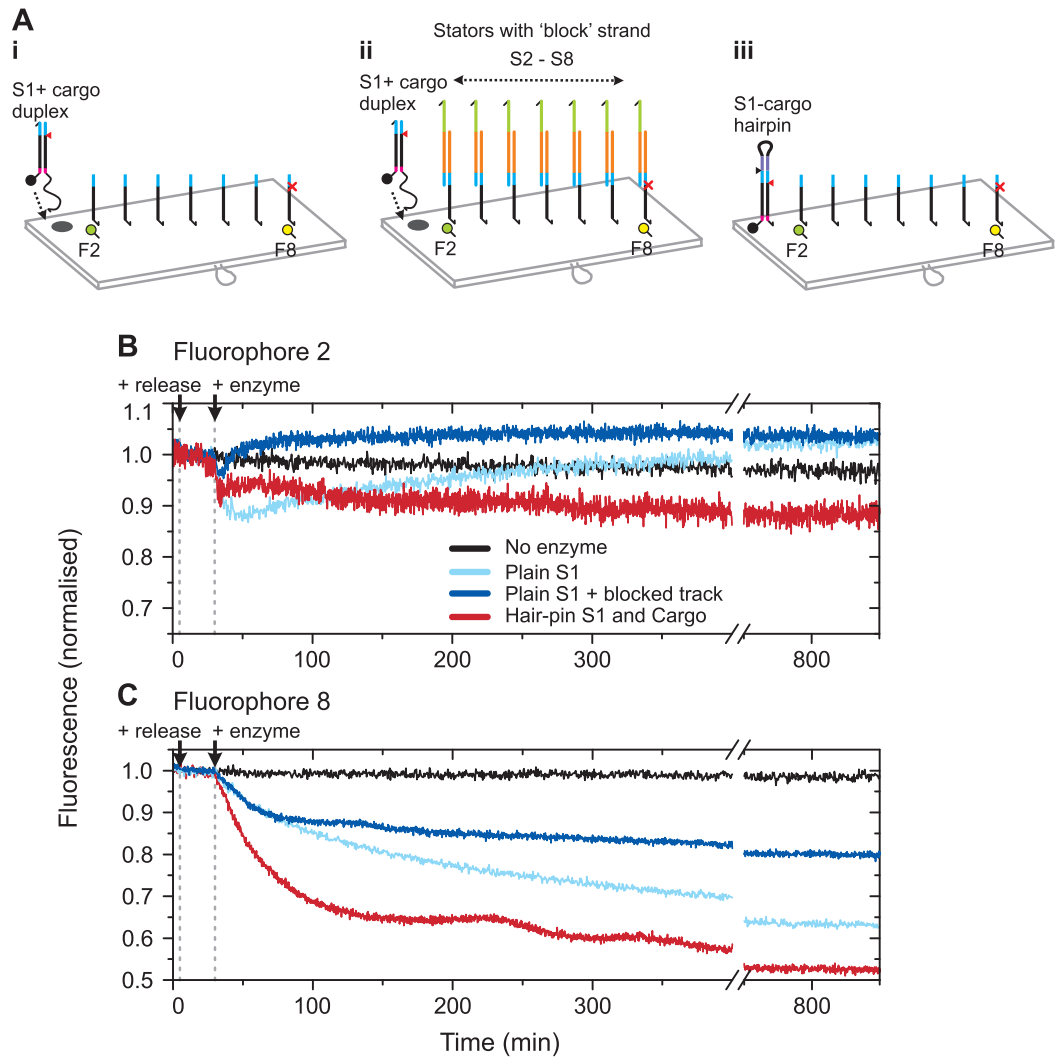


Figure 3.4: Different loading designs. **A i** motor can be loaded at the start of the track by omitting the first stator in assembly, and later repairing it with the $S_1$-motor duplex, **ii** this process is improved by adding a removable 'blocking' strand to the other stators, **iii** an alternative design in which the motor is initially bound to $S_1$ in a hairpin configuration and released by cleavage with a second enzyme (black triangle). **B, C** Fluorescence results for fluorophores $F_2$ and $F_8$ labelling stators $S_2$ and $S_8$ respectively. Traces are flat for the no enzyme control. After addition of enzyme, there is a dip in $F_2$ as the motor moves past this position, and an increase in quenching of $F_8$ as motor accumulates at the end of the track. For designs ii and iii the track was activated ~20 min before addition of the main enzyme by adding the release strand, or second enzyme respectively. Measurements were made at 27°C.

vent diffusion and incorrect loading, stators $S_2$-$S_8$ were reversibly protected by addition of a blocking strand. This strand hybridizes to an additional binding domain at the 5' ends of the stators and the first 6 nt, (a 'weak' block) or 10 nt (a 'strong' block) of the motor's binding site. The blocking strand contains a 15-nt single-stranded toehold (Yurke et al., 2000; Yurke and Mills Jnr, 2003) that allows the track to be activated by addition of a complementary release strand (Figure 3.4 A ii).

A second design was considered in which the motor-stator duplex initially consists of a hairpin formed from a single piece of ssDNA, as in Figure 3.4 A iii. In this design the restriction site for a second enzyme (scrFI) was incorporated into the neck of the hairpin directly above the standard motor sequence. On addition of the second enzyme, both strands of the hairpin are cut, leaving only the original motor and stator sequences. The fluorescence results for both designs are also shown in Figure 3.4 B and C. The most consistent behaviour was observed for the system in Figure 3.4 A ii, loaded with the $S_1$-motor duplex and a block on other stators. This loading design was used for all following experiments.

### 3.2.2 Blocked Tracks

As shown in Figure 3.3, two possible DNA origami tile designs were considered. These were both tested and the results are given in Figure 3.5. While the behaviour of the $F_2$ signal for all designs is very similar, the results differ markedly for $F_8$ at the end of the track . As mentioned above, if the motors must travel the length of the track before reaching this position, the $F_8$ signal is expected to decrease with a sigmoidal shape. For the first tile type, the $F_8$ signal for the weakly-blocked track decreases quite smoothly, while that for the strongly-blocked track has a more sigmoidal shape. The results for the second tile type are the most clearly sigmoidal, and show a greater yield of motor reaching the end of the track. The

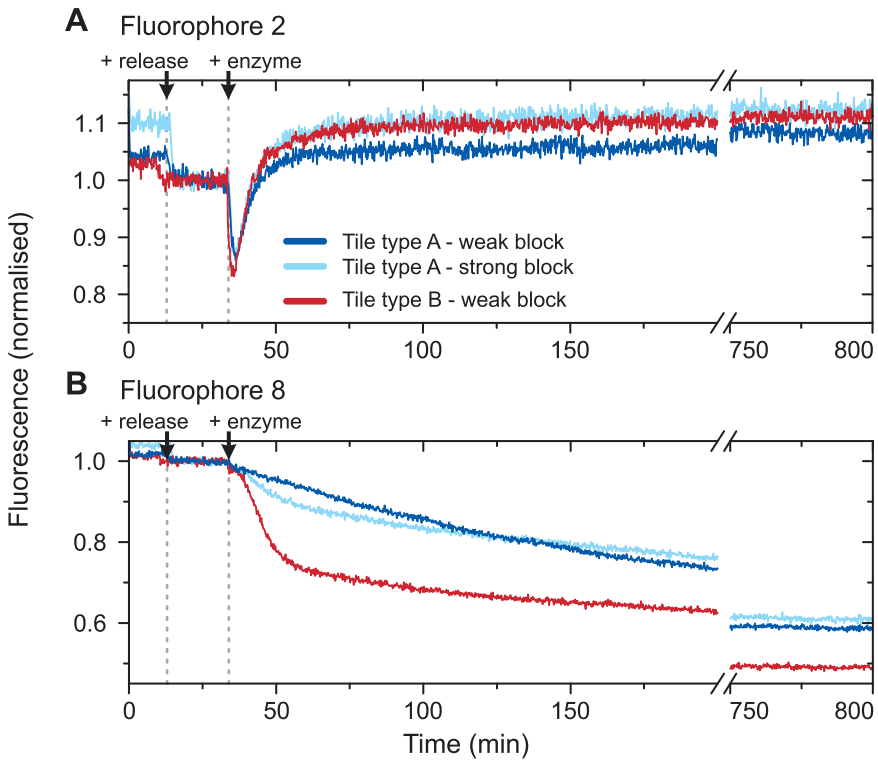


Figure 3.5: Comparison of different track designs. **A, B** Fluorescence results for fluorophores $F_2$ and $F_8$ on stators $S_2$ and $S_8$, for the two track designs in Figure 3.3. For tracks on tile type A (Figure 3.3 A), block strands with either a 6-nt overlap with the motor sequence (weak) or a 10-nt overlap (strong) are compared. Tile type B gave the best data, and is used for the rest of this Chapter and for Chapter 5. Measurements were made at 37°C.

reason for this improvement is not clear. It is possible that the reduced twist origami tile results in a slightly shortened step size. While the horizontal spacing between stators will be reduced by at most 1 bp (0.34 nm), the change in vertical spacing is not known. In other similar designs the vertical spacing of helices was found to be much smaller, 2 nm rather than 3 nm (Li et al., 2010). Measurements of the reduced twist tile size (Section 2.6) show that any such reduction in the vertical spacing for this tile is less than 10%. Nevertheless, these small changes in step-size, as well as a decrease in global twist, may have a significant effect on the motor, and result in the improved data quality seen in Figure 3.5. The reduced twist tile design was used in all following fluorescence experiments in this Chapter.

### 3.2.3 Complete and Broken Tracks

Once the track and tile designs had been refined, the behaviour of the motor was examined in more detail. Figure 3.6 shows the signal from fluorophores $F_1$, $F_2$, $F_3$ and $F_4$ positioned near stators $S_1$, $S_2$, $S_3$ and $S_4$ respectively. To prevent Förster resonance energy transfer (FRET) between closely-spaced fluorophores, tiles labelled with $F_1$, and $F_3$ or $F_4$, and tiles labelled with $F_2$ were prepared separately then mixed and observed at 37°C. In this experiment motor loading is observed, for all others the motor was loaded prior to purification and data collection. $F_1$ fluorescence decreases upon addition of a stoichiometric amount of the $S_1$-motor duplex, consistent with loading of the motor at the first track position. Fluorescence at the other positions is largely unchanged, demonstrating that there is very little transfer of the motor to the blocked stators $S_2$-$S_8$. A slight increase in $F_1$ and slight decreases in $F_2$-$F_4$ signals were observed when the release strand was added, consistent with slow diffusion of the motor.

Directed movement is initiated by addition of the nicking enzyme. An immediate increase in $F_1$ signal was observed, indicating motion of the motor away from

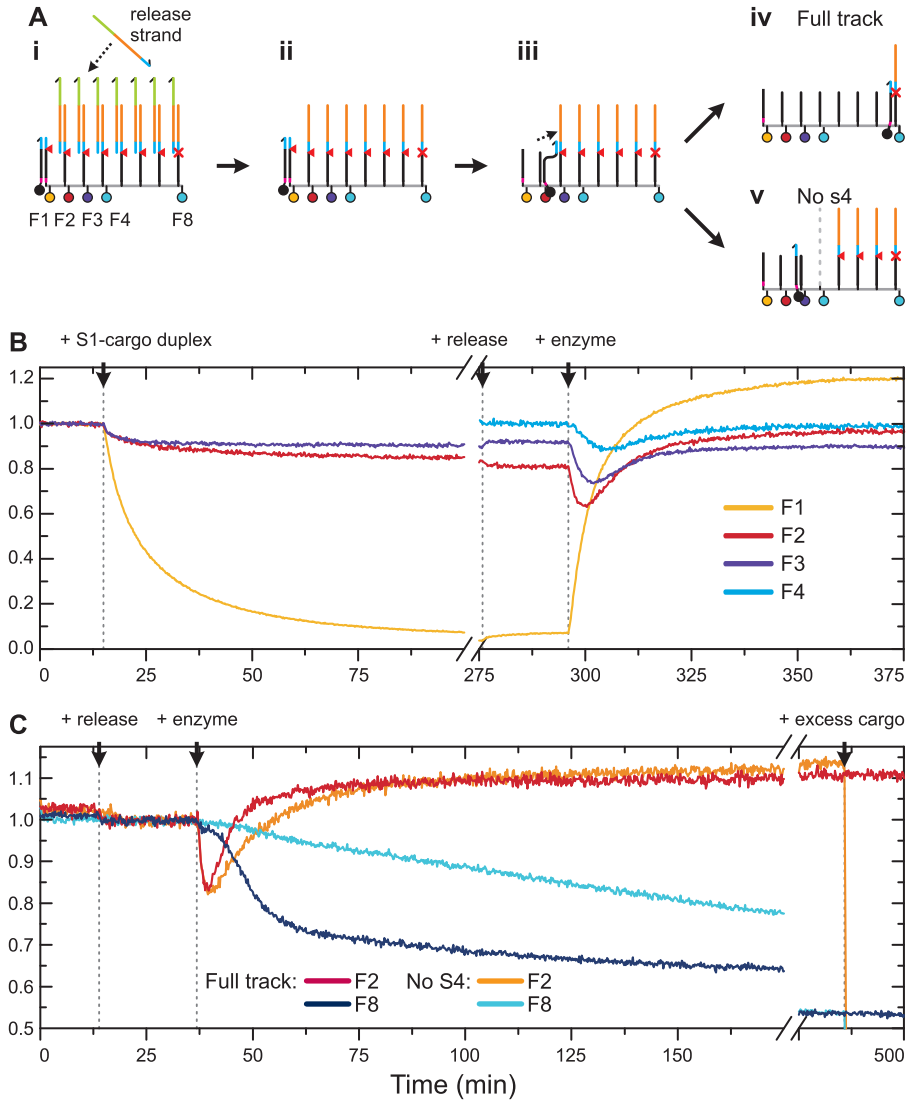


Figure 3.6: Fluorescence measurements of motor movement on intact and broken tracks. **A** Designed operating sequence: a motor carrying a quencher (Q) is loaded at position $S_1$ of an 8-stator track, blocking strands occupy stators $S_2$-$S_8$, preventing movement of the motor. **i, ii** Addition of a release strand removes the blockade. **iii** Active motion is triggered by addition of enzyme. Motor position is reported by quenching of fluorophores $F_1$, $F_2$, $F_3$, $F_4$ and $F_8$ by the motor. **B** Tracks labelled at $F_1$, $F_3$ mixed with tracks labelled at $F_2$ or $F_4$. **C** Fluorescence from tracks labelled at $F_2$, $F_8$. The quenching of $F_8$ that reports the arrival of motor at the end of an intact track is greatly reduced on tracks where stator $S_4$ is omitted.

$S_1$ as it is cut. Sequential, transient dips in $F_2$, $F_3$ and $F_4$ signals indicate that the motor has occupied and then moved past stators $S_2$, $S_3$ and $S_4$ in turn as they, too, are cut. After ∼30 minutes, the signals of all fluorophores return to a high steady state, consistent with accumulation of the motor strand at the distal end of the track. Figure 3.6 C shows the results of a similar experiment in which stators $S_2$ and $S_8$ were labelled. The same transient quenching of $F_2$ is observed, then the $F_8$ signal slowly and permanently decreases as the motor accumulates at the final stator. A simple model for stepping using first-order rate constants obtained from experiments on a short track (Bath et al., 2005) agrees quantitatively with the data (Section 3.2.4): the average motor speed is of order 0.1 $nms^{-1}$.

To test the dependence of stepping on the spacing of the stators along the track, a number of different 'broken' track configurations, omitting one or more stators, were tested (Figures 3.6, 3.7). The rate of quenching of $F_8$ fluorescence, indicating arrival of the motor at the end of the track, is reduced for damaged tracks, as expected. Nevertheless, some decrease in $F_8$ fluorescence, indicating delayed arrival of motor molecules at the final stator, was observed for all tracks.

In Figure 3.6 C, when stator $S_4$ is omitted, leaving a 12 nm gap in the track, the rate of quenching of the $F_8$ signal falls, consistent with a strongly reduced stepping rate cross the gap. In Figure 3.7 the decrease in arrival rate is observed to be greater for a track with an 18 nm gap, produced by omitting both $S_4$ and $S_5$, than for a 12 nm gap, produced by omitting $S_4$ only. It is inferred that motor strands can cross a gap in a track at a rate that depends on the gap size. Comparison with predictions of the model discussed in more detail in Section 3.2.4, modified to include a slow step, leads to an estimate of a ∼50× reduction in stepping rate across a 12 nm gap, and a ∼100× reduction for an 18 nm gap.

Motors were also found to reach $S_8$ at a faster rate for tracks broken in the middle ($S_4$) than for tracks broken at the end ($S_7$). To step directly from $S_6$ to $S_8$

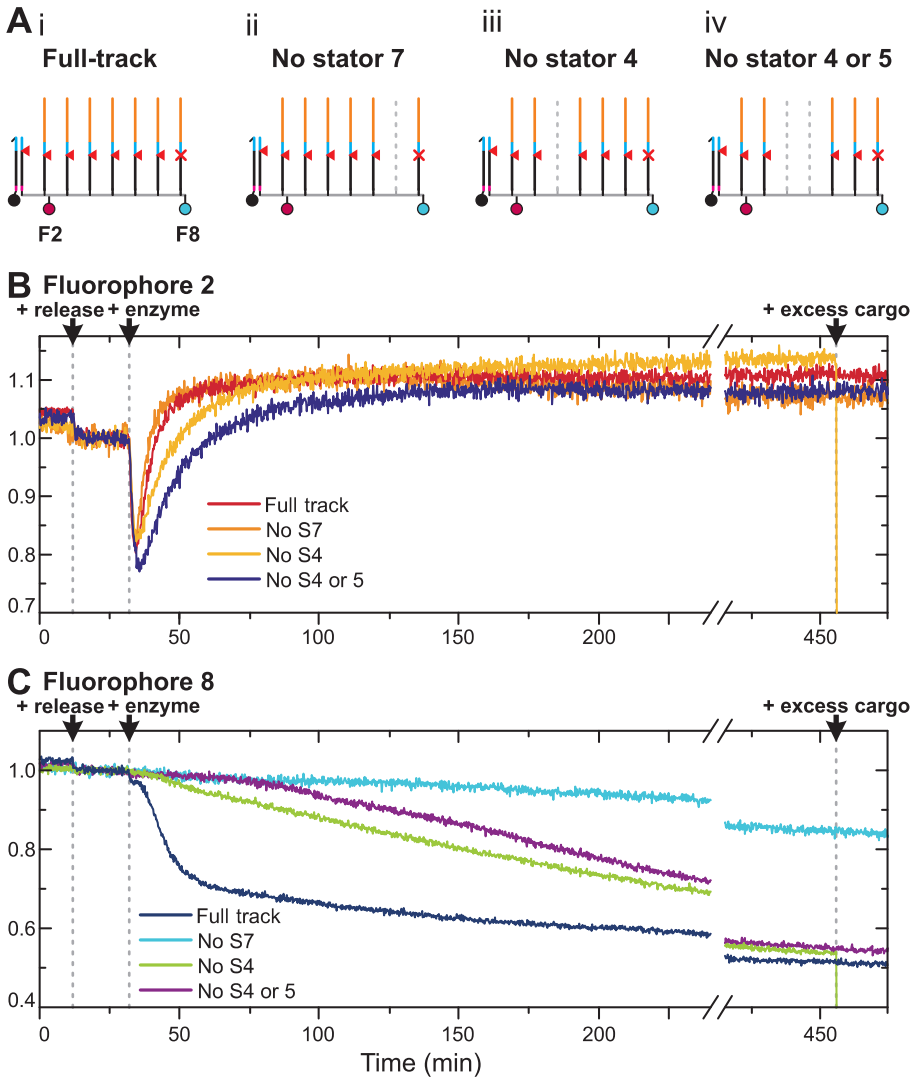


Figure 3.7: Stepping along gapped tracks. **A**Tracks compared: **i** full track ($S_1$-$S_8$), and tracks broken by omitting **ii** stator $S_7$, **iii** stator $S_4$, and **iv** stators $S_4$ and $S_5$. Staples bearing the omitted stators were replaced with unmodified staples. **B, C** Fluorescence from fluorophores $F_2$ (B) and $F_8$ (C) on each track was recorded at 37°C. The rate of quenching of $F_8$ fluorescence, indicating arrival of the motor at the end of the track, is reduced for damaged tracks, and depends on the size of the gap and its position along the track.

the motor must step onto a mismatched stator with a lower affinity for the motor, resulting in a further reduction in the rate of transfer across the gap, with very little reaching $S_8$ on this timescale. Thus, these results show that changing the step size along the track by omitting stators can be used to create a programmable delay.

As discussed above, motor reaches position $F_8$ at the end of the track more slowly for tracks damaged by the omission of one or more stators. A further experiment was used to determine what proportion of this motor reaches the end of the track by inter-molecular transfer between tiles, rather than crossing the gap in the track. This 'split-tile' design consists of two tile types. The first tile type carries stators $S_1$ to $S_3$, with fluorophore $F_2$, and is loaded with the motor on stator $S_1$. The second type carries stators $S_6$ to $S_8$, and $F_8$, and has no motor. The two tile types are combined, and observed together. The fluorescence results for fluorophore $F_2$ (Figure 3.8 B) show transient quenching as the motor moves past this position, as expected, and that the motor mechanism is not disrupted. The quenching of fluorophore $F_8$ at $S_8$ (Figure 3.8 C) is much less for the split-tile configuration than for the equivalent broken track. It is possible to conclude then that inter-tile transfer is slow, and almost all of the motor that reaches stator $S_8$ in damaged tracks is crossing the gap in an intramolecular step. These rates will be analysed in more detail in Section 3.2.5.

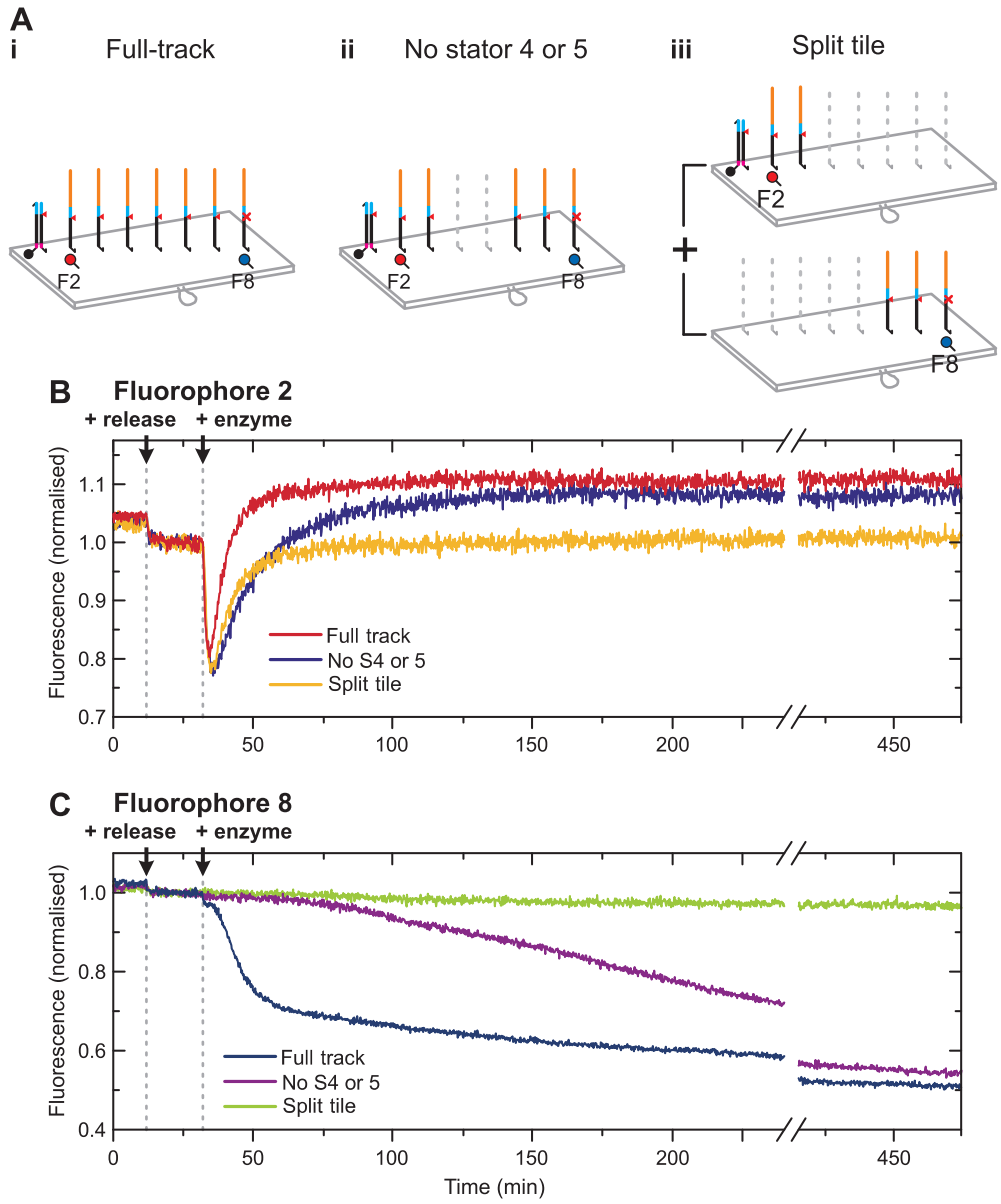


Figure 3.8: Inter-molecular transfer of motor for a 'split-tile' sample. **A** Three tracks are compared: **i** complete, **ii** broken by omitting stators $S_4$ and $S_5$, and **iii** a matching split-tile sample containing a mixture of two types of tile carrying incomplete tracks. **B** Fluorescence from fluorophore $F_2$ st $S_2$ shows transient quenching as the motor moves past this position in all samples. **C** Fluorescence from fluorophore $F_8$ at $S_8$. Quenching of the $F_8$ signal in the split-tile sample is much less than that observed for the track broken at stators $S_4$ and $S_5$. Measurements were made at 37°C.

### 3.2.4 Kinetic model for stepping

Unidirectional movement of the motor along the track is modelled using two first-order rate constants taken from measurements at 37°C on a short track with 3 stators, as in (Bath et al., 2005). Rate $k_1$ is used for stepping off the first stator, which is 2 nucleotides longer than all other stators, and rate $k_2$ is used for all other stators. Values for rates $k_1$ and $k_2$ are taken directly from (Bath et al., 2005). Once started, stepping in either the forward or backward direction is assumed to be unidirectional and motors cannot step onto a cut stator. The equations below are used to determine the fraction of stator $i$ occupied at time $t$, $c_i(t)$.

Motors stepping forward:

$$\frac{\mathrm{d}c_1(t)}{\mathrm{d}t} = -k_1 c_1(t)$$
$$\frac{\mathrm{d}c_{i+1}(t)}{\mathrm{d}t} = k_i c_i(t) - k_{i+1} c_{i+1}(t)$$
$$\frac{\mathrm{d}c_8(t)}{\mathrm{d}t} = k_7 c_7(t)$$
$$k_1 = 0.003 s^{-1}$$
$$k_{2-7} = 0.009 s^{-1}$$

Motors stepping backward:

$$\frac{\mathrm{d}c_1(t)}{\mathrm{d}t} = k_2 c_2(t)$$
$$\frac{\mathrm{d}c_i(t)}{\mathrm{d}t} = k_{i+1} c_{i+1}(t) - k_i c_i(t)$$
$$\frac{\mathrm{d}c_8(t)}{\mathrm{d}t} = -k_8 c_8(t)$$
$$k_{2-7} = 0.009 s^{-1}$$
$$k_8 = 0$$

In the ideal case, it is assumed that backwards steps do not occur, and that all the motor is initially loaded at stator $S_1$ and finishes at stator $S_8$. That is, that $c_1(0) = 1$ and $c_{2-8}(0) = 0$. A plot of the predicted signal $(1 - c_i(t))$ is shown for stators $S_1$, $S_2$, $S_3$, $S_4$ and $S_8$, along with the corresponding fluorescence data in Figure 3.9 (solid lines). The shape of the model and data are generally similar.

A second case is considered, in which 20% of motor is distributed evenly over stators $S_2$ - $S_8$ before the motor is activated. That is, that $c_1(0) = 0.8$ and $c_{2-8}(0) = \frac{0.2}{7}$. Motor loaded in the middle of the track is given an equal chance of taking an initial forward or backward step, after which it is restricted to one direction. Motor starting on each stator is considered separately, and the results for all 8 stators summed to give the final predictions. In this case the latent period before $F_8$ fluorescence begins to decay is reduced (Figure 3.9 A, broken lines), giving a better agreement with the data.

Table 3.1: Model and Data comparison.

| | Model (s) | Data (s) |
|---|---|---|
| $t_{0.5F1}$ | 231 | 230 ±10 |
| $t_{minF2}$ | 183 | 200 ±50 |
| $t_{minF3}$ | 317 | 370 ±10 |
| $t_{minF4}$ | 443 | 460 |
| $t_{0.5F8}$ | 929 | 700 ±50 |

This simple model is used to predict several features; the time for $F_1$ to increase to 50% ($t_{0.5F1}$), the time for $F_8$ to fall to 50% ($t_{0.5F8}$), and the time at which $F_2$, $F_3$ and $F_4$ are a minimum ($t_{minF2}$, $t_{minF3}$, $t_{minF4}$). These times are compared with values measured from fluorescence data (Table 3.1), error estimates are obtained from repeated fluorescence runs. The experimental results are in agreement with the predictions of the model, and the observed minima for $F_2$, $F_3$ and $F_4$ are sequential, as predicted. Thus, the results from the origami track data are consistent

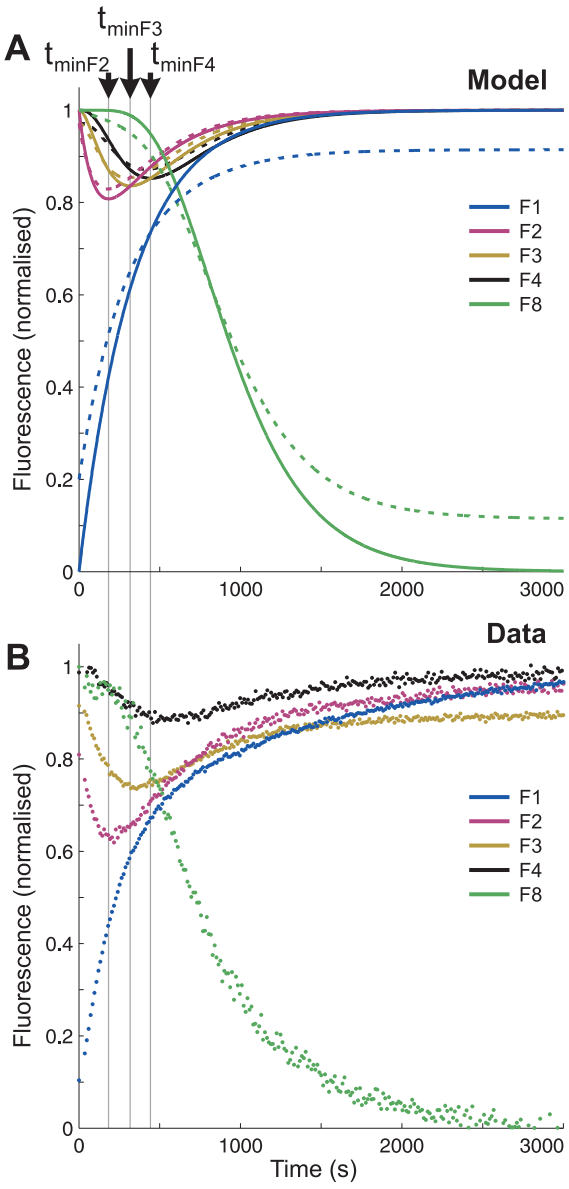


Figure 3.9: Kinetic model for stepping rate analysis. **A** Predicted time-dependence of normalized fluorescence signals $(1 - c_i(t))$ (i =1,2,3,4,8), **B** corresponding data, recorded at 37°C (Figure 3.6). Vertical lines indicating the predicted times at which $F_2$, $F_3$ and $F_4$ are a minimum are a guide to the eye, and show they occur sequentially in both model and data. Solid lines correspond to the ideal case, and dotted lines to non-ideal loading of the motor on $S_1$.

with the rate constants reported previously for a dsDNA track of 3 stators (Bath et al., 2005). The speed of the motor is estimated to be of order 0.1 $nms^{-1}$, and the time taken to cross the origami is predicted to be of order ∼10 min for the 8 stator track used in fluorescence measurements, and ∼20 min for a tile with a full length track of 17 stators.

The dependence of these rates on temperature and buffer conditions was also tested with the same model, and the results are shown in Figure 3.10. Reducing the temperature from 37°C to 25°C, and omitting the sodium chloride from the buffer, as is necessary in AFM experiments, leads to a reduction of the stepping rate by ∼3-fold, as estimated from the data.

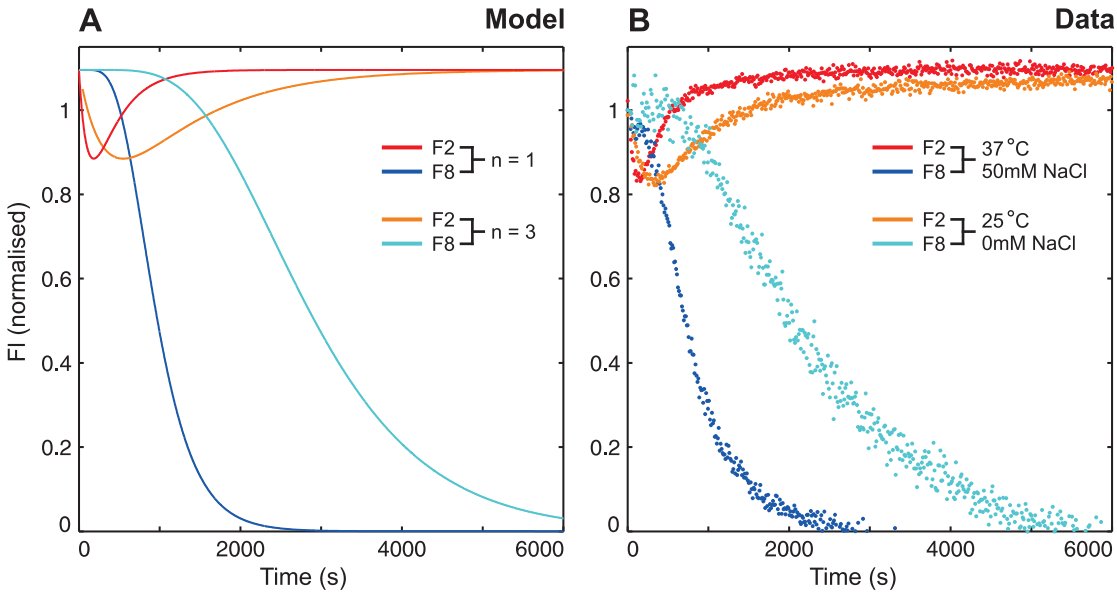


Figure 3.10: Dependence of stepping rate on temperature and buffer conditions. Model predictions for $F_2$ and $F_8$ fluorescence with rate constants reduced by a factor $n$. Data corresponding to two different sets of experimental conditions: 37°C with buffer used for fluorescence experiments (1x TAE, 12.5 mM magnesium acetate, 50 mM sodium chloride); 25°C, omitting the sodium chloride from the buffer. The data are consistent with a 3-fold reduction in stepping rate in the latter case.

### 3.2.5 Intermolecular Transfer

As discussed in Section 3.2.3, intermolecular transfer of motor between tracks on different origami tiles in solution is slow. However, as such transfer has the potential to severely limit operation of the motor, a further experiment was designed to determine this rate more accurately. This design consists of two tile types (Figure 3.11 A). Motor was loaded on Tile type 1, labelled at $S_8$ with Cy3.5, and mixed with an equal amount of Tile type 2, which is labelled at $S_8$ with a differently coloured fluorophore, Cy5. The final concentration of ∼12.5 nM for each tile type is approximately half that of a standard fluorescence experiment. Over very long time scales, inter-tile transfer of motor is detected by slow quenching of the $F_8$-Cy5 tiles and unquenching of the $F_8$-Cy3.5 tiles. If the same stepping rate of $k_s = 0.009s^{-1}$ as above is used, the data in Figure 3.11 D is consistent with a transfer rate, $k_t$, of order 5000× smaller than the stepping rate. Thus, on the time scale of motor movement transfer of motor between tracks is negligible.

### 3.2.6 Motor strand diffusion

Further control experiments were designed to measure the rate of undriven stepping between stators. To quantify this diffusion, short two-stator ($S_2$ and $S_3$) tracks were constructed and labelled with either $F_2$ or $F_3$, as in Figure 3.12 A. They were then combined and observed in the same measurement. Motor was loaded preferentially on $S_2$ by insertion of the $S_2$-motor duplex while blocking stator $S_3$. Diffusion of the motor is observed when the corresponding release strand is added (Figure 3.12 B). This reversible diffusion reaction is modelled by a simple set of differential equations with an analytical solution. A fit to both sets of data shown in Figure 3.12, yields an estimate for the rate constant for undriven stepping $k_d$ that is 13× slower than the driven stepping rate $k_s$.

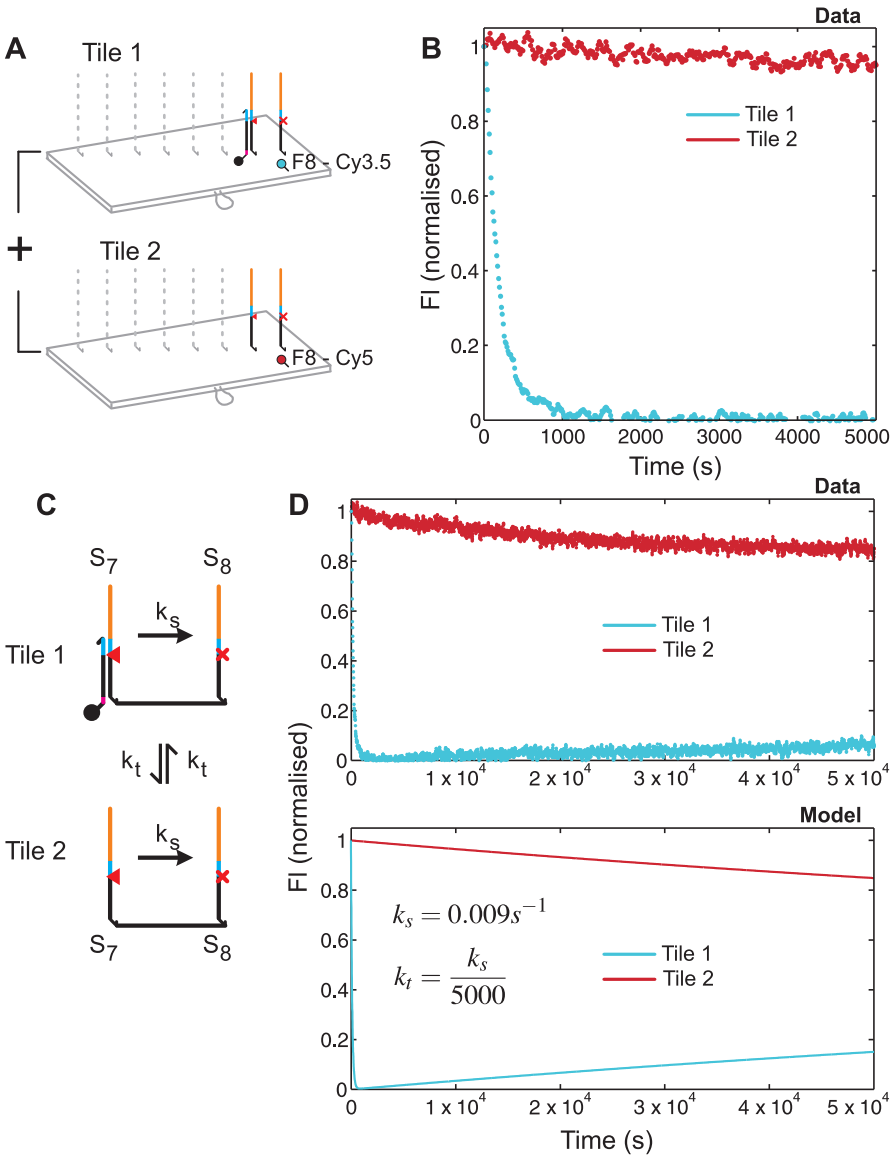


Figure 3.11: Rate of motor transfer between tiles. **A** Two-stator tracks ($S_7$, $S_8$) were used to quantify intermolecular transfer. **B** Initial rates of change of fluorescence from the $S_8$ labels indicate that stepping between stators on the same track is much quicker than transfer between tiles. **C** As a first approximation the system is modelled by two rates, for intra-tile stepping and inter-tile transfer ($kt \ll ks$). **D** The data is consistent with a transfer rate of order 5000× smaller than the driven stepping rate.

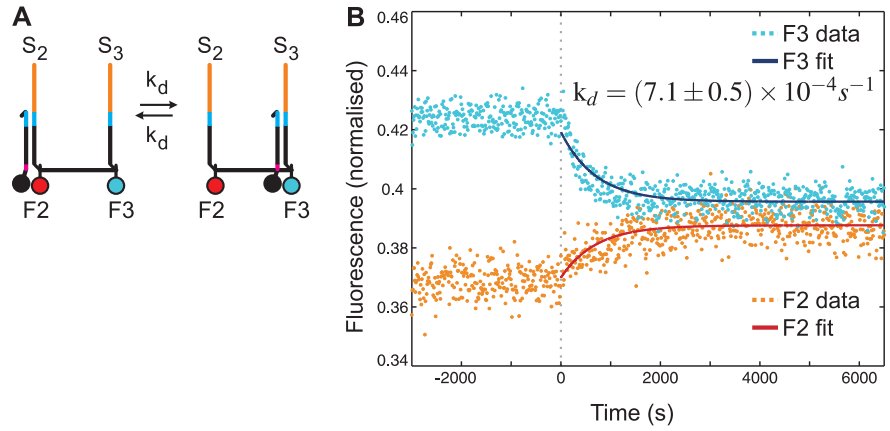


Figure 3.12: Diffusion of the motor without enzyme. **A** Simplified tracks with only two identical stators, $S_2$ and $S_3$, were used to quantify the rate of motor diffusion between stators. **B** Diffusion of the motor was observed after the corresponding release strand was added (t = 0). A fit to both sets of data, $F_2$ and $F_3$ fluorescence, yields an estimate for the rate constant for undriven stepping $k_d$ that is 13× slower than the driven stepping rate $k_s$.

$$\frac{\mathrm{d}c_2(t)}{\mathrm{d}t} = -k_d c_2(t) + k_d c_3(t)$$
$$\frac{\mathrm{d}c_3(t)}{\mathrm{d}t} = -k_d c_3(t) + k_d c_2(t)$$
$$c_2(t) = \frac{1}{2}(c_2(0) + c_3(0)) + \frac{1}{2}(c_2(0) - c_3(0))e^{-2k_d t}$$
$$c_3(t) = \frac{1}{2}(c_2(0) + c_3(0)) + \frac{1}{2}(c_3(0) - c_2(0))e^{-2k_d t}$$

## 3.3 AFM measurements

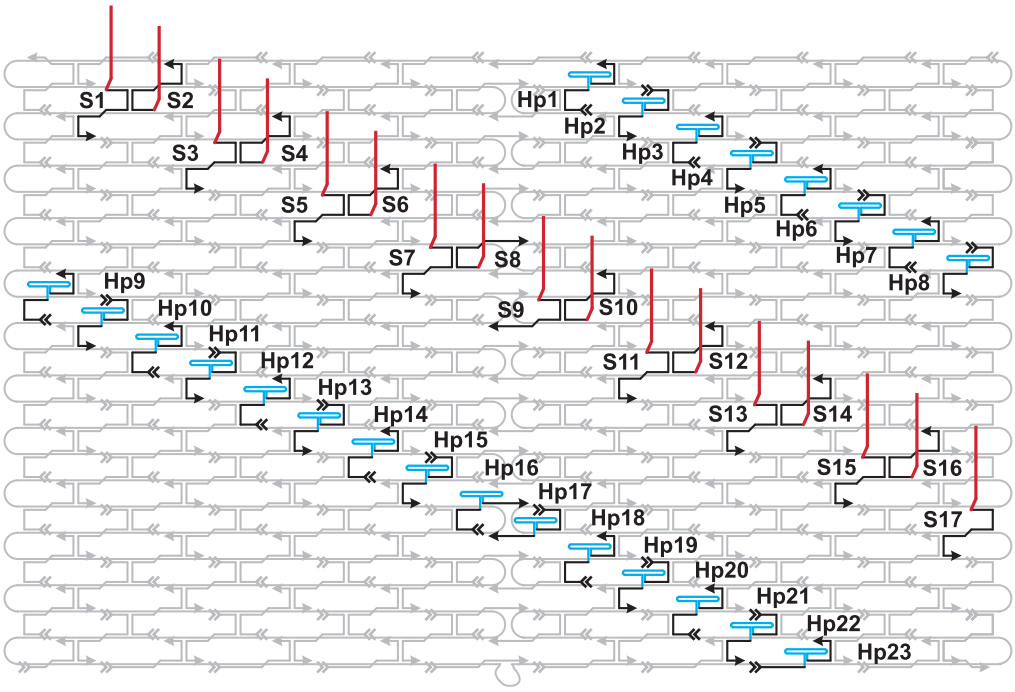


Figure 3.13: 'Burnt-bridges' DNA track design for AFM measurements. The original tile design is modified with 17 stators (red) and two rows of hairpin loops (blue) on opposite surfaces. The hairpin-modified staples form two parallel lines which act as reference markers for image registration in some measurements, and were omitted in others.

Atomic Force Microscopy (AFM) was used to probe the behaviour of single molecules of the motor-track system. A high-speed AFM imaging system (Ando et al., 2001; Endo, Katsuda, Hidaka and Sugiyama, 2010*a*) was used to observe transport of individual motor molecules along full, 17-stator tracks on an origami tile of the original design (Rothemund, 2006) (Figure 3.13). Such data can give information on heterogeneity within the sample, and also allows for a much more detailed analysis of the tiles. Experimental protocols are given in Appendix A.3, contributions to the data are outlined at the start of the Chapter.

### 3.3.1 Static Analysis

Initial characterisation of the DNA motor system makes use of static AFM images. Tracks were prepared with the motor at $S_1$ as for fluorescence experiments, but without the use of blocking strands. Samples were incubated with nicking enzyme for 0, 1 or 3 hours at 23°C, deposited on mica and observed. The distribution of measured motor positions at each time point was determined, and is shown in Figure 3.14. The high-resolution images allowed for clear differentiation between each of the 17 stator locations, and motor positions were identified by eye. Tile images with an unclear motor location or with no visible motor were discarded.

Of tiles with a detectable motor-stator duplex, 43% are located on $S_1$ at the initial time point with the rest approximately uniformly distributed along the track. The distribution shifts progressively down the track: by 3 hours, 35% of detectable motor has reached the end of the track. Histograms of the distribution of motor over stators were averaged over 3 independent trials with $N_1 = (28, 53, 41, 53)$, $N_2 = (40, 44, 46, 41)$, $N_3 = (41, 42, 39, 41)$ tiles counted for the 4 time steps in each trial respectively.

The simple kinetic model discussed in Section 3.2.4 can be extended to a 17-stator track, and used to predict the distribution of the motor at different time points, as shown in the inset of Figure 3.14. The rate constants used are one quarter those deduced from fluorescence measurements on a short test track. The motor is slowed by the lower temperature and different buffer conditions required for AFM measurements, as observed in fluorescence measurements shown in Figure 3.10.

Broken tracks were prepared by assembling tiles without stator $S_7$, which was replaced by an unmodified staple, leaving a 12 nm gap between $S_6$ and $S_8$. Motor was loaded at $S_1$ and the tiles were incubated with nicking enzyme at 23°C for 3 hours. The position of the motor on the track before and after addition of enzyme

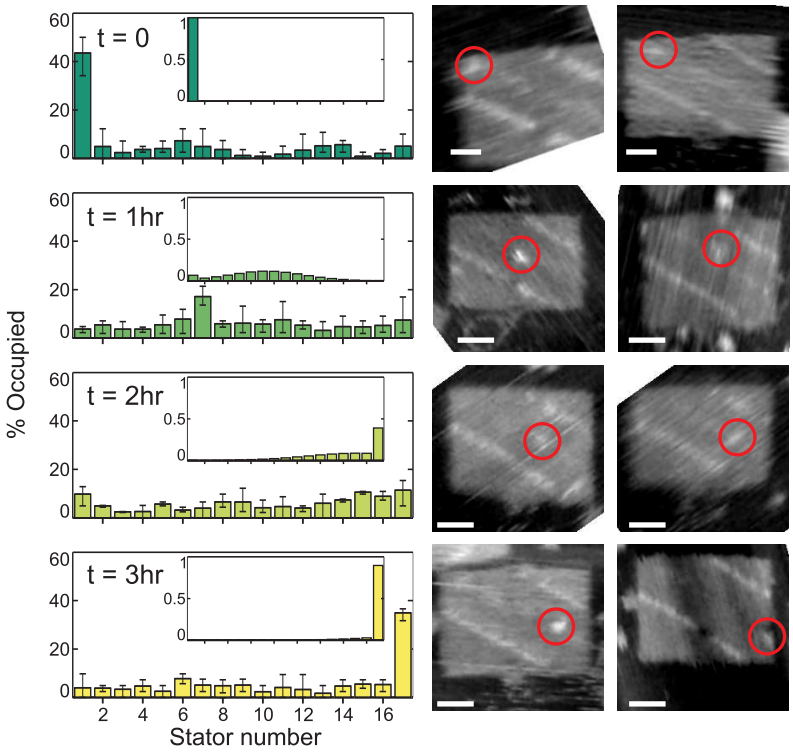


Figure 3.14: Observation of motor movement by AFM. 17-stator tracks with motor loaded at position $S_1$ were incubated with nicking enzyme at 23°C. The distribution of motor positions before addition of enzyme and after 1, 2 and 3 hours were determined by AFM. Representative images and histograms of motor positions are shown for each time point. Inset are motor distributions predicted by the simple kinetic model in Section 3.2.4, with the stepping rate reduced by a factor of 4. Scale bars 20 nm.

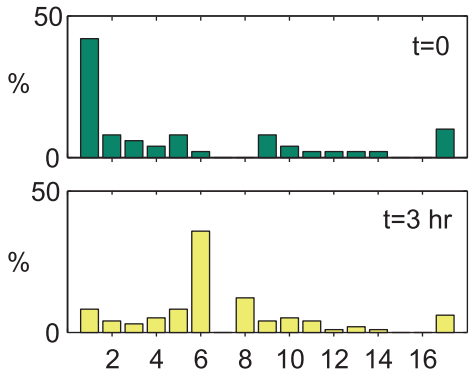


Figure 3.15: AFM measurement of tracks broken at $S_7$. The observed distribution of motor position shows that the motor moves from $S_1$ (41% at t=0) to $S_6$ (36% at t= 3 hr) but is largely unable to cross the gap left by the missing $S_7$ on this time scale.

was determined (N=51 at t=0, and N=98 at t=3 hr). Motor accumulates at $S_6$ (Figure 3.15), confirming the inference from fluorescence measurements that the motor visits each stator in turn and is delayed when it encounters a break in the track.

During the course of these static observations, it was found that the hairpin markers used for registration biased the tiles to stick face down on the mica surface. 76% of 127 tiles with hairpin markers were oriented such that stators faced towards the mica surface. It was thought that this may decrease the possibility of observing mobile motors on tracks, so these hairpin markers were omitted for the majority of results in the following section.

### 3.3.2 Movies and Kymographs

In addition to static images, the 0.1 $s^{-1}$ frame rate of the AFM was sufficient to capture the stepping of individual motor strands in real time. Tiles loaded with motor, without control of its initial position, were incubated briefly with enzyme then washed to remove excess enzyme and observed in buffer. Several movies

of motor stepping were captured. These image frames were used to construct kymographs representing the evolution of the measured height distribution along a track, as shown in Figures 3.16, 3.17 and 3.18.

Prior to construction of kymographs, image frames were registered to correct for sample and stage drift between frames, as described in Appendix A.3. Figure 3.19 shows a kymograph for the stationary hairpins on the origami tiles. These appear as vertical lines, confirming that the image registration process used to align the frames of the image sequences operates correctly.

Figure 3.16 presents the kymograph for the longest movie obtained. In this movie stepping occurs between four well-resolved, equally spaced positions on the track, interpreted as consecutive stators. The location of these stators is estimated by considering the histogram of motor positions in Figure 3.16, and taking the average values. The step size was measured to be $7.4 \pm 1.0$ nm, consistent with the spacing between stators.

In most regions of the kymograph the motor moves back and forth between adjacent stators with a mean transition time that is similar to or shorter than the AFM frame time. It is proposed that this corresponds to incomplete migration of the motor between a cut stator and an adjacent intact stator. Two transitions (marked * in Figure 3.16) can be identified at which the motor progresses irreversibly by one stator. These transitions are interpreted as complete transfer of the motor to the intact stator. It then dwells at this stator for some time, 100 s and 50 s in the two occurrences observed in this movie, before starting to step to the downstream stator. It is inferred that cleavage of the stator occurs during the dwell time, catalyzed by an enzyme that remains bound to the track.

Similar transitions between two or three adjacent stators were observed on tracks in other movies (Figures 3.17 and 3.18). The small number of steps in the shorter movies make it more difficult to estimate their step size. The steps were

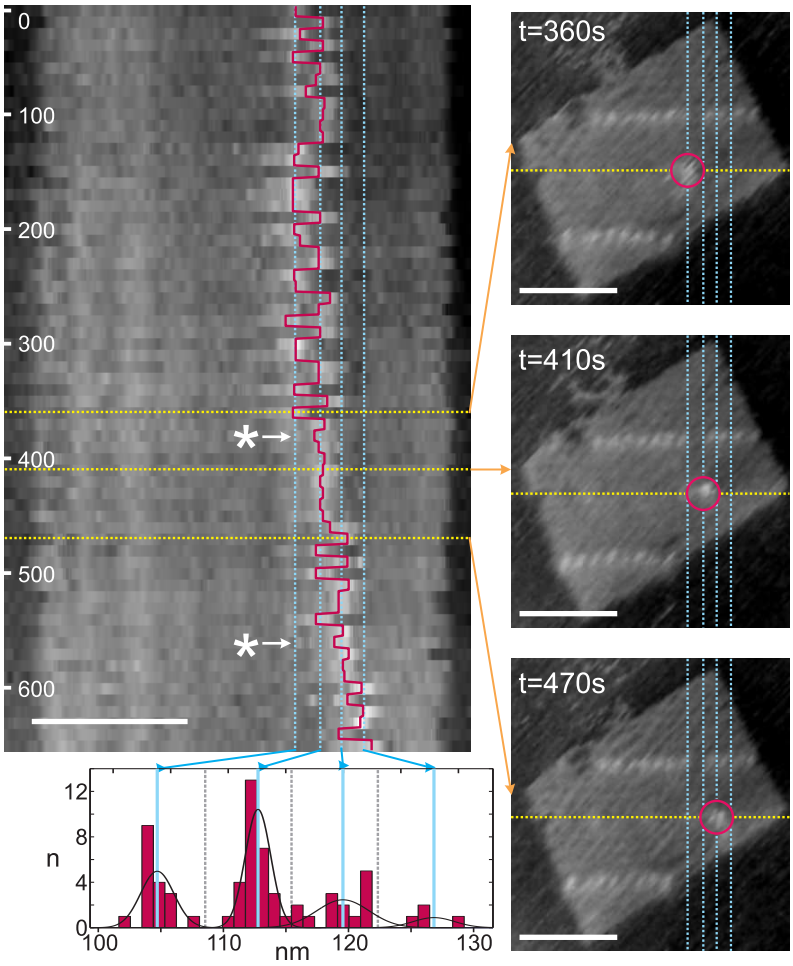


Figure 3.16: AFM observation of discrete steps of a single motor molecule. The main panel shows a kymograph, a stack of slices from successive frames, collected at 0.1 Hz, that correspond to the height profile along the track (3 of the 65 frames are shown on the right). The highest point on each profile, interpreted as the motor position, is marked in red. The motor steps between four stators (blue lines). Periods of rapid movement between adjacent stators are followed by slower transitions (*) in which the motor advances a single step. Scale bars 50 nm, time scale for the kymograph is in seconds.

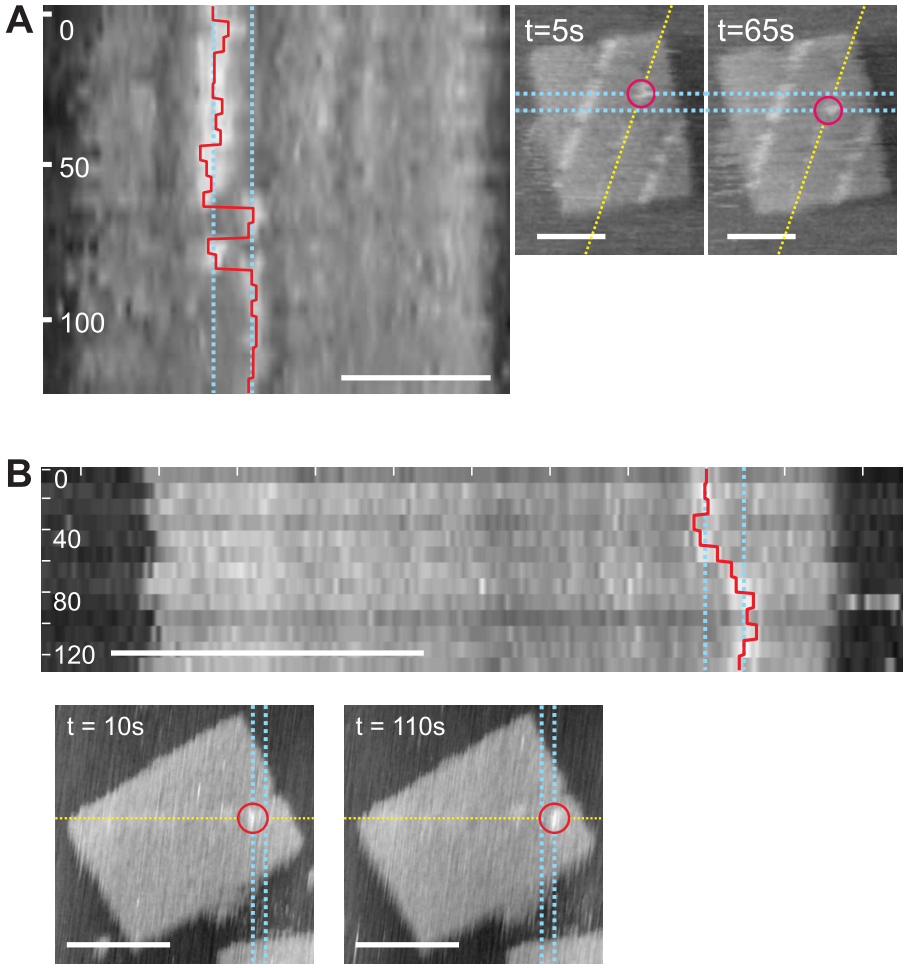


Figure 3.17: AFM Kymographs and image frames showing discrete steps of single motor molecules between adjacent stators in two additional movies. The second movie (B) is of a tile without hairpin markers. Scale bars are 50 nm, time scale for the kymograph is in seconds.

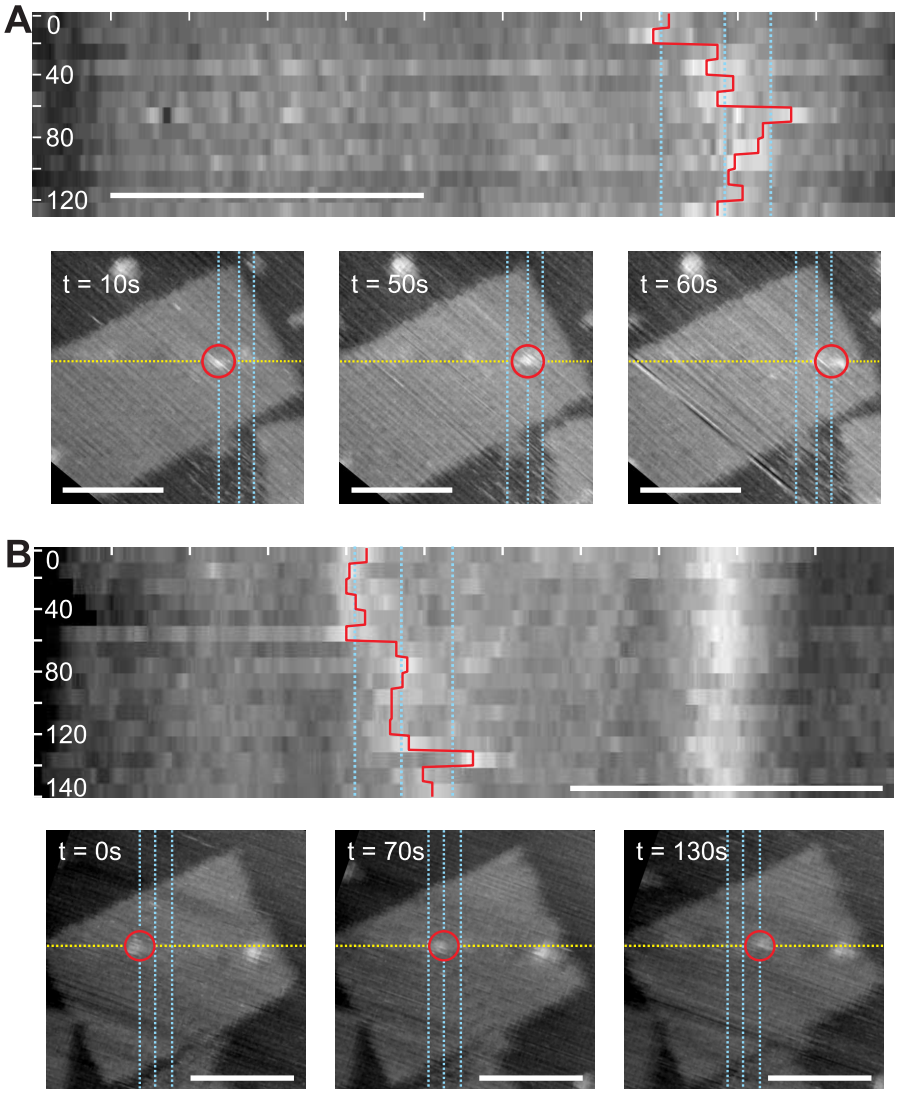


Figure 3.18: Kymographs and image frames showing discrete steps of single motor molecules from two additional AFM movies, in which stepping between three adjacent stators is observed. Both are of tiles without hairpin markers. Scale bars are 50 nm, time scales are in seconds.

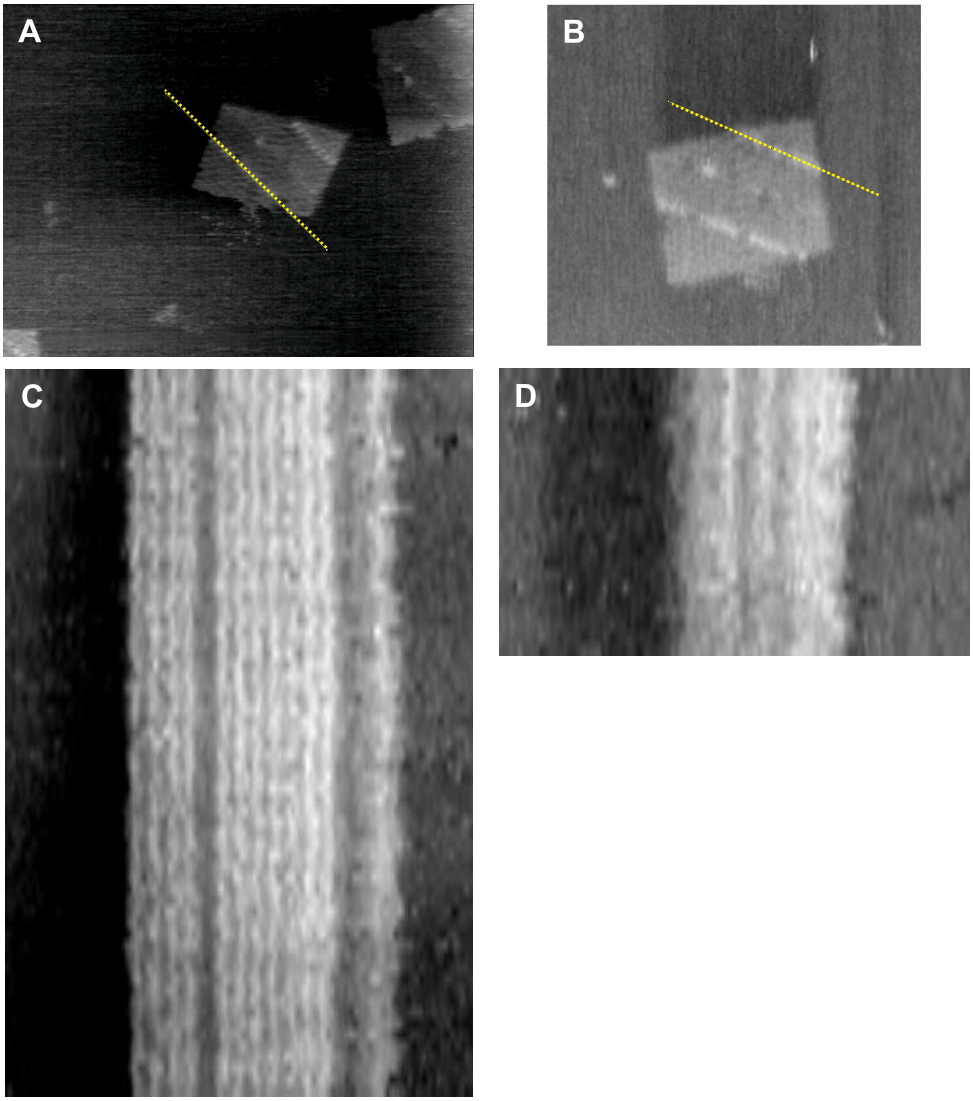


Figure 3.19: Kymograph controls. Kymographs, showing the evolution of rows of hairpin labels, constructed from AFM movies. Single frames (top) show selected loci (straight yellow lines), running along lines of hairpin-modified staples, for which the two kymographs (bottom) were constructed. The fixed hairpins appear as vertical lines in the kymograph.

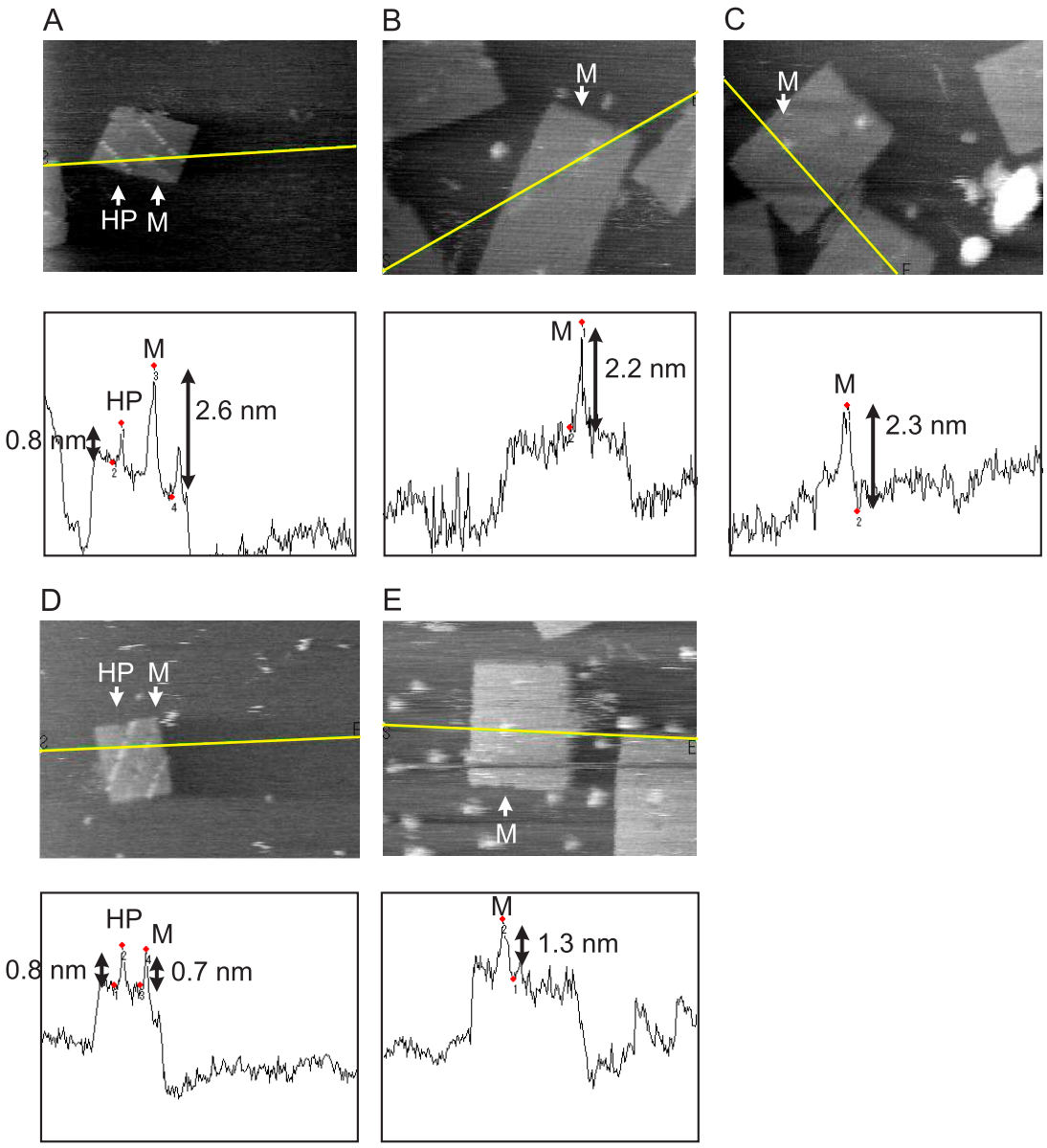


Figure 3.20: Height profiles from AFM movies. **A, B, C** Movies with at least one completed step, corresponding to kymographs in Figures 3.16, 3.17 and respectively. **D, E** Movies with no completed steps, corresponding to kymographs in Figure 3.18. Single frames (top) show a line (yellow), passing through the motor position, along which the height profile (bottom) is plotted. Measured heights of hairpins (HP) and motors (M) are indicated in nm.

estimated as 10 nm and 6 nm respectively for the single step movies in Figure 3.17A and B, and 9 nm and 8 nm for movies in Figure 3.18 A and B. This gives an average value of $8 \pm 1.5$ nm, which is consistent with the result from the longer movie (Figure 3.16) and the tile design (Figure 3.13).

After depositing the sample on the mica surface for AFM imaging, multiple wash steps are essential for achieving the high resolution required for identifying individual stator locations. Unfortunately, the majority of motors observed were static, consistent with dissociation of enzyme from the tracks during the wash steps. In all cases that movement was observed, the tiles were oriented such that the tracks faced towards the mica surface, possibly reducing enzyme dissociation. Height profiles of the motor in these images are consistent with the presence of enzyme (Figure 3.20). In movies showing completed steps, but not in the single-step movies, the height of the motor is significantly greater than that of a DNA hairpin. This observation is consistent with the interpretation that completed steps between stators are a result of the action of enzyme that remains bound to the motor, whereas reversible transitions between adjacent stators do not require the presence of enzyme.

## 3.4 Conclusions

In this chapter the controlled operation of a synthetic molecular transporter over a 100 nm track has been demonstrated. The motion is is found to be uniform, directional and processive. Experiments with broken tracks confirm that the motor does not dissociate - it is only displaced from a cut stator by transfer to an intact stator, and is always bound to the track by hybridization of at least 16 nucleotides. Successful modelling of both fluorescence and AFM results supports the conclusion that the average time per step is constant, independent of distance travelled. The

motor is programmably delayed by a gap in the track, and the step size could be used to tune the dwell time at each stator. For example, to match the required coupling time for reaction steps along a molecular assembly line.

Using high-speed, real-time AFM, discrete steps of a single motor were observed. The fast oscillation of the motor between adjacent stators in AFM movies could be the first direct observation of branch migration, and raises interesting questions about the motor mechanism. It was previously thought that release of the enzyme after cleavage was the rate limiting step (Bath et al., 2005). However, branch migration appears to take up a much longer proportion of each step cycle in the AFM movies. This suggests that a method for speeding up the branch migration to the next stator, for example by including mismatched bases, has the potential to dramatically increase the speed of the motor. Another unexpected feature of the data is that very few states were observed with a duplex midway between two stators. This suggests that branch migration favours two states: with only the 6-nt toe-hold of the motor bound to the next stator, or, with almost all the motor strand hybridised to the next stator. While this effect is not yet fully understood, it provides an important input into a theoretical model that is being developed for the burnt-bridges DNA motor. This model, based on the same approach as a previous theoretical study of the DNA tweezers (Ouldridge et al., 2010), may yield further insight into the process of stepping along the track and in turn lead to refinements of the motor design.

These results provide the most detailed analysis of a DNA motor on an extended track to date. Recently, a DNA spider was shown to move a similar distance, but in a longer time and with significantly less control over motor stepping (Lund et al., 2010). The precise control over both assembly and movement achieved here opens the way for the design of integrated systems that incorporate active transport, information processing and molecular assembly.

Chapter 4

# Piece-wise DNA origami track for a 'Two-foot' DNA motor

Chapter 3 describes a linear DNA origami track for an enzyme driven 'burnt-bridges' DNA motor. As discussed in Chapter 1, a number of more sophisticated DNA motor designs have been demonstrated on short test tracks. This Chapter describes the design and analysis of a DNA origami track for a second DNA motor design, a reversible 'two-foot' motor that walks along a ssDNA track (Green et al., 2008; Bath et al., 2009). This more general motor design mimics the hand-over-hand movement of linear protein motors, such as kinesin and myosin, found in the cell. It can be powered by either hydrolysis of DNA catalysed by an enzyme (Bath et al., 2009), or by hybridisation of DNA fuel loops in an all DNA motor-fuel-track system (Green et al., 2008). Unlike the burnt-bridges motor, and more like cellular motor systems, the track is re-usable. Depending on the fuel instructions added, the motor can also be directed either forward or backwards along the track.

An essential feature of the two-foot motor mechanism is competition between the two feet to hybridise to the same 'competition' domain on the track. If the

feet do not bind to adjacent sites, there will be no competition and no exposure of the toehold on either foot. Neither forward nor backward fuel strands will be able to interact with the motor. The ssDNA track presents a problem because single-stranded DNA is very flexible, with a persistence length of only around 2 nucleotides (Smith et al., 1992). This will allow the ssDNA track to bend around and the two feet to bind to non-adjacent sites, particularly after one foot has been lifted and placed back down. Previous studies of the motor on a ssDNA track were able to demonstrate only one motor cycle, that is, one foot pick-up and put-down process. This chapter presents a method for stretching the ssDNA track for the two-foot motor across a DNA origami tile. By anchoring it to the more rigid DNA origami substrate, the flexibility of the track will be reduced, and it may be possible to show multiple motor-cycles.

### AFM Data Contributions

Selected AFM data in this Chapter was collected on a high-speed AFM in collaboration with the Sugiyama Laboratory, Kyoto University, Japan. All experiments and protocols were designed by the author, and all samples were prepared by the author. Experimental protocols are as described in detail in Appendix A.3. AFM images were either obtained by the author at Oxford University, UK (Figures 4.3 and 4.5), or by microscope technician K. Hidaka at Kyoto University, Japan (Figures 4.4 and 4.11). All image analysis was completed by the author at Oxford University, UK.

## 4.1 Two-foot Motor Mechanism

The mechanism for the 'two-foot' DNA motor was briefly introduced in Chapter 1 (Section 1.3.2), and is shown in more detail in Figure 4.1. The motor may be driven either by a nicking enzyme (Figure 4.1 A), or a DNA hairpin fuel (Figure 4.1 B); both designs operate on the same principle. The track and feet both consist of two repeating domains, called 'competition' and 'binding' sites. If the two feet of the motor occupy adjacent binding sites on the track, they will both compete to bind to the intervening competition site (Figure 4.1 Ai, Bi). Neither foot will dominate, and both toe-holds will be exposed from time to time. The toe-hold sequences are the same. However, the 3' end of the front foot (right) and the 5' end of the back foot (left) are revealed by competition. This difference allows fuel strands to differentiate between the two identical feet. A 'forward' fuel consists of a single binding site followed by a single competition site. This fuel will preferentially pick up the foot with the 5' toehold exposed, which corresponds to lifting back foot (Figure 4.1 Aii, Biii). A 'reverse' fuel has the order of sites reversed, a single competition site followed by a single binding site. This fuel will pick-up the foot with the 3' toehold exposed, the front foot.

Once a foot has been picked up by the fuel strand, the fuel can be removed from the foot, to reset the motor, in two ways. For an enzyme-driven motor (Figure 4.1 A), mismatched bases in the foot-track duplex are repaired in the foot-fuel duplex. This repair corrects a defect in a recognition site for a nicking restriction enzyme, Nt.BbvCI, the same enzyme used with the burnt-bridges motor in Chapter 3. The fuel can then be cut by the enzyme, and the short fuel fragments dissociate from the foot (Figure 4.1 iii-iv). For the DNA-driven motor (Figure 4.1 B), the fuel interaction with the foot opens up a hairpin in the fuel strand. This opening catalyses the interaction of the fuel hairpin (H1) with a second hairpin (H2) in solution, which then strips the first hairpin off the motor foot (Figure 4.1 Biv-vi)

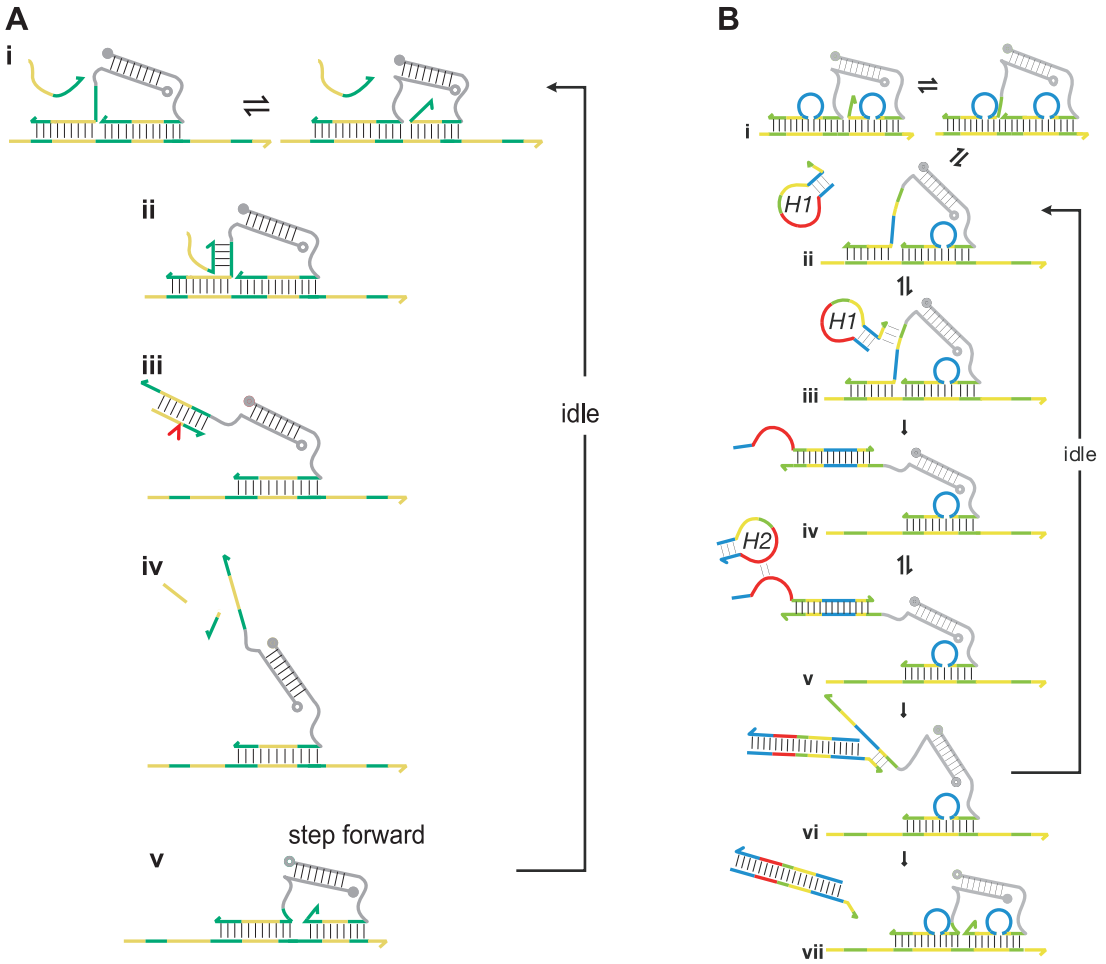


Figure 4.1: Mechanism of the two-foot DNA motor: **A** an enzyme-driven version (Bath et al., 2009), and **B** a DNA-driven version (Green et al., 2008). The two feet compete to hybridise to the middle 'competition' domain of the track (green)(**Ai**, **Bi**). If the right-hand (downstream) foot occupies the entire green section, a fuel strand in solution may lift up the back foot (**Aii**, **Bii**). In the enzyme-driven motor, a recognition site for a restriction enzyme is formed (**Aiii**). The enzyme cuts the fuel, and the short segments dissociate (**Aiv**). In the DNA-driven motor, a hairpin in the fuel strand (H1) is opened (**Biv**). The open loop interacts with a second hairpin (H2) in solution (**Bv**), removing the fuel from the foot (**Bvi**). Once free, the foot may be put down in the same place or one step forward (**Av**, **Bvii**). Directionality is gained from the fact that it is more likely to pick up the back foot: 30× more for the enzyme-driven motor, 100× for the DNA-driven motor. A reverse fuel, with the order of the competition and binding domains reversed, drives the motor in the opposite direction.

producing the waste duplex H1-H2. In both motor types, the foot is put down with no bias between returning to the binding site it just left (idle step) and stepping over the bound foot to the next adjacent binding site (forward step) (Figure 4.1 Av, Bvii). Directional movement is achieved by the fuel bias to preferentially pick up one foot. For the enzyme-driven motor the rate of picking up the correct foot is 30× faster (Bath et al., 2009), and for the DNA-driven motor it is 100× faster (Green et al., 2008).

## 4.2 Track design

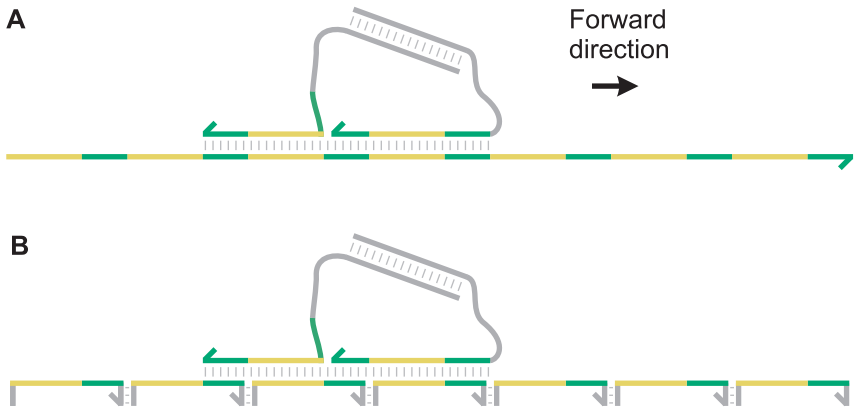


Figure 4.2: Tracks for the 'two-foot' DNA motor. **A** The motor was originally designed for a ssDNA track of alternating binding (yellow) and competition (green) domains. The forward motor direction is defined to be left to right. The front foot is on the right, and the back foot on the left. **B** A design for a piece-wise two foot motor track. The track is broken into segments of a sigle binding and competition domain. By anchoring segments periodically across a DNA origami tile the flexibility of the track should be reduced. Adjacent track segments contain complementary 3 nt 'neck' sequences to weakly hybridise them together, and ensure track continuity.

A schematic of the original design for the enzyme-driven two-foot motor and ssDNA track is shown in Figure 4.2 A (Bath et al., 2009). This Chapter presents

a 'piece-wise' design for the two-foot motor track. While the track was designed and tested for the enzyme-driven motor design (Figure 4.1 A), with small changes it would also be applicable to the DNA-driven version (Figure 4.1 B). The track is broken between the 3' end of a competition site (6 nt), and the 5' end of the next binding site (10 nt), and modified so that it can be periodically anchored to a DNA origami tile (Figure 4.2 B). The 16 nt track segments are attached at both ends to origami staple strands, and a short 3 nt linker is added to weakly hybridise adjacent track segments. The origami staples are modified at the centre of the staple sequence, such that track segments face upwards (out of the page) (Figure 4.3). For a DNA-driven version, the track segments would be 18 nt, consisting of a 6 nt competition domain and a 12 nt binding domain.

A number of track staple strands were designed and tested for different length two-foot motor tracks. The first design is for a three piece track, where the segments link round into a triangle (Figure 4.3). Both ends of each track segment are anchored by 16-nt of DNA origami staple, which is half a full length staple (32 nt) in the original origami design. Such a track would convert the linear motor into a rotational DNA motor. The second design is for a short linear track of 4 segments (Figure 4.4). Several variations of the staple length at either end of the track segment are tested for this design: 16-nt of staple at both ends (short), 32-nt at the 5' end and 16-nt at the 3' end (asymmetric), or 32-nt of staple at both ends (long). Finally, a full length origami track of 17 track segments was designed, with 16-nt of origami staple sequence at both ends of each track segment (Figure 4.5).

Each of the track designs was assembled and imaged by AFM. In all cases an appropriately sized track was observed at the correct position on the origami tile. For the longer track, resolution of the AFM images is good enough to assess continuity of the track. Initially tiles were annealed with a 5× excess of the modified track staples. Many of the resulting tracks have defects, or gaps, (Figure

4.5B), which would disrupt motor transport. Track tiles annealed with a 25× excess of the modified track staples were found to have far fewer defects (Figure 4.5 C). For the different staple variants of the 4-segment track, no difference is track quality was observed. However, individual track segments were not resolved, and so continuity could not be determined.

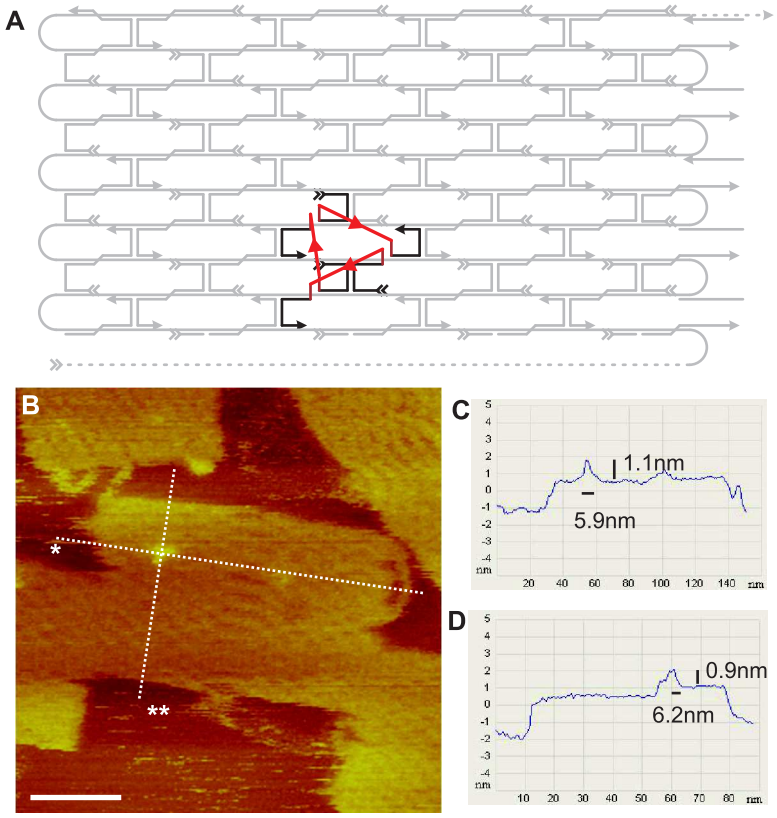


Figure 4.3: A 3-segment triangular track for the enzyme-driven two-foot DNA motor. **A** Three track segments (red) are arranged to form a continuous triangular track. Both ends of each segment are anchored by 16 nt of origami staple (black). The track is positioned in the top-left of the origami tile. **B** An AFM image of the tile, with height profiles measured along lines marked * (C) and ** (D). The track is in the correct position on the tile, and has similar dimensions to the design. Scale bar 50 nm.

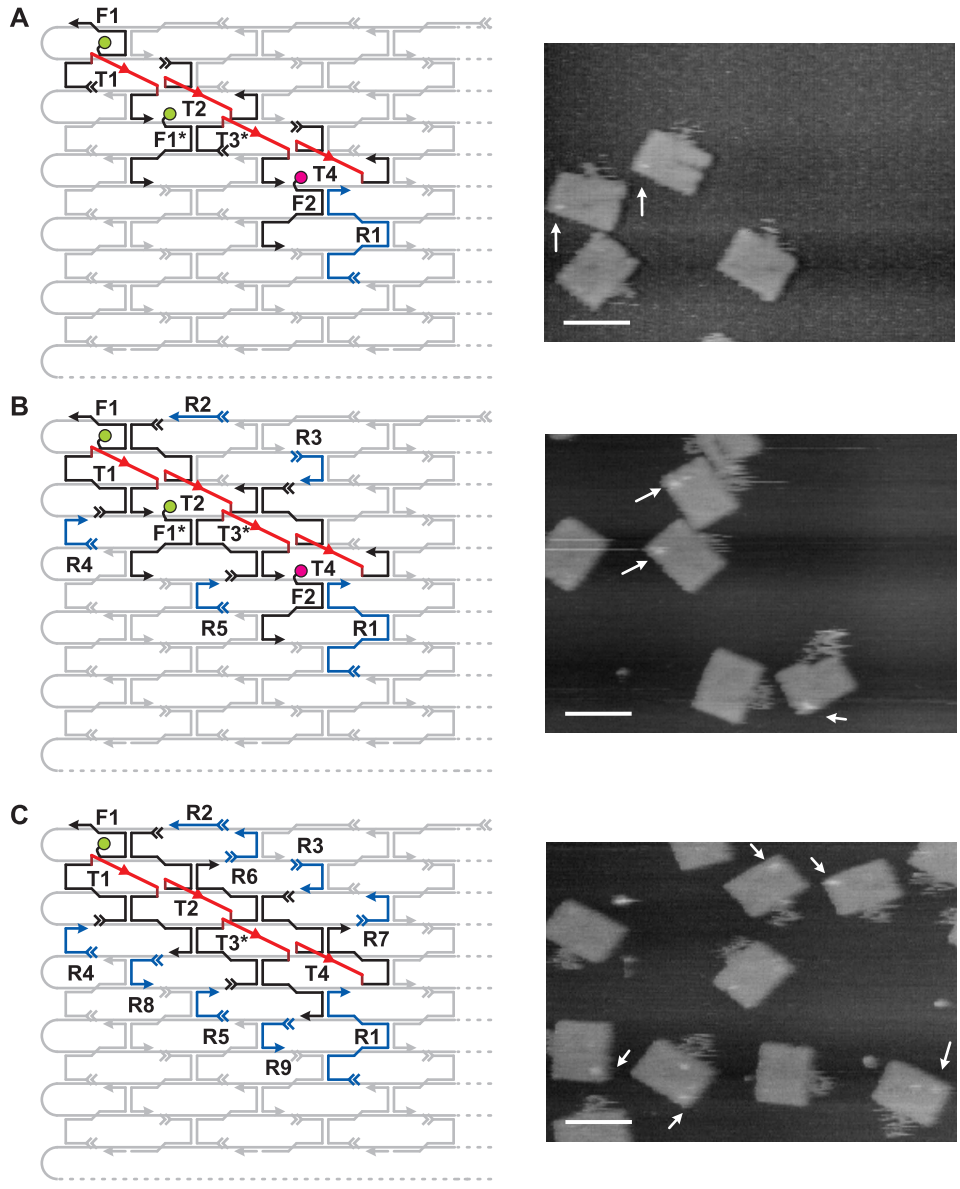


Figure 4.4: A 4-segment linear track for the enzyme-driven two-foot DNA motor. Track segments (red) are anchored to the tile by **A** 16 nt of staple at both ends, **B** 32 nt at the 5' end and 16 nt at the 3' end, or **C** 32 nt at both ends (all marked in black). Some adjacent staples are disrupted, and additional short staples (blue) are added to fill in gaps. The tracks are also labelled with fluorophores. AFM images of each design (right) show that tracks (arrows) are correctly assembled in all designs. Scale bars 100 nm.

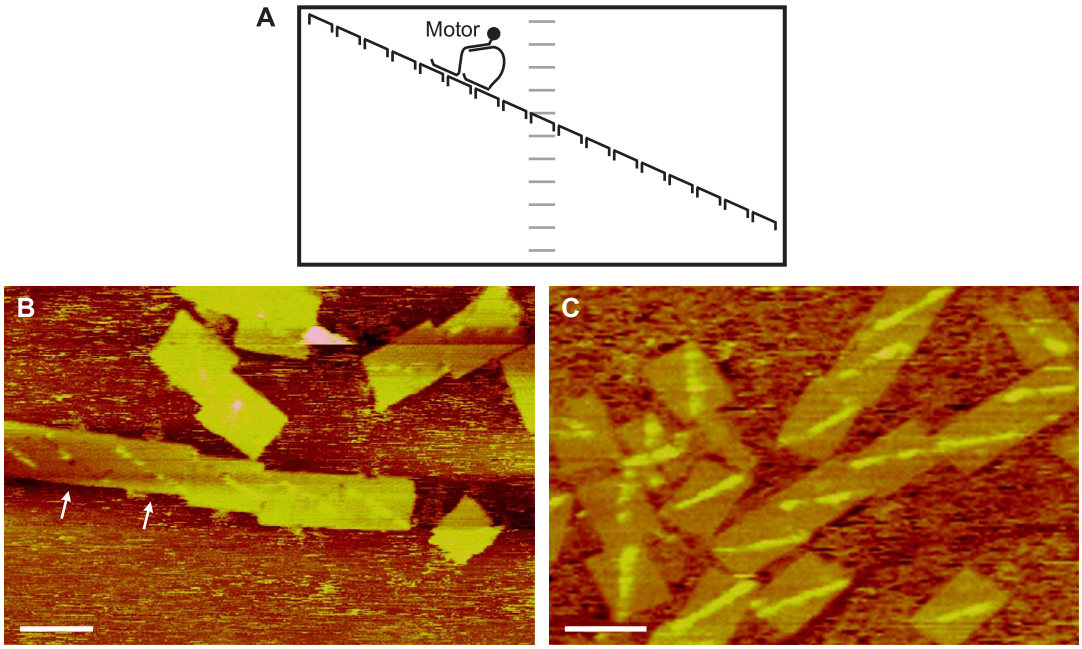


Figure 4.5: A full-length linear track for the enzyme-driven two-foot DNA motor. **A** 17 track segments are arranged to form a continuous linear track across a full DNA origami tile. Both ends of each segment are anchored by 16 nt of origami staple, as in Figure 4.3. The track runs diagonally across the origami tile from top left to bottom right. **B, C** AFM images of the tile, annealed with either 5× excess of track staples (B), or 25× excess. A reduced excess of track staples during assembly results in tracks with more defects (arrows). Scale bars 100 nm.

## 4.3 Ensemble Fluorescence Measurements

Piece-wise DNA origami tracks for the two-foot DNA motor were successfully assembled and characterised by AFM. As in Chapter 3, ensemble fluorescence quenching measurements were then used to characterise behaviour of the motor on the track. As previously, a method for synchronising motors by loading them preferentially at one site on the track is required for ensemble observations. In this case, a simplified version of the enzyme-driven motor is used in which one foot is only able to bind to a single unique site along the track. Details of experimental protocols are given in Appendix A.9.

### 4.3.1 Fixed Foot Motor

To synchronise motors in solution, a simplified version in which the two feet have two different binding sequences is used (Figure 4.6). This method was previously used for short ssDNA test tracks (Bath et al., 2009; Green et al., 2008). The fixed foot (F) can only bind to one track segment in the middle of a 4-segment linear track. The other, 'wild-type' (WT) foot can bind either to the left (upstream) or right (downstream) of the fixed foot. Both feet have the same competition domain, and the toeholds of the wild-type and fixed feet are exposed by competition as in the standard motor. The fixed foot cannot fully interact and be picked up by either fuel strand (Figure 4.6 Aii Bii). The wild-type foot can be lifted by the forward or reverse fuel accordingly depending on its location (Figure 4.6 Aiii Biii).

The two motor feet were hybridised together by the 16 nt linker, and the duplex PAGE purified away from free foot strand following the protocol in Appendix A.4. When the purified motor is added to the track it has an equal chance of binding in the two configurations shown in Figure 4.6 Ai and Bi. That is, with the wild-type foot either in front of or behind the fixed foot. For each configuration it is expected

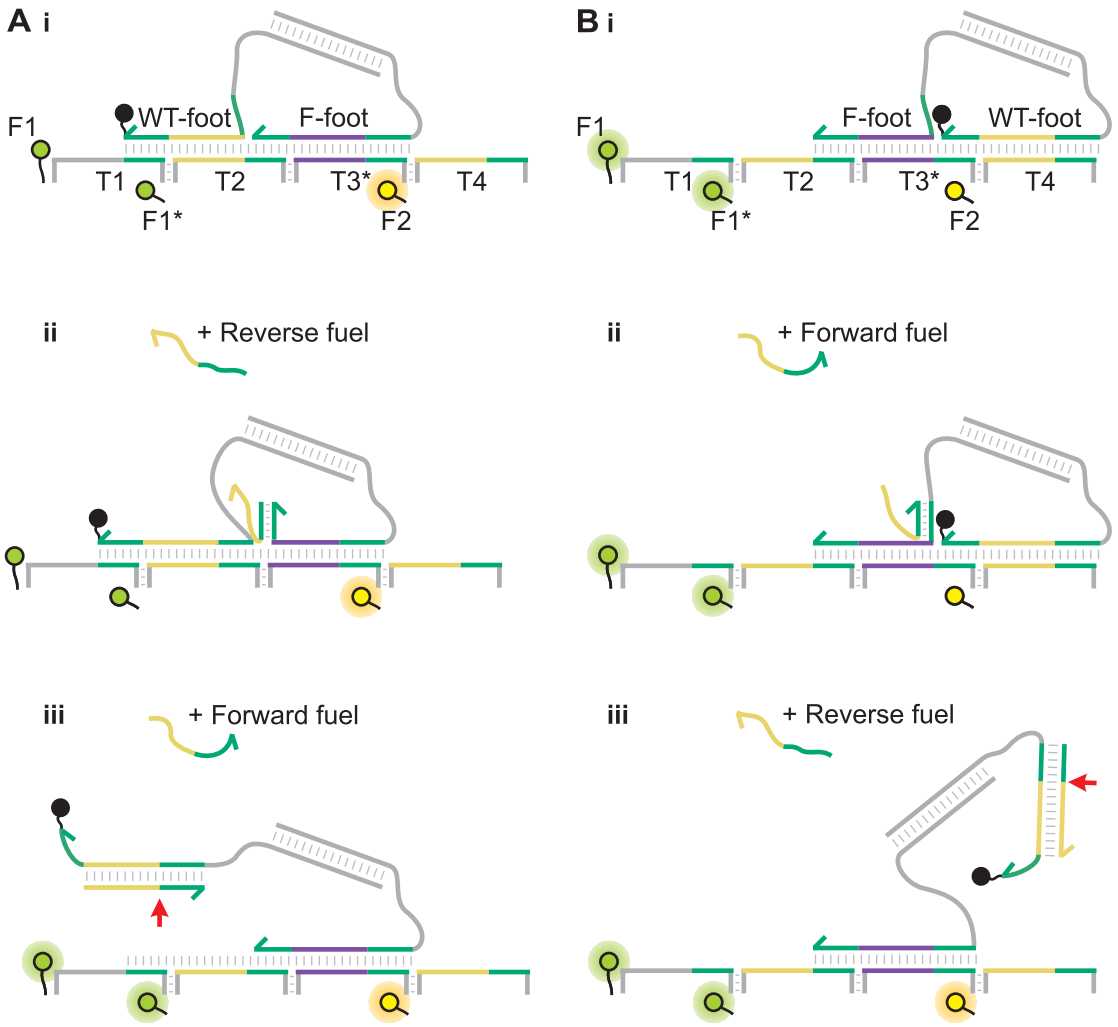


Figure 4.6: Schematic for a simplified two-foot motor with a fixed (F) and wild-type (WT) foot. When added to the track the motor binds in an equal mixture of configurations **A** and **B**. **i** Initially the WT foot quenches $F_1$ and $F_1$* (A) or $F_2$ (B). **ii, iii** In each configuration one fuel strand is inactive, while the other acts to pick up the WT foot and unquench the fluorophore. Once lifted, the WT-fuel duplex is cleaved by the enzyme (red arrow), and the cut fuel dissociates. The WT foot has an equal chance of returning to either initial state (A or B).

that only one fuel strand will interact with the WT foot to lift it up, and neither fuel will lift up the F foot. When the enzyme is added the fuel strand bound to the WT foot will be cleaved and dissociate, and the foot then has an equal chance of being put down in configuration Ai or Bi. Fluorophores are placed close to the track, with $F_1$ or $F_1$* labeling the upstream end of the track, and $F_2$ labeling the downstream end of the track. The 3' end of the WT foot caries a quenching molecule. If the motor is initially in configuration Ai (Figure4.6), the upstream fluorophore ($F_1$ or $F_1$*) will be quenched. If the motor is in configuration Bi, the downstream fluorophore ($F_2$) will be quenched.

Figure 4.7 A presents ensemble fluorescence results for the fixed-wildtype motor design tested on the 4-segment track with short staple sequences (Figure 4.4 A). Tracks labelled with $F_1$ and $F_2$ were assembled with a 5× excess of track staples. When a sub-stoichiometric amount ($\sim$ 0.75×) of purified motor is added, both fluorophores quench equally, indicating the motor binds equally in the two configurations in Figure 4.6. The effect of adding either fuel strand to the motor-track system is then compared. If the motor is in configuration B, the reverse fuel is expected to pick up the WT foot and unquench $F_2$ and the forward fuel is expected to have no effect (Figure 4.4 B ii, iii). The $F_2$ signal in Figure 4.7 is unquenched only on the addition of reverse fuel, as expected. The equivalent result is predicted for configuration A: the forward fuel should unquench $F_1$ and the reverse fuel should have no effect. However, this was not observed in the $F_1$ results. No unquenching was observed for either fuel, and instead quenching slowly increases with time. On addition of enzyme both $F_1$ and $F_2$ signals are expected to decrease again, as the WT foot is put back down in either configuration. The $F_2$ signal acts as expected, while the $F_1$ signal shows no change on the addition of enzyme.

The same experiment was tested on the 4-segment asymmetric staple track

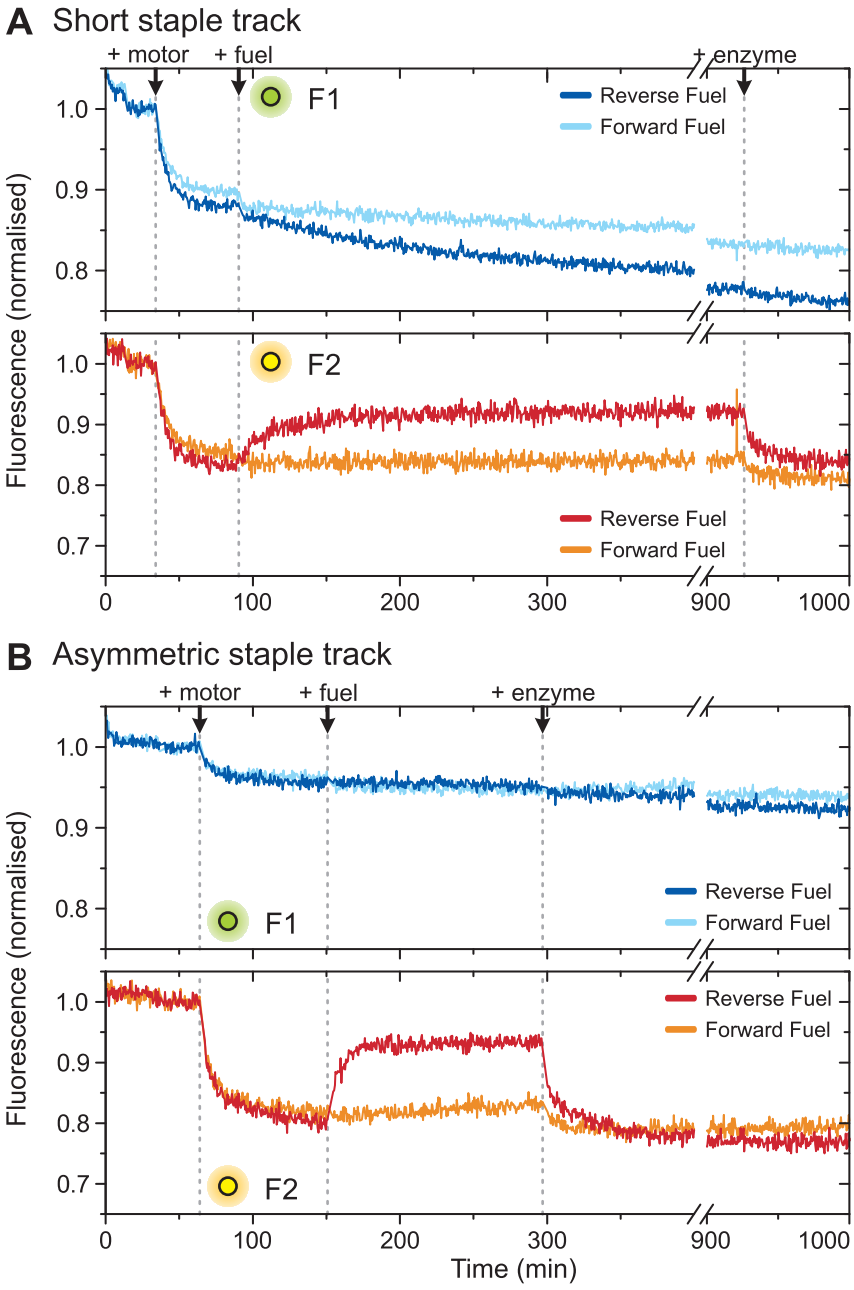


Figure 4.7: Ensemble fluorescence results for 4-segment motor tracks tested with a fixed foot motor. **A** Short and **B** Asymmetric staple track segments. The downstream fluorophore $F_2$ behaves as expected, the upstream label $F_1$ shows no pick-up with either fuel.

design, in which each 16 nt track segment is anchored at the 5' end by 32-nt of staple and 16-nt at the 3' end. The fluorescence results in Figure 4.7 B show the same behaviour as those in Figure 4.7 A. Both signals quench on addition of motor. $F_2$ unquenches on addition of only the reverse fuel, and re-quenches when the enzyme is added. $F_1$ remains flat on the addition of either fuel and enzyme. Neither design shows any ability to lift up a WT foot in configuration A.

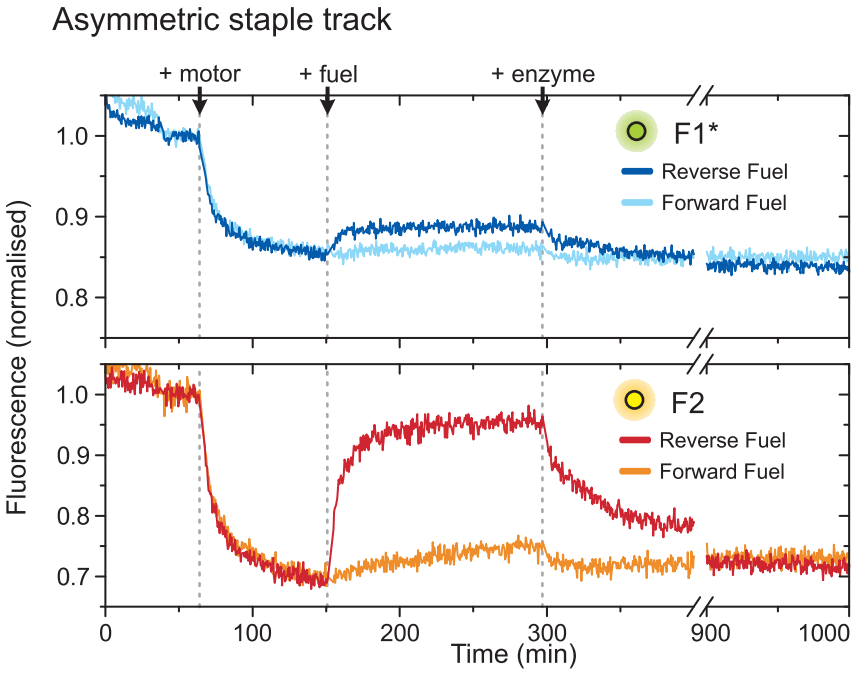


Figure 4.8: Ensemble fluorescence results for 4-segment motor tracks tested with a fixed foot motor. Asymmetric staple track segments are tested with the upstream fluorophore $F_1$* placed closer to the expected position of the quencher. The downstream fluorophore $F_2$ behaves as expected, the upstream label $F_1$ shows only slight leakage with the wrong fuel.

Due to the asymmetric placement of the fixed-foot binding track domain (Figure 4.6), fluorophores $F_1$ and $F_2$ will be different distances from the quencher in the two track configurations. It is possible that $F_1$ is simply too far away from the quencher for the effect of adding a fuel strand to be detected. To test this,

the alternative fluorophore $F_1$* is used, which is in an equivalent location to the quencher as $F_2$. The improved fluorophore design was tested with the 4-segment asymmetric track similarly to above (Figure 4.8). An additional difference is that this data is normalised to the fully quenched state, by adding excess free WT foot at the end of the experiment. The results show similar behaviour for $F_2$ as previously. In this case a small increase in $F_2$ is observed on addition of the forward fuel. This leakage is a feature of the original ssDNA track experiments and is thought to be caused by blunt-end strand displacement (Bath et al., 2009). The rate of leakage is slow compared to the rate of foot pick-up for the correct fuel. However, similarly to the results above, the $F_1$* signal is not unquenched significantly by either fuel. In fact, the amount of leakage for the wrong (reverse) fuel is slightly higher than that for the correct (forward) fuel. Thus, the piece-wise track is clearly acting to disrupt pick-up of a WT foot in configuration A.

### 4.3.2 Track defects

As the fluorescence results in Section 4.3.1 demonstrate, the modified two-foot motor does not act as expected on a piece-wise track anchored to DNA origami. Two possible explanations for this, and preliminary measures to address them, are discussed in this Section. Firstly, the correct behaviour of the motor assumes the track assembles with the required geometry, as in Figure 4.2 B. However, the origami tiles are assembled with an excess of track staple strands, and thus another track geometry is possible, in which two copies of each track staple are incorporated (Figure 4.9). The difference in energy of the two track assemblies is relatively small compared to the energy of the more than 7000 basepairs formed during tile assembly. Such 'super-stoichiometry' of origami staple strands is poorly understood, but is thought to be a factor limiting the size of arrays of 2D origami tiles and also the yields of more complex 3D origami structures (Rothemund, 2006; Douglas, Dietz,

Liedl, Högberg, Graf and Shih, 2009) (W. Shih, personal communication).

The effect of a super-stoichiometric track on observations of the motor in the fixed-foot motor experiments can be considered (Figure 4.9). Of the many possible motor configurations now possible, there are only two in which the two feet occupy adjacent binding sites. An additional complication is that when the WT foot is bound to the upstream adjacent binding site (Figure 4.9 B), the quencher on the 3' end of the foot remains far away from the origami-bound fluorophore. This results in very little expected change in fluorescence of $F_1$* when the foot is put down or picked up. This is consistent with the results in in Figures 4.7 and 4.8.

Preliminary experiments were used to test the possibility of improving track continuity by varying tile assembly conditions. Figure 4.10 shows the ensemble fluorescence results for an asymmetric staple track, the same as that used in Figure 4.8. The excess of track staples used in tile assembly was altered (3× and 25×), and two annealing protocols were used (Fast: 1° C $min^{-1}$, Slow: 0.05° C $min^{-1}$). For all samples quenching of both fluorophores is observed when purified motor is added. For each sample, the forward fuel is added, and after some time the reverse fuel is then added. As for previous results, in all samples $F_2$ shows a small amount of leakage with the forward fuel and clear pick-up of the foot on addition of the reverse fuel. $F_1$* behavior is again similar to the previous results, a small amont of foot pick-up is observed on addition of the forward fuel, and a similar (slow anneal) or even larger (fast anneal) amount of leakage seen for the reverse fuel. Both $F_1$* and $F_2$ are quenched after the addition of enzyme. Thus, variation of the tile assembly conditions does not restore the two foot motor to the expected behaviour. However, the changes in both fluorophores are larger for the fast anneal protocol, and slightly better for the 3× track staple excess. This may indicate that these conditions produce a slightly higher proportion of well-formed tracks.

Alterations to the track assembly conditions were found to have little effect

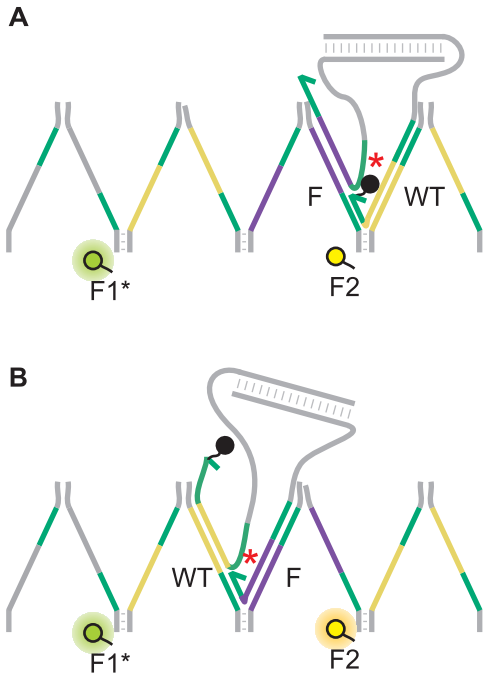


Figure 4.9: Schematic for a proposed disruption of the fixed-foot two-foot motor track. Two copies of each track staple are incorporated in the origami. The fixed foot (purple) now has two possible locations (**A** and **B**). For each one there is only one possible adjacent binding domain for the wild-type foot. The WT foot can be put down in other locations, but will not be lifted by the fuel. The first configuration (A) results in an $F_2$ signal that behaves as expected. The second configuration (B), results in a large distance between the quencher and $F_1$*, resulting in very little change in fluorescence when the foot is put down or picked up. This is consistent with the results in in Figures 4.7 and 4.8.

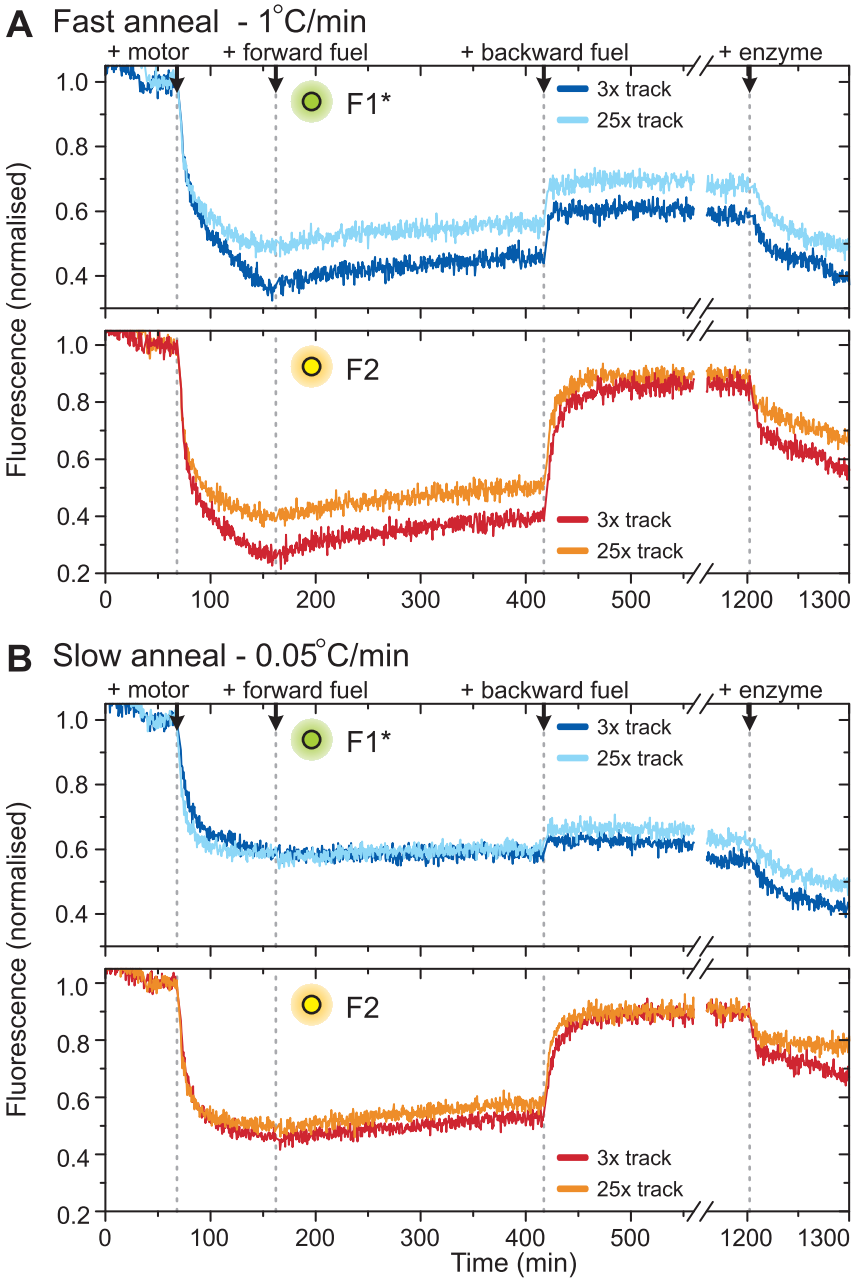


Figure 4.10: Ensemble fluorescence results for asymmetric motor tracks assembled with different conditions. The downstream fluorophore $F_2$ behaves as expected, the upstream label $F_1$* shows only slight leakage with the wrong fuel. Foot pick-up in the fast anneal samples is slightly greater.

on pick-up of the back foot by a forward-fuel strand. A second explanation arises from geometric considerations of a correctly formed track. Pick-up of the back foot by the forward fuel requires branch migration past a neck-linker in the track. At this point, a 4-arm structure is formed between two adjacent track segments, and the foot and fuel strands (Figure 4.6 Aii). Branch-migration past this intermediate structure requires rotation of the DNA helices, which may be hampered by the two track segments being anchored at both ends to the DNA origami tile. For the front foot, once the toe-hold has been exposed, branch migration past a neck-linker is avoided, and so displacement may be much faster. If this explanation is the case, the piece-wise track to be suitable only for a motor moving backwards. For a motor moving forwards, the neck-linker could be shifted along by one domain, so that track segments consist of a competition and then a binding domain. This would be a compromise, as the motor would not be reversible.

## 4.4 AFM measurements

High-speed AFM imaging was used to obtain movies of the fixed foot motor on the 4-segment track. Figure 4.11 shows image frames and kymographs for two such movies. The wild-type foot is labelled with 3'-biotin, and streptavidin (SA) is incubated with the sample to allow the two feet to be identified. In both movies obtained, the bright spot of the SA is in the upstream position (Figure 4.6 A). Prior to imaging, an excess of the reverse fuel was added to the sample. In both movies pick-up of the WT foot is observed. This was not expected to be the dominant behaviour for this configuration. The observed pick-up of the WT foot may be due to a 'leakage' interaction with the incorrect fuel. Because only two movies were obtained after many imaging attempts, a statistical comparison of the probability of lifting either the upstream foot or the downstream foot could not be made.

Alternatively, the decrease in intensity of the bright spot, which indicates the upstream foot in the AFM images, may be instead caused by interaction of the SA molecule with the AFM cantilever. In both movies a short time after the SA spot is removed, the bright spot of the other foot disappears. This is most likely further cantilever damage, as there is no fuel strand present that can pick up the fixed foot. This damage happens relatively quickly after the SA spot is removed. It is possible that, when one of the motor feet is lifted by fuel, the two linked duplexes of the lifted foot are more prone to being caught by the cantilever and stripped off. In either case, high-speed AFM analysis may not be suitable fo use with the two-foot motor, due to the increased likelihood of motor damage, and the difficulty in obtaining enough movie data to build up an average view of motor behaviour.

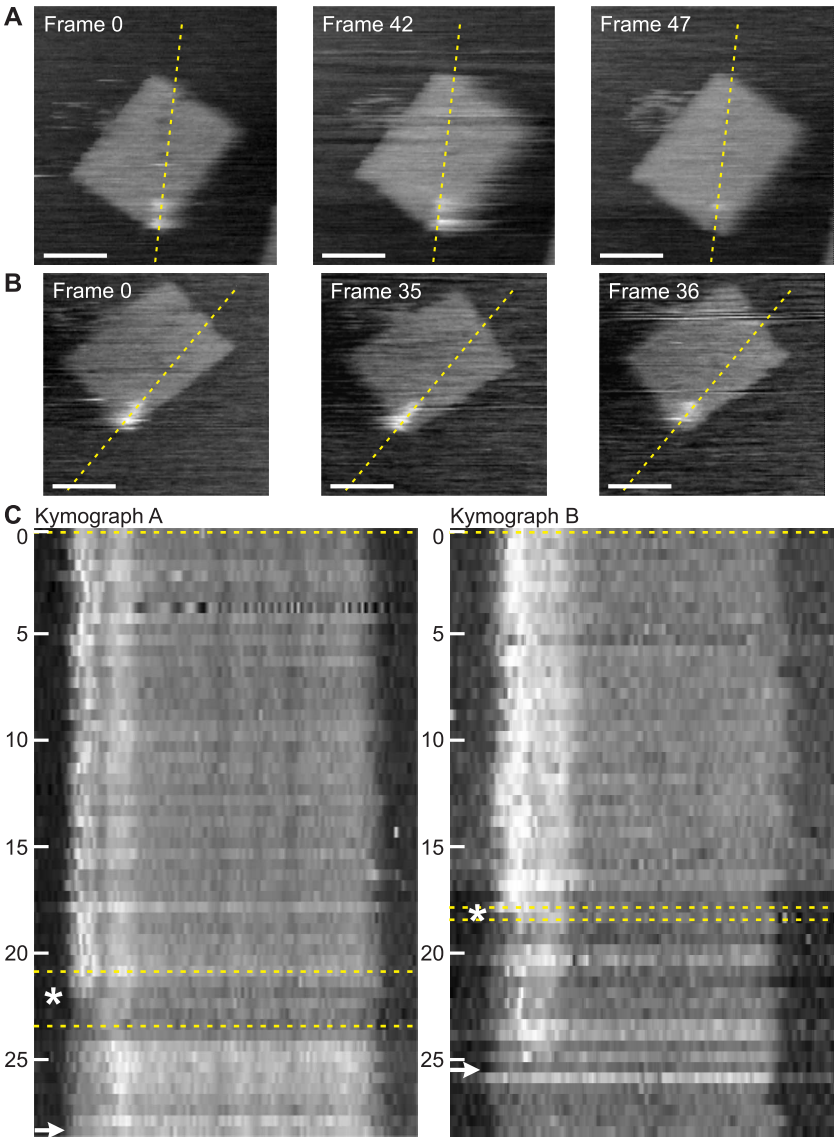


Figure 4.11: High-speed AFM movies of the two-foot motor. **A, B** Image frames and **C** kymographs for motors observed after the addition of reverse fuel. A SA-label on the WT foot shows this foot is in the upstream position. The WT-foot is removed first (*) in both movies, either due to leakage or cantilever damage. Removal of the fixed foot follows soon after (arrow), most likely due to cantilever damage. Time scale is in seconds, scale bars 50 nm.

## 4.5 Conclusions

This chapter presents preliminary investigations into the use of a piece-wise DNA origami track for an enzyme-driven two-foot DNA motor. Initial AFM characterisation suggested that tracks had been assembled as designed. However, ensemble fluorescence results for a modified motor on a short 4-segment track were unable to reproduce the motor behaviour, as previously observed on ssDNA tracks (Bath et al., 2009).

A 'super-stoichiometry' defect of the track, where multiple copies of track staples are incorporated in the tile, is proposed to explain these results. This defect is consistent with the observation that one fluorophore acts as expected and the other does not. Variations of the tile assembly method did not affect the results significantly. Motor operation could also be affected by the piece-wise track geometry. Branch migration for lifting the back foot must proceed past a 4-arm junction intermediate, whereas for the front foot is does not. This may affect the rates of the two processes, effectively making the forward fuel, which lifts up the back foot, inactive. It is not clear yet which of these explanations is true, and the observed motor behaviour could be a combination of both. If the second explanation is true then the track may be useful for a unidirectional version of the two-foot motor. Further tests on a longer track with the reverse fuel would reveal this.

Unfortunately, a piece-wise method for anchoring the two-foot motor track across a DNA origami tile is unsuitable, because it disrupts the most basic mechanism of the motor. Without the ability to pick up either foot, the motor will not be able to walk reversibly along the track as it is designed to do. Furthermore, while static AFM analysis of the system was found to be useful, high-speed AFM imaging of motor-track systems in operation was found to damage the tracks too much to be more informative.

In conclusion, the development of longer tracks for the two-foot DNA motor

still presents many challenges, both in their assembly and in observations of motor transport across them. Nevertheless, the results presented here provide important insight into future research directions, and adaptations of designs in this Chapter may lead to improvements. For example, a deliberate version of the piece-wise track in Figure 4.9, with longer neck linkers at the 'hills' between track segments and a wider anchor spacing may improve motor stepping. Tests on longer tracks could also determine if the motor is able to operate unidirectionally.

Alternatively, a continuous track length of many domains could be stretched out by a frame-style origami tile, such as those used in previous protein studies (Endo, Katsuda, Hidaka and Sugiyama, 2010*a*). This would avoid the geometric problems associated with a piece-wise track. Ideally, the DNA motor track could be introduced into a long piece of plasmid DNA, which could then be used as a template strand and folded into a DNA origami tile such that the track remains ssDNA. Inserting the track directly into the template strand would completely remove the possibility of any track super-stoichiometry, and its inherent problems. For observations, ensemble fluorescence measurements were able to give useful information about motor behaviour on shorter tracks with a fixed foot. To extend this work to longer tracks, it may be more informative to use single-molecule fluorescence measurements to track the behaviour of individual motors. Quantum dot labels on the motor and tile, as developed in Chapter 2, would facilitate this and this approach is currently being taken in further work.

Chapter 5

# DNA motor junctions

In Chapter 3 the movement of a 'burnt-bridges' DNA motor along a straight DNA origami track was demonstrated. Interestingly, the 2-dimensional nature of the DNA origami substrate immediately suggests the possibility of more complex track geometries and motor behaviour. In this chapter, movement of the burnt-bridges DNA motor through a bifurcating network of tracks is investigated. Methods are developed to control the path a motor takes at a junction in its track, based on either the addition of an external signal or an instruction programmed into the motor.

DNA motor-junction systems, in which motors are routed to destinations based on instructions encoded in the track or motor, or added externally, can act to process information in a sequential way. While there are a number of solution based approaches to DNA logic and computation (Stojanovic et al., 2002; Seelig, Soloveichik, Zhang and Winfree, 2006; Zhang et al., 2007), this track-based approach may have several advantages. Firstly, motors actively bring the components required for logic operations together. Signals are efficiently carried from one operation

to the next, in a defined order. Because the logical operations are performed sequentially, gate sequences and motifs may be re-used, an important feature if such systems are to be extended in complexity. All DNA logic gates designed so far have some degree of leakage into the incorrect state (Zhang et al., 2007; Zhang and Winfree, 2010; Seelig, Soloveichik, Zhang and Winfree, 2006): an additional benefit here is the ability to repeat 'leaky' gates along a track, improving their overall efficiency.

In binary logic all operations can be programmed with only two gate types, a NOT gate and either and an AND or OR gate. In DNA logic systems the logical values 0 and 1 are often represented by the absence or presence of a strand (Seelig, Soloveichik, Zhang and Winfree, 2006; Stojanovic et al., 2002). For this representation, the 0 signal is often difficult to identify uniquely. The absence of a strand can easily be caused by insufficient concentration or time to diffuse, and can be confused by the presence of leakage reactions. An alternative is to design gates that have two possible output strands, in a 'dual-rail', or complementary logic representation (Seelig, Soloveichik, Zhang and Winfree, 2006). The nucleotide sequence of the output provides the logical information (0, or 1) to downstream gates. For the bifurcating designs discussed here, the logical values 0 and 1 are encoded by the motor taking the left or right path at a junction, rather than by the presence or absence of a signal strand. Thus, the 0 signal is a real and detected event.

Finally, a number of recent advances have been made in using DNA motors to drive artificial molecular assembly lines, mimicking the ribosome in cells (He and Liu, 2010; Gu et al., 2010). The motor framework discussed here gives a method for directly linking logical operations to the production of molecules or nanoparticles. This leads to the possibility of an integrated system, that processes a number of input signals to compute a decision, then produces an output molecule in response.

## 5.1 Externally triggered junction

The first DNA motor junction investigated is one in which the direction of motor transport is controlled by the addition of an external trigger signal. In previous burnt-bridges track designs, all downstream stators were initially occupied by a blocking strand that binds to a 'binding' site at the 5' end of the stator and overlaps part of the motor sequence (Section 3.2.2, Figure 5.1A). The binding domains and blocking strands were the same for all stators on the track. In this design, selected stators are given unique binding domains. The corresponding block and release strands then target a specific stator, giving a method for selectively unblocking different elements of the track (Figure 5.1B, C).

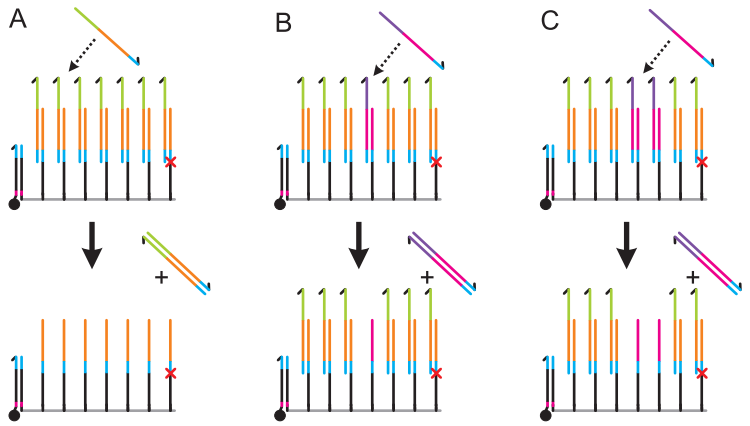


Figure 5.1: External trigger design. **A** Blocking strands are hybridised to stators by a 'binding' domain (orange) and removed by a release strand that binds to the toehold (light green). **B** Selected stators are given unique binding domains, and may be independently unblocked. **C** Independently blocked stators may be repeated, to make a stronger barrier.

### 5.1.1 Single Junction design

The external trigger junction was tested on a DNA motor track with a single bifurcation, shown in detail in Figure 5.2. The hexagonal array of nicks, at junctions

between staples, on the DNA origami tile give many possible junction geometries. A configuration was chosen in which the angles between the three paths that join at the node are approximately equal, with the aim of making all paths equally likely if the junction is open. As in Chapter 3, the total track length along either path is 7 steps ($S_1$- $S_{8R}$, $S_1$-$S_{8L}$); 3 steps ($S_1$-$S_4$) occur before the node and 4 afterwards ($S_4$-$S_{8R}$ or $S_4$-$S_{8L}$). The independently blocked stators occur directly after the node ($S_{5R}$ and $S_{5L}$), and are used to direct the motor down a particular path. The two stators after the node each have a unique binding and release sequence. All other stators have a standard block to aid in motor loading, as described in Chapter 3. All block and release sequences were designed to reduce cross-interaction using Nanex software (Goodman, 2005), and were tested for orthogonality with Nupack (Zadeh et al., 2010).

### 5.1.2 Single Junction fluorescence results

Ensemble fluorescence measurements were used to observe transport of a quenching molecule linked to the motor past a sequence of fluorophores on the junction track. This method is similar to that used in Chapter 3 to analyse straight tracks, and details of the experimental protocols are given in Appendix A.9. Initially, each half of the track ($S_1$- $S_{8R}$ or $S_1$-$S_{8L}$) was tested independently on tiles labelled at $F_1$, $F_3$ and $F_{8R}$ or $F_{8L}$, as appropriate (Figure 5.3). Both tracks act as expected: addition of the enzyme leads to a sharp increase in $F_1$, as the motor steps off $S_1$, followed by a transient dip in $F_3$, as the motor moves past this location. After a delay, a gradual and permanent quenching of $F_{8R}$ or $F_{8L}$ indicates motor arriving at the end of either the right or left branch of the track respectively.

Following this, the full junction track was tested (Figures 5.5 and 5.4). Tracks were labelled at $S_1$ with $F_1$, and then with two differently coloured fluorophores $F_{8R}$ and $F_{8L}$ at $S_{8R}$ and $S_{8L}$ respectively. The two independently blocked stators, $S_{5R}$

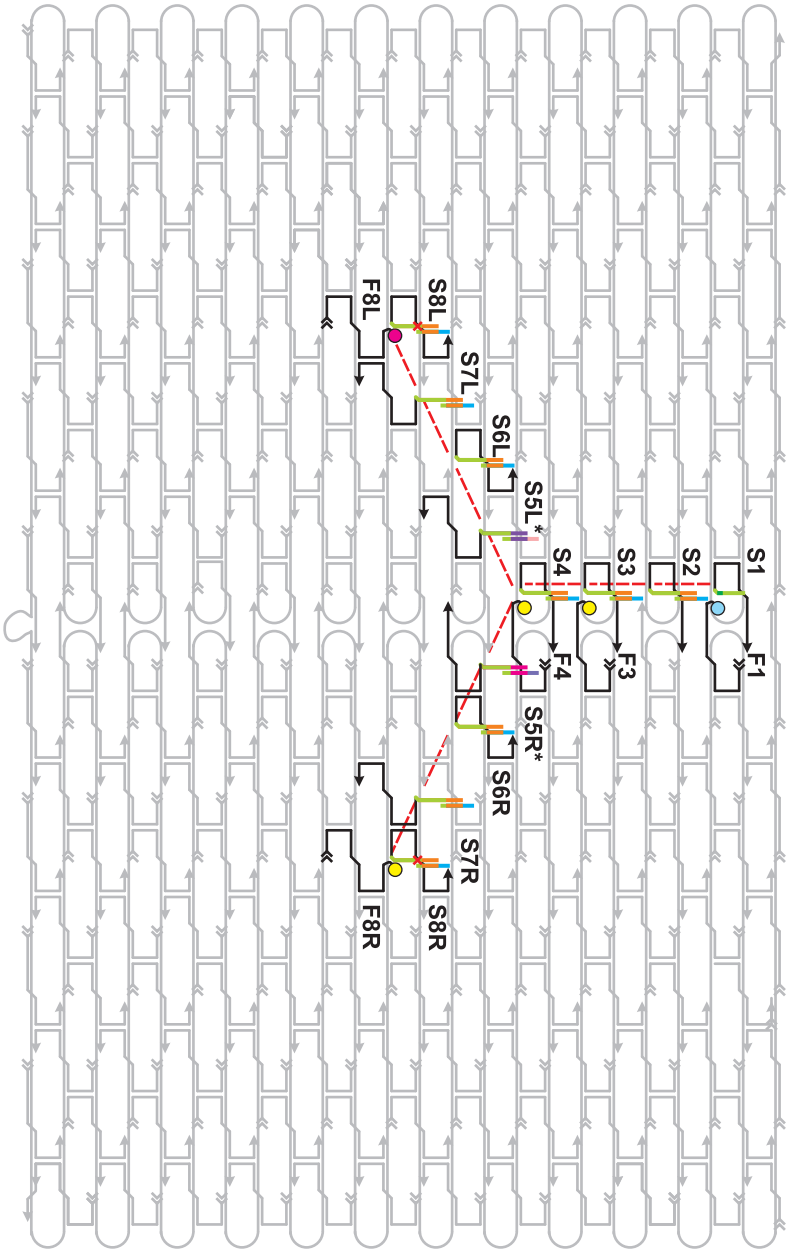


Figure 5.2: DNA tile schematic for a single-junction DNA motor track. Modified staples are labelled, the two independently blocked stators ($S_{5R}$* and $S_{5L}$*) occur directly after the node stator ($S_4$). Fluorophore-labelled staples ($F_1$, $F_3$, $F_{8R}$, $F_{8L}$) are used to observe transport of a quenching molecule along the track. A simplification of the track structure is shown (red dotted lines), and is used as a key in later Figures.

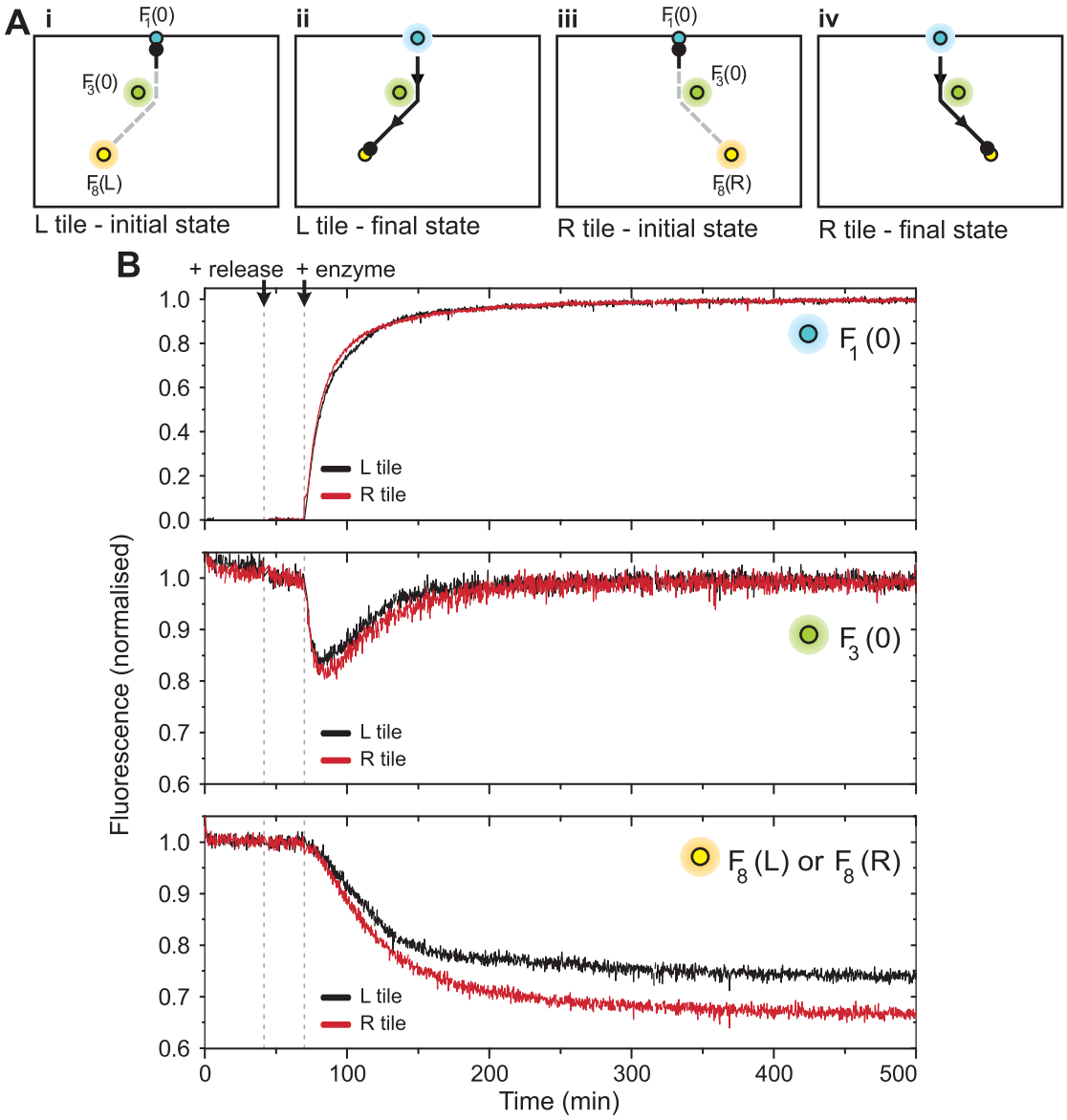


Figure 5.3: Ensemble fluorescence results for DNA motor tracks incorporating a corner. The two halves of a junction track were tested separately. **A** The expected initial and final states for **i-ii** the Left-track tile ($S_1$-$S_{8L}$) and **iii-iv** the Right-track tile ($S_1$-$S_{8R}$). **B** Fluorescence results for fluorophores $F_1$, $F_3$ and $F_{8L}$ or $F_{8R}$ placed along the track. The motor follows these 'bent' tracks similarly to the straight tracks analysed in Chapter 3. Both tracks are unblocked by the addition of the standard release strand (as used in Chapter 3), and one or both of the unique R- or L-release strands, for $S_{5R}$ and $S_{5L}$, 20 min before addition of enzyme.

and $S_{5L}$, have different blocking and release strands. The unique release strand for unblocking stator $S_{5R}$ is the instruction to take the right-hand path, and is referred to as the R-release, or 'R' in Figures. Similarly, the L-release is the unique release that unblocks stator $S_{5L}$ and opens the left-hand path to the motor. Three identical samples were prepared and the effect of adding different external trigger instructions compared. When R-release is added, $F_{8R}$ is quenched strongly, while $F_{8L}$ is largely unchanged (Figure 5.4B). Conversely, when L-release is added $F_{8L}$ is strongly quenched, and $F_{8R}$ is not. When both R- and L-release strands are added, both $F_{8R}$ and $F_{8L}$ are quenched equally, confirming that when the junction is open there is no bias between the two motor paths. To prove that the results in Figure 5.4 are independent of fluorophore choice, the fluorophore colours of $F_{8R}$ and $F_{8L}$ were reversed and identical behaviour was observed (Figure 5.5). In both sets of data, a small decrease in intensity is observed at the end of the wrong path, which is due to leakage of motor through the blocked stator into the wrong path. For example, there is a small decrease in $F_{8R}$ when the L-release is added in Figure 5.3.

In Section 3.2.2 blocking strands of different strengths were discussed. However, it was unknown whether even a strong blocking strand is sufficient to hold the motor in place indefinitely. Figure 5.6 shows the results for a junction experiment in which neither path is unblocked. Fluorophores $F_1$ (Joe) and $F_4$ (Cy3.5) along with either one or both of fluorophores $F_{8L}$ (Cy5) and $F_{8R}$ (Cy5) label the track. If the motor is trapped at $S_4$ by the two downstream blocked stators $S_{5R}$ and $S_{5L}$, $F_4$ should remain quenched. This was not observed to be the case, $F_4$ eventually returns to a high level (Figure 5.6B). A small amount of quenching of $F_{8L}$ and $F_{8R}$ is detected, indicating that some motor leaks through the blocked stators to reach either $S_{8R}$ and $S_{8L}$. However, this quenching is much less that for an open junction. This suggests that some motor is prevented from moving downstream

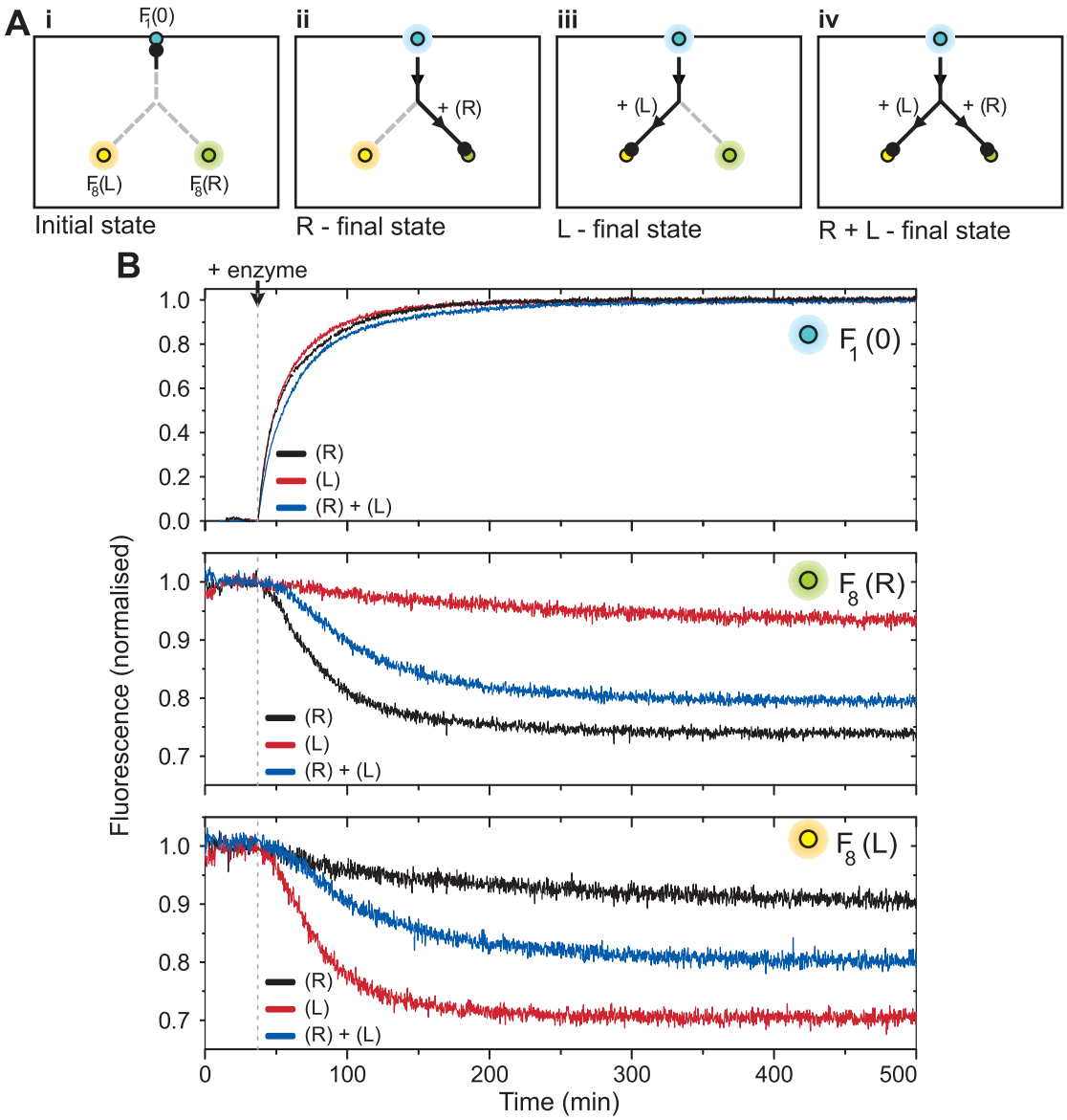


Figure 5.4: Ensemble fluorescence results for a single-junction DNA motor track. **A i** Expected initial state, and final states after the addition of **ii** R-release strand, **iii** L-release strand, or **iv** both R- and L-release strands. **B** Fluorescence intensities for fluorophores $F_1$ (Joe), $F_{8R}$ (Cy3.5) and $F_{8L}$ (Cy5). $F_{8R}$ is significantly quenched only if R-release is added. $F_{8L}$ is significantly quenched only if L-release is added. The small decrease of the other fluorophore indicates leakage into the wrong path. If both R- and L-release are added, motor is split evenly between the two paths. Instruction strands are added in ∼25× excess 20 min before addition of enzyme, all measurements at 37°C.

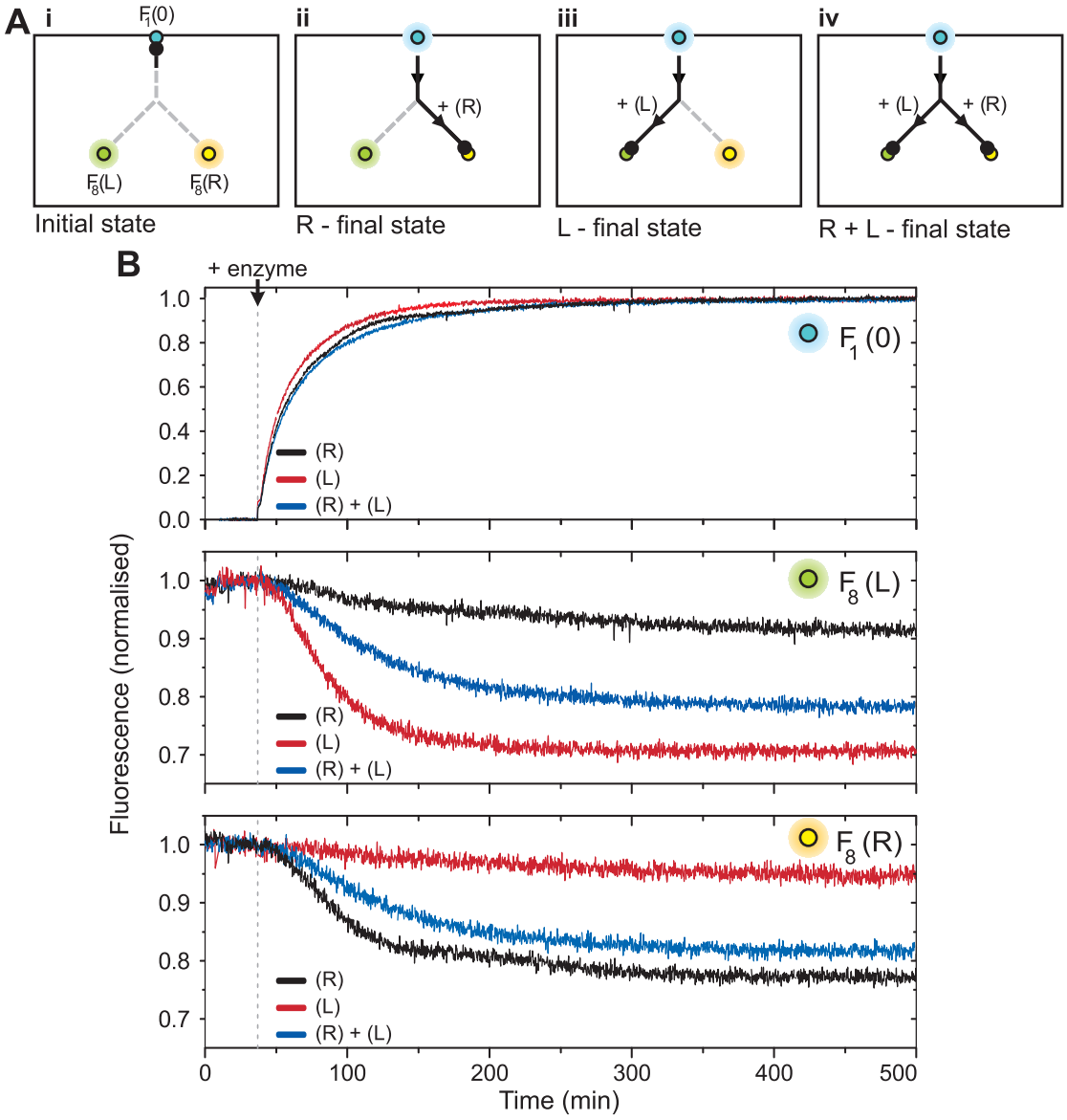


Figure 5.5: Ensemble fluorescence results for a single-junction DNA motor track. An identical experiment to that in Figure 5.4, except for the reversal of the fluorophore colours. Here $F_{8R}$ is Cy5 and $F_{8L}$ Cy3.5. Behaviour of the motor is unchanged, $F_{8R}$ is significantly quenched only if the R-release added, and $F_{8L}$ only if L-release is added, $F_{8R}$ and $F_{8L}$ quench equally if both R- and L-release are added. Instruction strands are added in $\sim$25$\times$ excess to track 20 min before addition of enzyme, all measurements at 37°.

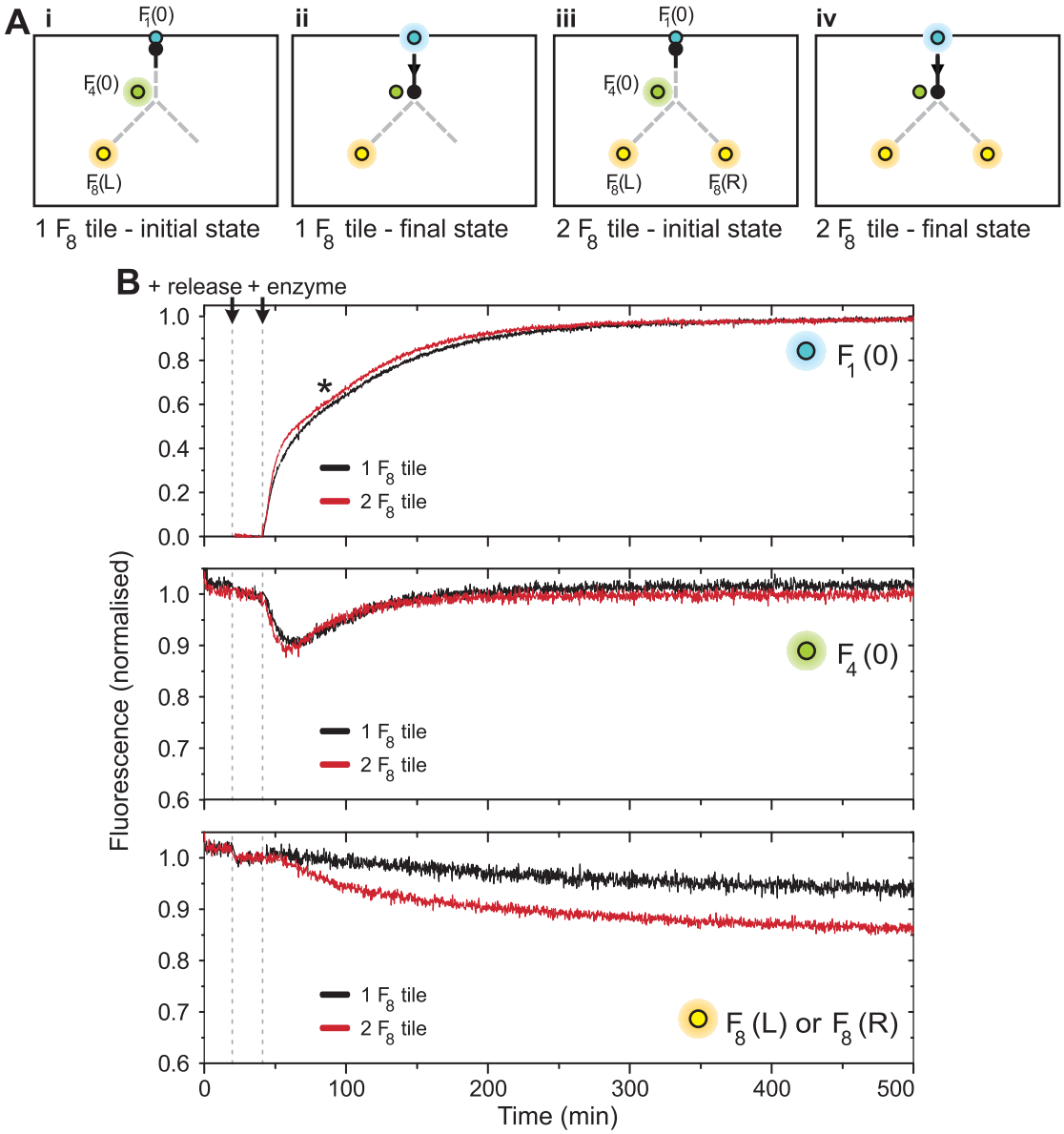


Figure 5.6: Ensemble fluorescence results for a single-junction DNA motor track for which both paths are closed. **A** Expected initial and final states for tiles labelled with $F_1$ and $F_4$ and either **i-ii** $F_{8L}$ or **iii-iv** $F_{8L}$ and $F_{8R}$. **B** Fluorescence results show that the motor is not held indefinitely at position $S_4$ before the blocks, as this fluorophore slowly unquenches. A small and approximately equal amount of quenching is seen in $F_{8L}$ and $F_{8R}$, indicating motor leaks forward into the R and L paths. The slight dip in the $F_1$ (*) curve suggests that some motor diffuses back towards $S_1$ where it is trapped by the additional 2 nt on this stator.

by the blocks, and will diffuse back towards $S_1$. In Chapter 3, diffusion between stators was estimated as $\sim$13$\times$ slower than enzyme-driven stepping. Stator blocking strands were designed to reduce the driven stepping rate, which may now be comparable in magnitude to the rate of backward diffusion. Thus, if the motor encounters a node at which all downstream stators are blocked, the diffusion process can no longer be neglected. The shape of the $F_1$ curve, which has a slight dip, supports this. This property of the motors, that they leak through or diffuse backwards at junctions for which neither path is open, will become important for the autonomously programmed motors discussed further in Section 5.3.

## 5.2 Externally triggered junction - 3 nodes

Following the success of the single externally-triggered junction discussed in Section 5.1, the system was extended to include three nodes or junctions. The two paths leading away from the junction in Section 5.1 both bifurcate again at a second junction, resulting in 4 possible paths. The design makes use of the fact that, because junctions are encountered sequentially, junction sequences can be re-used. Thus, the first junction design is unique, and the second junction design occurs twice. The four final stators of the system each correspond to a unique path through the system, and a unique combination of instructions.

### 5.2.1 Triple Junction design

The design for the triple-junction DNA motor track is shown in detail in Figure 5.7. The motor path across the DNA tile was chosen such that all three junctions have the same equal-angle configuration. The total track length along each of the 4 paths is now 12 steps ($S_1$- $S_{13LL}$, $S_{13LR}$, $S_{13RL}$, $S_{13RR}$). As above, 3 steps ($S_1$-$S_4$) occur before the first node. Six steps then occur between the first and second

nodes ($S_4$-$S_{10R}$ or $S_4$-$S_{10L}$), and there are 3 more steps after the second node ($S_{10R}$-$S_{13RR}$ or $S_{13RL}$, $S_{10L}$-$S_{13LL}$ or $S_{13LR}$). Directly downstream of each node there are a pair independently blocked stators, with different block and release sequences, that may be used to direct the motor down either the right or left-hand path. The instruction sequences for both second nodes are the same. That is, the two stators $S_{11LL}$ and $S_{11RL}$ are blocked and unblocked by the same block and release strands, as are $S_{11LR}$ and $S_{11RR}$. Thus, there are four unique instruction strands. (R,0)-release and (L,0)-release direct the motor down either the right or left-hand path at the first node. Similarly, (0,R)-release and (0,L)-release direct the motor down either the right or left-hand path at the second node. The four final stators ($S_{13LL}$, $S_{13LR}$, $S_{13RL}$, $S_{13RR}$) are expected to correspond to the 4 possible sets of instructions (L,0)+(0,L), (L,0)+(0,R), (R,0)+(0,L), (R,0)+(0,R).

### 5.2.2 Triple Junction fluorescence results

Ensemble fluorescence measurements were used to observe motor movement across the triple junction tiles. Before complete tracks were tested, the second pair of block and release strand sequences was tested on the right-hand half of the track (Figure 5.8 A). The tiles were labelled with 3 differently coloured fluorophores, $F_{7R}$, $F_{13RR}$ and $F_{13RL}$. The block strand for the first junction was omitted during tile assembly, and the effect of adding either (0,R)-release or (0,L)-release was tested and is shown in Figure 5.8. The second junction was found to work with a similar efficiency as the first design in Section 5.1.2. There is a longer delay before the fluorophores at the end of the tracks begin quenching, consistent with the longer 12-step tracks in this design. Surprisingly, a large enough proportion of the motors remain synchronised at $S_{7R}$, giving a detectable dip in $F_{7R}$ fluorescence as they pass this position. This provides a useful method for detecting which path the motor takes at the first node.

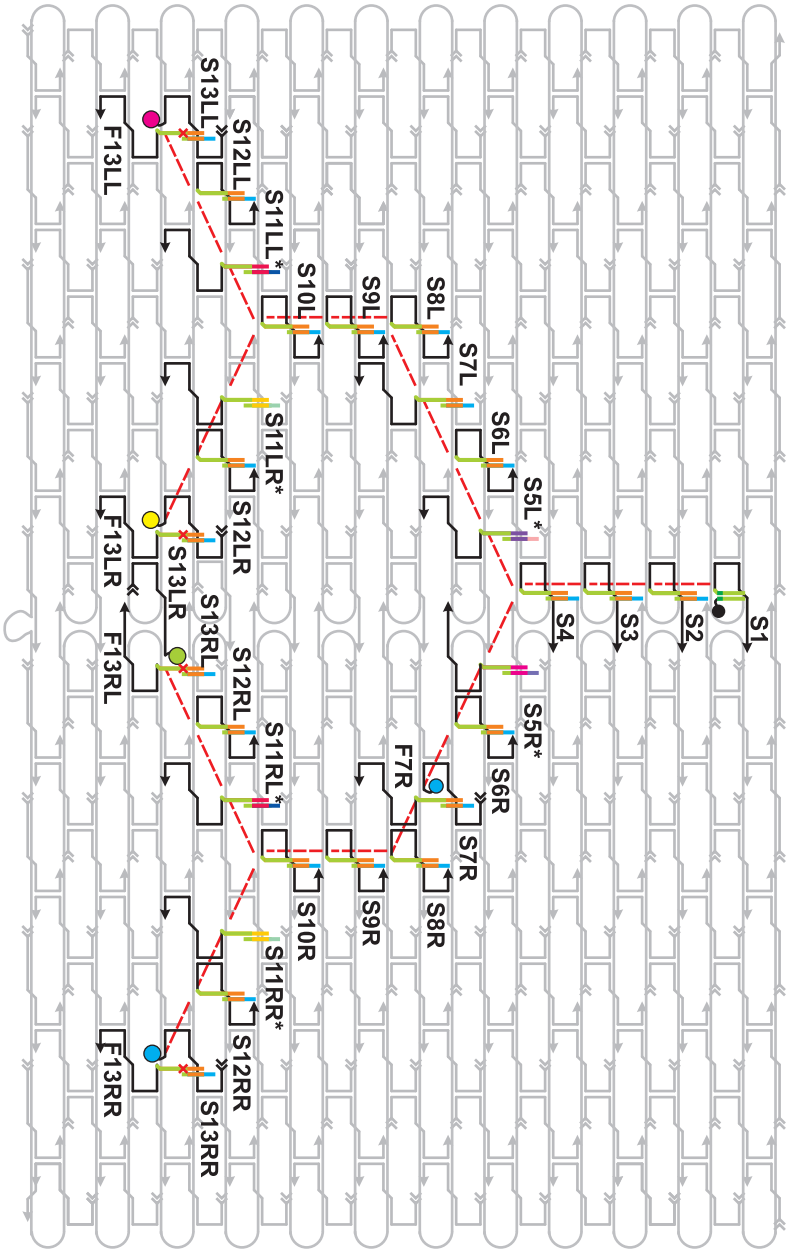


Figure 5.7: DNA tile schematic for a triple junction DNA motor track. Modified staples are labelled. A pair of independently blocked stators occur directly after each node stator. The same set of binding, blocking and release sequences are re-used at nodes 2 and 3 ($S_{10L}$ and $S_{10R}$). Fluorophores label the ends of the 4 motor paths. A simplification of the track structure is shown (red dotted lines), and is used as a key in later Figures.

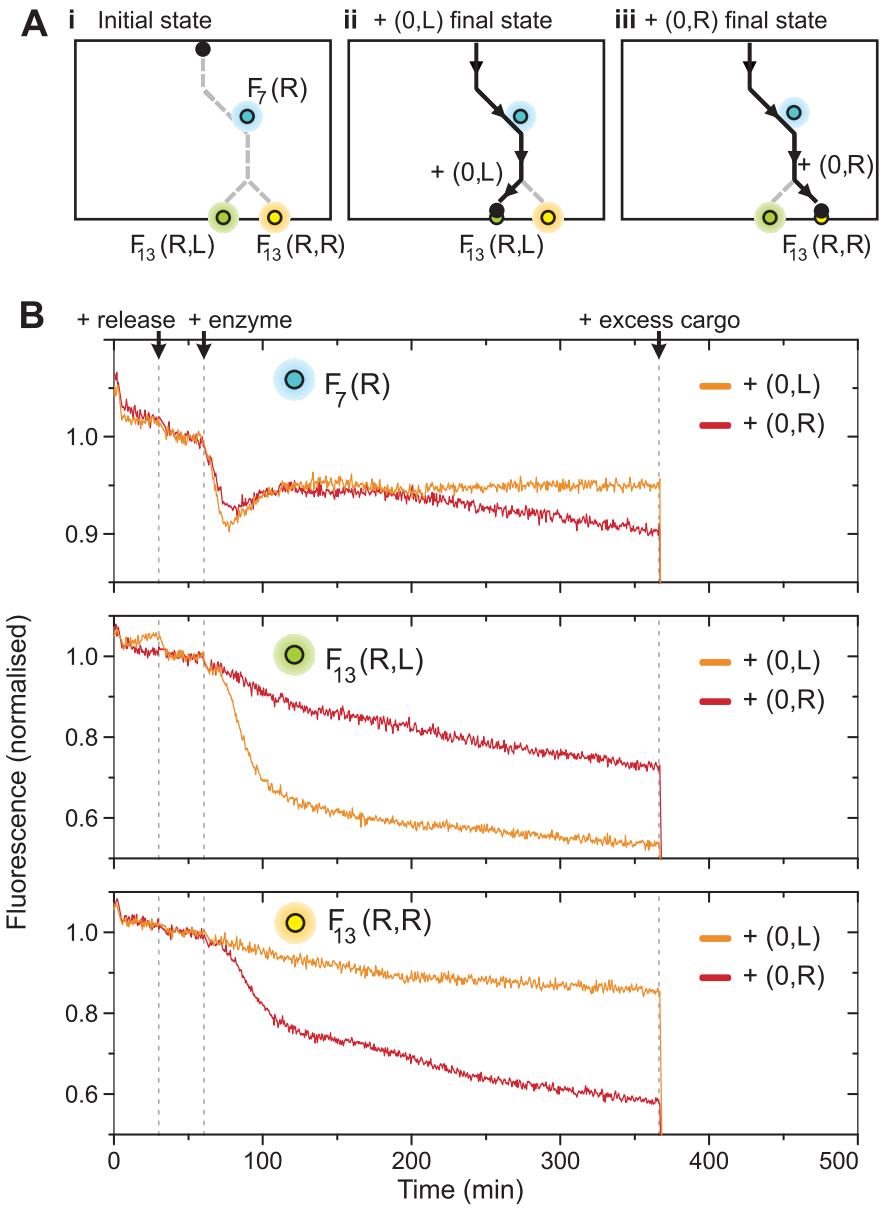


Figure 5.8: Ensemble fluorescence results for the right-hand side of the triple-junction DNA motor track. **A i** initial state and expected final states after the addition of **ii** (0,L)-release or **iii** (0,R)-release. **B** Results for fluorophores $F_{7R}$, $F_{13RR}$ and $F_{13RL}$. There is a dip in $F_{7R}$ as the motor moves past this location, and either $F_{13RR}$ or $F_{13RL}$ is strongly quenched depending on which instruction strand was added, as expected. This second set of junction sequences operates similarly to that in Section 5.1.2.

Two sets of experiments were used to test motor movement across the full triple junction track. Choosing four fluorophores that are well-spaced in wavelength, have similar intensities and are all quenched with similar efficiency by the same quenching molecule is difficult. Thus, the first set of experiments was performed on a 3-colour design (Figure 5.9 A). Stator $S_{7R}$ is labelled with $F_{7R}$ (Joe), and is used to determine which side of the track the motor has taken at node 1. Nodes 2 and 3 have the same set of labels. $S_{13RR}$ and $S_{13RL}$ are labelled by $F_{13RR}$(Cy5) and $F_{13RL}$(Cy3.5) and similarly $S_{13LR}$ and $S_{13LL}$ are labelled by $F_{13LR}$(Cy5) and $F_{13LL}$(Cy3.5).

Four identical samples were prepared, and tested with the four posible combinations of release strands. Results for $F_{7R}$ (Figure 5.9 B) show that a dip in this fluorophore occurs only if the (R,0)-release strand is added, but do not depend on the second release strand. The Cy3.5 signal, which is the sum $F_{13RL} + F_{13LL}$, shows quenching only if the (0,L)-release strand is added and does not depend on the first release strand. Similarly, the Cy5 signal, which reports $F_{13RR} + F_{13LR}$ quenches only if (0,R)-release is added, independently of the first release. As for the single-junction track, there is some leakage into the wrong path, as indicated by the small amount of quenching in the other fluorophore channel. For example, there is a slight decrease in the $F_{13LL}$+$F_{13RL}$ (Cy3.5) channel on addition of (0,R). Thus, the results from the three fluorophores allow the path of the motor through the junctions to be inferred. However, while these results are as expected from the design of the track, they do not definitively prove the final destination of the motor.

To show unambiguously that the motor occupies the correct final location, additional tests were made on a 4-colour design (Figure 5.10 A). In this design each of the 4 final stators $S_{13RR}$, $S_{13RL}$, $S_{13LR}$, $S_{13LL}$ is labelled with a unique fluorophore colour: $F_{13RR}$(Cy3), $F_{13RL}$(Cy3.5), $F_{13LR}$(Cy5), $F_{13LL}$(Cy5.5). The

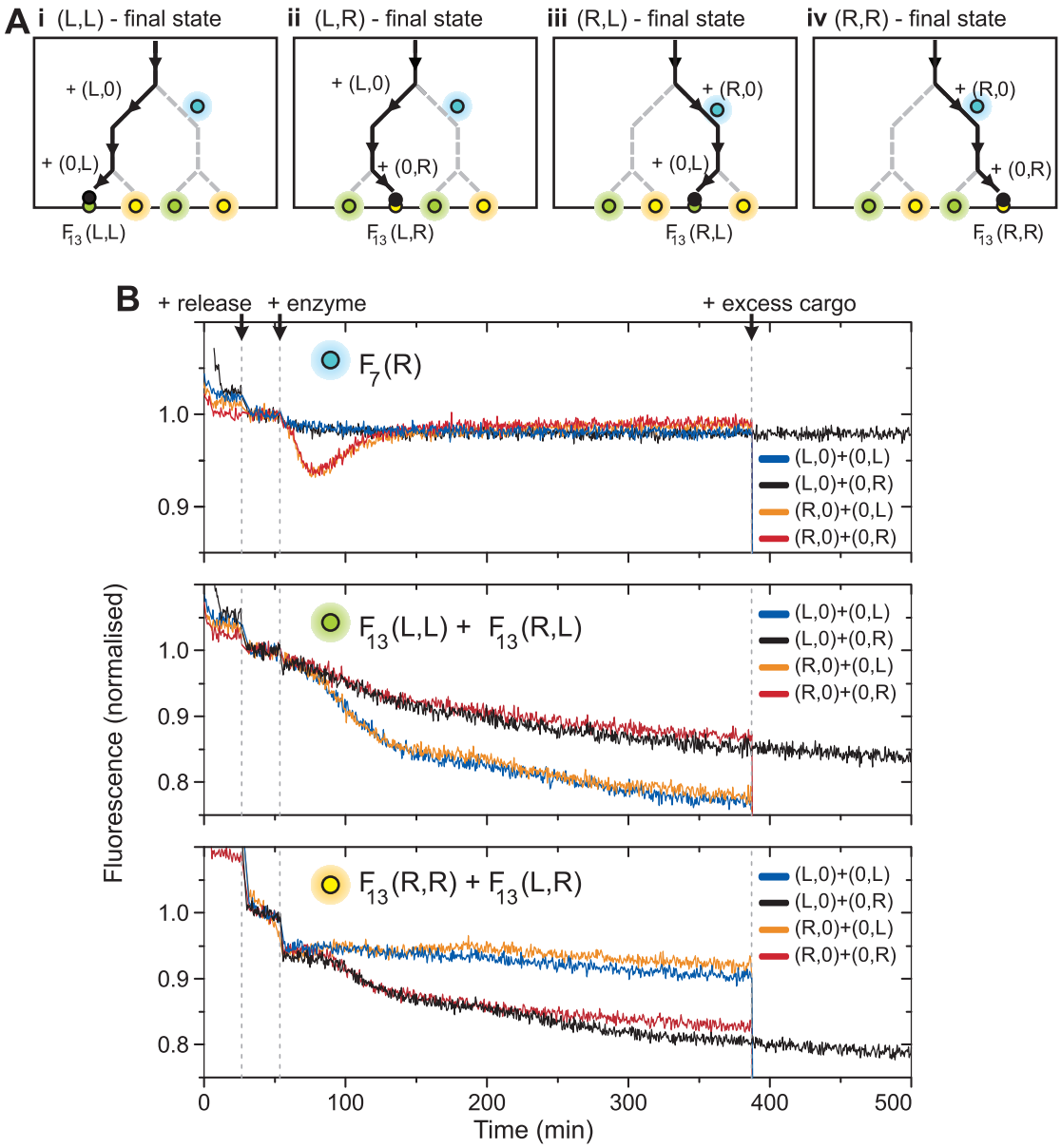


Figure 5.9: Ensemble fluorescence results for a 3-colour triple-junction DNA motor track. **A** Expected final states after the addition of instruction sets **i** (L,0)+(0,L), **ii** (L,0)+(0,R), **iii** (R,0)+(0,L), **iv** (R,0)+(0,R). **B** Results for fluorophores $F_{7R}$ (Joe), $F_{13LL}$ + $F_{13RL}$ (Cy3.5), and $F_{13LR}$ + $F_{13RR}$ (Cy5). There is a dip in $F_{7R}$ only if the first instruction is (R,0). Either Cy3.5 or Cy5 is strongly quenched depending on the instruction strand added for the second junction, (0,L) or (0,R).

equivalent set of results is shown in Figure 5.10B. As expected, each fluorophore is strongly quenched only when the correct instructions to direct the motor to that location are added. The requirements placed on fluorophore choice lead to lower quality data for this design, and the Cy5.5 signal was found to be particularly noisy. Extending such designs to many more paths will make the choice of fluorophores even more difficult and in general configurations similar to the 3-colour system above may be more useful.

However, the 4-colour experiments do reveal additional behaviour of the motor system. A small number of motors leak into the wrong path at the first junction, but then are correctly sorted by the second junction. For example, $F_{13RR}$ is strongly quenched by instructions (R,0) + (0,R) as expected, but is also partially quenched by leaked motor when instructions (L,0) + (0,R) are added. That is, for the (L,0) + (0,R) instruction, a small amount of motor leaks into the right-hand path at node 1. These motors are then correctly directed down the right-hand path at node 3, and finish on the stator labelled with $F_{13RR}$. This effect was hidden in the 3-colour data, and suggests the possibility of an error correcting design, where motors that have leaked into the wrong state could be routed back on to the correct path.

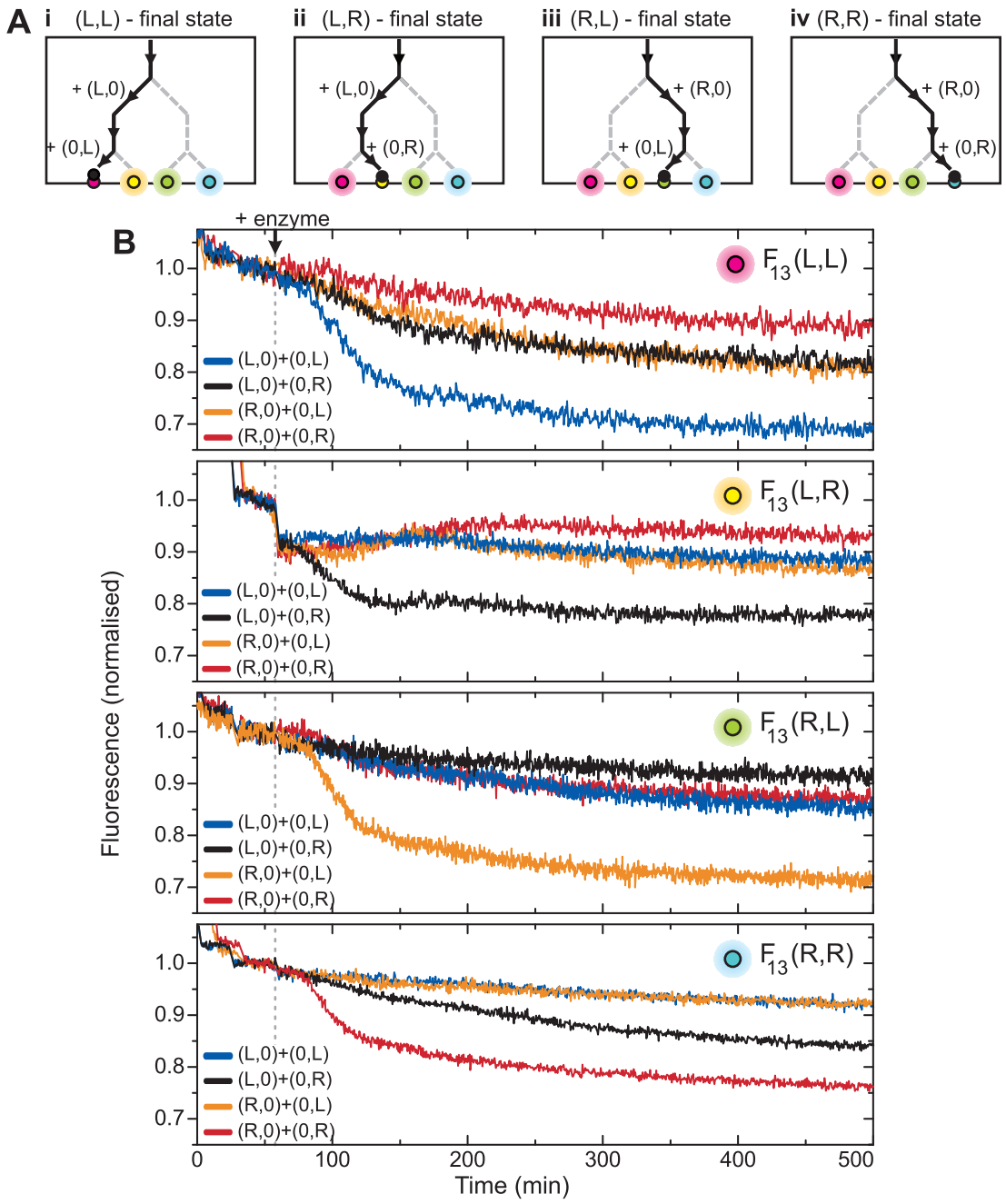


Figure 5.10: Ensemble fluorescence results for a 4-colour triple-junction DNA motor track. **A** Expected final states after the addition of instruction sets **i** (L,0)+(0,L), **ii** (L,0)+(0,R), **iii** (R,0)+(0,L), **iv** (R,0)+(0,R). **B** Each fluorophore is quenched only if the correct pair of instruction strands is added.

## 5.3 Motor triggered junctions

The results above demonstrate the controlled transport of a DNA motor through a bifurcating network of tracks. The path taken is determined by a set of external instructions added to the track before the motor is activated by the addition of enzyme. It is also interesting to consider a system in which these instructions are carried directly by the motor strand. This section describes the development of such a motor design.

In these designs, the principle of selectively unblocking a stator, by adding a release strand, remains the same. The two downstream stators at a node both have a unique blocking strand, and a corresponding unique release strand. The difference is that the toe-holds on the blocking strands are designed to react slowly with the release strands, by including secondary structure, such as hairpins or loops. The motor is then designed to act as a catalyst to unblock a specific stator, by interacting with either the block or release strand to unlock the secondary structure. The aim is to design a system in which both unique release strands are added at the start of an experiment, but only one will react with the motor-catalyst to unblock a stator. For example, if the motor-catalyst interacts with the block or release strand for the downstream stator on the right-hand path ($S_{5R}$ in Figure 5.1.1), it should be preferentially directed down the right-hand path (to $F_{8R}$), even if equal amounts of both the R- and L-release are added.

There are several requirements for such a design. The first is that the interaction between block and release must be slow enough in the absence of motor to ensure that the junction is not opened before the motor arrives. Secondly, as results in Section 5.1.2 demonstrated (Figure 5.6), the motor will not pause indefinitely at a junction where both paths are closed. Thus, the interaction between the block and release in the presence of the motor-catalyst must be fast enough to open one of the paths before the motor can leak through the blocked stators

or diffuse away from this node. Finally, a design in which the motor is unaltered by interacting with strands at the junction is preferable. This will result in a more generalizable system, as the motor can then go on to interact with further junctions.

Several versions of the motor-triggered junction were designed and tested experimentally. The interactions of blocked stators with their corresponding release strand, either in the presence of absence of the motor, were initially characterised on a short dsDNA test track using poly-acrylamide gel electrophoresis (PAGE), following the protocol in Appendix A.4. These results were used to refine elements of the designs, such as loop and toe-hold lengths. The most promising combinations were then tested by ensemble fluorescence measurements on a single-junction DNA origami track. The track used is identical to that discussed in Section 5.1.1, and the experimental protocol is given in Appendix A.9. The first two designs, described briefly in this Section, were found to produce very little bias between the two paths of the track. For brevity, results of the PAGE analysis for these less successful designs are given in Appendix B.1. The full experimental analysis for a third motor-triggered junction, which successfully achieves a bias between the two paths, is presented in Section 5.4. The bias values achieved for each junction are quantified in Table 5.1 in Section 5.5, at the end of the Chapter.

### 5.3.1 Initial designs

#### Motor-catalysed Hairpin block and release

The first design for a motor-triggered junction is shown in Figure 5.11. This design is based on the catalysed hybridisation of two hairpin strands, as introduced in Section 1.3.2 (Turberfield et al., 2003). Hairpins in the block toe-hold and release strand reduce their interaction rate. A catalyst that opens the release strand

hairpin, allowing it to unblock the stator, is tethered to the 3' end of the motor sequence (Figure 5.11). Two orthogonal sets of strands, one each for the R- and L-stator, were designed using Nanev (Goodman, 2005), and interactions were checked with Nupack (Zadeh et al., 2010). The basic motor sequence is the same as in previous designs, with the additional catalyst domain added to the 3' end with a 3-thymine linker. PAGE analysis of this design on a short test track (Appendix B.1.1), showed that the two sets of strands behaved quite differently. The leakage rate for the R-stator was high, and the catalysed reaction rate for the L-stator was low. Leakage and catalysed reaction rates were found to increase for both the R- and L-stator as the loop length was increased from 12 nt to 14 nt.

### Motor-catalysed Loop block

A second design for a motor-triggered junction is shown in Figure 5.12. In this design a region of unpaired nucleotides is included half-way along the binding domain of the block strand, such that when the block binds to the stator a loop, or bulge, is formed (Figure 5.12 i). The 3' end of the loop block has a short (6 nt) toe-hold. The 3' end of the motor strand is modified to include the sequence complementary to the toe-hold and an adjacent part of the binding domain. When the motor encounters the blocked stator, the two strands interact to open up the loop in the block strand. The open loop in the block can then interact with the complementary release strand in solution, allowing the release to strip the block strand off both the stator and the motor.

Two orthogonal sets of block, release and toe-hold sequences were designed, one each for the R- and L- stators downstream of the junction node. A range of shorter loop lengths were chosen (6, 8, 10, 12 nt) to reduce the high leakage reaction rate observed in the previous design. The release strands were designed

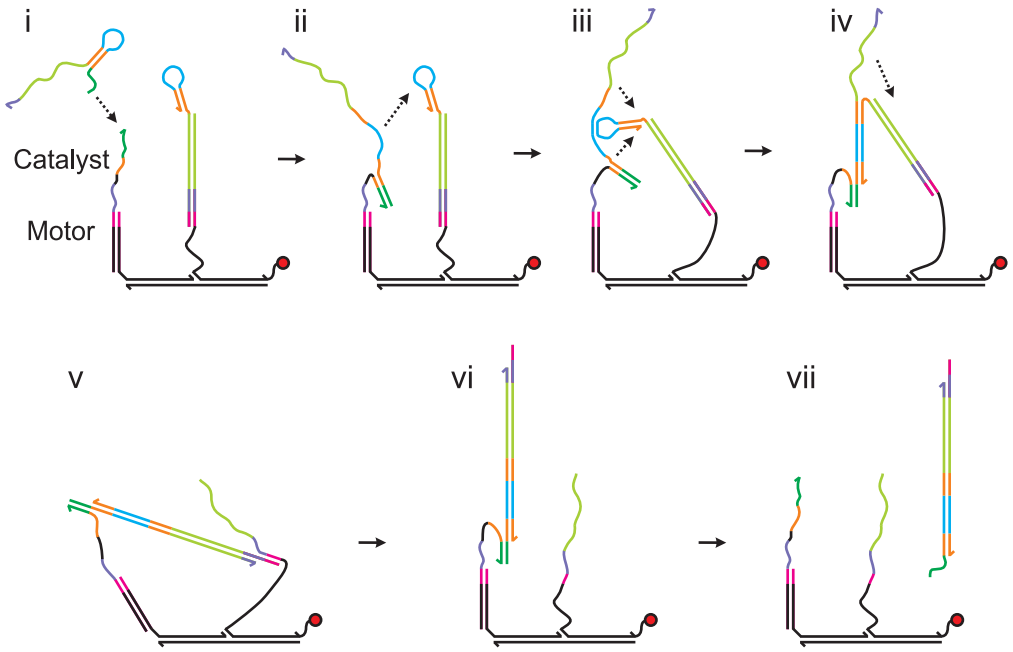


Figure 5.11: Schematic for a motor-catalyzed hairpin block and release design. **i** The hairpin block and release strands interact slowly due to their hairpin secondary structure (blue + orange). **ii** The release hairpin contains a second toe-hold (dark green). The catalyst strand that binds to this toehold and opens up the loop is tethered to the 3' end of the DNA motor sequence. **iii-v** The open release-motor complex interacts with the loop in the block hairpin and opens it. **v-vi** The release strand removes the block from the stator. **vii** Only 6 bp hold the release-block duplex to the motor, and it will eventually dissociate leaving the motor unchanged.

to have minimal secondary structure, to ensure a fast rate for the motor-catalysed unblocking reaction. PAGE analysis of this design (Appendix B.2.1) showed that both the R-and L-motor correctly catalyse the opening of only the R- and L-stator respectively. For loop lengths of 6 or 8 nt, both systems were found to have a relatively small amount of leakage compared to the hairpin design.

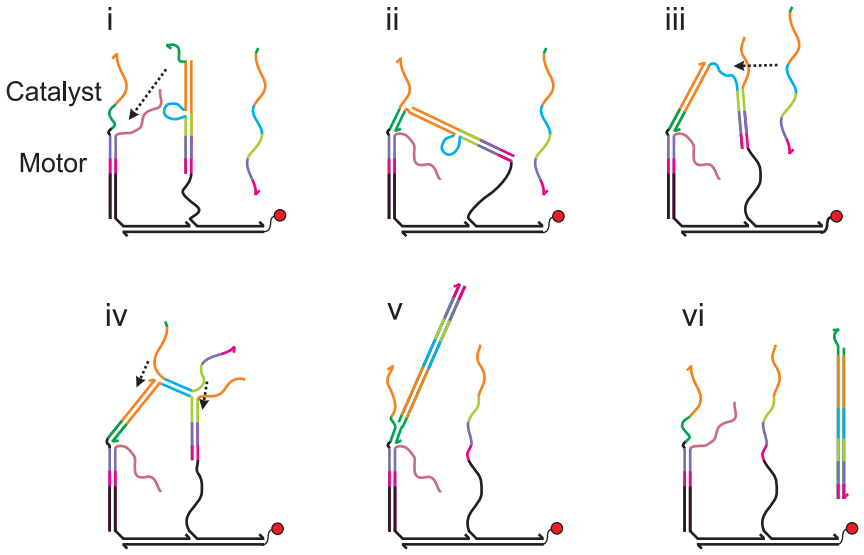


Figure 5.12: Design for a looped stator block that is opened by a motor-catalyst. **i** The block strand contains a loop of unpaired bases (blue) and a short toehold (dark green). The complementary release strand has minimal secondary structure, but contains only part of the toe-hold sequence (0 or 2 nt), and interacts slowly with the block. **ii-iii** The motor carries a sequence complementary to the block toe-hold and half of the binding domain (dark green + orange), which forms a complex with the blocked stator that acts to open up the loop (blue). **iv-v** The release strand interacts with the open loop, and branch migrates to strip the block off both the stator and the motor strand. **vi** The block-release duplex is bound to the motor strand by either 6-nt, for a 'short' release, or 4-nt, for a 'long' release. This will dissociate from the motor strand, leaving it free to interact with subsequent blocked stators.

### 5.3.2 Initial designs - fluorescence results

The hairpin block and release design was tested on a single-junction DNA origami track (Figure 5.13). For these experiments, the catalyst sequence was not tethered to the motor, but was instead added as a freely diffusing strand. Both R and L-release strands were added to the sample before addition of enzyme, along with either an R- or L-catalyst. Unfortunately, an equal amount of motor reaches both ends of the track, independent of the catalyst type added. The traces are similar to those observed previously for open tracks (Figures 5.5 and 5.4). This suggests that the lack of bias is caused by the leakage reaction between the block and release hairpins, possibly because the loops are too long. As the system did not operate as intended with the free catalyst strand in solution, this design was discarded.

Similarly, the loop block design was tested on a single-junction track (Figure 5.14). Based on the PAGE analysis (Appendix B.2.1), an 8 nt loop was chosen, and tested with both the short and the long release strands. The motor strand was modified to include the additional catalyst sequence to unblock either the right or left-hand side of the junction, and is denoted R-motor ($M_R$) or L-motor ($M_L$) accordingly. Either the R- or L-motor is loaded at the start of the track. Both R- and L-release strands are added to samples at the same time as the enzyme. Figure 5.14 B gives the results for long release strands, and Figure 5.14 C the results for short release strands. Unfortunately, in both sets of data the fluorophores $F_{8R}$ and $F_{8L}$ are both quenched, and there is only a very small difference between the behaviour of the two motors, $M_R$ and $M_L$.

#### Repeating blocked stators

To try and improve the bias of the $M_R$ and $M_L$ motors in the previous design, tracks were also assembled with two loop block stators ($S_{5R}$, $S_{6R}$ and $S_{5L}$, $S_{6L}$) downstream of the node along each path. This was expected to decrease the effect

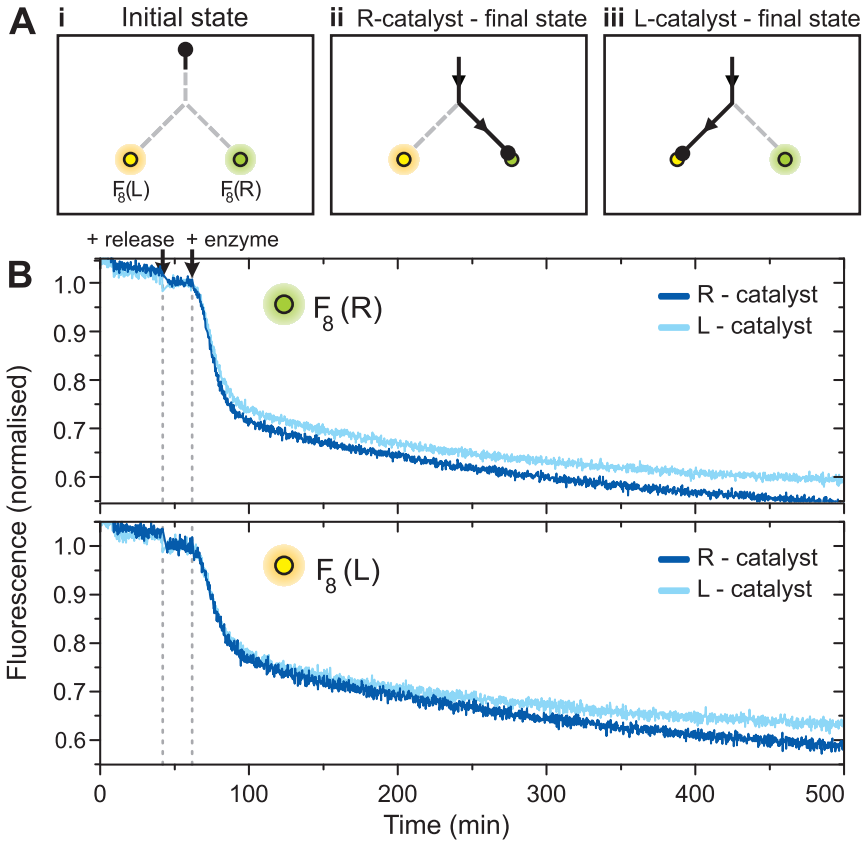


Figure 5.13: Ensemble fluorescence analysis of the hairpin block and release design on a single-junction DNA origami track. **A i** Initial state of the system, and final expected states in the presence of **ii** R-catalyst or **iii** L-catalyst. **B** Fluorescence results at the end of the two tracks. The motor quenches the fluorophores at both locations equally, independent of the catalyst added.

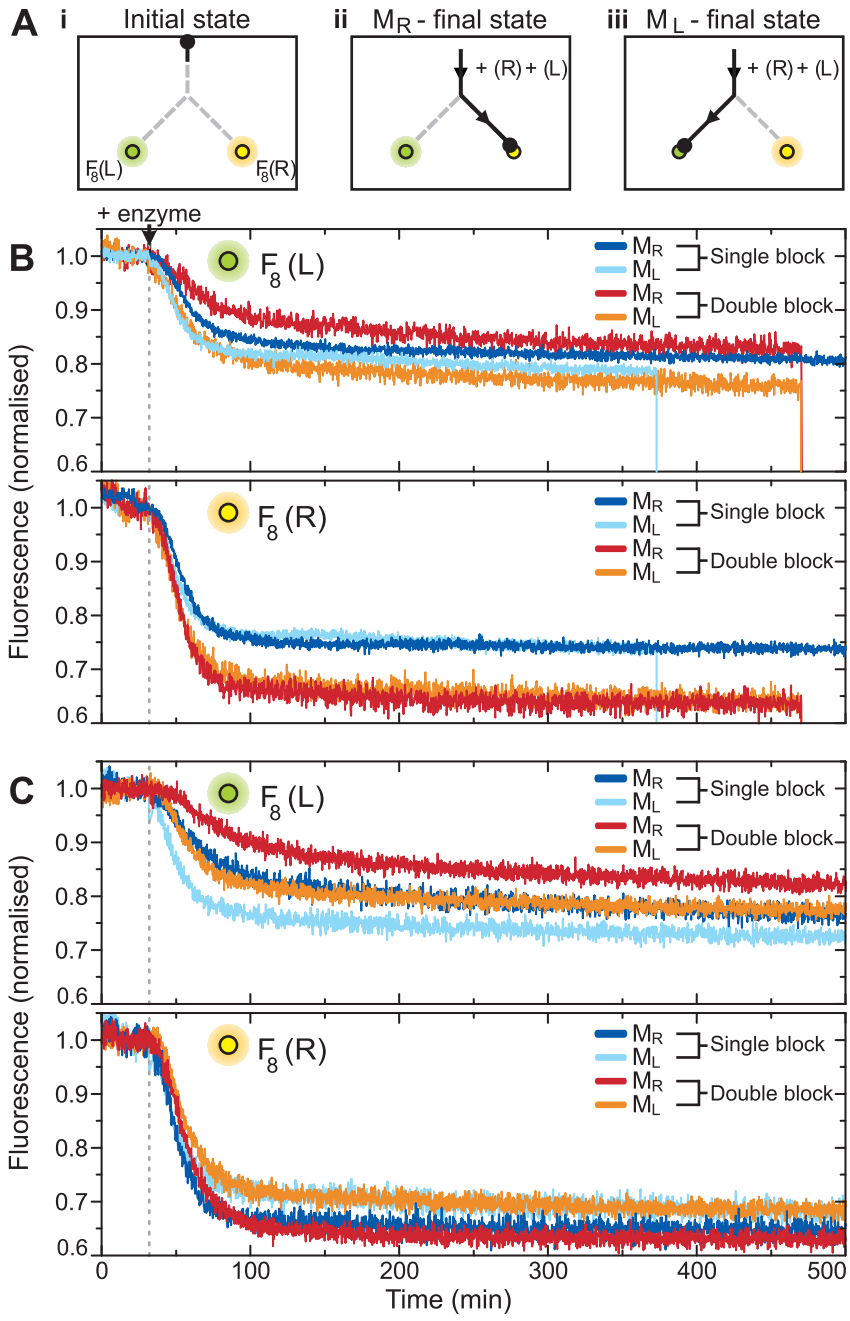


Figure 5.14: Ensemble fluorescence results for the loop-block design on a single-junction DNA origami track. **A i** Initial and final states for **ii** R-motor or **iii** L-motor. Results for tracks with **B** long or **C** short release strands. Tracks have either one or two blocked stators. There is a small difference in the quenching observed for $F_{8R}$ and $F_{8L}$, consistent with a slight bias towards the designed route.

of leakage, as both blocks must be removed before the path is opened. Results for the double-block track with either the long or short release are also shown in Figure 5.14 B and C. Similarly to the single-block track, only a small difference in the behaviour of the R- and L-motors was detected.

## 5.4 Motor-catalysed Loop block with a splice-release

The loop block design in Section 5.3.1 produced a small, but detectable, bias in the direction a DNA motors takes when it reaches a junction in a track. However, this effect was very small compared to that achieved by the addition of an external trigger strand in Section 5.1. The sequence of the release strand was chosen to have minimal secondary structure. A modification of this system is now introduced in which secondary structure is deliberately added to the release strand in order to improve the directional bias.

The improved design is shown in Figure 5.15. The design is similar to that in Figure 5.12, except now the two halves of the release strand are held together in a loop by an additional 'splice' strand. The splice strand binds to one half of the release strand binding domain (8 nt), and either 5, 7 or 8 nt of the other half. It is expected that the different length splices will slow down the leakage reactions by different amounts. The key difference in this scheme is that removal of the blocking strand from the stator proceeds through a 4-arm branch migration rather than a simpler strand displacement reaction. This results in the splice strand being left on the stator, but, as the splice does not overlap with the stator sequence, it should not prevent the motor from stepping forward. The uncatalysed reaction between two loop strands is expected to be of order 100× slower than between a single loop and and a plain ssDNA strand (Turberfield et al., 2003). Thus, the

leakage for designs with the additional splice strand is expected to be lower than for those without.

### 5.4.1 Splice release - PAGE analysis

Results for the loop block design (Section 5.3.2), showed that the short release strands with none of the toe-hold nucleotides were slightly better. For the splice-release design only short release strands were used. Poly-acrylamide gel electrophoresis (PAGE) was used to demonstrate that the splice strand slows down the leakage reaction between block and release strands in the absence of the motor-catalyst (Figure 5.16). Different loop lengths (6, 8, 10 nt) and splice lengths (0, 5, 7, 8 nt) were compared. For all loop lengths, addition of any length splice strand reduced the amount of leakage significantly. Indeed, for the 6 nt loop, with either 5, 7 or 8 nt splice, no leakage was observed for either the R- or L-track.

Following the success of this design in reducing leakage, further tests were made using the 6 nt loop block and release with the motor-catalyst (Figure 5.17). These samples were incubated at 37°C rather than room temperature, to better match conditions in fluorescence experiments. The results show that, for either the 5 or 7 nt splice, there is no leakage for the L-track. However, when motor is added, only a small amount of the track is unblocked. This is the opposite to earlier designs in Section 5.3.1, where leakage and catalysed unblocking were both high. The leakage and catalysed unblocking rates are both higher for the R-track than for the L-track. The effect of this on motor behaviour was uncertain, but the results suggest quite a different balance between the leakage and catalysed reactions than the previous designs, and so were further investigated on single-junction origami tracks.

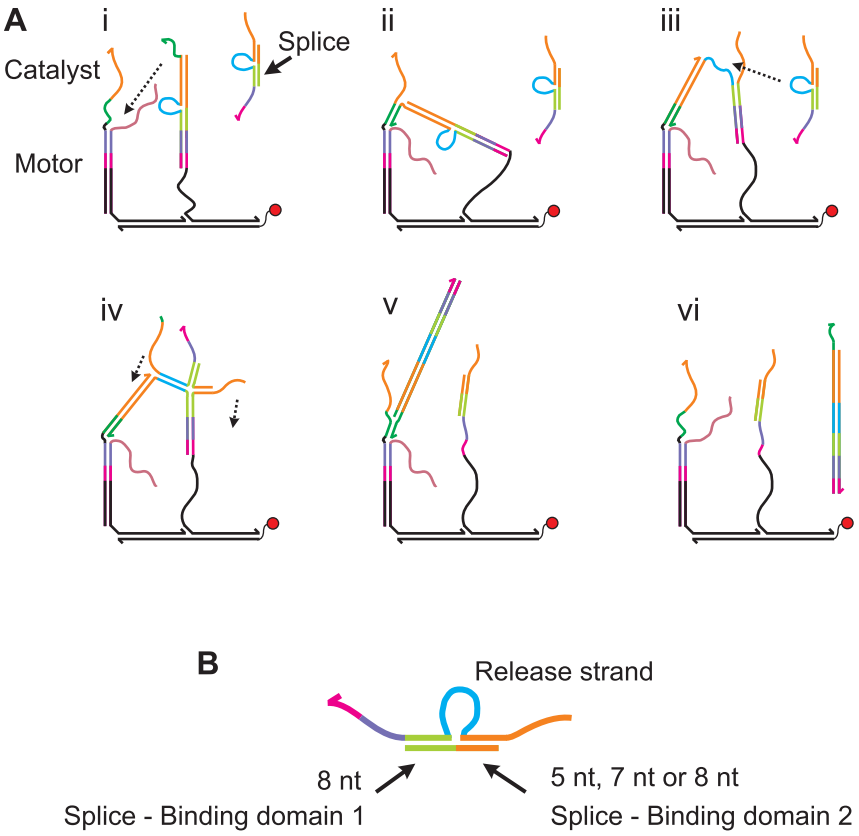


Figure 5.15: Design for a loop stator block with a 'splice' release strand. **A i** The block strand contains a loop of unpaired bases (blue) and a short toehold (dark green). The complementary release strand is held in a loop by a short splice strand (orange + light green). **ii-iii** The motor carries a sequence complementary to the block toe-hold and half of the binding domain (dark green + orange), which forms a complex with the blocked stator that acts to open up the loop (blue). **iv-v** The release strand interacts with the open loop, and a 4-arm branch migration is initiated in which the block is stripped off the stator and replaced with the shorter splice strand. The block is also stripped off the motor strand. **vi** The block-release duplex is bound to the motor strand by 6-nt. This will dissociate, leaving the motor strand unchanged. **B** Details of the splice-release: the two halves of the release strand are held together by a splice strand with an 8 nt binding domain on one side (green) and a variable length binding domain on the other side (orange). Splice strands with a second binding domain or 5, 7 or 8 nt were compared.

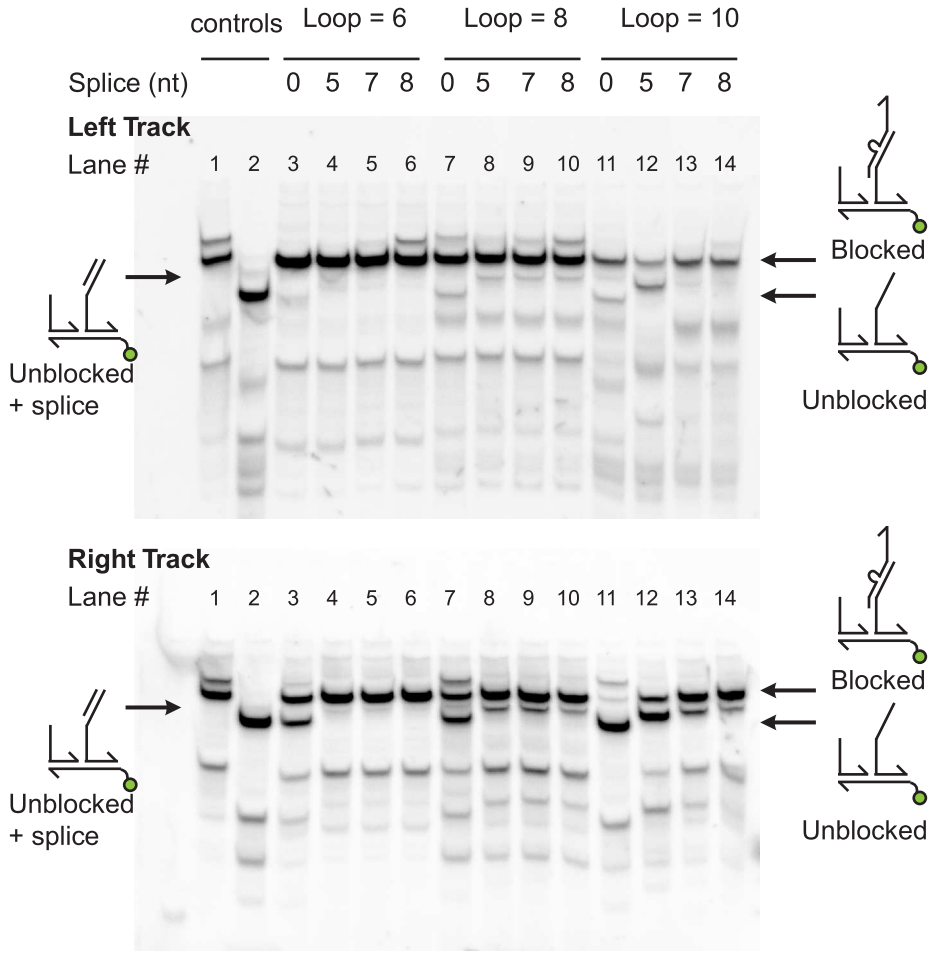


Figure 5.16: PAGE Analysis of the loop block and splice-release, with no motor-catalyst (Figure 5.15). Control lanes are (1) blocked and (2) unblocked tracks. Blocked tracks were incubated with plain release strands (0 nt) or with release strands pre-annealed with 5, 7 or 8-nt splices. Loop lengths are 6 nt (lanes 3-6), 8 nt (lanes 7-10) or 10 nt (lanes 11-14). Incubation times are 30 min at 25°. The addition of a splice strand reduces leakage for all loop lengths, and none at all is detected on on this timescale for the 6-nt loop.

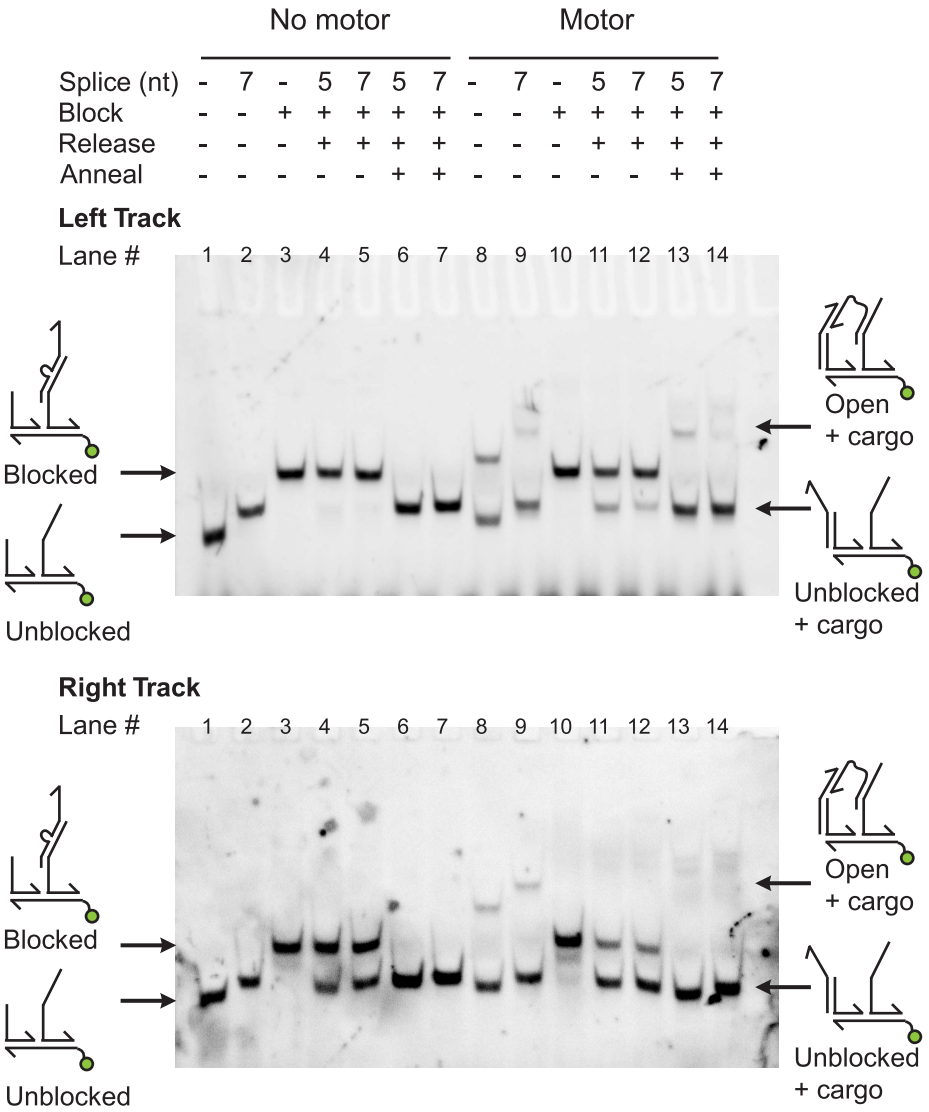


Figure 5.17: PAGE Analysis of the loop block and splice-release, with 6-nt loops (Figure 5.15). Tracks with (lanes 8-14) or without motor-catalyst (lanes 1-7) were compared. Control lanes are: (lanes 1, 8) unblocked, (lanes 2, 9) unblocked + splice, and (lanes 3, 10) blocked tracks. Blocked tracks were either incubated (lanes 4-5, 11-12) or annealed (lanes 6-7, 13-14) with release strands pre-annealed with 5 or 7 nt splices. Incubation is 10 min at 37°. The L-track leakage is very low, but so is motor-catalysed unblocking. Both rates are higher for the R-track, but samples with motor still show more unblocking than those without.

### 5.4.2 Splice release - fluorescence results

Figure 5.18 B shows the ensemble fluorescence results for the loop block and splice-release design, for a 6-nt loop and either a 5 or 7-nt splice strand. Tracks were loaded with either an R- or L-motor; both R- and L-release strands were pre-annealed with an excess of the splice strand and added to samples along with the enzyme. A large bias in the direction of the two motor types was observed; $F_{8R}$ is quenched strongly by R-motor, and $F_{8L}$ by L-motor. The bias achieved is significantly greater than for the plain release in Section 5.3.2 (Figure 5.14), and comparable in size to that of the external trigger junction in Section 5.1 (Figures 5.4 and 5.4).

Interestingly, the 7-nt splice gives slightly better results for $F_{8R}$ and the 5-nt splice for $F_{8L}$. This agrees with the gel analysis (Figure 5.17), which shows that the R-track leakage is faster and may require a longer splice. The two release strands were annealed with different splice lengths, to give the pairs: R+ 5nt-splice and L + 7nt-splice, or R+ 7nt-splice and L + 5nt-splice. The resulting fluorescence traces (Figure 5.18 C) show that the best directional bias is achieved with the R+7nt and L+ 5nt combination.

### 5.4.3 Splice release - repeating blocks

The splice-release design was also tested on tracks with two loop block stators on each downstream path from the node stator (Figure 5.19). If the system is operating as designed, motors should be able to interact with and unblock more than one blocked stator. A similar sized bias was observed for both the single and double-blocked tracks, indicating that this is the case. Additionally, the leakage of motor into the wrong path is smaller on the double-block track, particularly for the $F_{8L}$ signal.

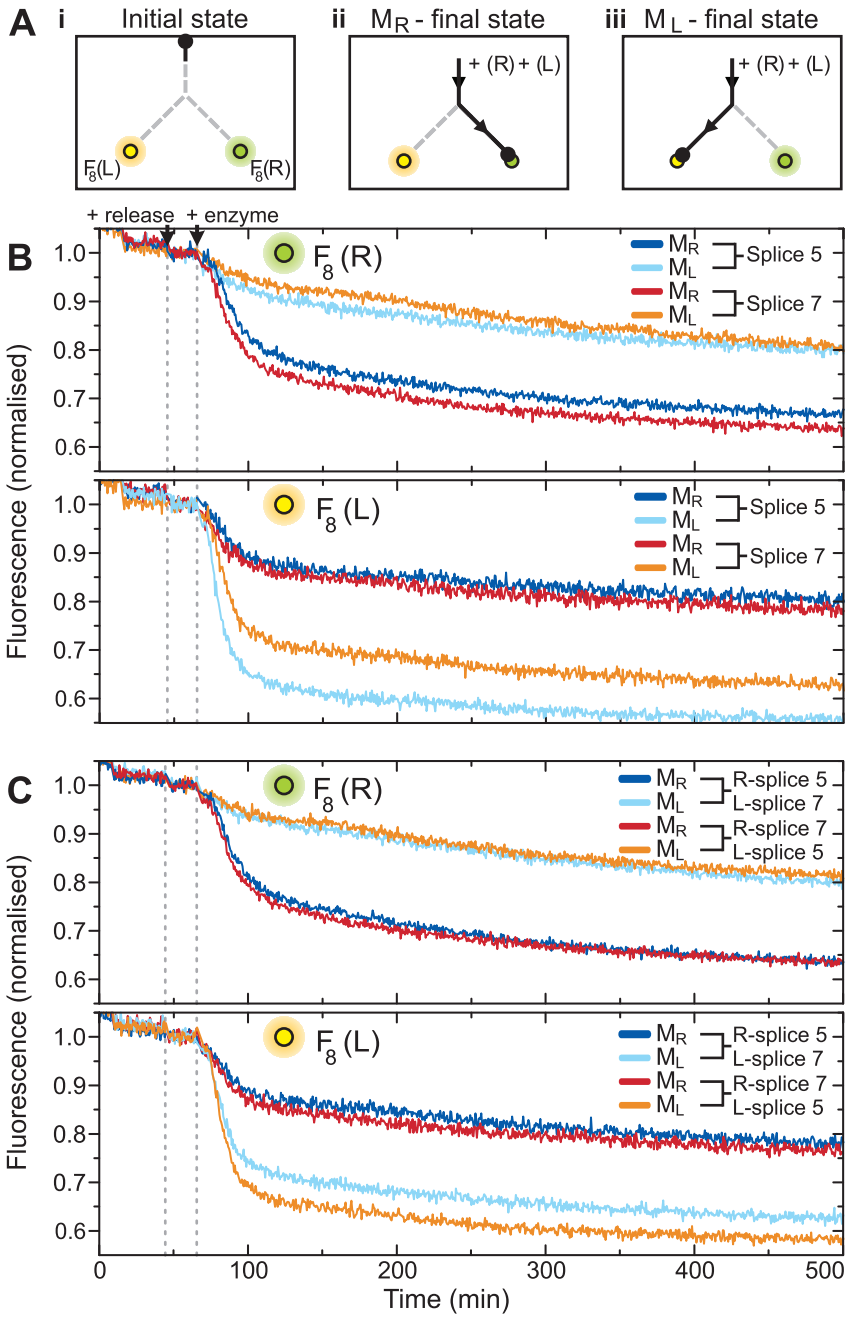


Figure 5.18: Ensemble fluorescence results for loop block and splice-release design. **A** **i** Initial and expected final states for **ii** R-motor or **iii** L-motor. Fluorescence results: **B** release strands with the same splice, and **C** release strands with different splice lengths. In all traces a strong directional bias is observed.

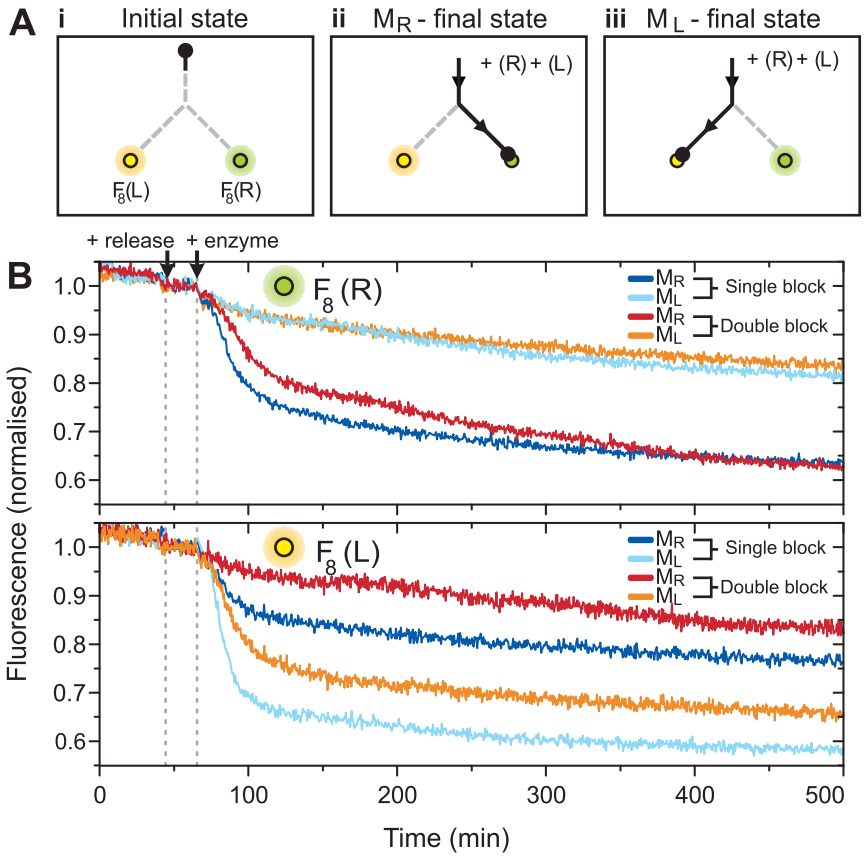


Figure 5.19: Ensemble fluorescence results for the loop block and splice-release on single and double-block stator tracks. **A i** Initial state of the system, and final expected states for **ii** R-motor or **iii** L-motor. **B** Fluorescence results for release strands R-splice 7 and L-splice 5, for tracks with either one or two loop block stators on each track downstream of the node. The directional bias is the same, but the absolute amount of motor leakage into the wrong state is reduced for the double-block tracks.

The final results in this chapter show the complete motor-catalysed unblocking system, by comparing an R-motor, L-motor and Plain-motor (Figure 5.20). Based on the results in Sections 5.4.1 and 5.4.2, the loop length was chosen as 6 nt, and a 5 nt splice was used with the R-release and a 7 nt splice with the L-release. These results demonstrate that the path a motor takes through a junction can be successfully encoded by instructions in the motor sequence. The discrimination achieved is similar in size to the addition of external instructions, in Section 5.1.1. If no relevant instructions are given, the motor splits evenly between the paths. The motor is unaltered by its interaction with the junction, and thus the system may be extended to many junctions by adding sequential instructions to the 3' end of the motor sequence. Practical limits on this would be the design of additional orthogonal catalyst and binding domains, and the length of the motor-catalyst strand.

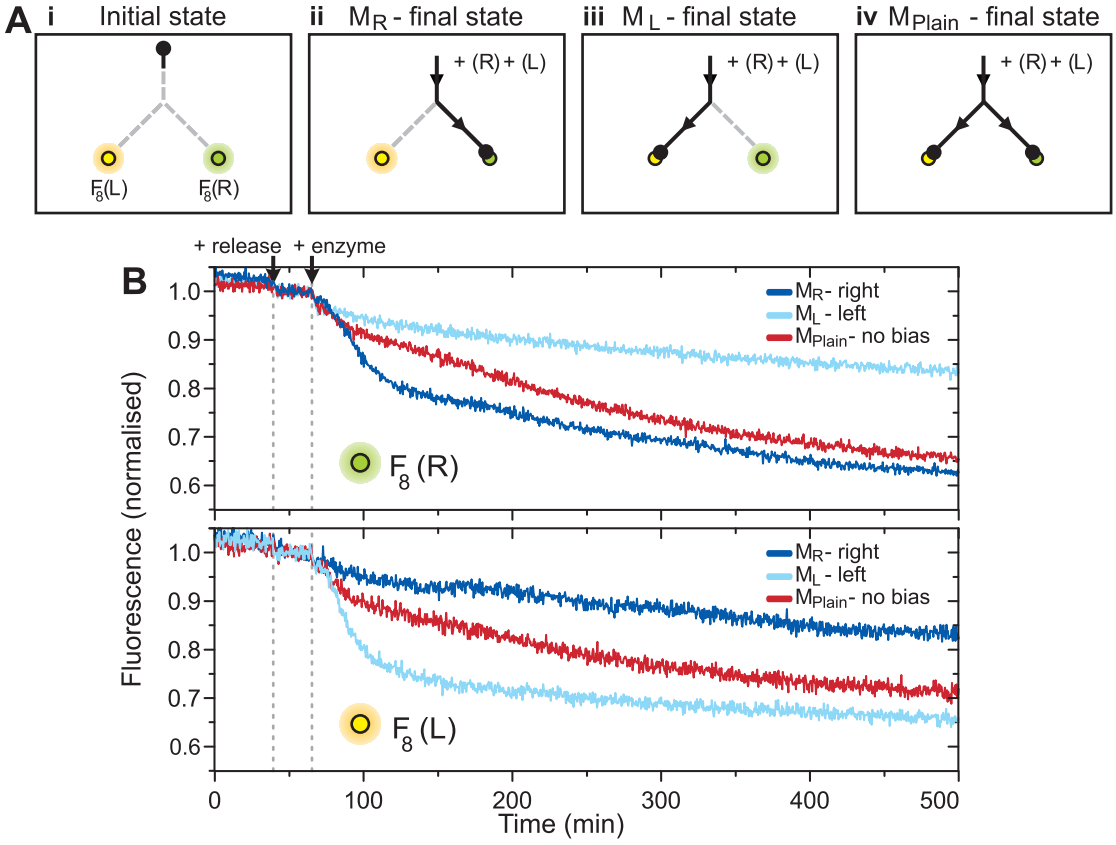


Figure 5.20: Ensemble fluorescence results for motors programmed to take particular paths through a junction. **A i** Initial state of the system, and final expected states for **ii** an R-motor programmed to take the right-hand path, **iii** an L-motor programmed to take the left-hand path, and **iiv** a Plain-motor programmed to split evenly down both paths. **B** Fluorescence results, all samples are treated with the same release strands, and differ only in an instruction sequence added to the 3' end of the motor sequence. The instruction determines the final destination of the motor, with very little leakage into the wrong path. The system is acting to 'read' the instruction sequence and sort the motors accordingly.

## 5.5 Conclusions

In this Chapter a 'burnt-bridges' DNA motor that can be controllably transported through a network of bifurcating DNA origami tracks is demonstrated. The path a motor takes through single- and triple-junction tracks can be controlled by adding external instruction sequences. For a single-junction track it was also shown that instructions can be carried by the motor sequence itself, and that motors can autonomously chose the correct path to travel down. It was found that designs were very sensitive to loop and strand lengths, and also to the particular DNA sequences. For example, the L-track was always less 'leaky' than the R-track, even though they were designed to have the same secondary structures and interaction strengths. The results in Section 5.4 show that other parameters, such as the number of block stators or the splice length, can be carefully tuned to reduce these effects.

Table 5.1 gives a summary of the directional bias values achieved for the range of single-junction designs tested. To quantify the bias observed in quenching of the two motor paths, the difference in the normalised $F_{8R}$ and $F_{8L}$ intensities was calculated a set time (2.5 hrs) after the addition of enzyme, and compared for each instruction given. The intensities were averaged over 10 minutes, and the differences given in Table 5.1. In an ideal case the bias after either an R-instruction ($I_R$) or an L-instruction ($I_R$) would be -1 or 1 respectively, and for a completely unbiased junction it would be 0. The difference between the two bias values ( $I_L$ - $I_R$) gives a measure of how good design is, and has a range of 0-2. The final loop block and splice-release design results in similar bias values (0.34-0.39) to those for the external trigger design in Section 5.1.1 (0.39-0.43).

Such control of a synthetic motor at the nanoscale is unprecedented, and this work represents a significant advance in creating programmable molecular robots, that respond to internal and external instructions to govern the route through

| Sample | $I_R$ | $I_L$ | $I_L$ - $I_R$ | $I_{plain}$ | Data |
|---|---|---|---|---|---|
| External trigger | | | | | |
| Single-junction (Cy5/Cy3.5) | -0.18 | 0.25 | 0.43 | -0.01 | Fig 5.5 |
| Single-junction (Cy3.5/Cy5) | -0.14 | 0.25 | 0.39 | 0.03 | Fig 5.4 |
| Triple-junction (RHS only) | -0.14 | 0.31 | 0.45 | | Fig 5.8 |
| Hairpin block and release | | | | | |
| R- or L-catalyst | -0.05 | -0.04 | 0.01 | | Fig 5.14 |
| Loop block and long release | | | | | |
| single block | -0.08 | -0.05 | 0.03 | | Fig 5.20 |
| double block | -0.21 | -0.12 | 0.09 | | Fig 5.20 |
| Loop block and short release | | | | | |
| single block | -0.15 | -0.04 | 0.11 | | Fig 5.20 |
| double block | -0.22 | -0.1 | 0.12 | | Fig 5.20 |
| Loop block and splice-release | | | | | |
| R-splice5 + L-splice5 | -0.12 | 0.27 | 0.39 | | Fig 5.25 |
| R-splice7 + L-splice7 | -0.13 | 0.21 | 0.34 | | Fig 5.25 |
| R-splice5 + L-splice7 | -0.13 | 0.2 | 0.33 | | Fig 5.25 |
| R-splice7 + L-splice5 | -0.12 | 0.26 | 0.38 | | Fig 5.25 |
| Double Loop block and splice-release | | | | | |
| R-splice7 + L-splice5 | -0.18 | 0.19 | 0.37 | -0.01 | Fig 5.27 |

Table 5.1: Summary of directional bias achieved in single-junction DNA origami tracks. $I_R = F_{8R}$ - $F_{8L}$ after addition of an R-instruction, and $I_L = F_{8R}$ - $F_{8L}$ after addition of an L-instruction. The values are calculated from fluorescence intensities 2.5 hrs after the addition of enzyme, average over 10 minutes. If $F_{8R} - F_{8L} \sim 0$ there is no bias between the two paths. If $F_{8R} - F_{8L} < 0$ there is a bias to the right-hand path, and if $F_{8R} - F_{8L} > 0$ there is a bias to the left-hand path. For a good design, adding an R-instruction ($I_R$) should bias the motor strongly to right, and an L-instruction ($I_L$) to left. The quantity $I_L$ - $I_R$ is a measure of how good the junctions design is. $I_{Plain}$ is the bias measured when either no instruction is added, or both R- and L- instructions are added

their environment. The autonomous motor system 'reads' and sorts different DNA sequences down different paths of a track. The system is sensitive to small sequence changes and could be modified to produce a system that sorts many similar DNA strands. For example, DNA from closely related bacterial species in solution could be identified and sorted along a bifurcating path that represents the phylogenetic tree of the species.

Finally, all the systems developed in this Chapter may be extended in track complexity. The final designs are robust, and because the motor encounters them sequentially, junction sequences can be re-used. The tracks could be directly linked to molecular assembly lines to produce a molecular output (Gu et al., 2010; He and Liu, 2010). The discrete nature of the DNA origami tiles also provides a method for building more complex track designs with a modular architecture. DNA origami tiles can be linked together in chains and larger aggregates by base-pair specific linkages (Rothemund, 2006; Endo, Sugita, Katsuda, Hidaka and Sugiyama, 2010; Douglas, Dietz, Liedl, Högberg, Graf and Shih, 2009). By adding different linking strands, the same set of basic tiles could re-programmed, even interactively, to achieve different motor functions and outputs.

Chapter 6

# $F_1$-ATPase DNA origami tiles

One of the most immediate applications of DNA nanostructures is in immobilising and manipulating complex biomolecules for biophysical studies. With DNA origami it is possible to engineer attachment site geometry with nanometre precision, and a range of attachment techniques are readily available for binding both proteins and nanoparticles. The resulting structures are compatible with the aqueous environment required by biological systems, and with a wide range of buffer and salt conditions, which can then be tailored to suit the target system. While a number of simple protein and RNA detection assays based on DNA origami have been developed (Ke et al., 2008; Sharma et al., 2007), perhaps the most exciting application of these ideas is in the study of active proteins, either bound to or interacting with the DNA tiles. For example, recent work has used the origami tiles as a scaffold for testing the effect of varying DNA tension on the activity of a site specific DNA methylation enzyme (Endo, Katsuda, Hidaka and Sugiyama, 2010*a*).

As discussed in detail in Chapter 1, $F_1$-ATPase is an extremely important and sophisticated rotary protein motor. In this Chapter a method for attaching $F_1$ protein to a DNA origami tile is presented. The successful incorporation of

actively rotating $F_1$ into a composite DNA-protein nanostructure has potential to reveal new information about the protein. It also provides a method for harnessing this extremely fast and efficient rotary motor for use as an active component in functional nanostructures. For example, the motor could be coupled to an artificial flagellum and used as part of a propulsion system.

## 6.1 DNA tile design for $F_1$-ATPase binding

In order to facilitate binding of the $F_1$-ATPase motor to a DNA origami tile, an attachment site was designed with three modified staple strands in a 6 nm triangle (Figure 6.1). Mid-way along the length of each modified staple is a tris-NTA. This is a chemical modification, consisting of three nitrilotriacetic acid groups, that chelates $Ni^{2+}$ ions in solution, which then form a coordination complex with histidine residues on a protein. Two types of $F_1$ protein are used in this chapter. The first, from *E. coli*, has 3 10-histidine ($His_{10}$) tags at the base of the $\beta$ subunits, and a biotin on the central $\gamma$ subunit. The second, from yeast, has 6 $His_{10}$ tags, one on each of the $\alpha$ and $\beta$ subunits, and a biotin on the $\gamma$ subunit. Initial designs were made for the *E. coli* $F_1$, and the triangular geometry of the attachment site matches the spacing of the His-tags on this protein (4.7 - 4.9 nm) (Bowler et al., 2007). A lack of active *E. coli* protein led to the use of yeast (*S. cerevisiae*) $F_1$ in later experiments, with the same DNA origami design.

To observe rotation of the $F_1$ motor, it must be firmly attached to a surface. Under the buffer conditions required by $F_1$ (10 mM MOPS, 50 mM KCl, 2 mM $MgCl_2$, pH 7), DNA tiles were previously shown to stick non-specifically to glass coverslips (Figure 2.9). An alternative design was also considered, in which tiles with biotin-modified staple strands are attached more permanently to streptavidin-coated glass (Figure 6.1 B). In this design, the biotinylated nicks are on the opposite

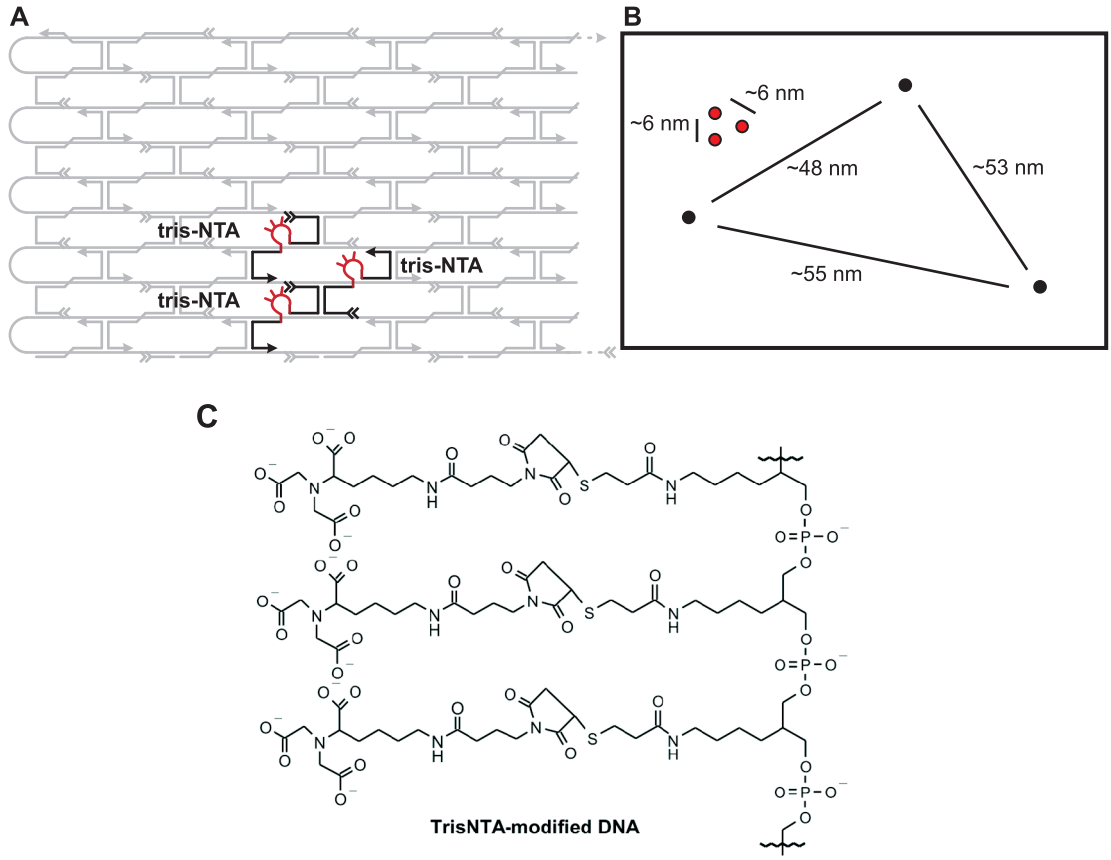


Figure 6.1: Schematic of a DNA origami tile designed to bind $F_1$-ATPase. **A** Staple diagram for the top left-hand corner of the tile, showing the three tris-NTA modified staples. The spacing of modified staples matches the ∼5 nm spacing of his-tags on the *E. coli* $F_1$ $\beta$-subunits. **B** Placement of the modified tris-NTA strands (red) and biotin modified staples (black). The phase of the DNA helix is such that biotin modified staples face down (into the page) and tris-NTA staples face up (out of the page), allowing tiles to act as an interface between the $F_1$ protein and streptavidin-coated glass. **C** Structure of NTA modified DNA. DNA staples internally modified with three amines are converted into tris-NTA modified DNA following published protocols (Goodman et al., 2009). Image from (Erben, 2007).

face of the tile to that of the tris-NTA modifications. Previous results, in Chapter 2 (Figure 2.10), show streptavidin binding to the biotin modified staples under AFM.

## 6.2 His-GFP on tris-NTA DNA Origami

Amine staple strands were modified with tris-NTA following published protocols (Figure 6.1 C) (Goodman et al., 2009), a detailed protocol is given in Appendix A.10. The successful modification was observed by a gel shift in a denaturing polyacrylamide gel (Figure 6.2 A). The tris-NTA strands were then tested for binding with a small and easily detected protein, a his-tagged version of green fluorescent protein (GFP). In gels the GFP was shifted, but failed to co-migrate with the modified DNA (Figure 6.2 B). This suggests that binding does occur, but that the DNA-GFP complex is not stable in the gel buffer with applied voltage, and dissociates as the sample is run into the gel. This was the case for a number of buffer conditions (TAE, TBE, tris-tricine).

### 6.2.1 Size Exclusion HPLC

Previous work used HPLC with a pre-packed size-exclusion column to test binding (Goodman et al., 2009). A similar method is used here to test the binding of his-GFP to DNA origami tiles incorporating the modified tris-NTA staples (Appendices A.6 and A.10.2). Samples were monitored for DNA absorption (260 nm) and GFP fluorescence (ex395/em512 nm). The size-exclusion column used is expected to give good separation of globular proteins with $M_W$ 5-5000 kDa, and has an exclusion limit of 40,000 kDa. This is the upper $M_W$ limit above which no separation is possible, and everything above this limit will elute in the void fraction.

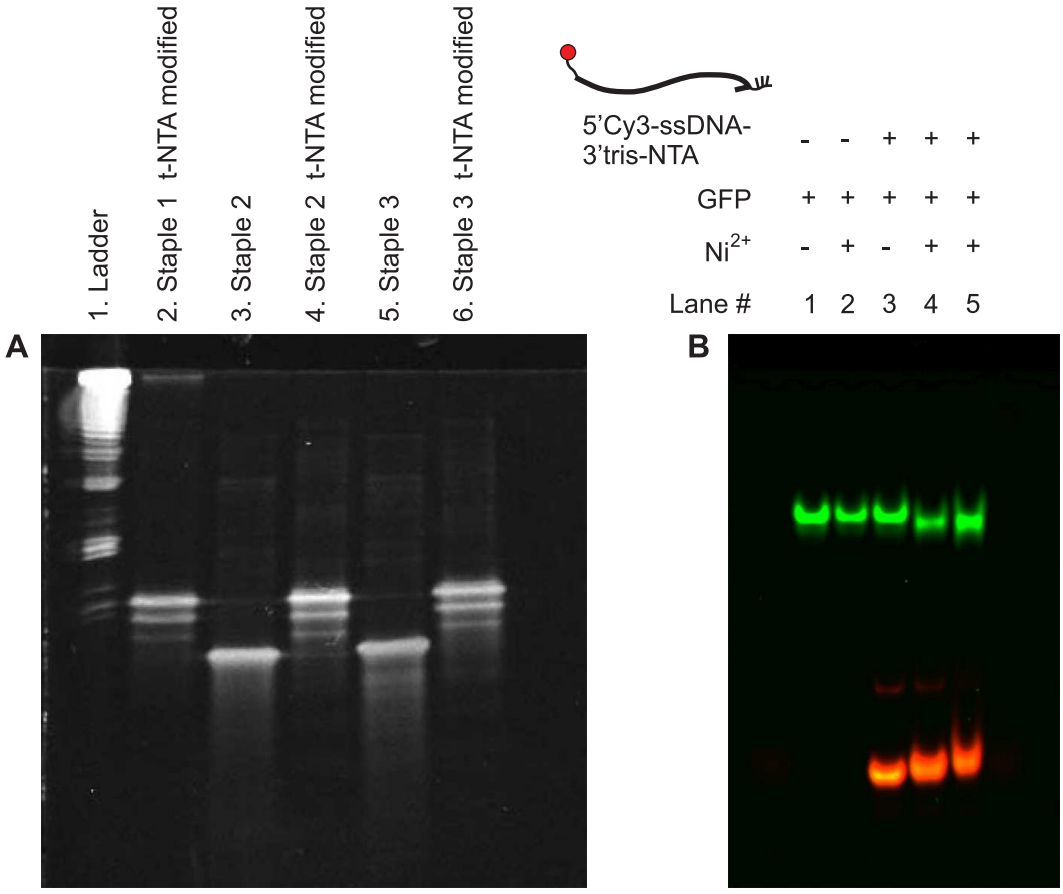


Figure 6.2: Polyacrylamide gels of tris-NTA modified ssDNA staples. **A** Denaturing gel of the initial amine (lanes 3, 5) and final NTA-modified (lanes 2, 4, 6) staple strands. The three bands for modified samples correspond to 1,2 and 3 NTA attachments. The top tris-NTA band was gel purified for use in later experiments. **B** Binding assay for a Cy3 labelled tris-NTA ssDNA strand and His-tagged GFP in a non-denaturing gel with tris-tricine buffer. Samples of His-GFP are incubated with the tris-NTA ssDNA with (lanes 4-5) and without (lane 3) $Ni^{2+}$. Red bands are the Cy3 label on the tris-NTA ssDNA (550/580 nm), green bands are GFP (395/512 nm). There is a slight shift in samples with $Ni^{2+}$ as expected, but the tris-NTA ssDNA and his-GFP do not co-migrate as a stable complex under these gel conditions.

A typical trace is shown in Figure 6.3: small molecules such as staple strands or protein fragments are delayed by the column and larger molecules and complexes elute earlier. Although the origami tiles have a $M_W$ (∼4000 kDa) below the exclusion limit, they have a much larger cross-sectional area than an equivalent weight globular protein, and elute in the void fraction (Figure 6.3 A, $t \sim 15min$). Staple strands (∼10 kDa) elute later (Figure 6.3 A, $t \sim 35min$), as does plain GFP (27 kDa, Figure 6.3 B, $t \sim 40min$). DNA tiles, with or without the tris-NTA modified staples, were incubated with $Ni^{2+}$ and his-GFP. A strong fluorescent peak coinciding with the DNA origami peak at 260 nm is observed only for the NTA tiles (+NTA). There is very little non-specific interaction of the protein with the plain (-NTA) tiles, or background fluorescence of the tiles. For the +NTA origami sample, two intermediate GFP binding peaks are also observed (Figure 6.3 B, $t \sim$ 28 and 34 min). The origami samples were synthesised with a 3× staple excess and were not purified prior to incubation with excess GFP; these peaks represent GFP binding to the excess tris-NTA staple strands.

To further examine binding of his-GFP to the DNA origami, tiles with either 1, 2 or 3 of the modified staple strands were compared (Figure 6.4). Fluorescence traces were normalised to the amount of DNA origami injected onto the column, as calculated by the area of the origami absorption peak ($t \sim 15min$). The amount of fluorescence in the origami peak increases with the number of NTA staple strands in the tile. These results confirm the modified staple strands are correctly incorporated into the tile, and that each tris-NTA attachment site is active and able to bind protein independently. The amount of binding is expected to increase linearly with the number of tris-NTA staples, and the slight increase in gradient in Figure 6.4 is not thought to be significant outside experimental errors. Fluorescence microscopy could be used to quantify the exact number of GFP molecules per tile, by analysis of step-wise photobleaching curves.

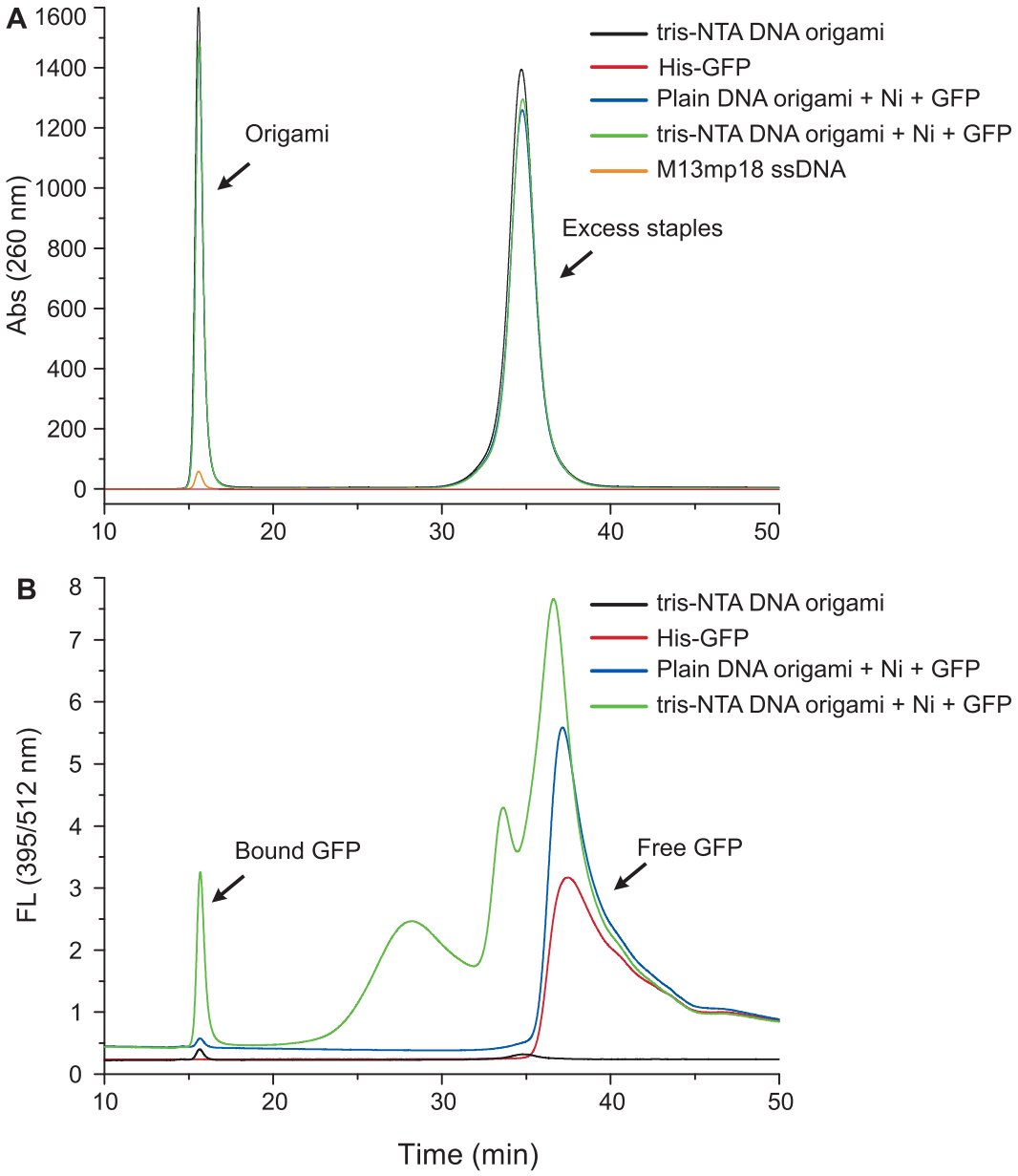


Figure 6.3: Size exclusion HPLC analysis of His-GFP binding to NTA-DNA origami tiles. **A** DNA is identified by absorption (260 nm), **B** protein is identified by fluorescence (ex395/em512 nm). DNA origami elute in the void fraction of the column, while excess staples or free GFP are delayed. Fluorescence is seen in the DNA origami peak only for tiles with the NTA staple strands, indicating specific binding.

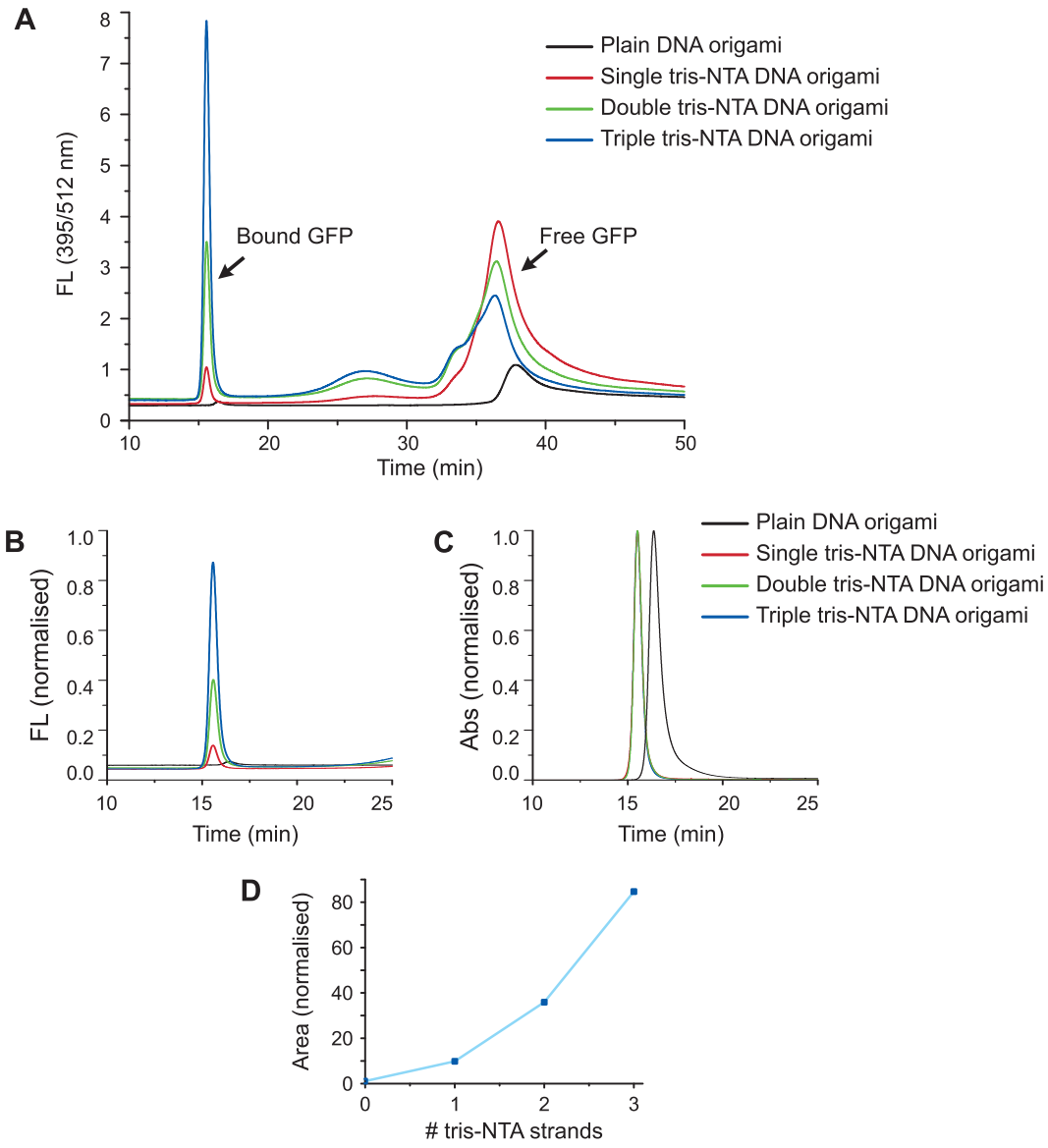


Figure 6.4: Size exclusion HPLC analysis of His-GFP binding to origami tiles with 1,2 or 3 tris-NTA modified staples. **A** The size of the fluorescence origami peak increases with the number of NTA staple strands on the tile. **B, C** Fluorescence peaks are normalised by the amount of DNA added to the column. **D** The amount of GFP binding is determined by the area of the fluorescence origami peak, normalised by the area of the DNA absorption peak. The amount of binding is proportional to the number of NTA strands on the tile.

## 6.3 His-$F_1$-ATPase on tris-NTA DNA Origami

### 6.3.1 Size Exclusion HPLC

In the previous section, the binding of His-GFP to NTA-DNA tiles was demonstrated by size-exclusion HPLC. A similar analysis is now shown for the $F_1$ protein motor, experimental details are given in Appendix A.10.2. The protein used, from *E. coli*, has 3 his-tags on the $\beta$ subunits and a biotin on the central $\gamma$ subunit. Fluorescent streptavidin (Alexa 532), binds to the biotin on the $\gamma$ subunit, and is used to detect the $F_1$ under HPLC. The origami tiles were transfered to a buffer compatible with $F_1$ (10 mM MOPS, pH 7, 50 mM KCl, 2mM $MgCl_2$), and incubated with $F_1$, a stoichiometric amount of $Ni^{2+}$, and an excess of SA-Alexa532. Figure 6.5 shows the results for two different tile to $F_1$ ratios, run on the size-exclusion column with the $F_1$ buffer. The exact protein concentration was unknown, and ratios were estimated. The $F_1$ protein ($M_W$ 380 kDa) is delayed by the column as expected (t$\sim$30 min). The smaller SA protein ($M_W$ 53 kDa) is delayed even more (t$\sim$45 min).

There is very little non-specific interaction of the fluorescent streptavidin with the tiles, and none of the control samples showed a strong peak in the void fraction, where the DNA origami are expected to elute (Figure 6.5 A). Thus, any fluorescence observed in the origami peak is attributed to $F_1$ protein binding to the tiles. The fluorescence peak in the void fraction is larger for DNA tiles with the modified staples (+NTA) than those without (-NTA) (Figure 6.5 B), confirming specific binding of the protein to the tiles. The normalised fluorescence peak area for the +NTA sample is 2.4$\times$ greater than for the -NTA sample. However, there also appears to be a large amount of non-specific binding. Both specific and non-specific peaks increase if more $F_1$ is added. The ratio of the fluorescence peak areas remains approximately the same, 1.9$\times$ greater for the +NTA sample. For

the sample with more $F_1$, the size of the free $F_1$ peak increases slightly relative to the bound peak, suggesting the actual stoichiometric ratio is somewhere between the two ratios tested (Figure 6.5 C).

Although these results provide strong evidence for specific binding, the high amount of non-specific binding was unexpected. Because it elutes in the void fraction of the column, the origami is not separated from larger complexes. Thus, it is possible that some of this peak is due to aggregated $F_1$. To confirm specific binding, and to further probe the samples, a fraction of the origami peak was collected from the column (Figure 6.6) and analysed by AFM.

### 6.3.2 AFM analysis

The tris-NTA $His_6$ bond has been measured to have an equilibrium dissociation constant ($K_d$) of order 10 nM, and an off-rate ($k_d$) of order $10^{-3}$ $s^{-1}$ (Lata et al., 2005; Goodman et al., 2009). The dissociation of an $F_1$ protein bound by three such tris-NTA-His links is expected to be even slower, especially if binding of the three sites is cooperative (Kramer and Karpen, 1998). It was thought that this may be slow enough to permit the further analysis of fractions purified by HPLC. Samples were taken directly from the HPLC and observed by AFM. Due to the the inherent difficulties of imaging protein samples under buffer by AFM, images were typically not obtained until $\sim$ 4-5 hrs after purification. Nevertheless, AFM images show binding of $F_1$ protein to the tiles for the +NTA sample (Figure 6.7). A raised area, similar in size to $F_1$, is observed in the top left-hand corner of $\sim$28% of tiles (N = 125). This is exactly the position on the tile of the attachment site (Figure 6.1). No tiles were observed with $F_1$ at any other location.

The purified -NTA control was also imaged by AFM after a similar time delay (Figure 6.8), and no $F_1$ binding to tiles at any position was observed. This suggests that non-specific binding of $F_1$ to the tiles has a faster off-rate than specific binding,

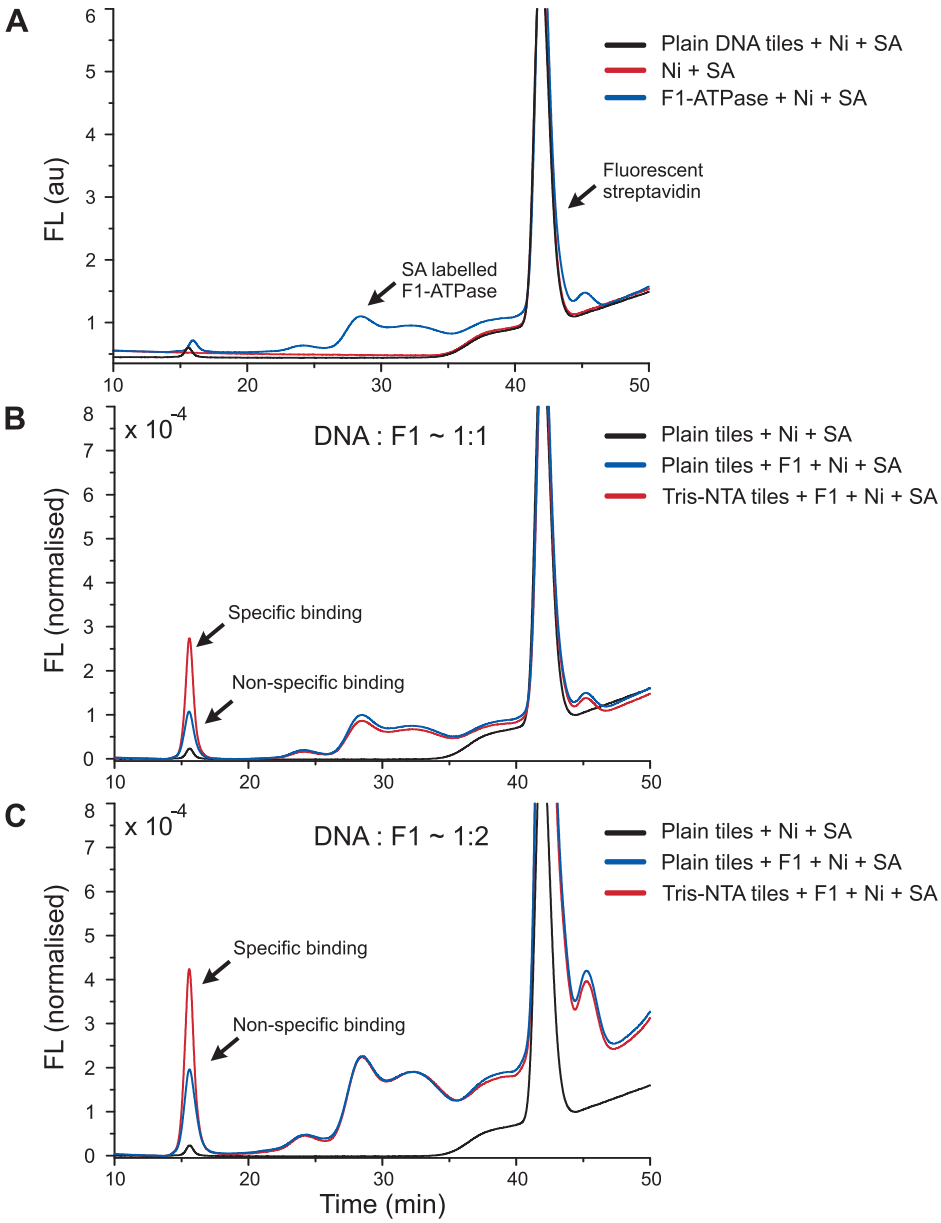


Figure 6.5: Size exclusion HPLC analysis of His-$F_1$-ATPase binding to NTA-DNA origami tiles. $F_1$ is identified by fluorescent streptavidin bound to a biotin on the $\gamma$ subunit (ex532/em554 nm). DNA origami elute in the void fraction of the column ($t \sim 15min$). **A** Control samples are delayed. **B, C** His-$F_1$ binding for two estimated protein to DNA ratios. Fluorescence in the DNA origami peak increases for tiles with the NTA staple strands. Non-specific binding is also high.

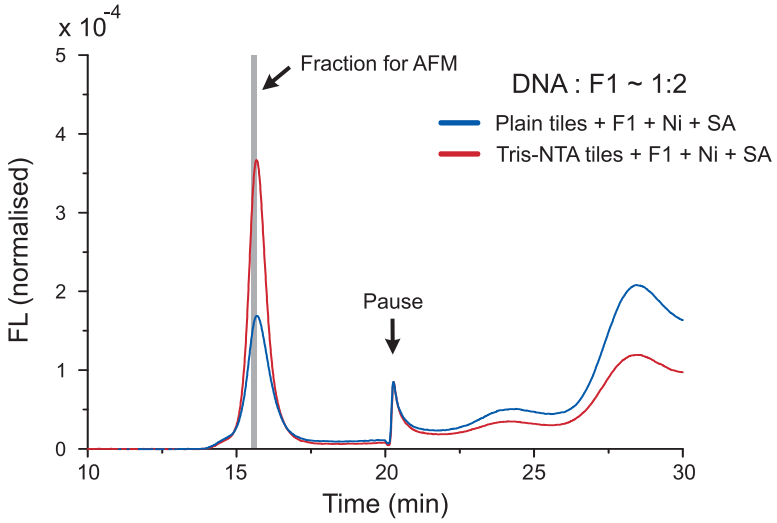


Figure 6.6: Size exclusion HPLC analysis of His-$F_1$-ATPase binding to NTA-DNA origami tiles. The fractions at the marked time were collected for AFM analysis. The HPLC runs were paused at $t \sim 20min$ to remove the collected fractions and then resumed.

somewhere between the 15 minute time frame for HPLC analysis and the 4 hours required for AFM. Free $F_1$ protein was not observed in the AFM sample, but may have been removed by the wash steps required for AFM sample preparation.

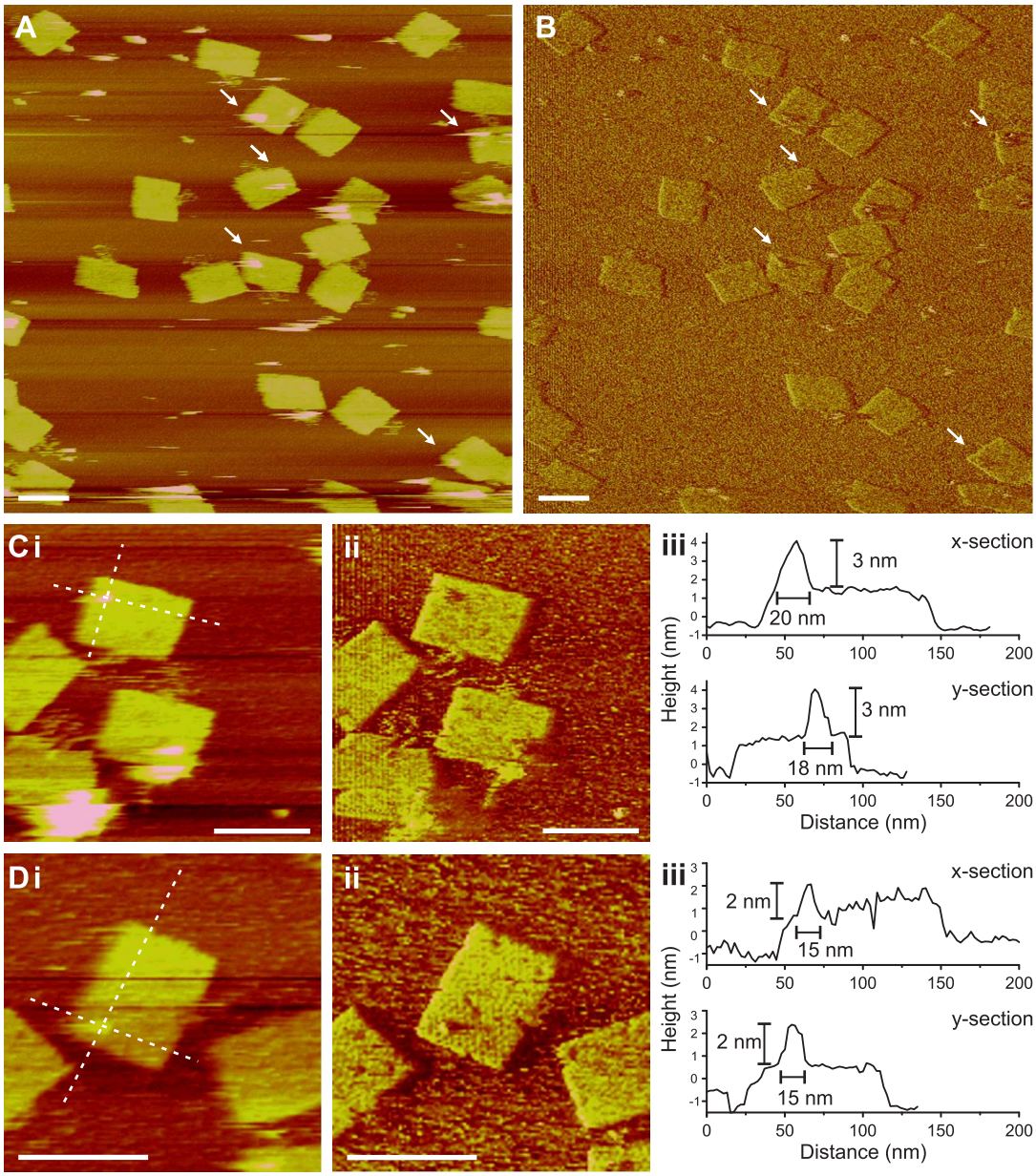


Figure 6.7: AFM images of $F_1$-ATPase bound to NTA DNA tiles. Samples were purified by size exclusion HPLC. **A, Ci, Di** Height images and **B, Cii, Dii** phase images show the protein as a bright spot (arrows), $\sim$ 28% (N=125) of tiles have such a spot, all of which coincide with the designed location of the tris-NTA modified staple strands. **Ciii, Diii** Height profiles along the lines indicated in (i), with dimensions as marked. All scale bars 100 nm.

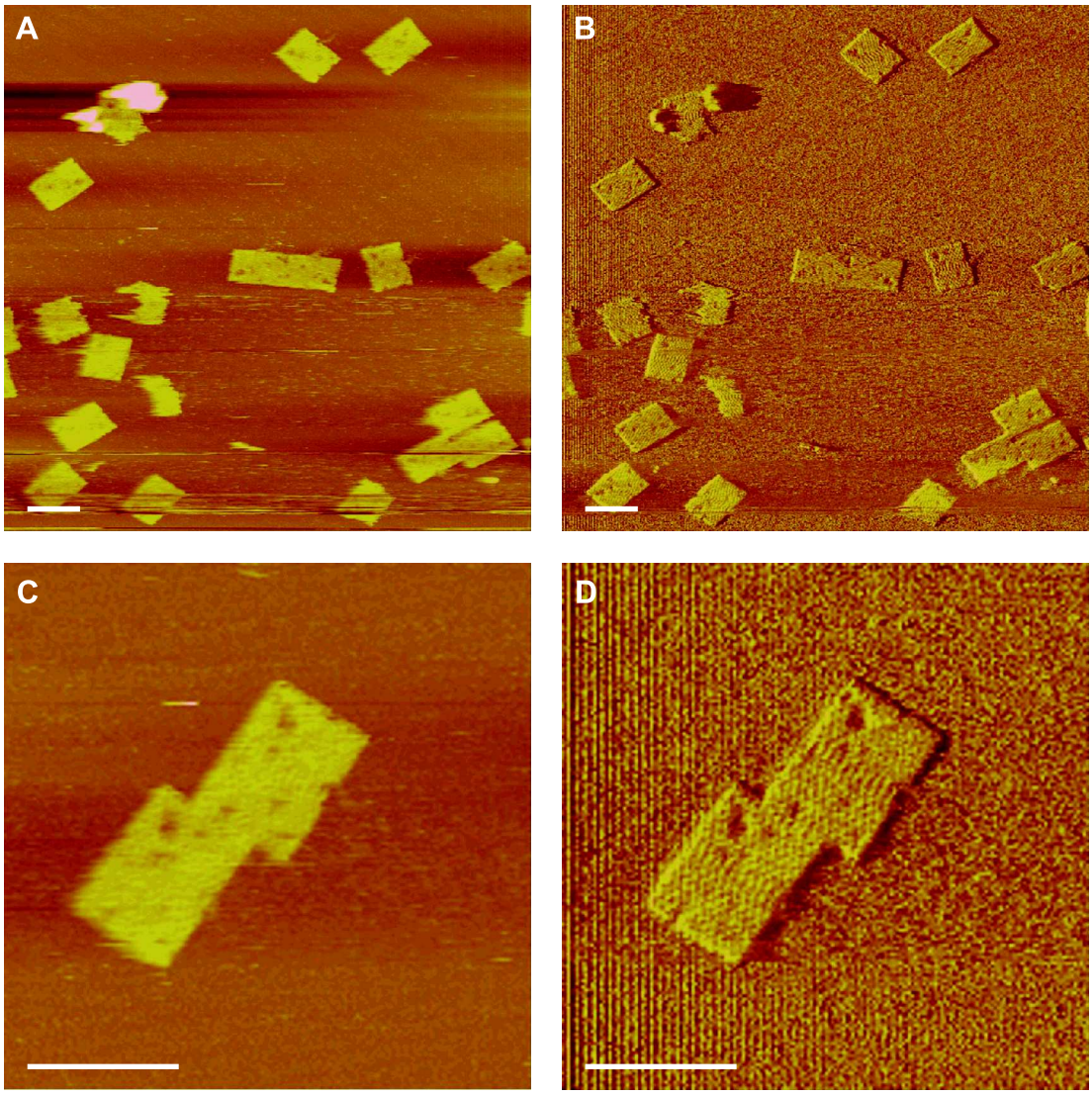


Figure 6.8: AFM images of the $F_1$-ATPase plain origami control samples. Samples were purified by size exclusion HPLC. **A, C** Height images and **B, D** phase images of typical tiles. No protein binding was observed, and instead the hole left by omitting the NTA modified staples is seen. Additional smaller defects are caused by the omission of staple strands modified with biotin. All scale bars 100 nm.

## 6.4 $F_1$-ATPase spinning on DNA tiles

As discussed in the previous sections, the *E. coli* $F_1$ was successfully bound to a DNA origami tile. However, the key question remains, is the protein active? That is, is $F_1$ on a DNA origami able to rotate in the presence of ATP? To answer this question, single-molecule rotation assays were performed on $F_1$ DNA origami samples. Rotation assays were performed on a laser dark-field microscope, identical to the one described in (Sowa et al., 2010). Experimental details are given in Appendix A.10.3.

Unfortunately, a lack of active *E. coli* $F_1$ protein meant a switch to yeast $F_1$ was required for these measurements. Although the binding site is slightly different, with 6 $His_{10}$ tags rather than 3, it was hoped that this protein would bind similarly to the tiles. Size-exclusion HPLC was used to test binding for these samples, and although the results are not as clear, show that specific binding still occurs (Figure 6.9 A). An alternative purification method using multiple spins through smaller hand-packed size exclusion columns was also tested (Figure 6.9 B). This method is the same as that used in Chapter 3 to purify DNA motor tiles, and is much faster than size-exclusion purification on an HPLC. It was hoped that this would reduce protein degradation during purification. Samples purified using this method were found to have a very much reduced amount of free protein, with only a slight decrease in the amount of protein coincident with the DNA origami peak.

Single-molecule measurements of rotating yeast $F_1$ bound to Ni-NTA-coated glass have been made previously (Bradley Steel, Unpublished Data, 2010). As a control experiment these results were repeated, and are shown in Figures 6.10 and 6.11. $F_1$ is bound to either NTA-coated or plain glass, and then labelled on the $\gamma$ subunit with SA-coated gold beads (60 nm). High-speed videos of the samples (10,000 Hz, 1 s, on average 16 videos per sample) are captured and analysed as in (Sowa et al., 2010). All samples contain sufficient ATP concentration to expect

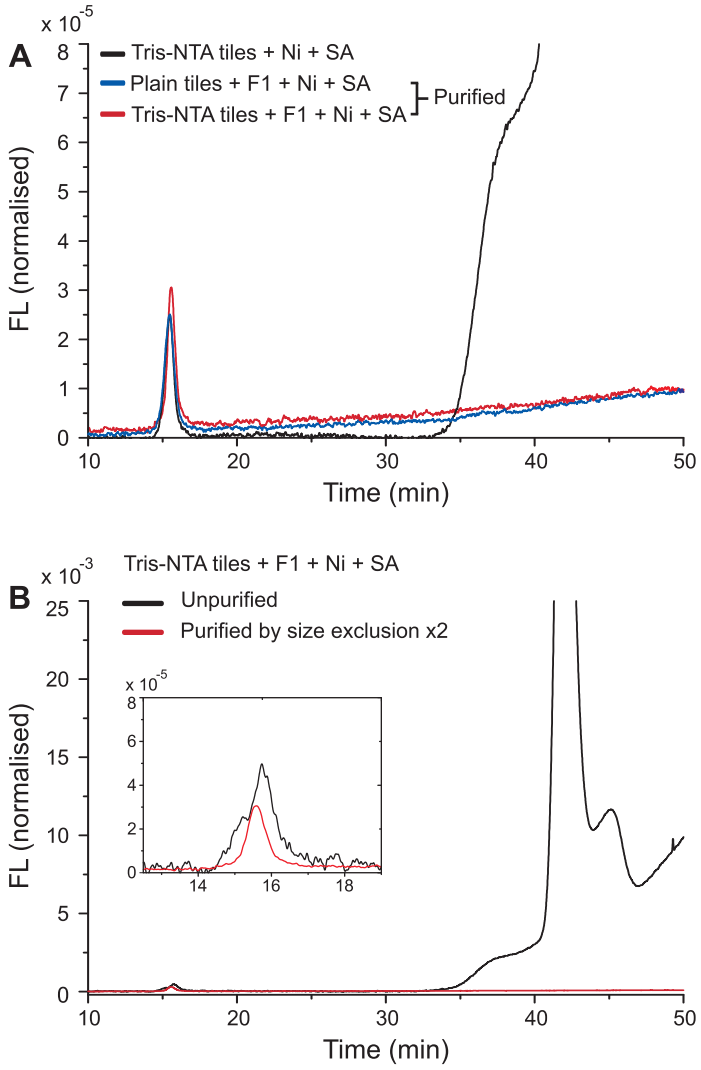


Figure 6.9: Size exclusion HPLC analysis of yeast $F_1$-ATPase binding to NTA-DNA origami tiles. The yeast $F_1$ is identified by fluorescent streptavidin bound to a biotin on the $\gamma$ subunit (ex532/em554 nm). DNA origami elute in the void fraction of the column ($t \sim 15min$). **A** A slight increase in fluorescence of the DNA origami peak is observed for the +NTA samples compared to the controls. $F_1$ samples are purified on small hand-packed size-exclusion columns prior to HPLC analysis, similarly to DNA motor tracks in Chapter 3. **B** Comparison of $F_1$ samples before and after purification, the free protein is removed from the purified sample, most of the bound $F_1$ remains (inset). Data quality is lower than previous results due to the much smaller $F_1$ amounts added to the column ($\sim$30$\times$ less).

rotation of $F_1$ (3 mM).

Two previously developed methods are used for an automated evaluation of the data (Bradley Steel, Unpublished, 2010). For each bead, the complex power spectrum is obtained from its trajectory ($(X(t), Y(t))$ to $Z = X + iY$), in which positive frequencies correspond to CCW rotation and negative to CW rotation (Berry et al., 1995). $F_1$ is expected to rotate only in a CCW direction, and so a large peak at positive frequencies often indicates good quality data. The difference between the area under the power spectrum for positive and negative frequencies, normalised to the total area, is used as the first quality measure, called the CCW bias (Figures 6.10 and 6.12). The second measure is the average speed of the motor, as determined by the gradient of the angle vs. time trace. An example power spectrum and angle-time trace for a 'good' spinner are shown in Figure 6.10 A and B. The corresponding XY and angular position data for the same bead are shown in Figure 6.11 A.

The CCW bias and average speed are calculated for each bead detected in the sample. Figure 6.10 shows the results for control samples with $F_1$ on NTA-coated or plain glass slides, or no $F_1$ protein at all. The corresponding X-Y and angle position data is shown for several highlighted points in Figure 6.11. Generally, points with high CCW bias values ($\geq 80\%$), and a high negative average speed, have good data traces with circular orbits and evidence of 120° steps. An example of intermediate (Figure 6.11 B) and poor quality data are also shown (Figure 6.11 C). Importantly, if no $F_1$ is present, no rotating beads are detected and the points in Figure 6.10 are all clustered around the origin.

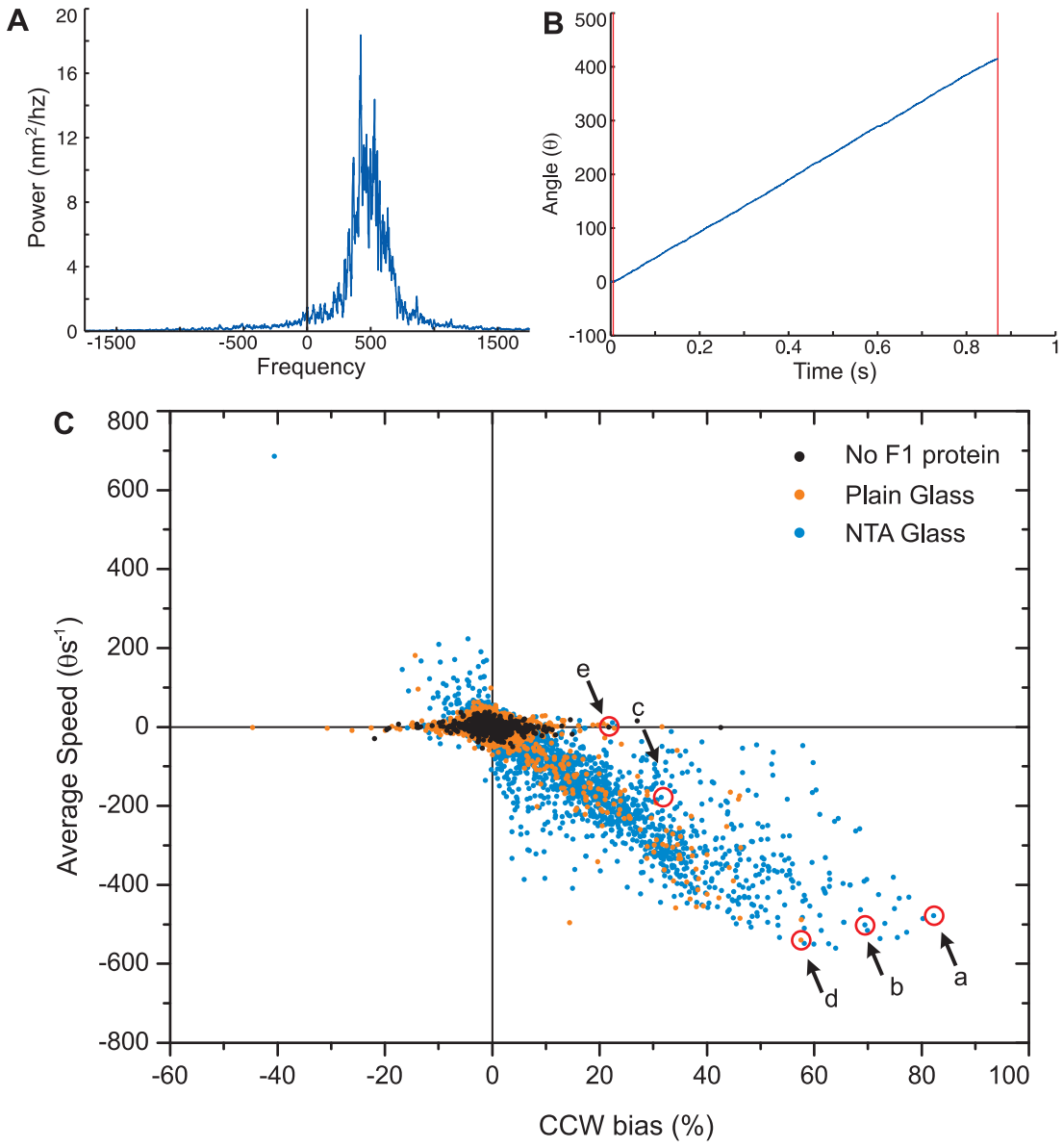


Figure 6.10: Laser Dark Field results for yeast $F_1$ on glass. Rotation of a 60 nm gold bead on the $\gamma$ subunit is observed at 10000 Hz. Beads are scored according to the asymmetry of their complex power spectrum (**A**), called the CCW bias, and the gradient of the $\theta$-time trace, the average speed (**B**). **C** The results for all videos are plotted together. Good quality data traces tend to be in the bottom right-hand of the plot. In the absence of protein, the points cluster around the origin. The position data for selected points are shown in Figure 6.11.

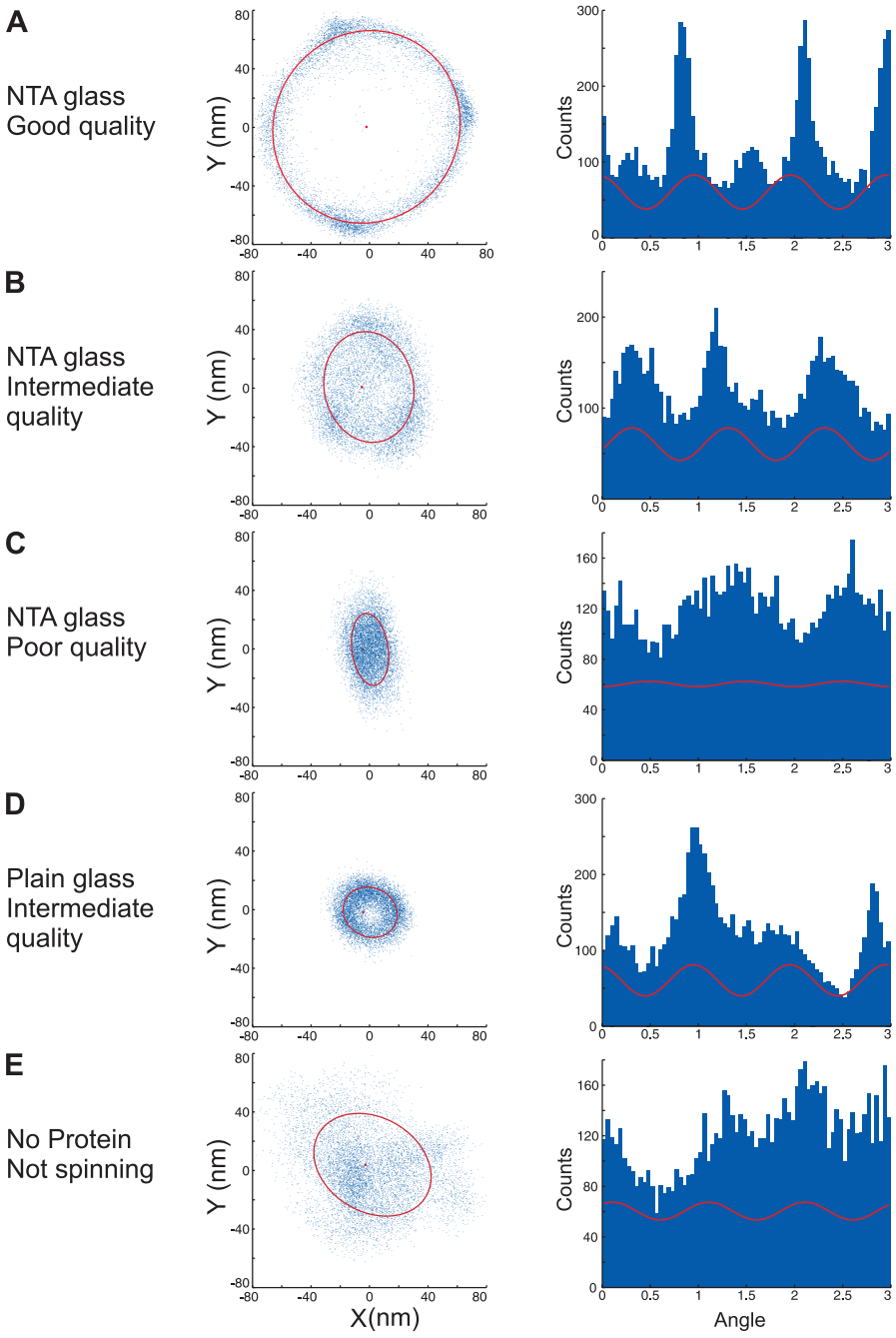


Figure 6.11: Laser Dark Field results for yeast $F_1$ on glass. X-Y position data (left) and $\theta$-time distributions (right) for points highlighted in Figure 6.10 C. Typical good, intermediate and poor quality spinners are shown for NTA glass (**A**, **B**, **C**). In the absence of $F_1$ non-spinning traces are observed (**E**).

The same rotation assay was also performed with $F_1$-DNA origami samples. The protein was incubated with the DNA tiles, either with or without NTA modified strands, and $Ni^{2+}$ for 30 minutes. Free protein was then purified away from protein bound to tiles using hand-packed size-exclusion columns, as for Figure 6.9 B. Similarly to above, the resulting samples were immobilised on plain glass, 60 nm SA-coated gold beads were used to label the $\gamma$ subunit, and videos recorded for 1 s at 10000 Hz. The resulting plot of the data quality is shown in Figure 6.12.

For all samples with NTA modified staple strands, there is good evidence of spinning beads. This is supported by the traces for selected points (Figure 6.13), which have circular orbits and evidence of 120° steps. In contrast, for the plain origami tile sample, the points are all clustered around the origin in Figure 6.12, and the corresponding traces (Figure 6.12) show no evidence of rotation. It is important to note that free protein was removed by purification prior to the spinning assays. If the free protein were not completely removed, the -NTA sample would be expected to be similar to the plain glass control in Figure 6.10. The fact that the -NTA data is the same as the no $F_1$ control confirms that the free protein was successfully removed from the samples. This supports the conclusion that the spinning beads observed in +NTA origami samples are $F_1$ motors rotating while bound to the DNA tiles. This is further supported by the AFM data, which demonstrates that the protein remains bound to the tiles many hours after purification (Figure 6.7). In these measurements, samples were tested ∼30 min after purification rather than the ∼4-5 hours for AFM experiments.

Several sample preparation methods were compared, with either 5× more $F_1$ protein added to the tiles, or tiles purified though 2× as many spins. Figure 6.14 shows a summary of the number of gold beads detected in each sample, and the proportion of those beads spinning, as determined by a CCW bias cut-off of 20%. The best protein to DNA concentration is the estimated 1:1 ratio, and purifying

the sample several times may be beneficial. While many more beads are detected in standard NTA-glass sample compared to the DNA origami samples, the proportion of spinning beads is similar. Importantly, the values for plain tiles are the same as for the no protein control.

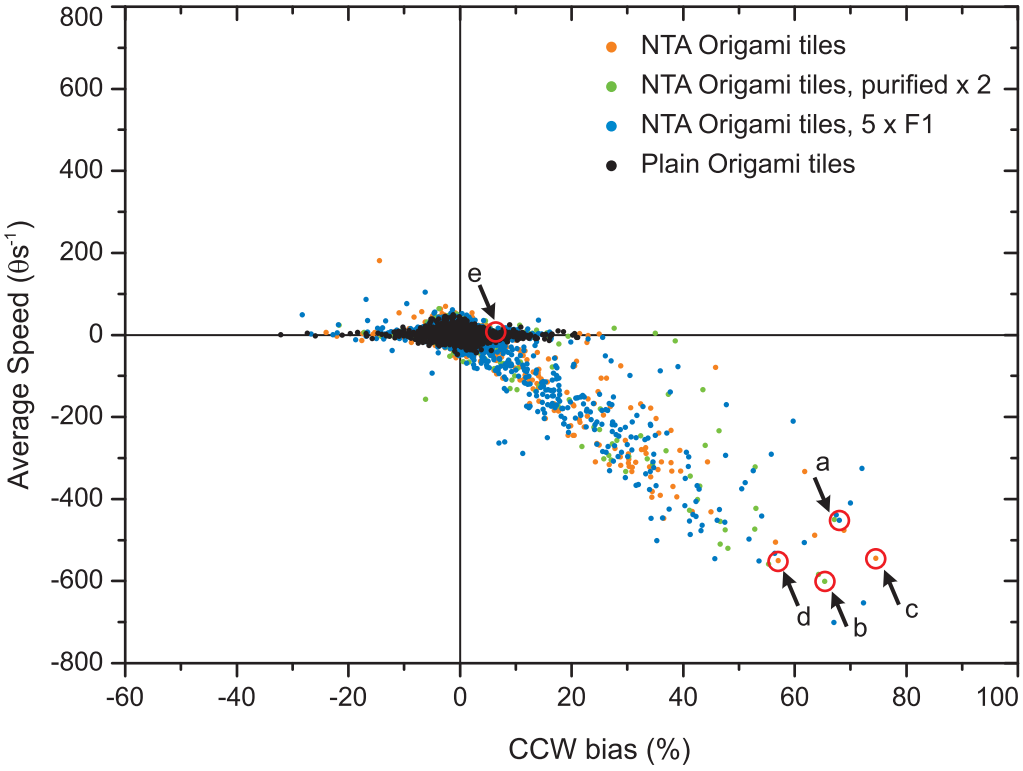


Figure 6.12: Laser Dark Field results for yeast $F_1$ on NTA-DNA origami. Rotation of a 60 nm gold bead on the $\gamma$ subunit is observed at 10000 Hz. Beads are scored according to CCW bias and average speed. Good quality data traces tend to be in the bottom right-hand of the plot. In the absence of protein, the points cluster around the origin. For all samples with the tris-NTA origami tiles, a number of good quality spinners are observed. When plain origami tiles are used, the points are clustered around the origin similarly to a no $F_1$ control. The position data for selected points are shown in Figure 6.13.

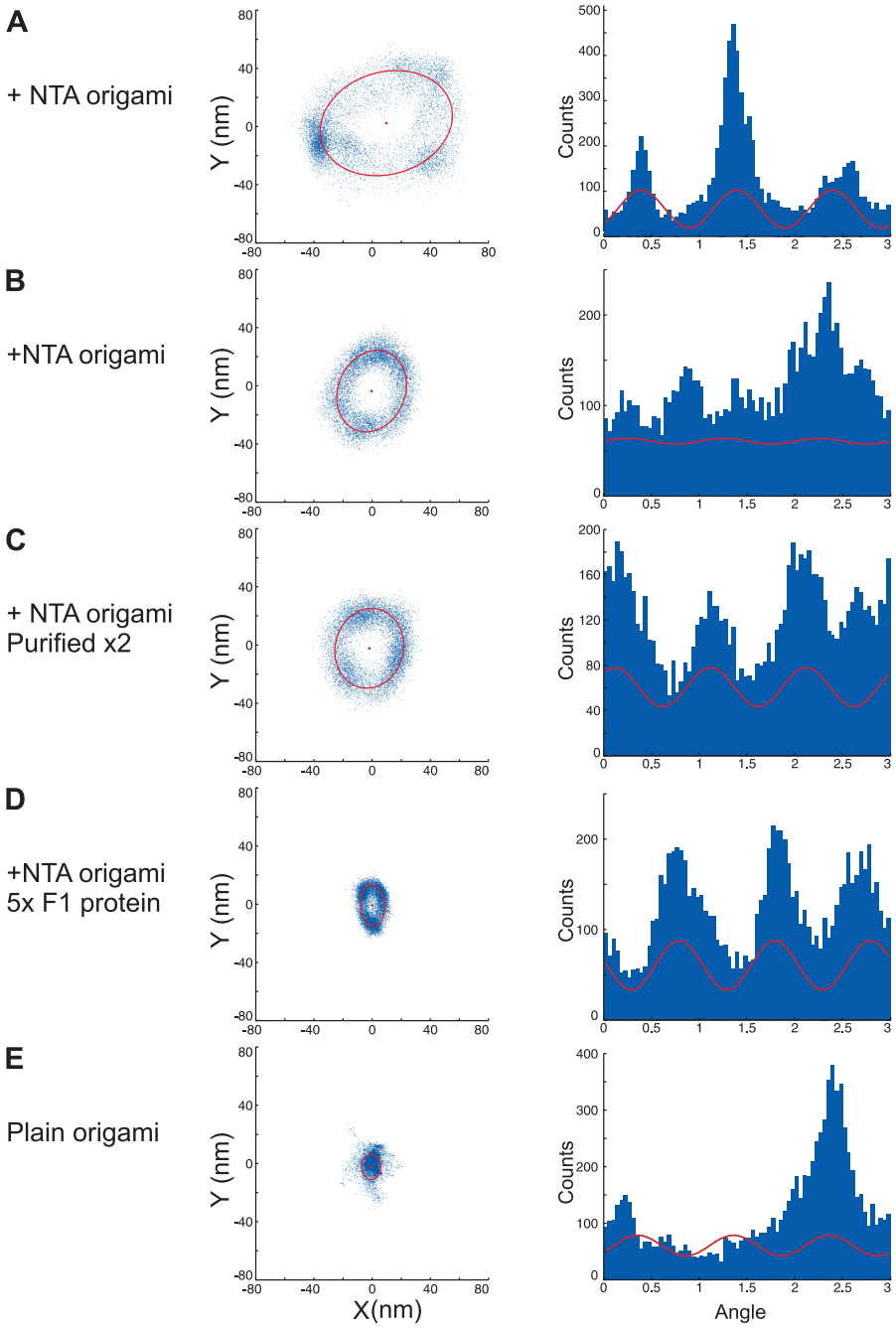


Figure 6.13: Laser Dark Field results for yeast $F_1$ on NTA-DNA origami. X-Y position data (left) and $\theta$-time distributions (right) for points highlighted in Figure 6.10 C. NTA-DNA tiles have high quality spinners (**A**, **B**, **C** and **D**). Only non-spinning traces are observed for plain tiles (**E**).

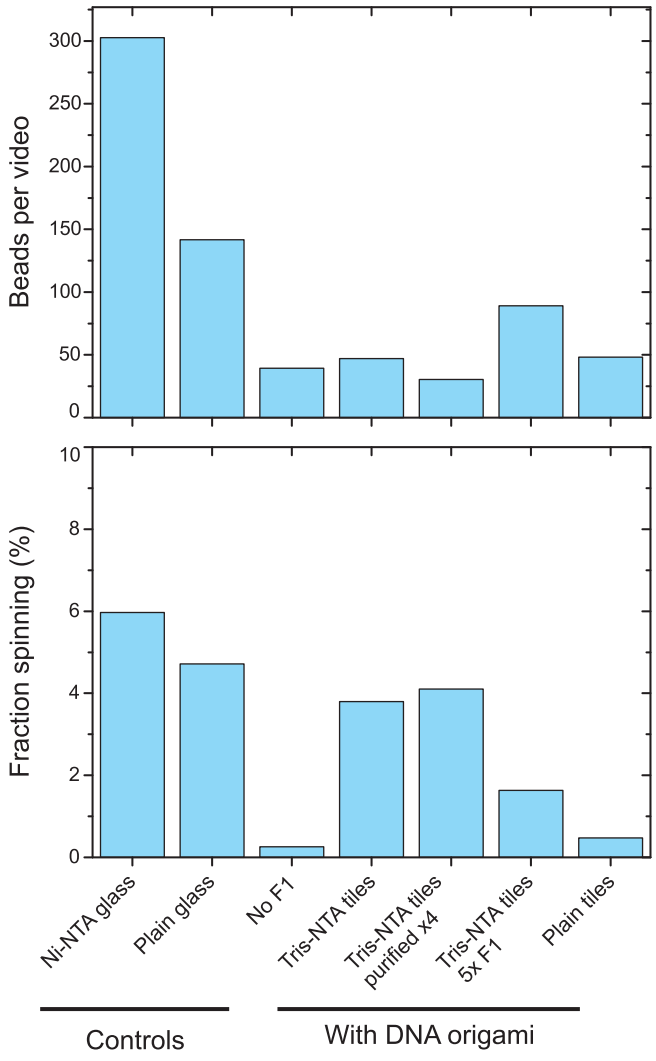


Figure 6.14: Summary of laser dark field results for yeast $F_1$. The number of beads per video (1 s, on average 16 videos per sample), and the percentage of those beads spinning (CCW bias $> 20\%$), for control and DNA origami samples. More beads stick for the standard NTA-glass, but the +NTA origami have a similar proportion of spinning beads even after free $F_1$ has been removed by purification. The results for plain tiles, also purified, are the same as for the no protein control. This strongly suggests $F_1$ motors are rotating on DNA origami tiles.

## 6.5 Conclusions

In this Chapter attachment of the rotary protein motor $F_1$-ATPase to a DNA origami substrate is investigated. DNA tiles with tris-NTA modified staple strands are assembled. Size-exclusion HPLC is used demonstrate that all three modified staple strands on each tile are able to bind His-tagged GFP. A similar HPLC analysis shows the tiles can also bind *E. coli* $F_1$-ATPase, and AFM is used to confirm the correct placement of the protein on the tiles. Finally, in a rotation assay using yeast $F_1$-ATPase, rotating beads are found only in origami samples with the NTA modified strands. The data obtained for the best beads have circular orbits, with 120° steps, and are of a similar quality to those obtained by existing methods. Free protein was removed from samples prior to the spinning assay, and the plain tile controls show no rotating beads. This is strong evidence that the rotating beads observed in NTA tile samples are not due to free protein non-specifically stuck to the glass, but are indeed active $F_1$-ATPase motors bound to DNA origami tiles.

This is the first time such a complex multimeric protein has been linked to a DNA origami substrate. Furthermore, the evidence here strongly supports the conclusion that the bound protein remains active and hydrolyses ATP producing rotation of the motor shaft. The final observations are of a DNA-protein motor complex that incorporates both the rationally designed DNA origami, and a naturally occurring protein motor.

The hybrid $F_1$-origami structure may bring about new ways to study the physical properties of the motor protein. For example, the yield of good quality spinners in $F_1$ assays is very low, typically 1 % (CCW bias $> 80\%$). One of the reasons proposed for this is that the angle at which the bead sticks to the motor shaft is not controlled. If the bead is directly centered, it will rotate on its axis, and no movement will be observed. For this reason asymmetric markers, such as pairs of beads

or elongated gold nanorods, are often used for rotation assays. Unfortunately, the processes for making such markers are also poorly controlled. Rather than using the origami tile to attach $F_1$ to glass, the system could be turned upside down, with the $\gamma$ unit attached to streptavidin-coated glass. Gold labelled DNA tiles could then be used as rotation markers, and would provide a new way for precisely controlling the geometry and attachment point of the marker to the motor. This would allow for better control of the orbit of the data trace, and may improve the yield of good data.

In addition to this, the behaviour of the motor is known to be sensitive to the load caused by viscous drag on the bead or marker. Generally, this drag scales with $r_o^3$ for the radius of orbit or eccentricity, but only with $r_b^2$ of the bead radius (Reid et al., 2006). The effect of different loads on the motor is typically tested by changing the bead size. However, this will have a smaller effect than changing the orbit, and is also constrained to the set of differently sized beads that are both available and visible under the microscope conditions. The DNA origami based markers may provide a useful tool for investigating load dependent properties of the motor.

Finally, such hybrid nanostructures provide the possibility of harnessing the high efficiency molecular motors found in biological systems as active components of synthetic nanostructures. For example, a propoulsion system could be assembled by anchoring the $F_1$-DNA tile to a vesicle, and then attaching an artificial flagellum made from 3-D DNA origami to the motor shaft. This could provide a useful alternative to the synthetic DNA motors designed and demonstrated in previous chapters. Presently, the greater control of DNA motor systems gives an advantage over protein motors, but with further work in this area the balance may shift, and the greater efficiency and speed of protein systems may outweigh it.

Chapter 7

# Summary

The overall aim of this thesis was to develop DNA origami based nanostructures that incorporate active transport. The approach taken was to use DNA origami tiles as a substrate for molecular motors, both synthetic DNA motors and a naturally occuring protein motor. Generally, the results obtained successfully demonstrated motion on origami tile substrates. The key results in each chapter are outlined below, and future research directions generated by this work are briefly described in Section 7.1.

A discussion of general aspects of origami tile assembly, design, processing and characterisation is presented in Chapter 2. The methods developed in the course of this work were critical in achieving the results in following chapters. In particular, the size-exclusion purification method for removing excess staple strands after tile assembly was used in all other chapters. DNA origami tiles were characterised by HPLC for the first time, using ion-exchange and size-exclusion columns. This was found to be an excellent technique for quantifying properties such as defect repair (Chapter 2) or protein binding (Chapter 6). Other projects have also benefited

from these results (Parminder Lally, D.Phil Thesis, 2010), and this Chapter should provide a useful resource for future work on DNA origami.

In Chapter 3, the controlled transport of a burnt-bridges DNA motor along a 100 nm DNA origami track was demonstrated. Both ensemble fluorescence and AFM were used to observe motor activity. The results agree with a simple kinetic model, giving a motor speed of order 0.1 $nms^{-1}$. The motion was found to be uniform, directional and processive, and the average time per step is independent of distance travelled. The step size was found to have a large effect on stepping rate, and could be tuned to match the time required for reaction steps of an autonomous molecular assembler. The use of high-speed real-time AFM allowed the observation of discrete steps of a single motor, the most detailed observation of any DNA motor mechanism to date. The AFM movies raise interesting questions about the motor mechanism, which could be addressed by modelling of the branch migration from one stator to the next in a similar way to previous work (Ouldridge et al., 2010). Overall, the precise control over device assembly and movement opens the way for the design of integrated systems that incorporate active transport and information processing with the synthesis of custom molecules.

The design of an origami track for a two-foot DNA motor, in Chapter 4, proved a more challenging task. Initial AFM analysis of several track designs showed successful assembly, but the tracks did not support the correct operation of the motor. For all the designs tested, only one of the two feet was raised by the fuel strands, and transport over extended tracks was not possible. A defect of the track, where two copies of each of the piece-wise segments is incorporated into the tile, is proposed as an explanation for the results. Possible geometric effects are also discussed. Refinements of the track design are suggested, such as inserting the track sequence directly into the template DNA strand of the origami. This approach would give much better control over track geometry.

Of the two linear DNA motors studied, the burnt-bridges motor track was far more successful. This motor was then chosen to investigate transport across a network of branched tracks in Chapter 5. Motors were directed down a path with either 1 or 3 bifurcations. This is the first time such a complex DNA motor track system has been assembled. The results demonstrate that the path taken by the motor can be controlled by instructions either added externally or pre-programed into the motor. This track-based approach to DNA logic has several strengths, particularly in terms of error correction. Firstly, motor leakage into the wrong state was reduced by placing two gates in series. Secondly, motors that do leak through into the incorrect path at one junction still correctly respond to the following instruction, and could be rerouted onto the correct path. For example, by creating tracks with loops. Linking these track networks to a set of assembly instructions (Gu et al., 2010; He and Liu, 2010) would provide an integrated system for processing multiple inputs and converting them directly into the synthesis of an output molecule.

In Chapter 6, a different approach is taken to assembling an active DNA origami structure. Rather than taking a molecular motor that has been designed *de novo*, the naturally occuring rotary motor $F_1$-ATPase is used. This is a complex multimeric protein that is sensitive to degradation, and only retains activity in specific conditions. Once assembled, the DNA tiles were found to be robust to changes of conditions, and could be kept in a buffer with as little at 2mM $Mg^{2+}$, as required by the protein. Binding of his-GFP and his-$F_1$ to tris-NTA origami tiles was shown by HPLC, and AFM analysis demonstrated that $F_1$ remains bound to the tiles many hours after purification. Single molecule observations of the $F_1$-origami complex show the motor is active and rotating, and data quality equivalent to existing techniques was obtained. This has inspired the design of new rotation assay configurations, which could achieve a greater yield of good quality data, and also

reveal new information about the protein mechanism. In particular, the DNA tiles could be used as markers to probe the effect of load on rotation of the motor in more detail.

## 7.1 The future

The results achieved in this thesis have lead to a number of ongoing research projects. Origami tracks for the burnt-bridges DNA motor are being adapted for use in a chemical assembly line by Dr Jonathan Bath in the Turberfield Group, Oxford University, and could also be linked to tracks with junctions. More complex junctions across a larger array of tiled origami structures may also be considered.

A coarse-grained DNA model, similar to that used in (Ouldridge et al., 2010) is being used by Petr Sulc in the Department of Theoretical Physics, Oxford University, to analyse transfer of the burnt-bridges motor from one stator to the next. This will aid in the interpretation of the AFM movie data in this thesis, and potentially suggest improvements of the motor design to increase the rate of enzyme-driven stepping and reduce the rate of diffusion.

The track sequence for the two-foot DNA motor has been inserted into a plasmid, which can be replicated by cell culture and then folded into an origami tile, by Dr Jonathan Bath in the Turberfield Group, Oxford University. This plasmid origami will be used to investigate movement of the two-foot motor with single-molecule fluorescence microscopy, using Qdot labelled tracks and motors.

Further work on the $F_1$-ATPase aspect of the project will involve adapting the origami tiles to act as rotation markers. The $F_1$ motor may also be harnessed to propel nanostructures around their environment, for example by anchoring it to a vesicle and attaching an artificial flagellum made from 3-D DNA origami to the motor shaft.

Appendix A

# Materials and methods

## A.1 DNA and Origami design

The original DNA origami rectangle (Type A) consists of a uniform set of 216 32-nt staples, taken directly from a previously published design (Rothemund, 2006). Staple sequences for this tile design are as in (Rothemund, 2006), Supplementary File 1, page 28. Tile design A is used in: Chapter 2 all results, Chapter 3 AFM experiments only, Chapter 4 all results, and Chapter 6 all results.

The second tile (Type B) is a variation of the first, modified to reduce global twist. Staple sequences for this tile design are as in Appendix C.1.2. Tile design B is used in: Chapter 3 fluorescence results, Chapter 5 all results. The naming convention follows (Rothemund, 2006), and is shown in Figure C.1. Type A tile staple names have prefix 'r', and type B have prefix 'M'.

Additional DNA sequences were designed using the Nanev software (Goodman, 2005), and secondary structure and interaction strengths of strands was tested using Nupack (Zadeh et al., 2010).

## A.2 Origami synthesis

Single-stranded M13mp18 DNA was ordered from USB (Affymetrix) as the template strand for the origami rectangle. Staple strands were purchased from Integrated DNA Technologies (IDT), modified or unmodified as listed in Appendix C. Synthesis buffer in all experiments is 1× tris-acetate buffer with 12.5 mM magnesium acetate (pH 8.3). Initial synthesis solutions contained 1.6 nM M13mp18 and 160 nM of each staple (100× excess). Template and staple concentrations were varied in Section 2.2. After this, all solutions for origami synthesis contained 50 nM M13mp18, 250 nM of each staple strand (5× excess), unless specified. The resulting solution was annealed from 95°C to 20°C in a PCR machine (BioRad) at an average rate of 1°C/minute in 0.1°C steps.

## A.3 Atomic Force Microscopy

Selected AFM data was collected through collaboration with the Sugiyama Laboratory, Kyoto University, Japan. The AFM results from Kyoto are: Chapter 3 all results, Chapter 4 Figures 4.4 and 4.11. All experiments and protocols were designed by the author. Samples were prepared by either the author (Chapter 4) or Y. Katsuda (Chapter 3), images were obtained by microscope technician K. Hidaka. All other AFM images in the thesis were obtained by the author at Oxford University, UK.

### A.3.1 Static images - Oxford

Origami samples were observed in a Veeco 'Nanoman' Atomic Force Microscope, in a solution of origami synthesis buffer (1×tris-acetate, 12.5 mM Magnesium acetate) in tapping mode. Increased $Mg^{2+}$ buffer concentrations of 30 mM and

60 mM were also used, higher resolution images were obtained more often with the higher salt buffer. Veeco NP-S AFM silicon nitride cantilever chips were used and the narrow 100$\mu$m tip was selected, which usually had a resonance frequency around 9 kHz. A mica surface was freshly cleaved, 5$\mu$L of 2 nM origami solution was added for 1 minute. The mica was washed three times with 30$\mu$L of buffer, and the AFM tip, mounted in a fluid cell, was lowered into this. Samples with protein were washed 5-10×. Samples were imaged in tapping mode; typical drive amplitude and amplitude set-point of 100 mV and 0.3 mV respectively were used to reduce sample damage. Once images were collected, they were flattened to 1st order in the Nanoman control software.

### A.3.2 High-speed imaging

AFM images and movies were obtained using a high-speed AFM imaging system (Nano Live Vision, RIBM, Tsukuba, Japan) with a silicon nitride cantilever (Olympus BL-AC10EGS). Samples (2 $\mu$L) were adsorbed onto a freshly cleaved mica surface for 5 min at room temperature and then washed three times with buffer (20 mM Tris-HCl pH 7.6, 1 mM EDTA, and 10 mM $MgCl_2$). Scanning was performed at 23°C in buffer solution using tapping mode. The AFM was calibrated with a silicon grating with 28 nm pitch. The long dimension of an origami tile (parallel to the DNA helices) is used as a subsidiary standard to determine the scale bars shown, which are consistent with the AFM calibration within the expected error.

#### Static images

Origami tiles (50 $\mu$L, 10 nM) were purified by hand-packed size-exclusion columns (Sephacryl S-300), with a 500 $\mu$L bead volume, spun at 1000 g for 4 minutes, repeated twice. The $S_1$-motor duplex (5×) was incubated with the DNA tiles

at 23°C for 1 hour. Samples were treated with 20 units of restriction enzyme Nt.BbvCI (New England Biolabs) in a 20 $\mu$L solution containing 20 mM Tris-HCl (pH 7.6), 1 mM EDTA and 10 mM $MgCl_2$ and incubated at 23°C for 0, 1, 2, and 3 hours. The motor position data for the histogram in Figure 3.14 was determined from images by Y. Katsuda, Kyoto University, Japan.

#### Movies

Samples were prepared as above, incubated with enzyme for ∼5 minutes, then deposited on mica. Excess enzyme was removed by washing with ∼50 $\mu$L buffer.

### A.3.3 Image analysis

AFM movie data was analysed by the author at Oxford University, UK. Height profile data was determined by K. Hidaka and Y. Katsuda at Kyoto University, Japan.

#### Registration

Sequential AFM images showed drift of the origami tiles within the imaging scan area. To correct movies with a large amount of drift, origami images were registered using MatLab Image Processing Toolbox (MathWorks). In this process, 4-6 control points, corresponding to hairpins on the DNA tile, were selected and their locations used to transform the target frame by linear translation, rotation and scaling to match a reference frame. Control points were selected by eye, and their location improved by maximizing the cross-correlation of a small area around the selected point in both images. To correct movies with only a small amount of drift, images were registered with a linear translation using the Turboreg function in ImageJ software (Abramoff et al., 2004).

**Kymographs**

In order to analyze the stepping behavior of the DNA motors, kymographs were created using the Kymograph plugin of ImageJ Image analysis software (Abramoff et al., 2004). AFM height measurements, averaged over a width of 5 pixels along a line corresponding to the DNA motor track, were stacked to create a 2D image. In the resulting kymograph, stationary features, such as hairpins or tile edges, appear as vertical lines and moving features, such as the DNA motor, appear as diagonal lines. The location of the motor in each image was approximated by the position of the maximum measured height along the motor track. Control kymographs were plotted along the rows of hairpins on the track tiles to confirm the correct registration of image frames.

## A.4 Gel Electrophoresis

Gel electrophoresis was used to analyse origami samples (agarose) in Chapter 2, and motor-catalysed unblocking on short test tracks (polyacrylamide) in Sections 5.3.1, 5.4 and B.2.1. In Chapter 6 denaturing and native (50 mM tris-tricine, pH 8) polyacrylamide gels were used to analyse tris-NTA ssDNA.

Gels were run on a Mini PROTEAN 3 gel kit (Bio-Rad Laboratories, USA). For imaging, gels with fluorescent staple strands were pre-scanned, and then all gels were stained with SyBr Gold (Invitrogen) Nucleic Acid Gel stain, and scanned on a BioRad Gel scanner with excitation/ filter pairs of 488/530 nm (SyBr Gold, FAM), 532/605 nm (TAMRA, JOE), or 488/630 nm (Qdots).

## A.4.1 Polyacrylamide

### Native

Samples in Chapter 5 were run on 12% 29:1 (mono:bis) polyacrylamide gels (Sigma), in 1× TAE buffer(Sigma) at 240 V at 4°C. His-GFP and tris-NTA strand gel in Chapter 6 was run on 50 mM tris, 50 mM tricine, 8% polyacrylamide gel at 240 V at 4°C.

### Denaturing

Modified tris-NTA staple strands were run in a two layer denaturing polyacrylamide gel (separating layer 22% acrylamide, 19:1, stacking layer 5% acrylamide, 29:1) with 7 M Urea, in a tris-glycine buffer at 120 V (first 10 minutes) and 300 V (60 minutes), at 25°C.

### PAGE purification

Hybridised two-foot motors and the modified tris-NTA strands were PAGE purified. Samples were run over a number of wells, and the required band cut out under UV shadowing. This piece of gel was then crushed and covered with $50\mu$L 1× TA (tris-acetate, pH 8.3) buffer overnight at room temperature to extract the purified strands. The gel was then filtered off with a Durapore PVDF 0.45$\mu$m filter tube, spun at 12,000g for 2 hours.

## A.4.2 Agarose

DNA Origami were run on 0.75% agarose gels (Fisher), in 1× TAE buffer at 60 V for 1-3 hrs at 4°C. M13mp18 template ssDNA runs faster than origami tiles in these gels. The gel comparing the two origami designs, types A and B, is 1.5% agarose. At this percentage, the ssDNA template runs more slowly than the origami tiles.

## A.5 Origami Purification

### A.5.1 Centrifugal Filtration

Origami samples were filtered with Microcon centrifugal filter units (Millipore), which contain a low-binding Ultracel cellulose membrane. Filters of 100 kDa (YM-10) and 50 kDa (YM-50) cut-off were tested. As in (Ke et al., 2008), samples were rinsed multiple times by centrifuging at 300g for 20 minutes to reduce the volume from 500$\mu$L to around 20 $\mu$L, then topping up with buffer and repeating.

### A.5.2 Hand-packed Ion-exchange columns

Ion-exchange columns (DEAE Sepharose, GE Healthcare) were hand-packed with 500 $\mu$L of resin (50 % beads). Excess buffer was drained under gravity, and the column was equilibrated with low salt buffer (100mM NaCl, 1xTA, 12.5mM Magnesium acetate) by washing 3× with 500 $\mu$L. Origami samples (10 - 100 $\mu$L) were added to the column bed in low salt buffer. The column was rinsed through with increasing salt strength, up to 1 M NaCl. Fractions of 500 $\mu$L were collected and concentrated before gel analysis in 100 kDa Microcon centrifugal filter units (YM-100), spun at 300g for 20 minutes.

### A.5.3 Hand-packed Size-exclusion columns

Size-exclusion columns (Sephacryl S-300 HR, GE Healthcare) were hand-packed to obtain a dry bead volume of ∼500 $\mu$L. The resin has a dsDNA cut-off of 118 bp. Columns were equilibrated by washing 3× with 500 $\mu$L of the required sample buffer, centrifuging for 1 minute at 1000g each time to remove excess buffer. Columns were dried by spinning at 1000g for 3 minutes; this step is essential to avoid diluting the final sample in excess buffer. Origami samples of (10-75 $\mu$L)

were added to the column bed and eluted by centrifugation at 1000 g for 4 minutes. This process was repeated three times. The sample is eluted in the buffer used to equilibrate the column.

## A.6 High Pressure Liquid Chromatography

HPLC analysis was performed on an Agilent 1200$^{TM}$ system equipped with diode array and fluorescence detectors.

### A.6.1 Ion-Exchange

HPLC with a pre-packed ion-exchange column was used to analyse origami samples in Sections 2.4 and 2.5. Samples were run on a DEAE Sepharose$^{TM}$ Fast Flow column (GE Healthcare), 1 mL column volume, with flow rate of 1 mL/min at 20°C. A stepped gradient of buffers A (1× TAE, 12.5mM $MgCl_2$, 100 mM NaCl) and B (1× TAE, 12.5mM $MgCl_2$, 1 M NaCl) was used to separate staples from assembled origami tiles. The gradient was increased to 22% buffer B, the point at which the staple strands elute, and kept at this value for 35-45 minutes to remove all excess staples, then increased sharply (5 min) to 100%. The origami elute in a fraction of ∼500 $\mu$L with ∼ 550 mM NaCl.

The absorbance of the eluent at 260 nm was used to detect DNA, and fluorescence (Ex/Em 550 nm/580 nm) was used to determine the amount of a single fluorescent staple strand inserted into the tiles. The area of the fluorescence peak for the labelled origami was normalized by the area of the corresponding DNA absorbance peak to allow comparison of repair efficiencies for different samples.

### A.6.2 Size-exclusion

Protein-origami samples in Chapter 6 were analysed with a pre-packed Superose 6 10/300 GL (GE Healthcare) size-exclusion column, with column volume of 24 mL. The optimal separation range is 5-5000 kDa for globular proteins, and the exclusion limit 40,000 kDa. Flow rate of 0.5 mL/min, at 10°C (*E. coli* $F_1$) or 15°C (yeast $F_1$), was used with constant buffer concentration for 100 min. GFP sample buffer was: 10 mM tris, 100 mM NaCl, pH 8. $F_1$-ATPase sample buffer was: 10 mM MOPS, 50 mM KCl, 2 mM $MgCl_2$, pH 7.0. Fractions of 500 $\mu$L were collected for AFM analysis.

### A.6.3 Reverse-phase

Some of the fluorophore labelled staple strands used for ensemble fluorescence experiments in Chapters 3 and 5, were purified with reverse-phase HPLC, which separates strands based on hydrophobicity under denaturing conditions. Purification was performed on a Waters XBridge$^{TM}$ OST C18 2.5 $\mu$m 4.6 x 50 mm column heated to 40°C. Flow rate was set at 1 mL/min with a linear gradient of the following buffers: buffer A, 0.1 M triethylammonium acetate (TEAA), 5% acetonitrile, pH 7.0; buffer B, 0.1 M triethylammonium acetate, 70% acetonitrile, pH 7.0. Fractions collected were combined and concentrated using a DNA120 Savant SpeedVac Concentrator. Oligonucleotides were quantified by measuring UV absorbance at 260 nm (A260) using a Cary 50 Probe UV-Vis Spectrophotometer equipped with a Hellman TrayCell adapter.

## A.7 Fluorescence Light Microscopy

Unpurified 2 nM DNA origami samples were added to a flow cell chamber constructed from two glass coverslips (Matsunami, Japan) separated by double-sided

tape, with a volume of 5-10 $\mu$L, and incubated for 5 minutes. SyBr gold DNA dye (Invitrogen) (1:10,000 dilution) was washed in, and incubated for a further 10 minutes. Chambers were then washed with 50 $\mu$L of buffer. Two buffers were used, either high $Mg^{2+}$ (1× TA, 30 mM $MgCl_2$), or low $Mg^{2+}$ (10 mM MOPs, 50 mM KCl, 2 mM $MgCl_2$). Origami samples were transferred into either buffer with a size-exclusion spin column (Bio-Rad, Micro Bio-Spin 6) prior to use. Samples were illuminated in epifluorescence mode with a mercury source lamp (Olympus) and imaged using an Andor iXon EMCCD (Andor, Ireland) on an inverted IX71 optical microscope (Olympus), with either a 40× (NA 0.9) lens or a 100× (NA 1.4) oil immersion lens .

## A.8 Quantum Dot labelling

Origami tiles were synthesised with a single 5'-biotin staple strand (5× excess) and purified with hand-packed ion-exchange columns, giving a final salt concentration of 600 mM NaCl. Tiles (500 $\mu$L of 1 nM) were incubated with 4× excess of QD655 quantum dots (Invitrogen) (2 $\mu$L of 1 $\mu$M stock), and Bovine Serum Albumin (BSA, Sigma) (15 $\mu$L of 100 mg/mL), for 30 minutes at room temperature. Samples were diluted to 100 mM NaCl, giving a final volume of 2.725 mL and tile concentration of 0.2 nM, then purified on hand-packed ion-exchange columns. Fractions of 500$\mu$L were collected for 100 mM NaCl (free Qdots) and 600 mM (origami) washes, and concentrated with centrifugal filters (YM-100) at 300×g for 20 min at 4°.

## A.9 Ensemble Fluorescence experiments

Origami samples were purified 3 times with hand-packed size-exclusion columns (Sephacryl S-300), with a 500 $\mu$L bead volume, spun at 1000 g for 4 minutes. This

gave a low background level for fluorescence measurements with only a small loss in sample. The samples were transfered into 1× tris-acetate buffer with 12.5 mM magnesium acetate and 50 mM NaCl (pH 8.3), with a final volume of 140 $\mu$L.

Fluorescence of origami track samples was measured as a function of time in a Cary Eclipse Fluorescence Spectrometer (Varian) in 100 $\mu$L quartz cuvettes (Starna). Mineral oil (Sigma) was added to cuvettes to prevent evaporation. Excitation and emission wavelengths were as follows: Cy3 (545 nm/565 nm), Cy5 (645 nm/665 nm), Cy3.5 (575 nm/595 nm), Cy5.5 (690 nm/710 nm), JOE (529 nm/555 nm). Slit widths were 5 nm (excitation) and 10 nm (emission). Fluorescence intensities were measured every 10 s, with an integration time of 1 s. Sample concentrations used were in the range 15 nM - 25 nM. Initial fluorescence signals (100 %) and the signals in the presence of excess motor (0 %) were used to set the base line and to normalize signals from different fluorophores.

For the burnt-bridges motor, blocked tracks were activated by adding 20× excess of the release strand, 20 minutes before addition of enzyme. Hairpin $S_1$-motor tracks were activated by addition of 10 units of restriction enzyme ScrFI (New England Biolabs) 20 minutes before addition of motor enzyme. Nicking enzyme Nt.BbvCI (New England Biolabs) is the enzyme used to power the motor, and was added to purified origami samples, such that the final solution contained 10 units of enzyme. For the two-foot motor stepping was initiated by addition of fuel strands (20× excess).

### A.9.1 Tile repair and motor loading

Origami tiles annealed with all but one of the staple strands were incubated with the missing staple following different protocols, and the insertion efficiency was quantified by ion-exchange HPLC.

**Loading the burnt-bridges motor**

On the basis of these results, incubation conditions used in fluorescence experiments to load the motor at the start of the track were chosen: 1 hour, at 37°C, with a 0.9× excess of the S1 + motor duplex. The S1 + motor duplex was pre-annealed by combining the stator S1 and motor at ratio 1:0.95, heating to 95°C, and cooling to 20°C in a PCR machine at a rate of 7.5°C/minute.

**Loading the two-foot motor**

The fixed and wild-type motor strands were hybridised together by annealing (as above), then PAGE purified. Fluorescence intensities were compared to ssDNA samples with known concentrations, and used to estimate the DNA origami concentration in the fluorimeter sample. A sub-stoichiometric (0.75×) amount of purified motor was added to the fluorimeter sample and mixed by pipetting.

## A.10 Tris-NTA DNA Origami tiles

### A.10.1 Tris-NTA modified DNA

Three staple strands were designed to have three internal NTA modifications. To achieve this, strands with 3 internal Amine modifications were purchased from Integrated DNA Technologies (IDT), and were chemically modified following published methods (Goodman et al., 2009; Erben, 2007). The chemical structures of the amine and tris-NTA DNA modifications are shown in Figure A.1. The staple strands were transferred into phosphate buffer (100 mM $Na_2HPO_4$, 100 mM NaCl, pH 7.3) using a size exclusion spin column (Bio-Rad Micro Bio-Spin 6). 30$\mu$L of DNA was then then combined with 6.75 $\mu$L of freshly dissolved SPDP (N-succinimidyl-3-(2-pyridyldithio)-propionate, 31.2 mg/ml in the organic solvent

DMSO), giving 0.8 mM DNA and 20 mM SPDP. SPDP is a crosslinker which converts each amine into a capped thiol group. After incubation at room temperature for 1 hour, excess SPDP was removed using a spin column. The thiol groups were then uncapped by reducing the disulphide bonds of the SPDP by adding 3.2 $\mu$L of 100mM TCEP and incubation at room temperature for 30 minutes. Malemide-NTA (Dojindo) was dissolved to 50 mg/ml in phosphate buffer and 3.5 $\mu$L was added to the DNA solution and incubated at room temperature for 1 hour, this adds an NTA group to each of the uncapped thiols. Excess malemide was removed by transferring the sample into phosphate buffer using another spin column. Tris-NTA strands are purified away from mono, bis and unmodified strands be denaturing PAGE

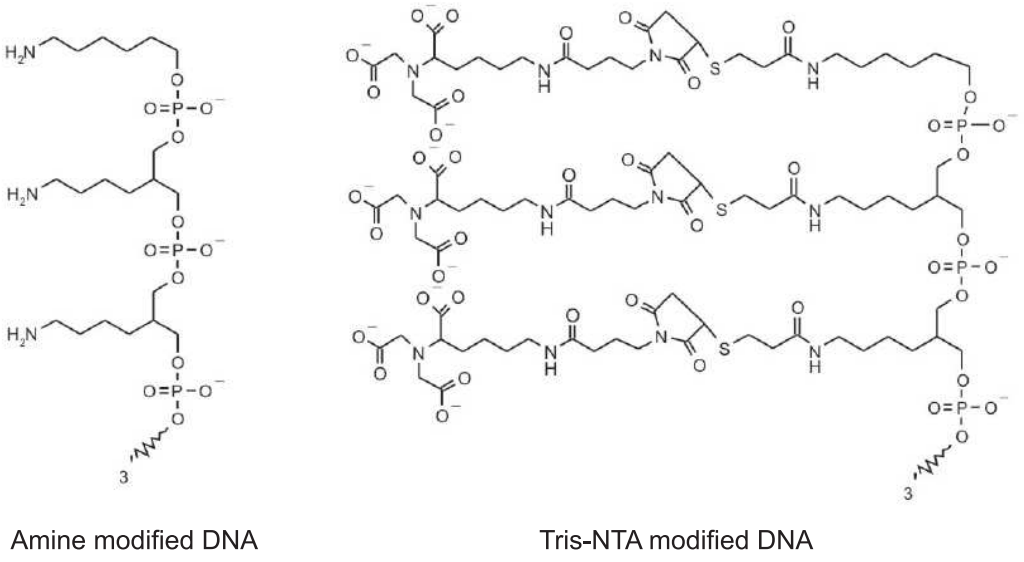


Figure A.1: **A** DNA strands were purchased with three internal amine modifications. **B** Amine groups were converted into NTA groups following the protocol in (Goodman et al., 2009). Images from (Erben, 2007).

## A.10.2 Protein binding to NTA tiles

### Green Fluorescent Protein

Recombinant $His_6$-GFP (rTurboGFP, Evrogen) was used to test the NTA origami tiles. Origami tiles (50 $\mu$L 50 nM) were synthesised with 2× NTA staple excess. Unpurified tiles were transferred into an EDTA free buffer (10 mM tris, 100 mM NaCl, 12.5 mM $MgCl_2$, pH 8) and incubated with a 5× GFP excess to NTA staples (2 $\mu$L 35 $\mu$M) and a 3× $Ni^{2+}$ excess (1.5 $\mu$L 100 $\mu$M $NiSO_4$), for 30 minutes at room temperature.

### $F_1$-ATPase

*E. coli* $F_1$-ATPase was bound to the NTA tiles in a similar protocol. His-tagged $F_1$-ATPase protein was purified, and labelled with biotin, by Tom Bilyard and Wi-Meng Ho, Berry Group, Department of Condensed Matter Physics, Oxford University. Tiles were pre-purified with hand-packed size-exclusion columns (2×) and transferred into a buffer compatible with $F_1$ (10 mM MOPS, 50 mM KCl, 2 mM $MgCl_2$, pH 7.0). Purified tiles (25 $\mu$L 50 nM) were incubated with $F_1$ (15 or 30 $\mu$L unknown stock concentration), $Ni^{2+}$ (3 $\mu$L 10 $\mu$M $NiSO_4$), and fluorescent streptavidin (Alexa 532, Invitrogen) (7.5 $\mu$L 10 $\mu$M), for 30 minutes at room temperature.

## A.10.3 $F_1$-ATPase rotation assay

### Protein binding

Rotation assays were performed with yeast $F_1$-ATPase. Purified and biotin-labelled His-tagged yeast $F_1$-ATPase was obtained from the Mueller Laboratory, Department of Biochemistry and Molecular Biology, Rosalind Franklin University of Medicine and Science, The Chicago Medical School. As for binding experiments,

NTA origami tiles were purified and transferred into an $F_1$ compatible buffer (10 mM MOPS, 50 mM KCl, 2 mM $MgCl_2$, 10.2 $\mu$M ATP pH 7.65). Purified tiles (30 $\mu$L 40 nM) were incubated with $F_1$ (2 $\mu$L estimated at 1.2 $\mu$M), $Ni^{2+}$ (2.16 $\mu$L 10 $\mu$M $NiSO_4$), and fluorescent streptavidin (Alexa 532, 4.8 $\mu$L 10 $\mu$M), for 30 minutes at room temperature. After incubation samples were purified again with hand-packed size-exclusion columns, either 2 or 4 times, to remove unbound $F_1$ and SA.

**Sample preparation**

Flow-cell chambers of $\sim$10 $\mu$L volumes were prepared as for light microscopy (Appendix A.7), with either plain glass or NTA coated coverslips (Bilyard, 2009). For control samples $F_1$ protein was added and incubated for 10 minutes. For origami samples, the purified samples described above were added and incubated for 10 minutes. Chambers were washed with 5 volumes of the $F_1$ buffer with 1 mg/ml BSA, incubated with DSP-streptavidin coated 60 nm gold beads ($F_1$ buffer, 1 mg/ml BSA) for 10 minutes, and then washed with 5 volumes again. Prior to imaging, 2 volumes of a rotation buffer was added to the chamber. This buffer is the same as the $F_1$ binding buffer, with an increased ATP concentration (3 mM) and an ATP regenerating system (20 unit/mL pyruvate kinase and 2 mM phosphoenolpyruvate). This is sufficient to keep the protein spinning for up to 1 hour of observation. Samples were then imaged by laser dark-field microscopy (Figure A.2).

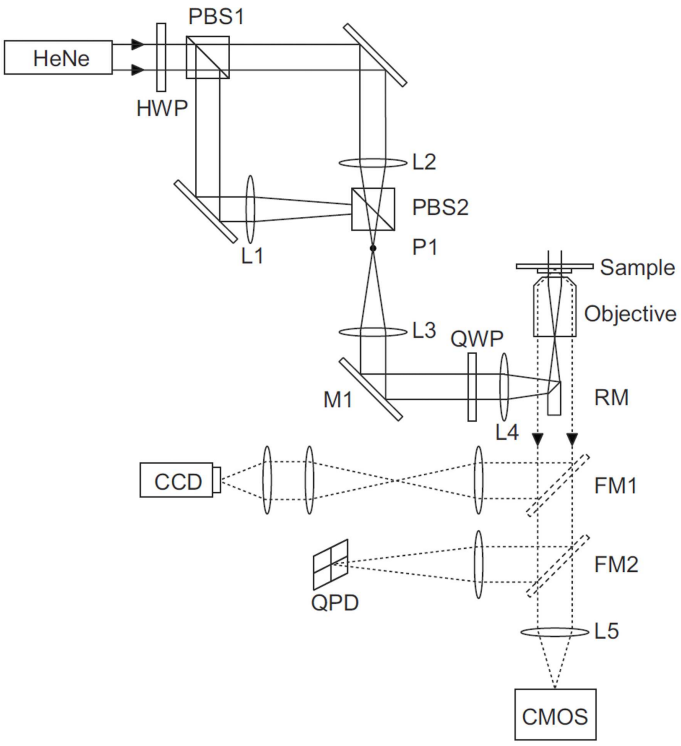


Figure A.2: Optical setup for a backscattering laser dark-field microscope (Sowa et al., 2010). This microscope has been used to show stepping behaviour of yeast $F_1$ (Bradley Steel, Unpublished data, 2010), and was used in Chapter 6. Light from a HeNe laser (633 nm) is focused onto the back focal plane of the objective lens via the small rod mirror (RM). The sample plane is illuminated with light parallel to the optic axis, and scattered light (dotted lines) from the sample is collected using the same objective lens as for illumination. The ring of scattered light that passes the RM is focused onto the high-speed camera (CMOS).

Appendix B

# Motor triggered Junctions - Additional Data

This Appendix contains additional experimental results for the motor-catalysed junctions discussed in Chapter 5. Several junction designs were tested and found to produce only a very small bias between the right and left hand paths of a single-junction track. The PAGE analysis of these unsuccessful designs, briefly discussed in Section 5.3, is given in this Appendix. This work assisted in the design the successful motor-catalysed system presented in Section 5.4.

## B.1 Motor-catalysed Hairpin block and release

Figure B.1 gives a schematic for an alternative version of the hairpin block and release motor design in Figure 5.11. In this design the catalyst strand is freely diffusing, rather than tethered to the motor. Both variations are analysed by PAGE, in Section B.1.1 below. The ensemble fluorescence results in Section 5.3.2 of the main text are for the freely diffusing catalyst.

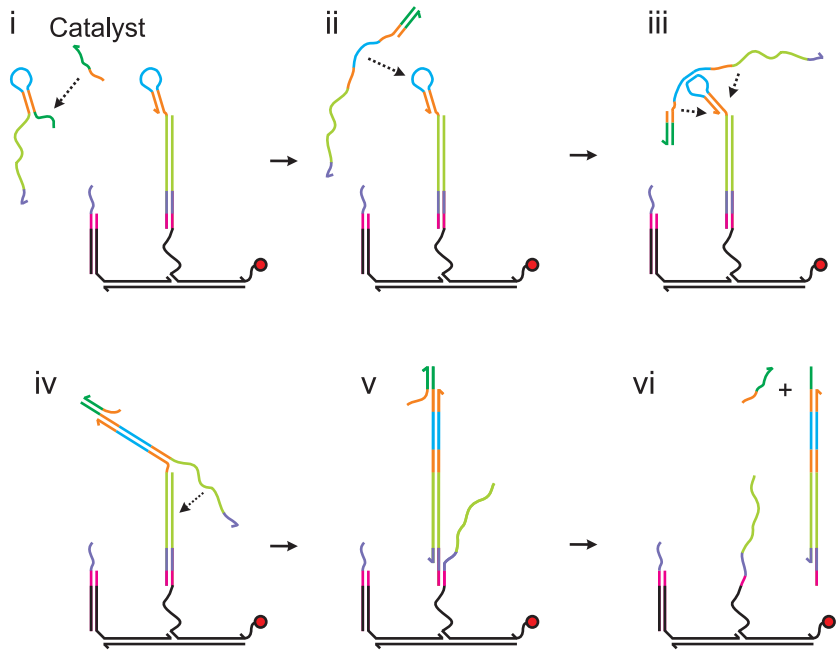


Figure B.1: Schematic for a hairpin block and release strand design with a freely diffusing catalyst. **i** The toehold (blue) to remove the block from the stator is hidden in a hairpin (orange); the complementary region of the release strand also forms a hairpin. The two hairpin sequences interact slowly due to their secondary structure. **ii** The release hairpin contains a second toe-hold (dark green) that interacts with a catalyst strand (dark green + orange) to open up the loop. **iii-v** The open release loop interacts with the loop in the block hairpin, and opens it. **vi-vii** The release strand removes the block from the stator.

### B.1.1 PAGE analysis

Strands with the required secondary structure were designed with two loop lengths, 12 nt and 14 nt. For each loop length there are two sets of block and release strands (R and L), one for each path downstream of the junction. PAGE analysis was used to test the proposed unblocking mechanism on a short test track (Figure B.2).

Blocked tracks annealed with the release strand show complete unblocking of both R and L-tracks in all gels, confirming that all tracks will unblock eventually. Without catalyst, 10 minutes after the addition of the release strand, bands corresponding to both blocked and unblocked track are observed. This indicates that the the track has started to unblock through a leakage reaction. This leakage increases with the loop length, and is present to a much greater degree for the R-track. In the presence of either catalyst or motor-catalyst, the R-track is almost completely unblocked, but the L-track is only very slightly unblocked. Overall the gel results are not ideal: the leakage for the R-stator is high, and the catalysed reaction for the L-stator is slow.

## B.2 Motor-catalysed Loop block

The second design discussed in Section 5.3.1 is for a block strand with a loop, or bulge. Strands were designed with 4 different loop lengths (6, 8, 10 or 12 nt) and two release types (long and short), for each of the two downstream paths (R and L). The long release strands have an additional 2 nt of the block toe-hold sequence, to promote dissociation of the block-release duplex from the motor.

### B.2.1 PAGE analysis

The large number of possible combinations were tested by PAGE analysis on a short test track. The four loop lengths were tested with the long release strand

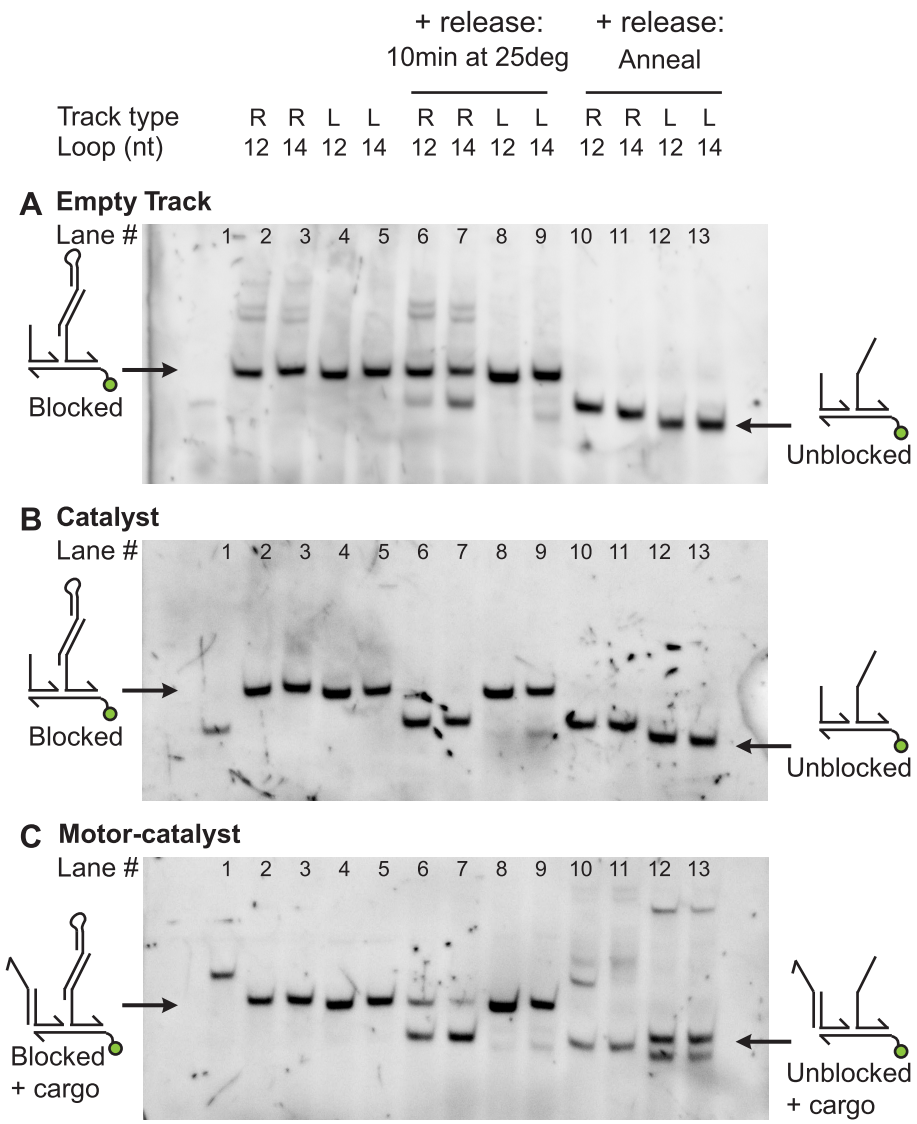


Figure B.2: PAGE Analysis of the hairpin block and release design. Short test tracks are prepared with one blocked stator (Lanes 2-5). Release strands are added to the blocked tracks, and incubated for 10 minutes (Lanes 6-9) or annealed (Lanes 10-13). Lane 1 is an unblocked track control. Hairpin loop lengths of 12 and 14 nt are tested for both the R and L tracks. The three gels show the difference between **A** no motor, **B** the catalyst in solution, and **C** a motor-bound catalyst strand. The gel bands are visualised by a FAM label on the short test track (Figure B.1), and the position of blocked and unblocked tracks are indicated.

for both R and L tracks in the absence of motor strand (Figure B.3), and with the correct motor strand (Figure B.4). In all cases, blocked tracks annealed with the release strand are completely unblocked, as designed. When blocked track are incubated at 25°C with the release for 10 minutes, the amount of unblocked track observed is a measure of the rate of the reaction.

For tracks with no motor, any unblocking detected is due to the leakage reaction between the release and block. Leakage was found to increase with loop length, and to be worse for R-tracks than for L-tracks (Figure B.3). Addition of the correct motor-catalyst dramatically increases the amount of unblocked track, for all loop lengths of both R- and L-tracks (Figure B.4). Thus, the motor strand efficiently catalyses unblocking of the stator. Tracks were also tested with the incorrect motor strand, that is, the R-track is tested with an L-motor designed to unblock an L-track and vice versa (Figure B.5). The amount of unblocking in the presence of the incorrect motor was the same as for no motor. This confirms there is no additional leakage due to interaction of the motor with the incorrect track, and that all leakage is due to release strand in solution interacting directly with the block strand. Thus, the R-motor and L-motor correctly catalyse the opening of only the R-track and L-track respectively, and for loops lengths of 6 or 8 nt have a relatively small amount of leakage.

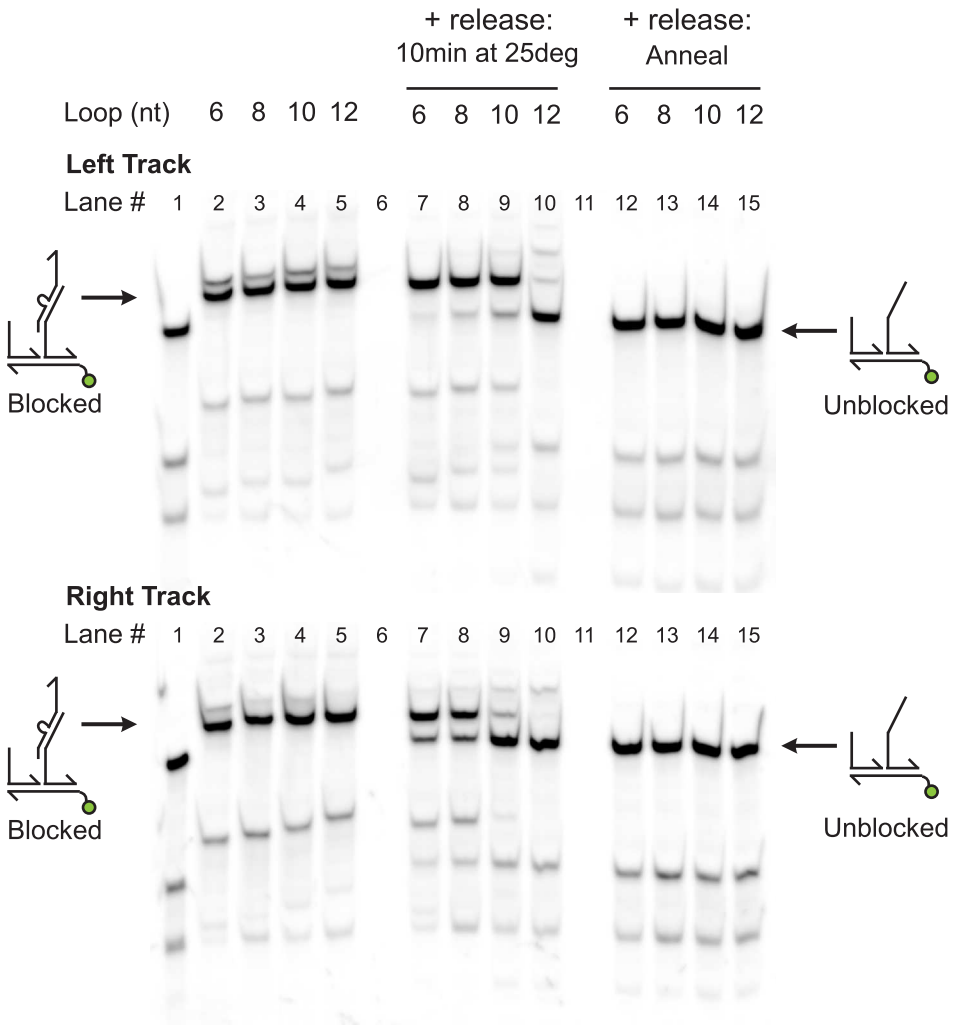


Figure B.3: PAGE Analysis of the loop block design with no motor strand (Figure 5.12). Short test tracks are prepared with one blocked stator (Lanes 2-5). Release strands are added to the blocked tracks, and incubated at 25°C for 10 minutes (Lanes 7-10) or annealed (Lanes 12-15). Lane 1 is an unblocked track control. Loop lengths of 6, 8, 10 and 12 nt are tested for both the L (top gel) and R (bottom gel) tracks. The gel bands are visualised by a FAM label on the short test track (Figure B.1), and the position of blocked and unblocked tracks are marked. The leak reaction between block and release in the absence of a loop-opening catalyst is observed in the incubated samples. Leakage increases with loop length, and is worse for the R-track than the L-track.

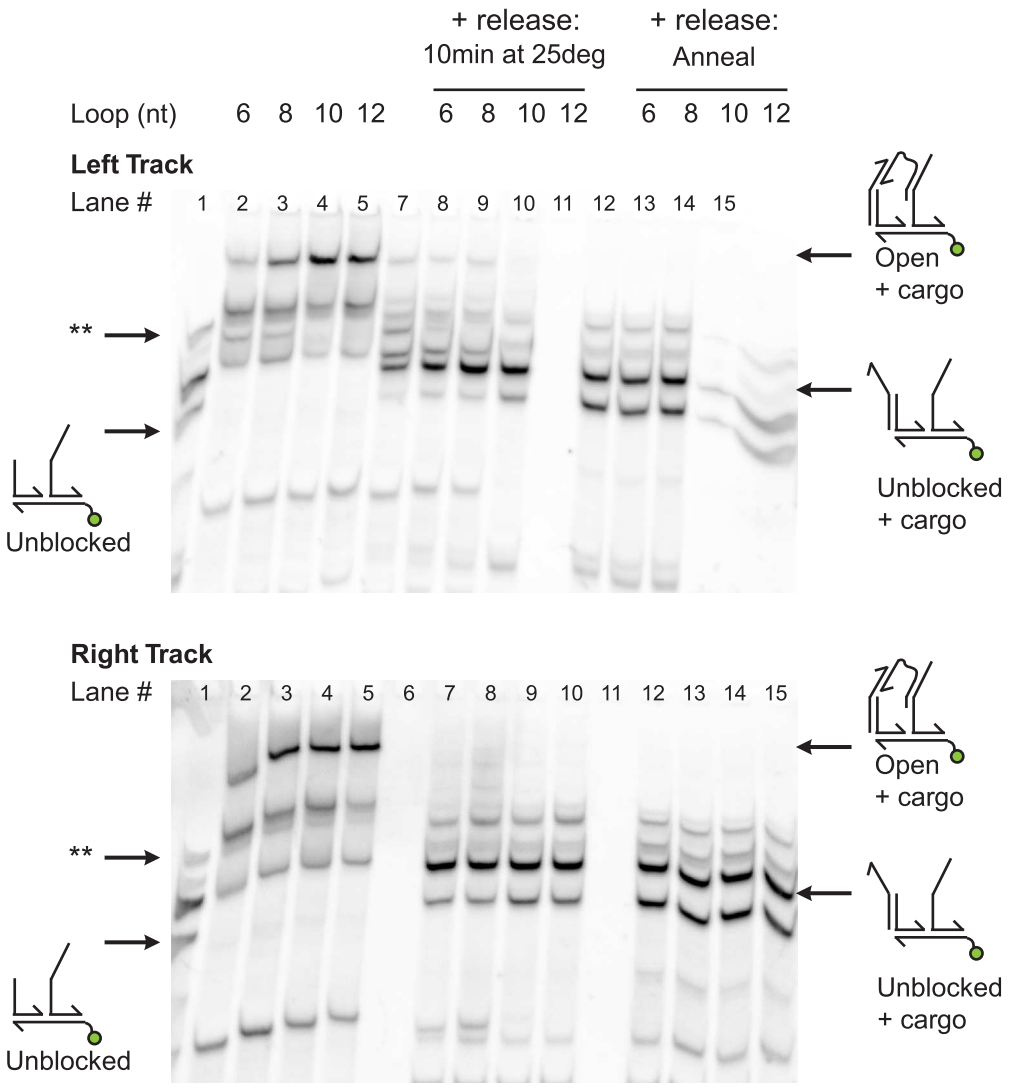


Figure B.4: PAGE Analysis of the loop block design with the correct motor strand (Figure 5.12). Blocked test tracks with motor strand (Lanes 2-5) are incubated (Lanes 7-10) or annealed (Lanes 12-15) with the release strand. Lane 1 is an unblocked track control. Loop lengths of 6, 8, 10 and 12 nt are tested for both the L (top gel) and R (bottom gel) tracks. Incubated samples show a much greater amount of unblocking with the motor than without (Figure B.3). The motor catalyses unblocking of the stator, as it is designed to do. A small amount of the blocked track samples were initially occupied by 0 or 2(**) motor strands, resulting in additional bands.

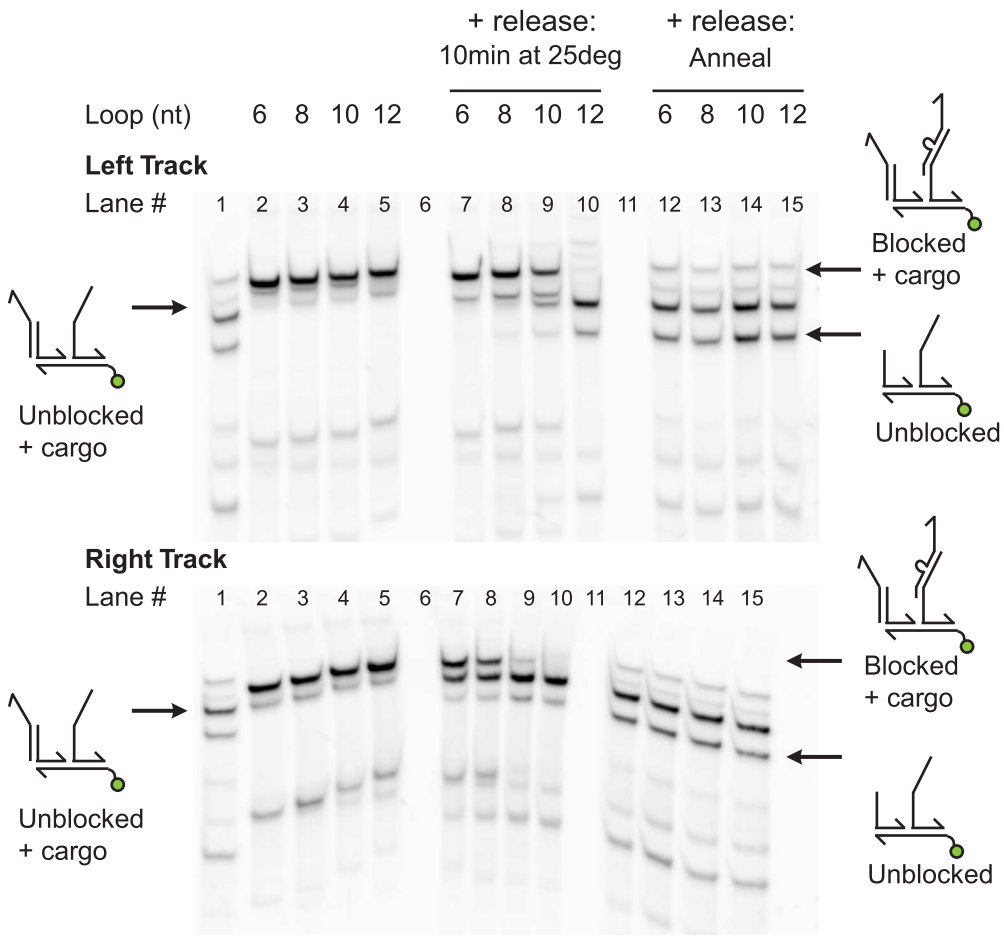


Figure B.5: PAGE Analysis of the loop block design with the wrong motor strand (Figure 5.12). Blocked test tracks are formed with the motor strand for the other track, R-motor + L-track and vice versa (Lanes 2-5). Samples are incubated (Lanes 7-10) or annealed (Lanes 12-15) with the release strand. Lane 1 is an unblocked track control. Loop lengths of 6, 8, 10 and 12 nt are tested for both the L (top gel) and R (bottom gel) tracks. Incubated samples show a similar amount of unblocking as the no motor samples in Figure B.3. The motor is not catalysing unblocking of the incorrect stator, and the leakage is due to the release and block strand interacting directly.

Appendix C

# DNA sequences

Synthetic DNA strands were purchased from Integrated DNA Technologies (IDT). Unmodified staples were purchased unpurified. Track staples were purchased PAGE-purified. Strands labelled with fluorophores or quenchers were purchased HPLC-purified; JOE, Cy3, Cy5, Cy5.5, IowaBlackRQ. Staples labelled with the fluorophore Cy3.5 were purchased unpurified with 3' amine modification and conjugated to Cy3.5 NHS ester dye (GE Healthcare) following manufacturers instructions, then purified by reverse-phase HPLC.

## C.1 DNA origami designs

### C.1.1 Original rectangle with seam

Staple strands for the original origami rectangle with seam are exactly as listed in (Rothemund, 2006), Supplementary Information File 1, page 28. Modified staples that are based on this design are indicated below.

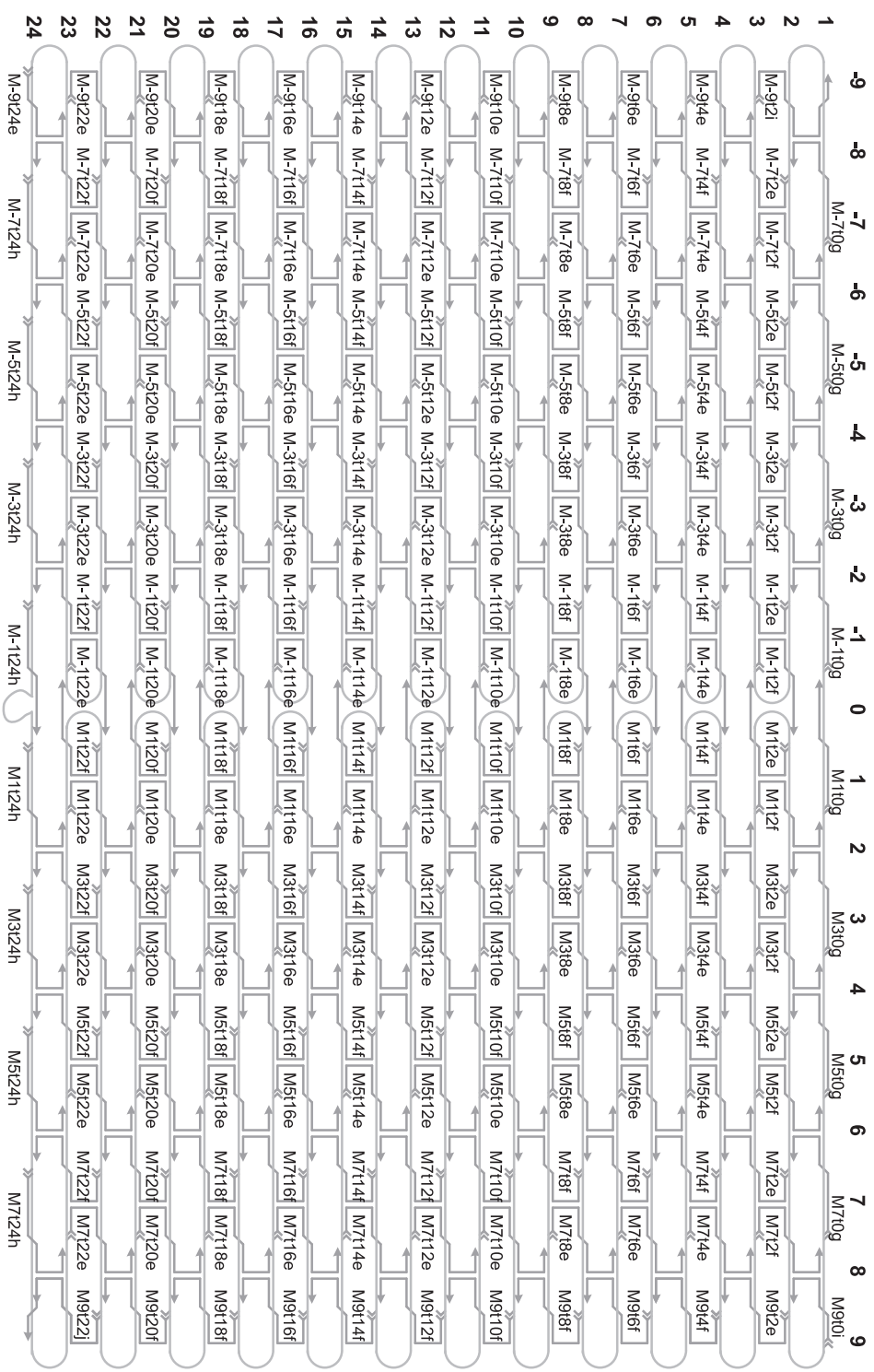


Figure C.1: Reduced twist origami tile. Staple sequences are in Table C.1.2.

### C.1.2 Reduced twist origami tile

Staple strands for the reduced twist origami designed in this thesis are given in Table C.1.2. The naming convention follows (Rothemund, 2006) (Figure C.1). For example, staple 'M-7t20e' is located on the left-hand side of the tile at the 7th crossover from the central seam, and has its longest section on the 20th helix from the top of the tile.

Unmodified staple strands for reduced twist rectangular origami tile, tile type B (Figure C.1)

| Name | Sequence |
|---|---|
| M1t0g | ATTCCACAGACAGCCCTCATAGTTAGCGTAA |
| M1t2f | GGATTAGGAGAGGCTGAGACTCCTGCATAACC |
| M1t2e | AAGTATTAATTAGCGGGGTTTTGCCTGTAGC |
| M1t4f | GCATTGACGAACCACCACCAGAGCGGAGATTT |
| M1t4e | CGCCACCAAGGAGGTTGAGGCAGAAACATGA |
| M1t6f | TTAGCAAGAATCACCAGTAGCACATTGGGCT |
| M1t6e | GCCAGCAAGCCGGAAACGTCACCCTCAGAGC |
| M1t8f | TCCTTATTAAAAGAACTGGCATGATAGCGAG |
| M1t8e | GAATACCCACGCAGTATGTTAGCGAATTAGA |
| M1t10f | TACAGAGAGTCAAAAATGAAAATAGGAAGCAA |
| M1t10e | TGTTTAACGAATAACATAAAAACTAATAACG |
| M1t12f | GCGCCCAATTTTCATCGTAGGAAAGGTGGCA |
| M1t12e | CGTTTTTATAGCAAGCAAATCAGCGATTTTT |
| M1t14f | CCAGTAATATTTAGGCAGAGGCAAATATGAT |
| M1t14e | AACATGTAAAGAGAATATAAAGTAAAGCAAGC |
| M1t16f | CCAATCGCTATATGTAAATGCTGCCAATAGG |
| M1t16e | TATATAACAAGACAAAGAACGCGACAACGCC |
| M1t18f | TCAAGAAAAAAAGAAGATGATGATTCAGGCT |
| M1t18e | ACCTGAGCACAAAATTAATTACATGGTTGGGT |
| M1t20f | ATGGCAATATCATATTCCTGATTCATAAAGT |
| M1t20e | GAATTATCTCATCAATATAATCCTTTCAATT |
| M1t22f | CAATCAATCTGAACCTCAAATATTGGTTCCG |
| M1t22e | TCACCTTGATCTGGTCAGTTGGCAAAGGAGCG |
| M1t24h | TAATAAAAGGGACATTCTGGCCACTAAAGCA |
| M3t0g | TCGTCACCAGTACAAACTACAACGCTCAGTAC |

to be cont'd on next page

Table C.1: Reduced twist origami DNA sequences

| Name (cont.) | Sequence (cont.) |
|---|---|
| M3t2f | CAGGCGGAGAACCTATTATTCTGGTCAGACG |
| M3t2e | CTATTTCGTAAGTGCCGTCGAGAACTGAGTT |
| M3t4f | ATTGGCCTCTCAGAGCCACCACCAATGAAAC |
| M3t4e | CCGCCACCTGATATTCACAAACAACCCCCTGC |
| M3t6f | CATCGATAGACTTGAGCCATTTGGAAACGTAG |
| M3t6e | CCGTCACCGCAGCACCGTAATCACCTCAGAA |
| M3t8f | AAAATACAACCGAGGAAACGCAAAGGGAAGC |
| M3t8e | AGAAGGAATACATAAAGGTGGCAAATTATCA |
| M3t10f | GCATTAGAAATCCAAATAAGAAAATATAGAA |
| M3t10e | TTTATCCCCGGGAGAATTAACTGAAGTTACC |
| M3t12f | GGCTTATCGCACTCATCGAGAACCCGACAAA |
| M3t12e | CAAGTACCCGGTATTCTAAGAACGCCATATTA |
| M3t14f | AGGTAAAGGAATCGCCATATTTAAGAAAACT |
| M3t14e | TTAATTGATAATTCTGTCCAGACTATTAAAC |
| M3t16f | TTTTCAAATTAACCTCCGGCTTATTAACAAT |
| M3t16e | CTACCTTTTATATTTTAGTTAATTAGTAGGGC |
| M3t18f | TTCATTTGGAGGCGAATTATTCATGATTGTT |
| M3t18e | ATCGCGCAAATTACCTTTTTTAACTGAGAGA |
| M3t20f | TGGATTATACAAAGAAACCACCAGAATCAACA |
| M3t20e | TTTGCGGAACTTCTGAATAATGGGTTACAAA |
| M3t22f | GTTGAAAGCAGCAAATGAAAAATACAGAGAT |
| M3t22e | AGAGCCAGGAATTGAGGAAGGTTATTATCAT |
| M3t24h | AGAACCCTTCTGACCTGAAAGCGCCACGCTG |
| M5t0g | AATAGGAACCCATGTACCGTAACGGGTTGAT |
| M5t2f | ATAAGTATTATAAACAGTTAATGATAAATCC |
| M5t2e | AGTGCCCGAGCCCGGAATAGGTGTGCAAGCCC |
| M5t4f | TCATTAAACCTCAGAGCCGCCACGTAGCGAC |
| M5t4e | ACCGCCTCGCCAGAATGGAAAGCTGAGTAAC |
| M5t6f | AGAATCAATATTCATTAAAGGTGACATATAA |
| M5t6e | ACGGAAATGTTTGCCTTTAGCGTCCACCGGA |
| M5t8f | AAGAAACGGCAGATAGCCGAACAAACACCCT |
| M5t8e | AAAAGTAACAAAGACACCACGGAAAAATATTG |
| M5t10f | GAACAAAGTTACAAAATAAACAGCGAGGCGT |
| M5t10e | TTTGCCAGTCAGAGGGTAATTGAGTTTTTAAG |
| M5t12f | TTTAGCGACATTCCAAGAACGGGGACGACAA |
| M5t12e | TTCCTTATACCTCCCGACTTGCGGAGCCTAA |
| M5t14f | TAAACAACAAAGCCAACGCTCAACTCATCTTC |
| M5t14e | ACCAGTATATGTTCAGCTAATGCGGCTGTCT |

to be cont'd on next page

Table C.1: Reduced twist origami DNA sequences

| Name (cont.) | Sequence (cont.) |
|---|---|
| M5t16f | TGACCTAAATCAAAATCATAGGTTGGAAACA |
| M5t16e | GTGAATTTATTTAATGGTTTGAAAAATTCTT |
| M5t18f | GTACATAATTGCTTTGAATACCAAAAGGGTTA |
| M5t18e | TCGCCTGAATCAATATATGTGAGAGTCAATA |
| M5t20f | GAACCTACAAAAGTTTGAGTAACATCTAAAA |
| M5t20e | TTAATTTTCATATCAAAATTATTTAACGGAT |
| M5t22f | TATCTTTAACCGCCTGCAACAGTGTAAGAATA |
| M5t22e | GTATTAACGGAGCACTAACAACTGAACGTTA |
| M5t24h | CGTGGCACAGACAATATTTTTGAGGCGGTCA |
| M7t0g | CACCACCCTCATTTTCAGGGATAATCACCGT |
| M7t2f | ACTCAGGAACGGGGTCAGTGCCTGCAGTCTC |
| M7t2e | AAGTTTTAGGTTTAGTACCGCCACTCAGAGC |
| M7t4f | TGAATTTACCGGAACCAGAGCCACAGACTGT |
| M7t4e | CAAAATCACCGTTCCAGTAAGCGCTGGTAAT |
| M7t6f | AGCGCGTTTGAGGGAGGGAAGGTTAAGTTTA |
| M7t6e | CAACCGATTTCATCGGCATTTTCGTTCATAAT |
| M7t8f | TTTTGTCATATCTTACCGAAGCCCCGCTAATA |
| M7t8e | GCAATAGCCAATCAATAGAAAATGCGACATT |
| M7t10f | TCAGAGAGACGAGCGTCTTTCCAGGAGGTTT |
| M7t10e | CAACGCTAATAACCCACAAGAATATGAAATA |
| M7t12f | TGAAGCCTAACCAATCAATAATCAGAACGCG |
| M7t12e | CATGTAGATAAATCAAGATTAGTTAATCTTAC |
| M7t14f | CCTGTTTATCATATGCGTTATACATACCGAC |
| M7t14e | GTTTAGTATCAACAATAGATAAGTTTACGAG |
| M7t16f | CGTGTGATTTAAGACGCTGAGAAGTGAATAAC |
| M7t16e | AGCTTAGAAAATAAGGCGTTAAAAAAAGCCT |
| M7t18f | CTTGCTTCCATCGGGAGAAACAATGCACGTA |
| M7t18e | ACCTTTTATGTAAATCGTCGCTAATAGCGAT |
| M7t20f | AAACAGAATTAAATCCTTTGCCCAATAGATT |
| M7t20e | AACTCGTAATAAAGAAATTGCGTAGTAACAGT |
| M7t22f | AGAGCCGTATAAAACAGAGGTGAATGGCTAT |
| M7t22e | AGCAGAAGCAATAGATAATACATAATTCGAC |
| M7t24h | TAGTCTTTAATGCGCGAACTGATAGAACCACC |
| M-1t0g | CGATCTAAAGTTTTGTCGTCTTTTTGCGCCG |
| M-1t2f | ACAATGACCGGTCGCTGAGGCTTCGATTATA |
| M-1t2e | GATATATTAACAACCATCGCCCACCAAGAGAA |
| M-1t4f | CCAAGCGCGCCTGATAAATTGTGCCCTGACG |
| M-1t4e | GTATCATCGAAACAAAGTACAACCGCCGCCA |

to be cont'd on next page

Table C.1: Reduced twist origami DNA sequences

| Name (cont.) | Sequence (cont.) |
|---|---|
| M-1t6f | AGAAACACTTTAATTTCAACTTTACCTCGTTT |
| M-1t6e | TGAGATGGCAGAACGAGTAGTAACATTACCA |
| M-1t8f | ACCAGACGGCAAAAGAAGTTTTGTTTTAATT |
| M-1t8e | AGGCTTTTACGATAAAAACCAAAATTAAGAC |
| M-1t10f | CGAGCTTCAGGTCAGGATTAGAGGCTATATT |
| M-1t10e | ACTCCAACAAAGCGAACCAGACCGCAGCCTT |
| M-1t12f | TTCATTTGACTAATAGTAGTAGCAGAGAAAGG |
| M-1t12e | TCAATTCTGGGCGCGAGCTGAAATCATTACC |
| M-1t14f | CCGGAGACGTTCTAGCTGATAAATTAAATTT |
| M-1t14e | ATTCAACCAGTCAAATCACCATCTTTTCGAG |
| M-1t16f | TTGTTAAACAAAAATAATTCGCGTGCCGGAA |
| M-1t16e | AACGCCATTCAGCTCATTTTTTAAATGCAAAT |
| M-1t18f | ACCAGGCAGTTGGGAAGGGCGATCTCACAAT |
| M-1t18e | GCGCAACTAAGCGCCATTCGCCAAACAAACA |
| M-1t20f | TCCACACATGGGGTGCCTAATGATGCCCCAG |
| M-1t20e | GTAAAGCCACATACGAGCCGGAAGATCAGATG |
| M-1t22f | CAGGCGAAAAAATCCCTTATAAATAGCGGTC |
| M-1t22e | AAATCGGCAATCCTGTTTGATGGCAAACCCT |
| M-1t24h | ACGCTGCGCGTAACCACCACACCCACGACCAG |
| M-3t0g | TAGTAAATGAATTTTCTGTATGGGGTGAATTT |
| M-3t2f | CTTAAACACGCTTTTGCGGGATCAATACACT |
| M-3t2e | TTAAAGGCGCTTGATACCGATAGCCAGACGT |
| M-3t4f | AAAACACTGCTCCATGTTACTTAACAAAGCT |
| M-3t4e | CGCGACCTCATCTTTGACCCCCAGGCAGGGAG |
| M-3t6f | GCTCATTCTTATGCGATTTTAAGCGAGGCAT |
| M-3t6e | GAATTACCAGTGAATAAGGCTTGTCGAAATC |
| M-3t8f | AGTAAGAGTAAAATGTTTAGACTGAGAGGAAG |
| M-3t8e | GGTAATAGCAACACTATCATAACATCATTGT |
| M-3t10f | CCCGAAAGCCTTTTGATAAGAGGTACATTTC |
| M-3t10e | TAATTGCTACTTCAAATATCGCGCCAGAGGG |
| M-3t12f | GCAAATGGCATACAGGCAAGGCAAGAGTAATG |
| M-3t12e | CAATAAATTCAATAACCTGTTTAAGTACCTT |
| M-3t14f | TGTAGGTATAGCTATTTTTGAGATGTAAACG |
| M-3t14e | GGAGAGGGAAGATTCAAAAGGGTTTAACATC |
| M-3t16f | TTAATATTCCAGCTTTCATCAACCACTCCAG |
| M-3t16e | TCCTGTAGTTGTTAAAATTCGCATTAATGCC |
| M-3t18f | CCAGCTTTGCTATTACGCCAGCTATAGCTGT |
| M-3t18e | GCCTCTTCCCGGCACCGCTTCTGGTCTGGCCT |

to be cont'd on next page

Table C.1: Reduced twist origami DNA sequences

| Name (cont.) | Sequence (cont.) |
|---|---|
| M-3t20f | TTCCTGTGTAATTGCGTTGCGCTAGAGAGTT |
| M-3t20e | ACTCACATTGAAATTGTTATCCGCGGTGCGG |
| M-3t22f | GCAGCAAGAGATAGGGTTGAGTGTAAAGGAGC |
| M-3t22e | ATAGCCCGCGGTCCACGCTGGTTGTGAGCTA |
| M-3t24h | GGGCGCTAGGGCGCTGGCAAGTGTCAAAAGA |
| M-5t0g | AAACAACTTTCAACAGTTTCAGCAATTGTAT |
| M-5t2f | CGGTTTATAAAGACAGCATCGGAAAGGCACCA |
| M-5t2e | CAGCAGCGCAGCTTGCTTTCGAGATTTTGCT |
| M-5t4f | ACCTAAAAGACGGTCAATCATAAAGAACCGG |
| M-5t4e | GAGGCGCACGAAAGAGGCAAAAGGTCACCCT |
| M-5t6f | ATATTCATCAGTCAGGACGTTGGTAATGCAG |
| M-5t6e | CATTATACTACCCAAATCAACGTAGCCGGAAC |
| M-5t8f | ATACATAAGCGGAATCGTCATAACAGAAGCA |
| M-5t8e | CCAATACTCGCCAAAAGGAATTAAACTGGCT |
| M-5t10f | AAGCGGATCTTAGAGCTTAATTGGCGAACGA |
| M-5t10e | GCGGATGGTGCATCAAAAAGATTAGATAGCGT |
| M-5t12f | GTAGATTTAGCAATAAAGCCTCATAGAACCC |
| M-5t12e | CAAAATTAAGTTTGACCATTAGATCATTTTT |
| M-5t14f | TCATATATCAGGTCATTGCCTGAACAGGAAG |
| M-5t14e | AAGGCTATTTTAAATGCAATGCCTAGAATTAG |
| M-5t16f | ATTGTATATAACAACCCGTCGGATGACGACGA |
| M-5t16e | TGAGCGAGAGCAAATATTTAAATGATCTACA |
| M-5t18f | CAGTATCGGCTGCAAGGCGATTAGGGTACCG |
| M-5t18e | GGGGATGTGCCTCAGGAAGATCGATTAAATG |
| M-5t20f | AGCTCGAAGTCGGGAAACCTGTCGACAGCTGA |
| M-5t20e | GCTTTCCATTCGTAATCATGGTCGGCGAAAG |
| M-5t22f | TTGCCCTTAAGAGTCCACTATTAGAACGTGG |
| M-5t22e | TTTGGAACCACCGCCTGGCCCTGCACTGCCC |
| M-5t24h | CGAGAAAGGAAGGGAAGAAAGCGTGTTCCAG |
| M-7t0g | AATAGAAAGGAACAACTAAAGGACTCCAAAA |
| M-7t2f | AAAAGGCTTACAGAGGCTTTGAGTAAACGGG |
| M-7t2e | GCAACGGCCCAAAAGGAGCCTTTGGAGTGAG |
| M-7t4f | TAAAATACAACTTTGAAAGAGGACTGGCTGAC |
| M-7t4e | AACTGACCGTAATGCCACTACGACGAGGGTA |
| M-7t6f | CTTCATCATAATAAAACGAACTAATCAGTTG |
| M-7t6e | ATCTACGTAGAGTAATCTTGACAGGGAACCG |
| M-7t8f | AGATTTAGCCTCAAATGCTTTAAAAAATCAG |
| M-7t8e | TGAATCCCGAATACCACATTCAACGAAGAAAA |

to be cont'd on next page

Table C.1: Reduced twist origami DNA sequences

| Name (cont.) | Sequence (cont.) |
|---|---|
| M-7t10f | GTCTTTACAGCTCAACATGTTTTATCATTCCA |
| M-7t10e | AATGCTGTCCTGACTATTATAGTATATTCAT |
| M-7t12f | TATAACAGCGGTTGTACCAAAAAGCCTTTAT |
| M-7t12e | AGCTAAATTTGATTCCCAATTCTCTGAATAT |
| M-7t14f | TTCAACGCAGAGAATCGATGAACGACCCCGGT |
| M-7t14e | AGCAAACAAAGGATAAAAATTTTGAGCATAA |
| M-7t16f | TGATAATCCGGCGGATTGACCGTCATCGTAA |
| M-7t16e | GGAACAAAAGAAAAGCCCCAAAAGAGTCTGG |
| M-7t18f | CCGTGCATGGTTTTCCCAGTCACGCATGCCTG |
| M-7t18e | AACGCCAGCTGCCAGTTTGAGGGTCTCCGTG |
| M-7t20f | CAGGTCGAGAATCGGCCAACGCGGGTGGTTT |
| M-7t20e | GCATTAATCTCTAGAGGATCCCCAGTTGGGT |
| M-7t22f | TTCTTTTCACGTCAAAGGGCGAACCCGATTT |
| M-7t22e | GGACTCCAACCAGTGAGACGGGCATGCCAGCT |
| M-7t24h | AGAGCTTGACGGGGAAAGCCGGCAAGAACGT |
| M9t0i | TTTTCCTCAGAACCGCCACCCCCTCAGA |
| M9t2f | ACCGCCACTTTTATGATACAGGAGTGTATCATACAT |
| M9t4f | GGCTTTTGTTTTTAGCGTTTGCCATCTTGTCATAGC |
| M9t6f | CCCCTTATTTTTCGCCAAAGACAAAAGGTCATATGG |
| M9t8f | TTTACCAGTTTTATAAGAGCAAGAAACATGAGTTAA |
| M9t10f | GCCCAATATTTTCTACAATTTTATCCTGGCTATTTT |
| M9t12f | GCACCCAGTTTTTAATATCCCATCCTAATCCTGAAC |
| M9t14f | AAGAAAAATTTTAATCATAATTACTAGATAAGAATA |
| M9t16f | AACACCGGTTTTTAGAATCCTTGAAAACTTAATTAA |
| M9t18f | TTTTCCCTTTTTGTCAGATGAATATACAGATTTTCA |
| M9t20f | GGTTTAACTTTTATTAGACTTTACAAACTTGAGGAT |
| M9t22j | TTAGAAGTTTTTATTAAAAATACCGAACGCCCTAAAACATCGCCTTTT |
| M-9t2i | ACTTTTTCTTTTTTTTCACGTTGAAAATATTGCGAATAATAATTTTTT |
| M-9t4e | GGTGTACATTTTATGAGGAAGTTTCCATGACTAAAG |
| M-9t6e | ACATTATTTTTTGACCAGGCGCATAGGCAGATGAAC |
| M-9t8e | GAAAACGATTTTACAGGTAGAAAGATTCACGGAACA |
| M-9t10e | ACTAAAGTTTTTGAATGACCATAAATCAACAGTTCA |
| M-9t12e | CCCTGTAATTTTACGGTGTCTGGAAGTTAATATGCA |
| M-9t14e | AAAACTAGTTTTTACTTTTGCGGGAGAACATTATGA |
| M-9t16e | AGGTCACGTTTTCATGTCAATCATATGTGTAATCGT |
| M-9t18e | AAACGACGTTTTTTGGTGTAGATGGGCGAATGGGAT |
| M-9t20e | GGCGGTTTTTTTGCCAGTGCCAAGCTTGACGTTGTA |
| M-9t22e | TATCACGGTTTTGCGTATTGGGCGCCAGCGGGGAGA |

to be cont'd on next page

Table C.1: Reduced twist origami DNA sequences

| Name (cont.) | Sequence (cont.) |
|---|---|
| M-9t24j | TTTTAACCCTAAAGGGAGCCAAACCGTC |
| Mem1 | TATTTACATTGGCAGATTCACCAGTCAC |
| Mem2 | TTTTGACGCTCAATCGTCTGAAATGGAT |
| Mem3 | AGGAAAAACGCTCATGGAAATACCTACA |
| Mem4 | AACAATATTACCGCCAGCCATTGCAAC |
| Mem5 | ACTATCGGCCTTGCTGGTAATATCCAG |
| Mem6 | ATCACTTGCCTGAGTAGAAGAACTCAA |
| Mem7 | AGCAATACTTCTTTGATTAGTAATAAC |
| Mem8 | GCCGCGCTTAATGCGCCGCTACAGGGC |
| Mem9 | GCGTACTATGGTTGCTTTGACGAGCAC |
| Mem10 | GTATAACGTGCTTTCCTCGTTAGAATC |
| Mem11 | AGAGCGGGAGCTAAACAGGAGGCCGAT |
| Mem12 | TAAAGGGATTTTAGACAGGAACGGTAC |
| Mem13 | GCCAGAATCCTGAGAAGTGTTTTTATA |
| Mem14 | ATCAGTGAGGCCACCGAGTAAAAGAGT |
| Mem15 | CTGTCCATCACGCAAATTAACCGTTGT |
| End of Table | |

## C.2 Oligos for Chapter 2

The biotin modified staple strands, and the TAMRA fluorophore-labelled staple are listed in Table C.2. These strands are based on tile design A, staple locations are indicated in the strand name.

Modified Staple Sequences used in Chapter 2

| Name | Sequence |
|---|---|
| r1t4e-5'biotin | /5Biosg/AACCAGAGACCCTCAGAACCGCCAGGGGTCAG |
| r7t20f-5'biotin | /5Biosg/CGGAATTATTGAAAGGAATTGAGGTGAAAAAT |
| r-7t14e-5'biotin | /5Biosg/TCAGGTCACTTTTGCGGGAGAAGCAGAATTAG |
| r-7t4e-3'TAMRA | GCTCCATGAGAGGCTTTGAGGACTAGGGAGTT/36-TAMSp/ |
| End of Table | |

# C.3 Oligos for Chapter 3

## C.3.1 Fluorescence experiments, Section 3.2

Modified staple sequences for the ensemble fluorescence experiments are given in Table C.3.1. Initial experiments were on tile type A (Figures 3.4 and 3.5). The rest of the results use tile type B. Both sets of staples are listed, colour codes refer to those used in Figure 3.3.

Modified Staple Sequences for Chapter 3 ensemble fluorescence experiments

| Name | Sequence |
|---|---|
| **Tile A design** | |
| Track Staples | |
| S1I (r-7t2f) | GGAACCTCAGCCCAACTAACATCGTTT |
| | GAGAATAGCTTTTGCGGGATCGTCGGGTAGCA |
| S2 (r-7t2e) | ACCATTCATACTCTATCCCCGGAACCTCAGCCCAACTAACATTTT |
| | AAAGGCCGAAAGGAACAACTAAAGCTTTCCAG |
| S3 (r-5t4f) | ACCATTCATACTCTATCCCCGGAACCTCAGCCCAACTAACATTTT |
| | TTTCATGAAAATTGTGTCGAAATCTGTACAGA |
| S4 (r-5t4e) | ACCATTCATACTCTATCCCCGGAACCTCAGCCCAACTAACATTTT |
| | CGCCTGATGGAAGTTTCCATTAAACATAACCG |
| S5 (r-3t6f) | ACCATTCATACTCTATCCCCGGAACCTCAGCCCAACTAACATTTT |
| | AGTAATCTTAAATTGGGCTTGAGAGAATACCA |
| S6 (r-3t6e) | ACCATTCATACTCTATCCCCGGAACCTCAGCCCAACTAACATTTT |
| | ACGAGTAGTGACAAGAACCGGATATACCAAGC |
| S7 (r-1t8f) | ACCATTCATACTCTATCCCCGGAACCTCAGCCCAACTAACATTTT |
| | GGAATTACTCGTTTACCAGACGACAAAAGATT |
| S8F (r-1t8e) | ACCATTCATACTCTATCCCCGGAACTTCAGCCCAACTAACATTTT |
| | CATAACCCGAGGCATAGTAAGAGCTTTTTAAG |
| Block and release strands | |
| block (weak) | GGTTCCGGGGATAGAGTATGAATGGTCCACCTTAAAAATGC |
| release (weak) | GCATTTTTAAGGTGGACCATTCATACTCTATCCCCGGAACC |
| block (strong) | CTGAGGTTCCGGGGATAGAGTATGAATGGTCCACCTTAAAAATGC |
| release (strong) | GCATTTTTAAGGTGGACCATTCATACTCTATCCCCGGAACCTCAG |
| Fluoresent Staples | |
| F2-3'Cy5 (r-7t4e) | GCTCCATGAGAGGCTTTGAGGACTAGGGAGTT/3Cy5Sp/ |

to be cont'd on next page

Table C.3: Modified Staples for Chapter 3 Fluoresence

| Name (cont.) | Sequence (cont.) |
|---|---|
| F8-3'Cy3 (r1t8f) | AAAAGTAATATCTTACCGAAGCCCAACACTAT/3Cy3Sp/ |
| Motor | |
| Motor-5'Q | /5IAbRQ/CGATGTTAGTTGGGCTGAGGTTCC |
| S1-M Hairpin-5'Q | /5IAbRQ/CGATGTTAGTTGGGCTGAGGTTCCCGGA |
| | CCGTTTCGGTCCGGGAACCTCAGCCCAACTAACATC |
| | GTTTGAGAATAGCTTTTGCGGGATCGTCGGGTAGCA |
| **Tile B design** | |
| Track Staples | |
| S1I (r-3t6f) | GGAACCTCAGCCCAACTAACATCGTTT |
| | GCTCATTCTTATGCGATTTTAAGCGAGGCAT |
| S2 (r-3t6e) | TCTTGTACCGTTTGCAGACTGGAACCTCAGCCCAACTAACATTTT |
| | GAATTACCAGTGAATAAGGCTTGTCGAAATC |
| S3 (r-1t8f) | TCTTGTACCGTTTGCAGACTGGAACCTCAGCCCAACTAACATTTT |
| | ACCAGACGGCAAAAGAAGTTTTGTTTTAATT |
| S4 (r1t10f) | TCTTGTACCGTTTGCAGACTGGAACCTCAGCCCAACTAACATTTT |
| | AGGCTTTTACGATAAAAACCAAAATTAAGAC |
| S5 (r1t10f) | TCTTGTACCGTTTGCAGACTGGAACCTCAGCCCAACTAACATTTT |
| | TACAGAGAGTCAAAAATGAAAATAGGAAGCAA |
| S6 (r1t10e) | TCTTGTACCGTTTGCAGACTGGAACCTCAGCCCAACTAACATTTT |
| | TGTTTAACGAATAACATAAAAACTAATAACG |
| S7 (r3t12f) | TCTTGTACCGTTTGCAGACTGGAACCTCAGCCCAACTAACATTTT |
| | GGCTTATCGCACTCATCGAGAACCCGACAAA |
| S8F (r3t12e) | TCTTGTACCGTTTGCAGACTGGAACTTCAGCCCAACTAACATTTT |
| | CAAGTACCCGGTATTCTAAGAACGCCATATTA |
| Block and release strands | |
| block | GGTTCCAGTCTGCAAACGGTACAAGAAAGTCGCTTCGCACA |
| release | TGTGCGAAGCGACTTTCTTGTACCGTTTGCAGACTGGAACC |
| Fluoresent Staples | |
| F1-3'Joe (M-3t4f) | AAAACACTGCTCCATGTTACTTAACAAAGCT/3JoeN/ |
| F2-3'Cy5 (M-3t8e) | GGTAATAGCAACACTATCATAACATCATTGT/3Cy5Sp/ |
| F3-3'Cy3.5 (M-1t6f) | AGAAACACTTTAATTTCAACTTTACCTCGTTT/3AmMO/ |
| F4-3'Cy3.5 (M1t8f) | TCCTTATTAAAAGAACTGGCATGATAGCGAG/3AmMO/ |
| F8-3'Cy3.5 (M3t14e) | TTAATTGATAATTCTGTCCAGACTATTAAAC/3AmMO/ |
| Motor | |
| Motor - 5'Q | IowaBlackRQ-CGATGTTAGTTGGGCTGAGGTTCC |
| End of Table | |

### C.3.2 AFM experiments, Section 3.3

Modified staple sequences for the AFM experiments are given in Table C.3.2. All experiments were on tile type A, colour codes refer to Figure 3.13.

Modified Staple Sequences for Chapter 3 AFM experiments

| Name | Sequence |
|---|---|
| Track | |
| BBs1i r-7t2f | GGAACCTCAGCCCAACTAACAT**CG**TTT |
| | GAGAATAGCTTTTGCGGGATCG TCGGGTAGCA |
| BBS2n r-7t2e | GGAACCTCAGCCCAACTAACATTTT |
| | AAAGGCCGAAAGGAACAACTAAAGCTTTCCAG |
| BBS3n r-5t4f | GGAACCTCAGCCCAACTAACATTTT |
| | TTTCATGAAAATTGTGTCGAAATCTGTACAGA |
| BBS4n r-5t4e | GGAACCTCAGCCCAACTAACATTTT |
| | CGCCTGATGGAAGTTTCCATTAAACATAACCG |
| BBS5n r-3t6f | GGAACCTCAGCCCAACTAACATTTT |
| | AGTAATCTTAAATTGGGCTTGAGAGAATACCA |
| BBS6n r-3t6e | GGAACCTCAGCCCAACTAACATTTT |
| | ACGAGTAGTGACAAGAACCGGATATACCAAGC |
| BBS7n r-1t8f | GGAACCTCAGCCCAACTAACATTTT |
| | GGAATTACTCGTTTACCAGACGACAAAAGATT |
| BBS8n r-1t8e | GGAACCTCAGCCCAACTAACATTTT |
| | CATAACCCGAGGCATAGTAAGAGCTTTTTAAG |
| BBS9n r1t10f | GGAACCTCAGCCCAACTAACATTTT |
| | CCTAATTTACGCTAACGAGCGTCTATATCGCG |
| BBS10n r1t10e | GGAACCTCAGCCCAACTAACATTTT |
| | TCTTACCAGCCAGTTACAAAATAAATGAAATA |
| BBS11n r3t12f | GGAACCTCAGCCCAACTAACATTTT |
| | GGTATTAAGAACAAGAAAAATAATTAAAGCCA |
| BBS12n r3t12e | GGAACCTCAGCCCAACTAACATTTT |
| | TAAGTCCTACCAAGTACCGCACTCTTAGTTGC |
| BBS13n r5t14f | GGAACCTCAGCCCAACTAACATTTT |
| | CATATTTAGAAATACCGACCGTGTTACCTTTT |
| BBS14n r5t14e | GGAACCTCAGCCCAACTAACATTTT |
| | AATGGTTTACAACGCCAACATGTAGTTCAGCT |
| BBS15n r7t16f | GGAACCTCAGCCCAACTAACATTTT |
| | TATGTAAACCTTTTTTAATGGAAAAATTACCT |
| BBS16n r7t16e | GGAACCTCAGCCCAACTAACATTTT |
| | TTGAATTATGCTGATGCAAATCCACAAATATA |

to be cont'd on next page

Table C.4: Modified Staples for Chapter 3 AFM

| Name (cont.) | Sequence (cont.) |
|---|---|
| BBS17f r9t18f | GGAAC**T**TCAGCCCAACTAACATTTT |
| | AAAACAAATTCATCAATATAATCCTATCAGAT |
| Hairpin markers | |
| HP1 r1t2e | TGCCTTGACTGCCTATTCCTCTTTTGAGGAACAAGTTTTCTTGT |
| | TTCGGAACAGGGATAG |
| HP2 r3t2f | CTGAAACAGGTAATAATCCTCTTTTGAGGAACAAGTTTTCTTGT |
| | GTTTTAACCCCTCAGA |
| HP3 r3t4e | GTTTGCCACCTCAGAGTCCTCTTTTGAGGAACAAGTTTTCTTGT |
| | CCGCCACCGATACAGG |
| HP4 r5t4f | CACCAGAGTTCGGTCATCCTCTTTTGAGGAACAAGTTTTCTTGT |
| | TAGCCCCCGCCAGCAA |
| HP5 r5t6e | TCACAATCGTAGCACCTCCTCTTTTGAGGAACAAGTTTTCTTGT |
| | ATTACCATCGTTTTCA |
| HP6 r7t6f | CCGGAAACACACCACGTCCTCTTTTGAGGAACAAGTTTTCTTGT |
| | GAATAAGTAAGACTCC |
| HP7 r7t8e | TGAACAAACAGTATGTTCCTCTTTTGAGGAACAAGTTTTCTTGT |
| | TAGCAAACTAAAAGAA |
| HP8 r9t8fT | TACATACATTTTGACGGGAGTCCTCTTTTGAGGAACAAGTTTTCTTGT |
| | AATTAACTACAGGGAA |
| HP9 r-9t10eT | ATATAATGTTTTCATTGAATTCCTCTTTTGAGGAACAAGTTTTCTTGT |
| | CCCCCTCAAATCGTCA |
| HP10 r-7t10f | AAACAGTTGATGGCTTTCCTCTTTTGAGGAACAAGTTTTCTTGT |
| | AGAGCTTATTTAAATA |
| HP11 r-7t12e | CAAAATTAAAGTACGGTCCTCTTTTGAGGAACAAGTTTTCTTGT |
| | TGTCTGGAAGAGGTCA |
| HP12 r-5t12f | TCCATATACATACAGGTCCTCTTTTGAGGAACAAGTTTTCTTGT |
| | CAAGGCAACTTTATTT |
| HP13 r-5t14e | GGTAGCTAGGATAAAATCCTCTTTTGAGGAACAAGTTTTCTTGT |
| | ATTTTTAGTTAACATC |
| HP14 r-3t14f | TATATTTTAGCTGATATCCTCTTTTGAGGAACAAGTTTTCTTGT |
| | AATTAATGTTGTATAA |
| HP15 r-3t16e | AAATAATTTTAAATTGTCCTCTTTTGAGGAACAAGTTTTCTTGT |
| | TAAACGTTGATATTCA |
| HP16 r-1t16f | GTTAAAATTTTAACCATCCTCTTTTGAGGAACAAGTTTTCTTGT |
| | ATAGGAACCCGGCACC |
| HP17 r-1t18e | TTCGCCATTGCCGGAATCCTCTTTTGAGGAACAAGTTTTCTTGT |
| | ACCAGGCAAACAGTAC |
| HP18 r1t18f | CTTTTACACAGATGAATCCTCTTTTGAGGAACAAGTTTTCTTGT |

to be cont'd on next page

Table C.4: Modified Staples for Chapter 3 AFM

| Name (cont.) | Sequence (cont.) |
|---|---|
| | TATACAGTAAGCGCCA |
| HP19 r1t20e | GGATTTAGCGTATTAATCCTCTTTTGAGGAACAAGTTTTCTTGT |
| | ATCCTTTGTTTTCAGG |
| HP20 r3t20f | TTATTAATGCCGTCAATCCTCTTTTGAGGAACAAGTTTTCTTGT |
| | TAGATAATCAGAGGTG |
| HP21 r3t22e | GAATGGCTAGTATTAATCCTCTTTTGAGGAACAAGTTTTCTTGT |
| | CACCGCCTCAACTAAT |
| HP22 r5t22f | GCCACGCTATACGTGGTCCTCTTTTGAGGAACAAGTTTTCTTGT |
| | CACAGACAACGCTCAT |
| HP23 r5t24h | GGAAATACCTACATTTTCCTCTTTTGAGGAACAAGTTTTCTTGT |
| | TGACGCTCACCTGAAA |

End of Table

# C.4 Oligos for Chapter 4

Modified Staples for Two-Foot motor Track in Chapter 4

| Name | Sequence |
|---|---|
| **3-segment Triangle Track** | |
| T1 | CCAGGCGCTTAATCATTGCGTCAACTGAACGAGCAGCCTTAGATTTAGTGGTTTAA |
| T2 | TTTGCCAGATCAGTTGAAGGTCAACTGAACGAGCAGCGACATAGTAAACCATAAAT |
| T3 | AAAGATTCAGGGGGTAGTCGTCAACTGAACGAGCAGCGCATGTGAATTACAGGTAG |
| **4-segment Linear Track** | |
| Short (16 nt) staples | |
| T1 | CAGCGAAATTTTAACTTTCAGTTCCCAATACGCAGCATC |
| | GTCGGATCGTCGGGTAGCA |
| T1a | CAGCGAAATTTTAACTTTCAGTTCCCAATACGCCGCACC |
| | GTCGGATCGTCGGGTAGCA |
| T2 | GAGAATAGCTTTTGCGGACCTTCAGCTTCAGCATCAACTGAGGACTAGGGAGTT |
| T2a | GAGAATAGCTTTTGCGGACCCAACCACCCAGCATCAACTGAGGACTAGGGAGTT |
| T3 | GCTCCATGAGAGGCTTGTTGCATACCGCCAGCATCGTCTCGAAATCTGTACAGA |
| T4 | TTTCATGAAAATTGTGGACCTTCAGCTTCAGCATCAACGCTGACCTTGTATCAT |
| T4a | TTTCATGAAAATTGTGGACGCTCAAAGCATCTCAAAACGCTGACCTTGTATCAT |
| Asymmetric staples | |
| AT1 | CGGAACGAACCCTCAGCAGCGAAAAACTTTCAGTTCCCAATACGCAGCATC |

to be cont'd on next page

Table C.5: Modified Staple Sequences for Chapter 4

| Name | Sequence (cont.) |
|---|---|
| (cont.) | |
| | GTC GGATCGTCGGGTAGCA |
| AT1a | CGGAACGAACCCTCAGCAGCGAAAAACTTTCAGTTCCCAATACGCCGCACC |
| | GTC GGATCGTCGGGTAGCA |
| AT2 | TTTCTGTAAGCGGAGTGAGAATAGCTTTTGCGGACCTTCAGCTTCAGCATC |
| | AAC TGAGGACTAGGGAGTT |
| AT2a | TTTCTGTAAGCGGAGTGAGAATAGCTTTTGCGGACCCAACCACCCAGCATC |
| | AAC TGAGGACTAGGGAGTT |
| AT3 | ATGAACGGCGCGACCTGCTCCATGAGAGGCTTGTTGCATACCGCCAGCATC |
| | GTC TCGAAATCTGTACAGA |
| AT4 | AGGCTTGCAAAGACTTTTTCATGAAAATTGTGGACCTTCAGCTTCAGCATC |
| | AAC GCTGACCTTGTATCAT |
| AT4a | AGGCTTGCAAAGACTTTTTCATGAAAATTGTGGACGCTCAAAGCATCTCAA |
| | AAC GCTGACCTTGTATCAT |
| Long (32 nt) staples | |
| LT1 | CGGAACGAACCCTCAGCAGCGAAAAACTTTCAGTTCCCAATACGCAGCATC |
| | GTC GGATCGTCGGGTAGCAACGGCTACTTACTTAG |
| LT1a | CGGAACGAACCCTCAGCAGCGAAAAACTTTCAGTTCCCAATACGCCGCACC |
| | GTC GGATCGTCGGGTAGCAACGGCTACTTACTTAG |
| LT2 | TTTCTGTAAGCGGAGTGAGAATAGCTTTTGCGGACCTTCAGCTTCAGCATC |
| | AAC TGAGGACTAGGGAGTTAAAGGCCGAAAGGAAC |
| LT2a | TTTCTGTAAGCGGAGTGAGAATAGCTTTTGCGGACCCAACCACCCAGCATC |
| | AAC TGAGGACTAGGGAGTTAAAGGCCGAAAGGAAC |
| LT3 | ATGAACGGCGCGACCTGCTCCATGAGAGGCTTGTTGCATACCGCCAGCATC |
| | GTC TCGAAATCTGTACAGACCAGGCGCTTAATCAT |
| LT4 | AGGCTTGCAAAGACTTTTTCATGAAAATTGTGGACCTTCAGCTTCAGCATC |
| | AAC GCTGACCTTGTATCATCGCCTGATGGAAGTTT |
| LT4a | AGGCTTGCAAAGACTTTTTCATGAAAATTGTGGACGCTCAAAGCATCTCAA |
| | AAC GCTGACCTTGTATCATCGCCTGATGGAAGTTT |
| Extra staples | |
| E1 | ACAGTTTCTGGGATTTTGCTAAACTTTT |
| E2 | ACGGTCAATTTTGACAGCAT |
| E3 | ACGTTAGTAAATGAAT |
| E4 | CGATTTTAGAGGACAG |
| E5 | AATAATAAGGTCGCTG |
| E6 | CCGGAACGCTGACCAA |
| E7 | AACTAAAGCTTTCCAG |
| E8 | TGTGAATTACAGGTAG |

to be cont'd on next page

Table C.5: Modified Staple Sequences for Chapter 4

| Name | Sequence (cont.) |
|---|---|
| (cont.) | |
| E9 | CCATTAAACATAACCG |
| R | TTTGCCAGATCAGTTGAGATTTAGTGGTTTAATTTCAACTATAGGCTG |
| **17-segment Linear Track** | |
| T1 | CAGCGAAATTTTAACTTTCAGTTCTTCAGCTTCAGCATCGTC GTCGGATCGTCGGGTAGCA |
| T2 | GAGAATAGCTTTTGCGGACCTTCAGCTTCAGCATCGTCAACTGAGGACTAGGGAGTT |
| T3 | GCTCCATGAGAGGCTTGTTCTTCAGCTTCAGCATCGTCGTCTCGAAATCTGTACAGA |
| T4 | TTTCATGAAAATTGTGGACCTTCAGCTTCAGCATCGTCAACGCTGACCTTGTATCAT |
| T5 | TTTCAACTATAGGCTGGTTCTTCAGCTTCAGCATCGTCGTCGCTTGAGAGAATACCA |
| T6 | AGTAATCTTAAATTGGGACCTTCAGCTTCAGCATCGTCAACATACATAAACACCAGA |
| T7 | CCAAAATATAATGCAGGTTCTTCAGCTTCAGCATCGTCGTCCAGACGACAAAAGATT |
| T8 | GGAATTACTCGTTTACGACCTTCAGCTTCAGCATCGTCAACGACTTCAATTCCAGAG |
| T9 | TTTTAATTGCCCGAAAGTTCTTCAGCTTCAGCATCGTCGTCGAGCGTCTATATCGCG |
| T10 | CCTAATTTACGCTAACGACCTTCAGCTTCAGCATCGTCAACTATCATTCATCCTGAA |
| T11 | CTAATTTATCTTTCCTGTTCTTCAGCTTCAGCATCGTCGTCAAAATAATTAAAGCCA |
| T12 | GGTATTAAGAACAAGAGACCTTCAGCTTCAGCATCGTCAACCTTAATTGACAATAGA |
| T13 | AGGCGTTACAGTAGGGGTTCTTCAGCTTCAGCATCGTCGTCGACCGTGTTACCTTTT |
| T14 | CATATTTAGAAATACCGACCTTCAGCTTCAGCATCGTCAACTTGGGTTACTAAATTT |
| T15 | AAATCAATGGCTTAGGGTTCTTCAGCTTCAGCATCGTCGTCAATGGAAAAATTACCT |
| T16 | TATGTAAACCTTTTTTGACCTTCAGCTTCAGCATCGTCAACTGAAACAAAATTTCAT |
| T17 | TGGATTATGAAGATGAGTTCTTCAGCTTCAGCATCGTCGTCTATAATCCTATCAGAT |

End of Table

Motor and Fluorophore strands for Chapter 4

| Name | Sequence |
|---|---|
| **Motor strands** | |
| foot1-WT | AGACTAACGATAATACTTTTGATGCTGAGGCTGAGGGATGCT |
| foot1-F | AGACTAACGATAATACTTTTGATGCTGGCGGTATGCGATGCT |
| foot2-WT-3'Q | GTATTATCGTTAGTCTTTTTGATGCTGAGGCTGAGGGATGCT/3IAbRQ/ |
| **Fluorescent staples** | |
| F1b 5' Cy3 | /5Cy3Sp/ACGGCTACTTACTTAGCCGGAACGCTGACCAA |
| F1 5' Cy3 | /5Cy3Sp/ACAGTTTCTGGGATTTTGCTAAACTTTT |
| F2 5' Cy5 | /5Cy5Sp/CCAGGCGCTTAATCATTGTGAATTACAGGTAG |
| **Fuel strands** | |
| Forward fuel | CCTCAGCCTCAGCATC |
| Reverse fuel | AGCATCCCTCAGCCTC |

End of Table

## C.5 Oligos for Chapter 5

Modified staple strands for Linear Junction Tracks in Chapter 5

| Name | Sequence |
|---|---|
| **Single-Junction Track** | |
| S1 M-1t2e | GGAACCTCAGCCCAACTAACATCGTTT |
| | GATATATTAACAACCATCGCCCACCAAGAGAA |
| S2 M-1t4e | TCTTGTACCGTTTGCAGACTGGAACCTCAGCCCAACTAACATTTT |
| | GTATCATCGAAACAAAGTACAACCGCCGCCA |
| S3 M-1t6e | TCTTGTACCGTTTGCAGACTGGAACCTCAGCCCAACTAACATTTT |
| | TGAGATGGCAGAACGAGTAGTAACATTACCA |
| S4 M-1t8e | TCTTGTACCGTTTGCAGACTGGAACCTCAGCCCAACTAACATTTT |
| | AGGCTTTTACGATAAAAACCAAAATTAAGAC |
| S5R M1t10f | ACCATTCATACTCTATCCCCGGAACCTCAGCCCAACTAACATTTT |
| | TACAGAGAGTCAAAAATGAAAATAGGAAGCAA |
| S6R m1t10e | TCTTGTACCGTTTGCAGACTGGAACCTCAGCCCAACTAACATTTT |
| | TGTTTAACGAATAACATAAAAACTAATAACG |
| S7R M3t12f | TCTTGTACCGTTTGCAGACTGGAACCTCAGCCCAACTAACATTTT |
| | GGCTTATCGCACTCATCGAGAACCCGACAAA |
| S8R M3t12e | TCTTGTACCGTTTGCAGACTGGAAC**T**TCAGCCCAACTAACATTTT |
| | CAAGTACCCGGTATTCTAAGAACGCCATATTA |
| S5L M-1t10f | GCAATCTCGTCACGCCTGTAGGAACCTCAGCCCAACTAACATTTT |
| | CGAGCTTCAGGTCAGGATTAGAGGCTATATT |
| S6L M-3t10e | TCTTGTACCGTTTGCAGACTGGAACCTCAGCCCAACTAACATTTT |
| | TAATTGCTACTTCAAATATCGCGCCAGAGGG |
| S7L M-3t12f | TCTTGTACCGTTTGCAGACTGGAACCTCAGCCCAACTAACATTTT |
| | GCAAATGGCATACAGGCAAGGCAAGAGTAATG |
| S8L M-5t12e | TCTTGTACCGTTTGCAGACTGGAAC**T**TCAGCCCAACTAACATTTT |
| | CAAAATTAAGTTTGACCATTAGATCATTTTT |
| **Triple-Junction Track** | |
| S8R M3t12e | TCTTGTACCGTTTGCAGACTGGAACCTCAGCCCAACTAACATTTT |
| | CAAGTACCCGGTATTCTAAGAACGCCATATTA |
| S9R M3t14e | TCTTGTACCGTTTGCAGACTGGAACCTCAGCCCAACTAACATTTT |
| | TTAATTGATAATTCTGTCCAGACTATTAAAC |
| S10R M3t16e | TCTTGTACCGTTTGCAGACTGGAACCTCAGCCCAACTAACATTTT |
| | CTACCTTTTATATTTTAGTTAATTAGTAGGGC |
| S11RL M3t18f | ACTTATTACTCTATGAAGACGGAACCTCAGCCCAACTAACATTTT |
| | TTCATTTGGAGGCGAATTATTCATGATTGTT |
| S12RL M1t18e | TCTTGTACCGTTTGCAGACTGGAACCTCAGCCCAACTAACATTTT |

to be cont'd on next page

Table C.7: Modified Track Staples for Chapter 5

| Name (cont.) | Sequence (cont.) |
|---|---|
| | ACCTGAGCACAAAATTAATTACATGGTTGGGT |
| S13RLF M1t20f | TCTTGTACCGTTTGCAGACTGGAACTTCAGCCCAACTAACATTTT |
| | ATGGCAATATCATATTCCTGATTCATAAAGT |
| S11RR M5t18f | AGCTAAATCTCGGCCACGTAGGAACCTCAGCCCAACTAACATTTT |
| | GTACATAATTGCTTTGAATACCAAAAGGGTTA |
| S12RR M5t18e | TCTTGTACCGTTTGCAGACTGGAACCTCAGCCCAACTAACATTTT |
| | TCGCCTGAATCAATATATGTGAGAGTCAATA |
| S13RRF M7t20f | TCTTGTACCGTTTGCAGACTGGAACTTCAGCCCAACTAACATTTT |
| | AAACAGAATTAAATCCTTTGCCCAATAGATT |
| S8L M-5t12e | TCTTGTACCGTTTGCAGACTGGAACCTCAGCCCAACTAACATTTT |
| | CAAAATTAAGTTTGACCATTAGATCATTTTT |
| S9L M-5t14e | TCTTGTACCGTTTGCAGACTGGAACCTCAGCCCAACTAACATTTT |
| | AAGGCTATTTTAAATGCAATGCCTAGAATTAG |
| S10L M-5t16e | TCTTGTACCGTTTGCAGACTGGAACCTCAGCCCAACTAACATTTT |
| | TGAGCGAGAGCAAATATTTAAATGATCTACA |
| S11LL M-5t18f | ACTTATTACTCTATGAAGACGGAACCTCAGCCCAACTAACATTTT |
| | CAGTATCGGCTGCAAGGCGATTAGGGTACCG |
| S12LL M-7t18e | TCTTGTACCGTTTGCAGACTGGAACCTCAGCCCAACTAACATTTT |
| | AACGCCAGCTGCCAGTTTGAGGGTCTCCGTG |
| S13LLF M-7t20f | TCTTGTACCGTTTGCAGACTGGAACTTCAGCCCAACTAACATTTT |
| | CAGGTCGAGAATCGGCCAACGCGGGTGGTTT |
| S11LR M-3t18f | AGCTAAATCTCGGCCACGTAGGAACCTCAGCCCAACTAACATTTT |
| | CCAGCTTTGCTATTACGCCAGCTATAGCTGT |
| S12LR M-3t18e | TCTTGTACCGTTTGCAGACTGGAACCTCAGCCCAACTAACATTTT |
| | GCCTCTTCCCGGCACCGCTTCTGGTCTGGCCT |
| S13LRF M-1t20f | TCTTGTACCGTTTGCAGACTGGAACTTCAGCCCAACTAACATTTT |
| | TCCACACATGGGGTGCCTAATGATGCCCCAG |

**Block and Release Strands**

| | |
|---|---|
| block1 | GGTTCCAGTCTGCAAACGGTACAAGAAAGTCGCTTCGCACA |
| release1 | TGTGCGAAGCGACTTTCTTGTACCGTTTGCAGACTGGAACC |
| (R,0) instruction | |
| block 2 | CTGAGGTTCCGGGGATAGAGTATGAATGGTCCACCTTAAAAATGC |
| release2 | GCATTTTTAAGGTGGACCATTCATACTCTATCCCCGGAACCTCAG |
| (L,0) instruction | |
| block3 | CTGAGGTTCCTACAGGCGTGACGAGATTGCCGATCAAAGCAGTGC |
| release3 | GCACTGCTTTGATCGGCAATCTCGTCACGCCTGTAGGAACCTCAG |
| (0,L) instruction | |

to be cont'd on next page

Table C.7: Modified Track Staples for Chapter 5

| Name (cont.) | Sequence (cont.) |
|---|---|
| block4 | CTGAGGTTCCGTCTTCATAGAGTAATAAGTGACACCCTGGTCGAA |
| release4 | TTCGACCAGGGTGTCACTTATTACTCTATGAAGACGGAACCTCAG |
| (0,R) instruction | |
| block5 | CTGAGGTTCCTACGTGGCCGAGATTTAGCTCCCCTTGTGTCCGCG |
| release5 | CGCGGACACAAGGGGAGCTAAATCTCGGCCACGTAGGAACCTCAG |
| **Fluorescent strands** | |
| F1-Joe M1t2f | GGATTAGGAGAGGCTGAGACTCCTGCATAACC /3JoeN/ |
| F8R-Cy5 M3t14e | TTAATTGATAATTCTGTCCAGACTATTAAAC /3Cy5Sp/ |
| F8L-Cy5 M-5t14e | AAGGCTATTTTAAATGCAATGCCTAGAATTAG /3Cy5Sp/ |
| F13RR-Cy3 M7t18f | CTTGCTTCCATCGGGAGAAACAATGCACGTA /3Cy5Sp/ |
| F13LR-Cy5 M-1t18f | ACCAGGCAGTTGGGAAGGGCGATCTCACAAT /3Cy5Sp/ |
| F13LL-Cy5.5 M-7t18f | CCGTGCATGGTTTTCCCAGTCACGCATGCCTG /3Cy55Sp/ |
| F13RR-Cy5 M7t18f | CTTGCTTCCATCGGGAGAAACAATGCACGTA /3Cy5Sp/ |
| F7R-Joe M3t10f | GCATTAGAAATCCAAATAAGAAAATATAGAA /3JoeN/ |
| F3-Am M1t6f | TTAGCAAGAATCACCAGTAGCACATTGGGCT /3AmMO/ |
| F4-Am M1t8f | TCCTTATTAAAAGAACTGGCATGATAGCGAG /3AmMO/ |
| F8R-Am M3t14e | TTAATTGATAATTCTGTCCAGACTATTAAAC /3AmMO/ |
| F8L-Am M-5t14e | AAGGCTATTTTAAATGCAATGCCTAGAATTAG /3AmMO/ |
| F13RL-Am M-1t20e | GTAAAGCCACATACGAGCCGGAAGATCAGATG /3AmMO/ |
| F13LL-Am M-7t18f | CCGTGCATGGTTTTCCCAGTCACGCATGCCTG /3AmMO/ |

End of Table

## Motor-Catalysed Block and Release Sequences for Chapter 5

| Name | Sequence |
|---|---|
| **Test-track Strands** | |
| S1 | TCTTGTACCGTTTGCAGACTGGAACCTCAGCCCAACTAACATCG TTTAGGCTTTTACGATAAAAA |
| S2R | ACCATTCATACTCTATCCCCGGAACCTCAGCCCAACTAACATTTT TACAGAGAGTCAAAAATG |
| S2L | GCAATCTCGTCACGCCTGTAGGAACCTCAGCCCAACTAACATTTT TACAGAGAGTCAAAAATG |
| Track | FAM - CATTTTTGACTCTCTGTATTTTTATCGTAAAAGCCT |
| **Hairpin block and relase** | |
| HP mR | CGATGTTAGTTGGGCTGAGGTTCCTTTAATAAGACGTGGAC |
| HP mL | CGATGTTAGTTGGGCTGAGGTTCCTTTGGTGCCGCTTGATA |

to be cont'd on next page

Table C.8: Block and Release Sequences for Chapter 5

| Name (cont.) | Sequence (cont.) |
|---|---|
| HP catalystR | TTTAATAAGACGTGGAC |
| HP catalystL | TTTGGTGCCGCTTGATA |
| HPblock R 14 | CTGAGGTTCCGGGGATAGAGTATGAATGGTGTCTTATT |
| | TTACGAGTGCTCCGAATAAGAC |
| HPblock L 14 | CTGAGGTTCCTACAGGCGTGACGAGATTGCGCGGCACC |
| | CTTCTAGCATGGTCGGTGCCGC |
| HPrelease R 14 | GTCCACGTCTTATTCGGAGCACTCGTAA |
| | AATAAGACACCATTCATACTCTATCCCCGGAA |
| HPrelease L 14 | TATCAAGCGGCACCGACCATGCTAGAAG |
| | GGTGCCGCGCAATCTCGTCACGCCTGTAGGAA |
| HPblock R 12 | CTGAGGTTCCGGGGATAGAGTATGAATGGTGTCTTATT |
| | TACGAGTGCTCCAATAAGAC |
| HPblock L 12 | CTGAGGTTCCTACAGGCGTGACGAGATTGCGCGGCACC |
| | TTCTAGCATGGTGGTGCCGC |
| HPrelease R 12 | GTCCACGTCTTATTGGAGCACTCGTA |
| | AATAAGACACCATTCATACTCTATCCCCGGAA |
| HPrelease L 12 | TATCAAGCGGCACCACCATGCTAGAA |
| | GGTGCCGCGCAATCTCGTCACGCCTGTAGGAA |
| **Loop block and relase** | |
| LPblock R 12 | CTGAGGTTCCGGGGATTTCTTCGCACTTAGAGTATGAATGGTGTCCAC |
| LPblock L 12 | ACACCATTCATACTCTAAGTGCGAAGAAATCCCCGGAACCTCAG |
| LPrelease R 12 | CTGAGGTTCCTACAGGCCGTAATAAAAGCGTGACGAGATTGCTATCAA |
| LPrelease L 12 | TAGCAATCTCGTCACGCTTTTATTACGGCCTGTAGGAACCTCAG |
| LPrelease R 12s | ACCATTCATACTCTAAGTGCGAAGAAATCCCCGGAACCTCAG |
| LPrelease L 12s | GCAATCTCGTCACGCTTTTATTACGGCCTGTAGGAACCTCAG |
| LPblock R 10 | CTGAGGTTCCGGGGATTCTTCGCACTAGAGTATGAATGGTGTCCAC |
| LPblock L 10 | ACACCATTCATACTCTAGTGCGAAGAATCCCCGGAACCTCAG |
| LPrelease R 10 | CTGAGGTTCCTACAGGCGTAATAAAACGTGACGAGATTGCTATCAA |
| LPrelease L 10 | TAGCAATCTCGTCACGTTTTATTACGCCTGTAGGAACCTCAG |
| LPrelease R 10s | ACCATTCATACTCTAGTGCGAAGAATCCCCGGAACCTCAG |
| LPrelease L 10s | GCAATCTCGTCACGTTTTATTACGCCTGTAGGAACCTCAG |
| LPblock R 8 | CTGAGGTTCCGGGGATCTTCGCACAGAGTATGAATGGTGTCCAC |
| LPblock L 8 | ACACCATTCATACTCTGTGCGAAGATCCCCGGAACCTCAG |
| LPrelease R 8 | CTGAGGTTCCTACAGGGTAATAAACGTGACGAGATTGCTATCAA |
| LPrelease L 8 | TAGCAATCTCGTCACGTTTATTACCCTGTAGGAACCTCAG |

to be cont'd on next page

Table C.8: Block and Release Sequences for Chapter 5

| Name (cont.) | Sequence (cont.) |
|---|---|
| LPrelease R 8s | ACCATTCATACTCTGTGCGAAGATCCCCGGAACCTCAG |
| LPrelease L 8s | GCAATCTCGTCACGTTTATTACCCTGTAGGAACCTCAG |
| LPblock R 6 | CTGAGGTTCCGGGGATTTCGCAAGAGTATGAATGGTGTCCAC |
| LPblock L 6 | ACACCATTCATACTCTTGCGAAATCCCCGGAACCTCAG |
| LPrelease R 6 | CTGAGGTTCCTACAGGTAATAACGTGACGAGATTGCTATCAA |
| LPrelease L 6 | TAGCAATCTCGTCACGTTATTACCTGTAGGAACCTCAG |
| LPrelease R 6s | ACCATTCATACTCTTGCGAAATCCCCGGAACCTCAG |
| LPrelease L 6s | GCAATCTCGTCACGTTATTACCTGTAGGAACCTCAG |
| Splice strands | |
| LPsplice R 5 | CCGGGGATAGAGT |
| LPsplice L 5 | CCTACAGGCGTGA |
| LPsplice R 7 | CCGGGGATAGAGTAT |
| LPsplice L 7 | CCTACAGGCGTGACG |
| LPsplice R 8 | CCGGGGATAGAGTATG |
| LPsplice L 8 | CCTACAGGCGTGACGA |
| End of Table | |

## C.6 Oligos for Chapter 6

Tris-NTA DNA strands for Chapter 6

| Name | Sequence |
|---|---|
| r-5t6f3Amine | CCAGGCGCTTAATCAT T - 3x amine - T TGTGAATTACAGGTAG |
| r-5t8e3Amine | TTTGCCAGATCAGTTG T - 3x amine - T AGATTTAGTGGTTTAA |
| r-5t8f3Amine | AAAGATTCAGGGGGTA T - 3x amine - T ATAGTAAACCATAAAT |
| End of Table | |

# Bibliography


Abrahams, J., Leslie, A., Lutter, R. and Walker, J. (1994), Structure at 2.8 å of $F_1$-ATPase from bovine heart mitochondria, *Nature* **370**, 621–628.

Abramoff, M. D., Magelhaes, P. J. and Ram, S. J. (2004), Image processing with imageJ, *Biophotonics International* **11**(7), 36–42.

Alberts, B., Johnson, A., Lewis, J., Raff, M., Roberts, K. and Walter, P. (2002), *Molecular Biology of the Cell*, fourth edn, Garland Science, New York.

Aldaye, F. A., Senapedis, W. T., Silver, P. A. and Way, J. C. (2010), A structurally tunable DNA-based extracellular matrix, *Journal of the American Chemical Society* **132**, 14727–14729.

Aldaye, F. A. and Sleiman, H. F. (2007), Modular access to structurally switchable 3D discrete DNA assemblies, *Journal of the American Chemical Society* **129**(44), 13377.

Andersen, E. S., Dong, M., Nielsen, M. M., Jahn, K., Subramani, R., Mamdouh, W., Golas, M. M., Sander, B., Stark, H., Oliveira, C. L. P., Pedersen, J. S., Birkedal, V., Besenbacher, F., Gothelf, K. V. and Kjems, J. (2009), Self-assembly of a nanoscale DNA box with a controllable lid, *Nature* **459**, 73–76.

Ando, T., Kodera, N., Takai, E., Maruyama, D., Saito, K. and Toda, A. (2001), A high-speed atomic force microscope for studying biological macromolecules., *Proceedings of the National Academy of Sciences USA* **98**, 12468–12472.

Ariga, T. (2008), The concerted nature between three catalytic subunits driving the $F_1$ rotary motor, *BioSystems* **93**, 68–77.

Barish, R. D., Rothemund, P. W. K. and Winfree, E. (2005), Two computational primitives for algorithmic self-assembly: Copying and counting, *Nano Letters* **5**(12), 2586 – 2592.

Bath, J., Green, S. J., Allen, K. E. and Turberfield, A. J. (2009), Mechanism for a directional, processive, and reversible DNA motor, *Small* **5**(13), 1513–1516.

Bath, J., Green, S. and Turberfield, A. J. (2005), A free-running DNA motor powered by a nicking enzyme, *Angew. Chem. Int. Ed.* **44**(28), 4358–4361.

Bath, J. and Turberfield, A. (2007), DNA nanomachines, *Nature Nanotechnology* **2**, 275–284.

Benenson, Y., Gil, B., Adar, U. B.-D. R. and Shapiro, E. (2004), An autonomous molecular computer for logical control of gene expression, *Nature* **429**, 423–429.

Berg, H. C. (2003), The rotary motor of bacterial flagella, *Annual Review of Biochemistry* **72**, 19–54.

Berg, J. M., Tymoczko, J. L. and Stryer, L. (2002), *Biochemistry*, fifth edn, W H Freeman, New York.

Berry, R. M., Turner, L. and Berg, H. (1995), Mechanical limits of bacterial flagellar motors probed by electrorotation, *Biophysical Journal* **69**(1), 280–286.

Bilyard, T. (2009), Single Molecule Studies of $F_1$-ATPase and the Application of External Torque, PhD thesis, Department of Condensed Matter Physics, University of Oxford.

Boersma, A. J., Megens, R. P., Feringa, B. L. and Roelfes, G. (2010), DNA-based asymmetric catalysis, *Chem. Soc. Rev.* **39**, 2083–2092.

Bois, J. S., Venkataraman, S., Choi, H. M. T., Spakowitz, A. J., Wang, Z.-G. and Pierce, N. A. (2005), Topological constraints in nucleic acid hybridization kinetics, *Nucelic Acids Research* **33**, 4090–4095.

Bowler, M., Montgomery, M., Leslie, A. and Walker, J. (2007), Ground state structure of $F_1$-ATPase from bovine heart mitochondria at 1.9 å resolution, *Journal of Biological Chemistry* **282**(19), 14238–14242.

Boyer, B. (1997), The ATP synthase: a splendid molecular machine, *Annual Review of Biochemistry* **66**, 717–749.

Bromley, E. H. C., Channon, K., Moutevelis, E. and Woolfson, D. N. (2008), Peptide and protein building blocks for synthetic biology: From programming biomolecules to self-organized biomolecular systems, *ACS Chemical Biology* **3**(1), 38–50.

Bromley, E. H. C., Kuwada, N. J., Zuckermann, M. J., Samii, R. D. L., Blab, G. A., Gemmen, G. J., Lopez, B. J., Curmi, P. M. G., Forde, N. R., Woolfson, D. N. and Linke, H. (2009), The tumbleweed: towards a synthetic protein motor, *HFSP Journal* **3**(3), 204–212.

Bromley, E. H. C., Sessions, R. B., Thomson, A. R. and Woolfson, D. N. (2009), Designed $\alpha$-helical tectons for constructing multicomponent synthetic biological systems, *Journal of the American Chemical Society* **131**, 928–930.

Carstairs, H. (2008), A DNA-Kinesin Based Molecular Shuttle and Studies of DNA Kagome Arrays, PhD thesis, Department of Condensed Matter Physics, University of Oxford.

Carstairs, H. M. J., Lymperopoulos, K., Kapanidis, A. N., Bath, J. and Turberfield, A. J. (2009), DNA monofunctionalization of quantum dots, *ChemBioChem* **10**, 1781–1783.

Cheglakov, Z., Weizmann, Y., Braunschweig, A. B., Wilner, O. I. and Willner, I. (2008), Increasing the complexity of periodic protein nanostructures by the rolling-circle-amplified synthesis of aptamers, *Angew. Chem. Int. Ed.* **47**, 126–130.

Chen, Y., Wang, M. and Mao, C. (2004), An autonomous DNA nanomotor powered by a DNA enzyme., *Angew. Chem. Int. Ed.* **43**(27), 3554–3557.

Chhabra, R., Sharma, J., Ke, Y., Liu, Y., Rinker, S., Lindsay, S. and Yan, H. (2007), Spatially addressable multiprotein nanoarrays templated by aptamer-tagged DNA nanoarchitectures, *Journal of the American Chemical Society* **129**, 10304–10305.

Chworos, A., Severcan, I., Koyfman, A. Y., Weinkam, P., Oroudjev, E., Hansma, H. G. and Jaeger, L. (2004), Building programmable jigsaw puzzles with RNA, *Science* **306**, 2068–072.

Coy, D. L., Wagenbach, M. and Howard, J. (1999), Kinesin takes one 8-nm step for each ATP that it hydrolyzes, *J. Biol. Chem.* **274**(6), 3667–3671.

Dietz, H., Douglas, S. M. and Shih, W. M. (2009), Folding DNA into twisted and curved nanoscale shapes., *Science* **325**, 725–730.

Ding, B. and Seeman, N. C. (2006), Operation of a DNA robot arm inserted into a 2D DNA crystalline substrate, *Science* **314**, 1583.

Dittmer, W. U., Kempter, S., Rädler, J. O. and Simmel, F. C. (2005), Using gene regulation to program DNA- based molecular devices, *Small* **1**(7), 709–712.

Douglas, S. M., Chou, J. J. and Shih, W. M. (2007), DNA-nanotube-induced alignment of membrane proteins for NMR structure determination, *Proceedings of the National Academy of Sciences USA* **104**(16), 6644–6648.

Douglas, S. M., Dietz, H., Liedl, T., Högberg, B., Graf, F. and Shih, W. M. (2009), Self-assembly of DNA into nanoscale three-dimensional shapes., *Nature* **459**, 414–418.

Douglas, S. M., Marblestone, A. H., Teerapittayanon, S., Vazquez, A., Church, G. M. and Shih, W. M. (2009), Rapid prototyping of three-dimensional DNA-origami shapes with caDNAno, *Nucelic Acids Research* **37**, 5001–5006.

Eigler, D. M. and Schweizer, E. K. (1990), Positioning single atoms with a scanning tunnelling microscope, *Nature* **344**, 524–526.

Endo, M., Hidaka, K., Kato, T., Namba, K. and Sugiyama, H. (2009), DNA prism structures constructed by folding of multiple rectangular arms, *Journal of the American Chemical Society* **131**, 15570–15571.

Endo, M., Katsuda, Y., Hidaka, K. and Sugiyama, H. (2010*a*), Regulation of DNA methylation using different tensions in the double strands constructed in a defined DNA nanostructure, *Journal of the American Chemical Society* **132**, 1592–1597.

Endo, M., Katsuda, Y., Hidaka, K. and Sugiyama, H. (2010*b*), A versatile DNA nanochip for direct analysis of DNA base-excision repair, *Angew. Chem. Int. Ed.* **49**, 9412–9416.

Endo, M., Sugita, T., Katsuda, Y., Hidaka, K. and Sugiyama, H. (2010), Programmed-assembly system using DNA jigsaw pieces., *Chem. Eur. J.* **16**, 5362–5368.

Erben, C. (2007), Self-assembled DNA cages, PhD thesis, Department of Condensed Matter Physics, University of Oxford.

Erben, C. M., Goodman, R. P. and Turberfield, A. J. (2006), Single-molecule protein encapsulation in a rigid DNA cage, *Angew. Chem. Int. Ed.* **45**, 7414–7417.

Feng, L., Park, S., Reif, J. and Yan, H. (2003), A two-state DNA lattice switched by DNA nanoactuator, *Angew. Chem. Int. Ed.* **42**, 4342–4346.

Förster, T. (1965), *Modern Quantum Chemistry*, Academic, New York, pp. 93–137.

Gao, B., Sarveswaran, K., Bernstein, G. H. and Lieberman, M. (2010), Guided deposition of individual DNA nanostructures on silicon substrates, *Langmuir* **26**(15), 12680–12683.

Gartner, Z. J. and Liu, D. R. (2001), The generality of DNA-templated synthesis as a basis for evolving non-natural small molecules, *Journal of the American Chemical Society* **123**, 6961–6963.

Goodman, R. P. (2005), Nanev: a program employing evolutionary methods for the design of nucleic acid nanostructures, *Biotechniques* **38**(4), 548–550.

Goodman, R. P., Erben, C. E., Malo, J., Ho, W. M., McKee, M. L., Kapanidis, A. N. and Turberfield, A. J. (2009), A facile method for reversibly linking a recombinant protein to DNA, *ChemBioChem* **10**, 1551–1557.

Goodman, R. P., Schaap, I. A. T., Tardin, C. F., Erben, C. M., Berry, R. M., Schmidt, C. F. and Turberfield, A. J. (2005), Rapid chiral assembly of rigid DNA building blocks for molecular nanofabrication, *Science* **310**, 1661–1665.

Green, S., Bath, J. and Turberfield, A. J. (2008), Coordinated chemomechanical cycles: A mechanism for autonomous molecular motion, *Physical Review Letters* **101**(23), 238101.

Green, S., Lubrich, D. and Turberfield, A. J. (2006), DNA hairpins: Fuel for autonomous DNA devices, *Biophysical Journal* **91**(8), 2966–2975.

Grubmeyer, C., Cross, R. L. and Penefsky, H. S. (1982), Mechanism of ATP hydrolysis by beef heart mitochondrial ATPase. rate constants for elementary steps in catalysis at a single site, *The Journal of Biological Chemistry* **257**(20), 12092–12100.

Gu, H., Chao, J., Xiao, S. J. and Seeman, N. C. (2010), A proximity-based programmable DNA nanoscale assembly line., *Nature* **465**, 202–205.

Guo, P. (2010), The emerging field of RNA nanotechnology, *Nature nanotechnology* **5**, 833–842.

Han, D., Pal, S., Liu, Y. and Yan, H. (2010), Folding and cutting DNA into reconfigurable topological nanostructures, *Nature Nanotechnology* **5**, 712–717.

Hausrath, A. C., Grüber, G., Matthews, B. W. and Capaldi, R. A. (1999), Structural features of the gamma subunit of the Escherichia coli $F_1$ ATPase revealed by a 4.4-å resolution map obtained by x-ray crystallography, *Proceedings of the National Academy of Sciences USA* **96**(24), 13697–13702.

He, Y. and Liu, D. R. (2010), Autonomous multistep organic synthesis in a single isothermal solution mediated by a DNA walker, *Nature Nanotechnology* **5**, 778–782.

He, Y. and Mao, C. (2006), Balancing flexibility and stress in DNA nanostructures, *ChemComm* pp. 968–969.

He, Y., Ye, T., Su, M., Zhang, C., Ribbe, A. E., Jiang, W. and Mao, C. (2008), Hierarchical self-assembly of DNA into symmetric supramolecular polyhedra, *Nature* **452**, 198–201.

Heiter, D., Lunnen, K. D. and Wilson, G. G. (2005), Site-specific DNA-nicking mutants of the heterodimeric restriction endonuclease R.BbvCI, *Journal of Molecular Biology* **348**, 631–640.

Iijima, S. and Ichihashi, T. (1993), Single-shell carbon nanotubes of 1-nm diameter, *Nature* **363**, 603–605.

Iko, Y., Tabata, K. V., Sakakihara, S., Nakashima, T. and Noji, H. (2009), Acceleration of the ATP-binding rate of $F_1$-ATPase by forcible forward rotation, *FEBS Letters* **583**, 3187–3191.

Itoh, H., Takahashi, A., Adachi, K., Noji, H., Yasuda, R., Yoshida, M. and Kinosita, K. (2004), Mechanically driven ATP synthesis by $F_1$-ATPase, *Nature* **427**, 465–468.

Junge, W., Sielaff, H. and Engelbrecht, S. (2009), Torque generation and elastic power transmission in the rotary $F_O F_1$-ATPase, *Nature* **459**, 364–370.

Jungmann, R., Liedl, T., Sobey, T., Shih, W. and Simmel, F. (2008), Isothermal assembly of DNA origami structures using denaturing agents, *Journal of the American Chemical Society* **130**, 10062 – 10063.

Jungmann, R., Steinhauer, C., Scheible, M., Kuzyk, A., Tinnefeld, P. and Simmel, F. C. (2010), Single-molecule kinetics and super-resolution microscopy by fluorescence imaging of transient binding on DNA origami, *Nano Letters* **10**, 4756–4761.

Kabaleeswaran, V., Shen, H., Symersky, J., Walker, J. E., Leslie, A. G. W. and Mueller, D. M. (2009), Asymmetric structure of the yeast $F_1$ ATPase in the absence of bound nucleotides, *Journal of Biological Chemistry* **284**(16), 10546–10551.

Ke, Y., Lindsay, S., Chang, Y., Liu, Y. and Yan, H. (2008), Self-assembled water-soluble nucleic acid probe tiles for label-free RNA hybridization assays, *Science* **319**, 180–183.

Ke, Y., Sharma, J., Liu, M., Jahn, K., Liu, Y. and Yan, H. (2009), Scaffolded DNA origami of a DNA tetrahedron molecular container, *Nano Letters* **9**, 2445–2447.

Kershner, R. J., Bozano, L. D., Micheel, C. M., Hung, A. M., Fornof, A. R., Cha, J. N., Rettner, C. T., Bersani, M., Frommer, J., Rothemund, P. W. K. and Wallraff, G. M. (2009), Placement and orientation of individual DNA shapes on lithographically patterned surfaces, *Nature Nanotechnology* **4**, 557–561.

Koumura, N., Zijlstra, R. W. J., van Delden, R. A., Harada, N. and Feringa, B. L. (1999), Light-driven monodirectional molecular rotor, *Nature* **401**, 152–155.

Kramer, R. H. and Karpen, J. W. (1998), Spanning binding sites on allosteric proteins with polymer-linked ligand dimers, *Nature* **395**, 710–713.

Lata, S., Reichel, A., Brock, R., Tampé, R. and Piehler, J. (2005), High-affinity adaptors for switchable recognition of histidine-tagged proteins., *Journal of the American Chemical Society* **127**, 10205–10215.

Li, Z., Liu, M., Wang, L., Nangreave, J., Yan, H. and Liu, Y. (2010), Molecular behavior of DNA origami in higher-order self-assembly, *Journal of the American Chemical Society* **132**, 13545–13552.

Liedl, T., Högberg, B., Tytell, J., Ingber, D. E. and Shih, W. M. (2010), Self-assembly of three-dimensional prestressed tensegrity structures from DNA, *Nature Nanotechnology* **5**, 520–524.

Liu, H., Chen, Y., He, Y., Ribbe, A. E. and Mao, C. (2006), Approaching the limit: Can one DNA oligonucleotide assemble into large nanostructures?, *Angew. Chem.* **118**, 1976–1979.

Liu, Y., Lin, C., Li, H. and Yan, H. (2005), Aptamer-directed self-assembly of protein arrays on a DNA nanostructure, *Angew. Chem. Int. Ed.* **44**, 4333–4338.

Lo, P. K., Karam, P., Aldaye, F. A., McLaughlin, C. K., Hamblin, G. D., Cosa, G. and Sleiman, H. F. (2010), Loading and selective release of cargo in DNA nanotubes with longitudinal variation, *Nature Chemistry* **2**, 319–328.

Lubrich, D., Bath, J. and Turberfield, A. J. (2005), Design and assembly of double-crossover linear arrays of micrometre length using rolling circle replication, *Nanotechnology* **16**, 1574–1577.

Lund, K., Manzo, A. J., Dabby, N., Michelotti, N., Johnson-Buck, A., Nangreave, J., Taylor, S., Pei, R., Stojanovic, M. N., Walter, N. G., Winfree, E. and Yan, H. (2010), Molecular robots guided by prescriptive landscapes, *Nature* **465**, 206–210.

Malo, J., Mitchell, J. C., Vnien-Bryan, C., Harris, J. R., Wille, H., Sherratt, D. J. and Turberfield, A. J. (2005), Engineering a 2D protein-DNA crystal, *Angew. Chem. Int. Ed.* **44**, 3057–3061.

Markham, N. R. and Zuker, M. (2005), DINAMelt web server for nucleic acid melting prediction, *Nucelic Acids Research* **33**, W577–W581.

Maune, H. T., Han, S.-P., Barish, R. D., Bockrath, M., Goddard-III, W. A., Rothemund, P. W. K. and Winfree, E. (2009), Self-assembly of carbon nanotubes into two-dimensional geometries using DNA origami templates, *Nature Nanotechnology* **5**, 61–66.

McKee, M., Milnes, P., Bath, J., Stulz, E., Turberfield, A. and O'Reilly, R. (2010), Multistep DNA-templated reactions for the synthesis of functional sequence controlled oligomers, *Angew. Chem. Int. Ed.* **49**(43), 7948–7951.

Modi, S., Swetha, M. G., Goswami, D., Gupta, G. D., Mayor, S. and Krishnan, Y. (2009), A DNA nanomachine maps spatiotemporal pH changes in living cells, *Nature Nanotechnology* **4**, 325–330.

Moll, D., Huber, C., Schlegel, B., Pum, D., Sleytr, U. B. and Sara, M. (2002), S-layer-streptavidin fusion proteins as template for nanopatterned molecular arrays, *Proceedings of the National Academy of Sciences USA* **99**(23), 14646–14651.

Nakanishi-Matsui, M., Kashiwagi, S., Hosokawa, H., Cipriano, D. J., Dunn, S. D., Wada, Y. and Futai, M. (2006), Stochastic high-speed rotation of Escherichia coli ATP synthase $F_1$ sector: The $\epsilon$ subunit-sensitive rotation, *Journal of Biological Chemistry* **281**, 4126–4131.

Nakanishi-Matsui, M., Kashiwagi, S., Ubukata, T., Iwamoto-Kihara, A., Wada, Y. and Futai, M. (2007), Rotational catalysis of Escherichia coli ATP synthase $F_1$ sector: Stochastic fluctuation and a key domain of the subunit, *The Journal of Biological Chemistry* **282**(28), 20698–20704.

Nangreave, J., Han, D., Liu, Y. and Yan, H. (2010), DNA origami: a history and current perspective, *Current Opinion in Chemical Biology* **14**, 608–615.

Noji, H., Yasuda, R., Yoshida, M. and Kinoshita Jnr, K. (1997), Direct observation of the rotation of $F_1$-ATPase, *Nature* **386**, 299–302.

Numajiri, K., Kimura, M., Kuzuya, A. and Komiyama, M. (2010), Stepwise and reversible nanopatterning of proteins on a DNA origami scaffold, *ChemComm* **46**, 5127–5129.

Omabegho, T., Sha, R. and Seeman, N. C. (2009), A bipedal DNA brownian motor with coordinated legs, *Science* **324**(5923), 67–71.

Ouldridge, T. E., Louis, A. A. and Doye, J. P. K. (2010), DNA nanotweezers studied with a coarse-grained model of DNA, *Physical Review Letters* **104**, 178101.

Park, S., Pistol, C., Ahn, S. J., Reif, J. H., Lebeck, A. R., Dwyer, C. and LaBean, T. H. (2006), Finite-size, fully addressable DNA tile lattices formed by hierarchical assembly procedures, *Angew. Chem.* **118**, 749–753.

Pei, R., Taylor, S. K., Stefanovic, D., Rudchenko, S., Mitchell, T. E. and Stojanovic, M. N. (2006), Behavior of polycatalytic assemblies in a substrate-displaying matrix, *Journal of the American Chemical Society* **128**, 12693–12699.

Pilizota, T., Bilyard, T., Bai, F., Futai, M., Hosokawa, H. and Berry, R. (2007), A programmable optical angle clamp for rotary molecular motors, *Biophysical Journal* **93**(1), 264–275.

Reid, S. W., Leake, M. C., Chandler, J. H., Lo, C.-J., Armitage, J. P. and Berry, R. M. (2006), The maximum number of torque-generating units in the flagellar motor of Escherichia coli is at least 11, *Proceedings of the National Academy of Sciences USA* **103**(21), 8066–8071.

Rondelez, Y., Tresset, G., Nakashima, T., Kato-Yamada, Y., Fujita, H., Takeuchi, S. and Noji, H. (2005), Highly coupled ATP synthesis by $F_1$-ATPase single molecules, *Nature* **433**(7027), 773–777.

Rothemund, P. (2006), Folding DNA to create nanoscale shapes and patterns, *Nature* **440**, 297–302.

Rothemund, P. W. K., Papadakis, N. and Winfree, E. (2004), Algorithmic self-assembly of DNA sierpinski triangles, *PloS Biology* **2**(12), e424.

Sacc, B., Meyer, R., Erkelenz, M., Kiko, K., Arndt, A., Schroeder, H., Rabe, K. S. and Niemeyer, C. M. (2010), Orthogonal protein decoration of DNA origami, *Angew. Chem. Int. Ed.* **49**, 9378–9383.

Sannohe, Y., Endo, M., Katsuda, Y., Hidaka, K. and Sugiyama, H. (2010), Visualization of dynamic conformational switching of the g-quadruplex in a DNA nanostructure, *Journal of the American Chemical Society* **132**, 16311–16313.

Seelig, G., Soloveichik, D., Zhang, D. Y. and Winfree, E. (2006), Enzyme-free nucleic acid logic circuits, *Science* **314**, 1585.

Seelig, G., Yurke, B. and Winfree, E. (2006), Catalyzed relaxation of a metastable DNA fuel, *Journal of the American Chemical Society* **128**(37), 12211–12220.

Seeman, N. (1982), Nucleic acid junctions and lattices, *J. theor. Biol.* **99**, 237–247.

Sharma, J., Chhabra, R., Andersen, C., Gothelf, K., Yan, H. and Liu, Y. (2007), Toward reliable gold nanoparticle patterning on self-assembled DNA nanoscaffold, *Journal of the American Chemical Society* **130**, 7820–7821.

Sharma, J., Chhabra, R., Liu, Y., Ke, Y. and Yan, H. (2006), DNA-templated self-assembly of two-dimensional and periodical gold nanoparticle arrays, *Angew. Chem.* **118**, 744 –749.

Shen, W., Zhong, H., Neff, D. and Norton, M. L. (2009), NTA directed protein nanopatterning on DNA origami nanoconstructs, *Journal of the American Chemical Society* **131**, 6660–6661.

Sherman, W. B. and Seeman, N. C. (2004), A precisely controlled DNA biped walking device, *Nano Letters* **4**, 1203–1207.

Shih, W., Quispe, J. and Joyce, G. (2004), A 1.7-kilobase single-stranded DNA that folds into a nanoscale octahedron, *Nature* **427**, 618–621.

Shimabukuro, K., Yasuda, R., Muneyuki, E., Hara, K. Y., Kinosita, K., and Yoshida, M. (2003), Catalysis and rotation of $F_1$ motor: Cleavage of ATP at the catalytic site occurs in 1 ms before 40° substep rotation, *PNAS* **100**(25), 14731–14736.

Shin, J. S. and Pierce, N. A. (2004), A synthetic DNA walker for molecular transport, *Journal of the American Chemical Society* **126**, 10834–10835.

Simmel, F. (2009), Processive motion of bipedal DNA walkers, *ChemPhysChem* **10**(15), 2593–1597.

Smith, S. B., Finzi, L. and Bustamante, C. (1992), Direct mechanical measurements of the elasticity of single DNA molecules by using magnetic beads, *Science* **258**, 1122–1126.

Soong, R. K., Bachand, G. D., Neves, H. P., Olkhovets, A. G., Craighead, H. G. and Montemagno, C. D. (2000), Powering an inorganic nanodevice with a biomolecular motor, *Science* **290**, 1555–1558.

Sowa, Y., Steel, B. C. and Berry, R. M. (2010), A simple backscattering microscope for fast tracking of biological molecules., *Review of Scientific Instruments* **81**, 113704.

Steinhauer, C., Jungmann, R., Sobey, T. L., Simmel, F. C. and Tinnefeld, P. (2009), DNA origami as a nanoscopic ruler for super-resolution microscopy, *Angew. Chem. Int. Ed.* **48**, 8870–8873.

Stephanopoulos, N., Liu, M., Tong, G. J., Li, Z., Liu, Y., Yan, H. and Francis, M. B. (2010), Immobilization and one-dimensional arrangement of virus capsids with nanoscale precision using DNA origami, *Nano Letters* **10**, 2714–2720.

Stojanovic, M. N., Mitchell, T. E. and Stefanovic, D. (2002), Deoxyribozyme-based logic gates, *Journal of the American Chemical Society* **124**, 3555–3561.

Stojanovic, M. N. and Stefanovic, D. (2003), A deoxyribozyme-based molecular automaton, *Nature Biotechnology* **21**(9), 1069–1074.

Stoykovich, M. P., Müller, M., Kim, S.-O., Solak, H. H., Edwards, E. W., de Pablo, J. J. and Nealey, P. F. (2005), Directed assembly of block copolymer blends into nonregular device-oriented structures, *Science* **308**(5727), 1442–1446.

Subramani, R., Juul, S., Rotaru, A., Andersen, F. F., Gothelf, K. V., Mamdouh, W., Besenbacher, F., Dong, M. and Knudsen, B. R. (2010), A novel secondary DNA binding site in human topoisomerase I unravelled by using a 2D DNA origami platform, *ACS Nano* **4**(10), 5969–5977.

Suzuki, H., Yamada, A., Oiwa, K., Nakayama, H. and Mashiko, S. (1997), Control of actin moving trajectory by patterned poly(methylmethacrylate) track, *Biophysical Journal* **72**, 1997–2001.

Svoboda, K. and Block, S. M. (1994), Force and velocity measured for single kinesin molecules, *Cell* **77**(5), 773–784.

Taira, S., Du, Y. Z., Hiratsuka, Y., Konishi, K., Kubo, T., Uyeda, T. Q., Yumoto, N. and Kodaka, M. (2006), Selective detection and transport of fully matched DNA by DNA-loaded microtubule and kinesin motor protein, *Biotechnol. Bioeng.* **95**(3), 533–538.

Tang, L., Johnson, K. N., Ball, L. A., Lin, T., Yeager, M. and Johnson, J. E. (2001), The structure of Pariacoto virus reveals a dodecahedral cage of duplex RNA, *Nature Structual Biology* **8**(1).

Tian, Y., He, Y., Peng, Y. and Mao, C. (2005), A DNA enzyme that walks processively and autonomously along a one-dimensional track., *Angew. Chem. Int. Ed.* **44**, 4355–4358.

Tian, Y. and Mao, C. (2004), A pair of DNA circles continuously rolls against each other, *Journal of the American Chemical Society* **126**, 11410–11411.

Travers, A. A. (2004), The structural basis of DNA flexibility, *Phil. Trans. R. Soc. Lond. A* **362**, 1423–1438.

Travers, A. A. and Thompson, J. M. T. (2004), An introduction to the mechanics of DNA, *Phil. Trans. R. Soc. Lond. A* **362**, 1265–1279.

Turberfield, A. J., Mitchell, J. C., Yurke, B., Mills Jnr, A. P., Blakey, M. I. and Simmel, F. C. (2003), DNA fuel for free-running nanomachines, *Physics Review Letters* **90**(11), 118102.

Venkataraman, S., Dirks, R., Rothmund, P., Winfree, E. and Pierce, N. (2007), An autonomous polymerization motor powered by DNA hybridization, *Nature Nanotechnology* **2**, 490–494.

Voigt, N. V., Tørring, T., Rotaru, A., Jacobsen, M. F., Ravnsbæk, J. B., Subramani, R., Mamdouh, W., Kjems, J., Mokhir, A., Besenbacher, F. and Gothel, K. V. (2010), Single-molecule chemical reactions on DNA origami, *Nature Nanotechnology* **5**, 200–203.

von Delius, M., Geertsema, E. M., Leigh, D. A. and Tang, D.-T. D. (2010), Design, synthesis, and operation of small molecules that walk along tracks, *Journal of the American Chemical Society* **132**, 16134–16145.

Wang, Y., Singh, U. and Mueller, D. M. (2007), Mitochondrial genome integrity mutations uncouple the yeast Saccharomyces cerevisiae ATP synthase, *The Journal of Biological Chemistry* **282**(11), 8228–8236.

Wilson, D. S. and Szostak, J. W. (1999), In vitro selection of functional nucleic acids, *Annual Review of Biochemistry* **68**, 611–647.

Winfree, E., Liu, F., Wenzler, L. A. and Seeman, N. C. (1998), Design and self-assembly of two-dimensional DNA crystals, *Nature* **394**.

Yan, H., LaBean, T. H., Feng, L. and Reif, J. H. (2003), Directed nucleation assembly of DNA tile complexes for barcode-patterned lattices, *Proceedings of the National Academy of Sciences USA* **100**(14), 8103–8108.

Yan, H., Park, S., Finkelstein, G., Reif, J. and LaBean, T. (2003), DNA-templated self-assembly of protein arrays and highly conductive nanowires, *Science* **301**, 1882–1884.

Yan, H., Zhang, X., Shen, Z. and Seeman, N. C. (2002), A robust DNA mechanical device controlled by hybridization topology, *Nature* **415**, 62–64.

Yasuda, R., Noji, H., Kinosita, K. and Yoshida, M. (1998), $F_1$-ATPase is a highly efficient molecular motor that rotates with discrete 120° steps, *Cell* **93**, 1117–1124.

Yasuda, R., Noji, H., Yoshida, M., Kinoshita Jnr, K. and Itoh, H. (2001), Resolution of distinct rotational substeps by sub millisecond kinetic analysis of $F_1$-ATPase, *Nature* **410**, 898–904.

Yildiz, A., Forkey, J. N., McKinney, S. A., Ha, T., Goldman, Y. E. and Selvin, P. R. (2003), Myosin V walks hand-over-hand: single fluorophore imaging with 1.5-nm localization, *Science* **300**, 2061–2065.

Yildiz, A. and Selvin, P. R. (2005), Fluorescence imaging with one nanometer accuracy: Application to molecular motors, *Accounts of Chemical Research* **38**(7), 574–582.

Yildiz, A., Tomishige, M., Vale, R. D. and Selvin, P. R. (2004), Kinesin walks hand-over-hand, *Science* **303**, 676–678.

Yin, P., Choi, H. M. T., Calvert, C. R. and Pierce, N. (2008), Programming biomolecular self-assembly pathways, *Nature* **451**, 318–322.

Yin, P., Yan, H., Daniell, X. G., Turberfield, A. J. and Reif, J. H. (2004), A unidirectional DNA walker that moves autonomously along a DNA track., *Angew. Chem. Int. Ed.* **43**, 4906–4911.

York, J., Spetzler, D., Xiong, F. and Frasch, W. (2008), Single-molecule detection of DNA via sequence-specific links between $F_1$-ATPase motors and gold nanorod sensors., *Lab Chip* **8**(3), 415–419.

Yurke, B. and Mills Jnr, A. P. (2003), Using DNA to power nanostructures., *Genetic programming and Evolvable Machines* **4**, 111–122.

Yurke, B., Turberfield, A. J., Mills Jnr, A. P., Simmel, F. and Neumann, J. L. (2000), A DNA-fuelled molecular machine made of DNA, *Nature* **406**(6796), 605–608.

Zadeh, J., Steenberg, C., Bois, J., Wolfe, B., Pierce, M., Khan, A., Dirks, R. and Pierce., N. (2010), Nupack: analysis and design of nucleic acid systems, *J Comput Chem* **32**(1), 170–173.

Zhang, D. Y., Turberfield, A. J., Yurke, B. and Winfree, E. (2007), Engineering entropy-driven reactions and networks catalyzed by DNA, *Science* **318**, 1121–1125.

Zhang, D. Y. and Winfree, E. (2010), Robustness and modularity properties of a non-covalent DNA catalytic reaction, *Nucleic Acids Research* **38**, 4182–4197.

Zhang, Y. and Seeman, N. C. (1994), Construction of a DNA-truncated octahedron, *Journal of the American Chemical Society* **116**, 1661–1669.

Zhang, Z., Zeng, D., Ma, H., Feng, G., Hu, J., He, L., Li, C. and Fan, C. (2010), A DNA-origami chip platform for label-free SNP genotyping using toehold-mediated strand displacement, *Small* **6**(17), 1854–1858.

Zhao, Z., Yan, H. and Liu, Y. (2010), A route to scale up DNA origami using DNA tiles as folding staples, *Angew. Chem. Int. Ed.* **49**, 1–5.

Zheng, J., Birktoft, J. J., Chen, Y., Wang, T., Sha, R., Constantinou, P. E., Ginell, S. L., Mao, C. and Seeman, N. C. (2009), From molecular to macroscopic via the rational design of a self-assembled 3D DNA crystal, *Nature* **461**, 74–77.

Zhou, M., Liang, X., Mochizuki, T. and Asanuma, H. (2010), A light-driven DNA nanomachine for the efficient photoswitching of RNA digestion, *Angew. Chem. Int. Ed.* **49**, 2167–2170.

Zhu, L., Lukeman, P. S., Canary, J. W. and Seeman, N. C. (2003), Nylon/DNA: Single-stranded DNA with a covalently stitched nylon lining, *Journal of the American Chemical Society* **125**, 10178–10179.